UNIVERSITY OF TURKU

STUDYING WEAKLY MAGNETIZED NEUTRON STARS VIA POLARIZED X-RAYS

Anna Bobrikova

TURUN YLIOPISTON JULKAISUJA – ANNALES UNIVERSITATIS TURKUENSIS
SARJA - SER. AI OSA - TOM. 769 | ASTRONOMICA - CHEMICA - PHYSICA - MATHEMATICA | TURKU 2026

University of Turku

Faculty of Science
Department of Physics and Astronomy
Astronomy
Doctoral programme in Exact Sciences

Supervised by

Professor Juri Poutanen
Department of Physics and Astronomy
University of Turku
Turku, Finland

Docent Sergey Tsygankov
Department of Physics and Astronomy
University of Turku
Turku, Finland

Reviewed by

Dr. Alessandro Patruno
Institute of Space Sciences (ICE-CSIC)
Barcelona, Spain

Dr. Maria Diaz Trigo
European Southern Observatory (ESO)
Garching bei München, Germany

Opponent

Professor Manuel Linares Alegret
Norwegian University of Science and Technology (NTNU)
Trondheim, Norway

The originality of this publication has been checked in accordance with the University of Turku quality assurance system using the Turnitin OriginalityCheck service.

AI tools were used in the preparation of this dissertation for grammar checking and image quality enhancement.

Cover Image: Cosmic Winds of Change. Artist's impression of the powerful winds blowing from the bright X-ray source GX 13+1 © European Space Agency – ESA

ISBN 978-952-02-0834-9 (PRINT)
ISBN 978-952-02-0835-6 (PDF)
ISSN 0082-7002 (PRINT)
ISSN 2343-3175 (ONLINE)
Painosalama Oy, Turku, Finland, 2026

To my beloved grandfather,
Robert Iivonen,

who was born in 1942 in Strelna, Soviet Union;
who was relocated again and again,
along with tens of thousands of other Ingrian Finns;
who was neglected and discriminated against because of his origin;
who dedicated his life to honest work and to supporting the Ingrian community;
who died in 2025 in Heinola, Finland, a citizen and a proud Finn.

Joke's on them, Grandpa.

Thanks to you, we all made it home. And now, it seems,
all of us have finally made it at home.

UNIVERSITY OF TURKU
Faculty of Science
Department of Physics and Astronomy
Astronomy
BOBRIKOVA, ANNA: Studying weakly magnetized neutron stars via polarized X-rays
Doctoral dissertation, 118 pp.
Doctoral programme in Exact Sciences
June 2026

ABSTRACT

Neutron stars (NSs) are among the most extreme objects in the Universe. More massive than the Sun, smaller than the city of Turku, and denser than the atomic nuclei, they generate remarkable gravitational fields and influence their surroundings in space in unique ways. With their extreme gravity and strongest magnetic fields in the Universe, NSs are exceptional laboratories for studying the behavior of matter and light under conditions that cannot be reproduced on Earth. Consequently, studying NSs is crucial not only for astrophysics but also for fundamental physics.

In my doctoral research, I studied NSs residing in low-mass X-ray binary systems (LMXBs). In such systems, the extreme gravity of the NS affects the companion star, namely, it strips matter from the surface of the companion and attracts it towards the NS, forming an accretion flow. Once this matter reaches the NS surface, it heats up and emits radiation primarily in the X-ray range. The exact geometry of the accretion flow remains unknown; however, it is expected to depend on the balance between the NS magnetic field strength and the accretion rate. In some systems, the magnetosphere is strong enough to shape the accretion flow so that the matter follows the magnetic field lines and is directed towards the NS magnetic poles; such systems are known as accreting pulsars. In other systems, accretion happens at higher rates, and magnetosphere does not affect the accretion flow, so the matter falls onto the NS equator; these systems are referred to as weakly magnetized neutron stars (WMNS), and the brightest objects in the X-ray sky (after Sun) belong to this class. In my research, I worked with the WMNS systems as well as with a subclass of pulsars known as accreting millisecond pulsars (AMPs).

For decades, NSs has been studied with spectroscopic and timing instruments. These methods, however effective, are not particularly sensitive to the geometry of the accretion flow. Polarimetry, the study of the preferred directions of light wave oscillations, is the best approach at our disposal for investigating the geometrical configuration of the binary systems. X-ray polarimetry was barely available before late 2021, when the first ever mission dedicated to the X-ray polarimetry, *Imaging X-ray Polarimetry Explorer (IXPE)*, was launched. Since then, dozens of NS-LMXBs have been observed. During my doctoral research, I worked on IXPE observations of more than 15 WMNS systems and the only observation so far of an AMP. I contributed to the IXPE data analysis by developing analytical models for the expected polarized emission from these systems. The most significant results of this work are presented in this dissertation.

TURUN YLIOPISTO
Matemaattis-luonnontieteellinen tiedekunta
Fysiikan ja tähtitieteen laitos
Tähtitiede
BOBRIKOVA, ANNA: Studying weakly magnetized neutron stars via polarized X-rays
Väitöskirja, 118 s.
Eksaktien tieteiden tohtoriohjelma
Kesäkuu 2026

TIIVISTELMÄ

Neutronitähdet (NS) kuuluvat maailmankaikkeuden äärimmäisimpiin kohteisiin. Aurinkoa massiivisempina, Turun kaupunkia pienempinä ja atomiytimiä tiheämpinä ne tuottavat poikkeuksellisen voimakkaita painovoimakenttiä ja vaikuttavat ympäristöönsä avaruudessa ainutlaatuisin tavoin. NS tutkimus on keskeistä paitsi astrofysiikan myös perustavanlaatuisen fysiikan kannalta.

Väitöskirjatutkimuksessani tutkin NS pienimassaisissa röntgenkaksoisjärjestelmissä (LMXB). Tällaisissa järjestelmissä NS äärimmäinen painovoima vaikuttaa seuralaistähteen siten, että se riistää ainetta tämän pinnalta ja vetää sitä puoleensa muodostaen kertymävirtauksen. Kun tämä aine saavuttaa NS pinnan, se lämpenee ja säteilee pääasiassa röntgenalueella. Kertymävirtauksen tarkkaa geometriaa ei tunneta, mutta sen odotetaan riippuvan NS magneettikentän voimakkuuden ja kertymänopeuden välisestä tasapainosta. Joissakin järjestelmissä magnetosfääri on riittävän voimakas muokatakseen kertymävirtausta siten, että aine seuraa magneettikentän kenttäviivoja ja ohjautuu NS magneettisille navoille; tällaisia järjestelmiä kutsutaan akkretoiviksi pulsareiksi. Toisissa järjestelmissä kertymänopeus on suurempi eikä magnetosfääri vaikuta merkittävästi kertymävirtaukseen, jolloin aine putoaa NS ekvaattorille. Näitä järjestelmiä kutsutaan heikosti magnetoituneiksi neutronitähdiksi (WMNS), ja tähän luokkaan kuuluvat röntgentaivaan kirkkaimmat kohteet Auringon jälkeen. Tutkimuksessani työskentelin sekä WMNS-järjestelmien että erään pulsarien alaluokan, akkretoivien millisekuntipulsarien (AMP) kanssa.

NS on tutkittu vuosikymmenten ajan spektroskooppisilla ja ajoitusmittauksiin perustuvilla instrumenteilla. Nämä menetelmät ovat tehokkaita, mutta ne eivät ole erityisen herkkiä kertymävirtauksen geometrialle. Polarimetria, eli valoaallon värähtelysuuntien tutkimus, on paras käytettävissämme oleva menetelmä näiden kaksoistähtijärjestelmien geometrian selvittämiseksi. Röntgenpolarimetria oli käytännössä saatavilla vasta loppuvuodesta 2021 lähtien, jolloin ensimmäinen röntgenpolarimetriaan omistettu avaruusluotain, Imaging X-ray Polarimetry Explorer (IXPE), laukaistiin. Tämän jälkeen kymmeniä NS-LMXB-järjestelmiä on havaittu. Väitöskirjatyöni aikana työskentelin yli viidentoista WMNS-järjestelmän sekä toistaiseksi ainoan AMP-havainnon IXPE-aineiston parissa. Osallistuin IXPE-datan analyysiin kehittämällä analyyttisiä malleja näiden järjestelmien odotetulle polarisoidulle säteilylle. Tämän työn merkittävimmät tulokset esitetään tässä väitöskirjassa.

Acknowledgements

Looking back on the path that led me to this moment, I still struggle to comprehend how exactly I ended up here.

After majoring in mineralogy, working as an event coordinator and as a hairdresser, and seemingly choosing the most peculiar paths over the rational and obvious ones, I somehow managed to reach the milestone of defending a doctorate in astronomy. Without the slightest doubt or bias, I attribute this achievement to the endless support of the people around me rather than to any individual genius of my own. With an overwhelming feeling of gratitude, I mention only a handful here, in no particular order.

Above all, this dissertation is a tribute to my teachers and supervisors.

My deepest gratitude goes to Prof. Juri Poutanen, who kindly invited me to join his group and, over five years of my doctoral research, showed nothing but support and patience despite my limited knowledge, strong opinions, and somewhat unconventional collaboration practices (no, I will not share this on Overleaf either; let it go). His guidance shaped me as an astrophysicist; his trust helped secure my place in the X-ray community; most importantly, his kindness and understanding made me realize that science is hard, but it doesn't have to be brutal. I am also thankful to my second supervisor, Doc. Sergey Tsygankov, for always being there for his students and for the impeccable organization of our group meetings. Dr. Tuomo Salmi supervised my first research project in high-energy astrophysics, which took almost two years and resulted in Paper I of this dissertation. I am also grateful to Doc. Alexandra Veledina, who supervised Paper V of this thesis, for her enthusiasm and relentless attention to detail.

My journey toward astronomy did not begin at the University of Turku; rather, it began in middle school, after which I spent years, and eventually decades, finding ways to evade astronomy. I'm thankful to Yelena V. Zhabrunova, my school physics teacher, who also coordinated an astronomy club in our lyceum, and to Lyubov D. Yegorova, my math and geometry teacher, who introduced me to the exact sciences and made them feel accessible, useful, and compelling enough for me to pursue a degree in Applied Mathematics and Physics. Among those I met at St. Petersburg State University, I am especially grateful to Prof. Boris P. Lavrov, who helped me see a future in science, and Prof. Alexander Z. Devdariani, who supervised my first attempts at research and relentlessly told me "Не боги горшки обжигают", which

loosely translates to “Experts are only people, too.” It took quite some time for me to realize what these two esteemed professors were trying to teach me through both their words and their example, but they gave me enough hope to move forward. At the University of Siegen, I owe special thanks to Prof. Dr. Markus Risse, Dr. Marcus Niechciol, and Dr. Philip Rühl, who believed in me long before I did, introduced me to the field of high-energy physics, and warmly welcomed my many returns to Siegen.

Speaking of warm welcomes, I owe a great deal of thanks to the team at the Italian IXPE Headquarters at the INAF-IAPS institute in Rome and their director, Dr. Paolo Sofitta, who hosted and supported me during two research visits to their institute. My research path would have looked very different without the kind invitation of Dr. Alessandro Di Marco; both he and Dr. Fabio La Monaca are now among my closest collaborators and dear friends. I’m particularly thankful for the support they showed me during the writing of Paper II; leading a collaboration paper is a challenge for any researcher, let alone a third-year PhD student, but it felt manageable with their help.

Of all the papers that I co-authored during my doctoral research, only a small fraction were written without international collaborators. I benefited greatly from being part of the IXPE Science Team; I would especially like to thank Dr. Alessandro Papitto, Dr. Phil Kaaret, Dr. Mason Ng, Swati Ravi, and Dr. Andrea Gnarini, and I will shamelessly refer the reader to the Paper II author list for the full list of names I should have put here.

Beyond the IXPE collaboration, I have been fortunate to work closely with the X(PSI)-Men team, more formally known as the group of Prof. Anna L. Watts at the University of Amsterdam, and especially with Dr. Bas Dorsman, who relentlessly drew me into his projects and allowed me to contribute to the further development of the model derived in Paper I.

Enough about foreign lands, though; I’m happy to acknowledge the constant support from the Turku HEA group. Throughout my doctoral research, they kept me sane and social. (Well, they did their absolute best on both counts; don’t judge them too harshly.) Many thanks to my fellow doctoral researchers: Armin, Vlad, Vadzim, Yasir, Varpu, Sofia, Ale, Anagha, Anastasiia. What an incredible team we make! I’m grateful for all the conversations about both science and surviving, the endless support, our regular complaining sessions, and the chat for the most desperate times. Credit also goes to our post-docs, Yannis and Greg, who guided us through the struggles of academia and showed us that there is, in fact, life after the doctoral defense. I am excited to see what it looks like for myself now.

Balancing work and life is hard when your work seems to encompass your life; I’m grateful that I always had at least one choir-related activity to keep one foot in the world outside academia. The choral family at Turku Cathedral adopted me as one of their own; special thanks go to the TCYC choir, the tenors of the Oratory

Choir, Mari Schildt, and, above all, Anu Åberg. I also greatly appreciate the support of the European Choral Association, which has been both an inclusive community and my Plan B, something warm and grounding, yet powerful enough to balance a demanding scientific career. I owe a great deal to my colleagues from the two Youth Committees, the Board, and the Team. I want to mention Sonja Greiner and Dermot O'Callaghan in particular; thank you for always finding a place for me in your schedules, teams, and hearts.

Returning to science, I am grateful to the reviewers of this dissertation, Dr. Alessandro Patruno and Dr. Maria Diaz Trigo, for their time and for their thoughtful comments, suggestions, and corrections. I thank Prof. Manuel Linares for agreeing to serve as the opponent at my doctoral defense.

The work presented in this dissertation would not have been possible without the financial support of the Finnish Cultural Foundation, the research visit programs AHEAD2020 and ACME TNA, and the Centre of Excellence in Neutron-Star Physics.

The life behind this dissertation would not have been possible without my family. My warmest thanks are for my dearest friends, Poli and Kate. My mother, Dina, my sister, Kseniia, and my partner, Vlad, have been my greatest sources of love, strength, and happiness.

September 2026
Anna Bobrikova

Table of Contents

Acknowledgements **6**

Table of Contents **9**

Abbreviations **11**

List of Original Publications **13**

1 X-ray polarimetry **18**
1.1 Polarimetric properties of light 18
1.2 Thomson vs. Compton scattering 20
1.3 Imaging X-ray Polarimetry Explorer 21

2 Neutron stars **24**
2.1 Formation and main characteristics 24
2.2 Internal structure and the equation of state 25
2.3 Neutron star zoo 27
2.4 Neutron stars in low-mass X-ray binaries 30
2.4.1 NS-LMXB evolution 30
2.4.2 Accretion via Roche Lobe overflow 32

3 Non-pulsating weakly magnetized neutron stars **34**
3.1 Main characteristics 34
3.2 Spectral components 36
3.2.1 Boundary layer 37
3.2.2 Spreading layer 39
3.2.3 Accretion disk truncation 40
3.3 Classification and state transitions 40
3.4 X-ray polarimetry of weakly magnetized neutron stars 43
3.4.1 Theoretical predictions 43
3.4.2 Observational results 45
3.5 GX 13+1 46

4 Accreting millisecond pulsars **48**

4.1 Main characteristics 48
4.2 Pulse profile 49
4.3 X-ray polarimetry of accreting millisecond pulsars 51

5 Future prospects 53
5.1 New X-ray polarimetric instruments 53
5.2 Weakly magnetized neutron stars 54
5.3 Accretion millisecond pulsars 54

6 Summary of the original publications 56
I Polarized radiation from an accretion shock in accreting millisecond pulsars using exact Compton scattering formalism 56
II Discovery of a strong rotation of the X-ray polarization angle in the galactic burster GX 13+1 56
III New polarimetric study of the galactic burster GX 13+1 . . . 57
IV Polarized radiation from the spreading layer of weakly magnetized neutron stars 57
V Breaking the symmetry: X-ray polarization from a spreading layer on a tilted weakly magnetized neutron star 57

List of References 59

Original Publications 63

Abbreviations

AMP	accreting millisecond pulsar
ASI	Italian Space Agency
BL	boundary layer
CCD	color-color diagram
EoS	equation of state
eXTP	enhanced X-ray Timing and Polarimetry mission
FB	flaring branch
GOSox	Globe Orbiting Soft X-ray
HA	hard apex
HB	horizontal branch
HBOs	horizontal branch oscillations
HFN	high frequency noise
HID	hardness-intensity diagram
IS	island state
IXPE	Imaging X-ray Polarimetry Explorer
LB	lower banana
LFN	low frequency noise
LMXB	low-mass X-ray binary
NASA	National Aeronautics and Space Agency
NB	normal branch
NBOs	normal branch oscillations
NICER	Neutron star Interior Composition ExploreR
NS	neutron star
OSO 8	Orbiting Solar Observatory
PA	polarization angle

PD	polarization degree
QPO	quasi-periodic oscillations
RMP	rotation-powered millisecond pulsar
RVM	rotating vector model
RXTE	Rossi X-ray Timing Explorer
SA	soft apex
SL	spreading layer
UB	upper banana
VLFN	very low frequency noise
WD	white dwarf
WMNS	weakly magnetized neutron star
X-PSI	X-ray Pulse Simulation and Inference code
XRISM	X-Ray Imaging and Spectroscopy Mission

List of Original Publications

This dissertation is based on the following original publications, which are referred to in the text by their Roman numerals:

I A. Bobrikova, V. Loktev, T. Salmi, and J. Poutanen
Polarized radiation from an accretion shock in accreting millisecond pulsars using exact Compton scattering formalism
Astronomy & Astrophysics, 2023; 678: A99.

II A. Bobrikova, S. V. Forsblom, F. La Monaca, A. Di Marco, J. Poutanen, M. Ng, S. Ravi, V. Loktev, J. J. E. Kajava, F. Ursini, et al. (IXPE collaboration)
Discovery of a strong rotation of the X-ray polarization angle in the galactic burster GX 13+1
Astronomy & Astrophysics, 2024; 688: A170.

III A. Bobrikova, A. Di Marco, F. La Monaca, J. Poutanen, S. V. Forsblom, and V. Loktev
New polarimetric study of the galactic burster GX 13+1
Astronomy & Astrophysics, 2024; 688: A217.

IV A. Bobrikova, J. Poutanen, and V. Loktev
Polarized radiation from the spreading layer of weakly magnetized neutron stars
Astronomy & Astrophysics, 2025; 696: A181.

V A. Bobrikova, A. Veledina, J. Poutanen, and V. Loktev
Breaking the symmetry: X-ray polarization from a spreading layer on a tilted weakly magnetized neutron star
Astronomy & Astrophysics, submitted.

The original publications have been reproduced with the permission of the copyright holders.

List of publications not included in the thesis

VI M. Cocchi, A. Gnarini, S. Fabiani, F. Ursini, J. Poutanen, F. Capitanio, A. Bobrikova, R. Farinelli, A. Paizis, L. Sidoli, et al. (IXPE collaboration)
Discovery of strongly variable X-ray polarization in the neutron star low-mass X-ray binary transient XTE J1701−462
Astronomy & Astrophysics, 2023; 674: L10.

VII A. Di Marco, F. La Monaca, J. Poutanen, T. D. Russell, A. Anitra, R. Farinelli, G. Mastroserio, F. Muleri, F. Xie, M. Bachetti, et al. (IXPE collaboration, incl. A. Bobrikova)
First detection of X-ray polarization from the accreting neutron star 4U 1820−303
The Astrophysical Journal Letters, 2023; 953: L22.

VIII F. La Monaca, A. Di Marco, J. Poutanen, M. Bachetti, S. E. Motta, A. Papitto, M. Pilia, F. Xie, S. Bianchi, A. Bobrikova, et al. (IXPE collaboration)
Highly Significant Detection of X-Ray Polarization from the Brightest Accreting Neutron Star Sco X-1
The Astrophysical Journal Letters, 2024; 960: L11.

IX J. Rankin, F. La Monaca, A. Di Marco, J. Poutanen, A. Bobrikova, V. Kravtsov, F. Muleri, M. Pilia, A. Veledina, R. Fender, et al. (IXPE collaboration)
X-Ray Polarized View on the Accretion Geometry in the X-Ray Binary Circinus X-1
The Astrophysical Journal Letters, 2024; 961: L8.

X S. Fabiani, F. Capitanio, R. Iaria, J. Poutanen, A. Gnarini, F. Ursini, R. Farinelli, A. Bobrikova, J.F. Steiner, J. Svoboda, et al. (IXPE collaboration)
Discovery of a variable X-ray polarization with the energy-dependent polarization angle from the accreting neutron star GX 5−1
Astronomy & Astrophysics, 2024; 684: A137.

XI M. L. Saade, P. Kaaret, A. Gnarini, J. Poutanen, F. Ursini, S. Bianchi, A. Bobrikova, F. La Monaca, A. Di Marco, F. Capitanio, et al.
X-Ray Polarimetry of the Dipping Accreting Neutron Star 4U 1624−49
The Astrophysical Journal, 2024; 963: 133.

XII F. Ursini, A. Gnarini, F. Capitanio, A. Bobrikova, M. Cocchi, A. Di Marco, S. Fabiani, R. Farinelli, F. La Monaca, J. Rankin, et al.

Review: The IXPE View of Neutron Star Low-Mass X-ray Binaries
Galaxies, 2024; 12(4).

XIII F. Ursini, A. Gnarini, S. Bianchi, A. Bobrikova, F. Capitanio, M. Cocchi, S. Fabiani, R. Farinelli, P. Kaaret, G. Matt, et al.
X-ray spectropolarimetry of the bright atoll Serpens X-1
Astronomy & Astrophysics, 2024; 690: A200.

XIV A. Bobrikova & S. V. Forsblom.
Accretion onto weakly magnetized neutron stars: polarization theory and its application to X-ray burster GX 13+1
Astronomische Nachrichten, 2024; 364(1): e20240128.

XV F. La Monaca, A. Di Marco, R. M. Ludlam, A. Bobrikova, J. Poutanen, S. Li, and F. Xie
X-ray spectropolarimetric characterization of GX 340+0 in the horizontal branch: A highly inclined source?
Astronomy & Astrophysics, 2024; 691: A253.

XVI A. Gnarini, R. Farinelli, F. Ursini, S. Bianchi, F. Capitanio, G. Matt, M. Ng, A. Tarana, A. Bobrikova, M. Cocchi, et al.
First spectropolarimetric observation of the neutron star low-mass X-ray binary GX 3+1
Astronomy & Astrophysics, 2024; 692: A123.

XVII A. Papitto, A. Di Marco, J. Poutanen, T. Salmi, G. Illiano, F. La Monaca, F. Ambrosino, A. Bobrikova, M. C. Baglio, C. Ballocco, et al.
Discovery of polarized X-ray emission from the accreting millisecond pulsar SRGA J144459.2−604207
Astronomy & Astrophysics, 2025; 694: A37.

XVIII A. Di Marco, F. La Monaca, A. Bobrikova, L. Stella, A. Papitto, J. Poutanen, M. C. Baglio, M. Bachetti, V. Loktev, M. Pilia, et al.
X-Ray Dips and Polarization Angle Swings in GX 13+1
The Astrophysical Journal Letters, 2025; 979: L47.

XIX T. Salmi, B. Dorsman, A. L. Watts, A. Bobrikova, A. Di Marco, V. Loktev, A. Papitto, M. Pilia, J. Poutanen, and J. Rankin.
Modelling polarized X-ray pulses from accreting millisecond pulsars with X-PSI, using different hot spot locations and shapes
Monthly Notices of the Royal Astronomical Society, 2025; 538(4): 2562–2568.

XX B. Dorsman, T. Salmi, A. L. Watts, M. Ng, S. Kamath, A. Bobrikova, J. Poutanen, V. Loktev, Y. Kini, D. Choudhury, et al.
Parameter constraints for accreting millisecond pulsars with synthetic NICER data
Monthly Notices of the Royal Astronomical Society, 2025; 538(4): 2853–2868.

XXI A. Tarana, F. Capitanio, A. Gnarini, S. Fabiani, F. Ursini, S. Bianchi, C. Ferrigno, M. Parra, M. Cocchi, R. Farinelli, et al. (incl. A. Bobrikova)
X-ray spectro-polarimetry analysis of the weakly magnetized neutron star X-ray binary GX 9+1
Astronomy & Astrophysics, 2025; 698: A245.

XXII F. La Monaca, A. Bobrikova, J. Poutanen, F. Coti Zelati, M. Pilia, A. Veledina, M. Bachetti, V. Loktev, and F. Xie.
IXPE view of the Sco-like source GX 349+2 in the normal branch
Astronomy & Astrophysics, 2025; 702: A40.

XXIII F. La Monaca, A. Di Marco, F. Coti Zelati, A. Bobrikova, R. M. Ludlam, J. Poutanen, A. Marino, S. Li, F. Xie, H. Feng, et al.
X-ray spectropolarimetric characterisation of the Z source GX 340+0 in the normal branch
Astronomy & Astrophysics, 2025; 702: A101.

XXIV B. Dorsman, T. Salmi, A. L. Watts, M. Ng, A. Bobrikova, V. Loktev, J. Poutanen, and J. Wilms.
Pulse profile modelling of the accretion-powered millisecond pulsar SAX J1808.4−3658 using NICER data from its 2019 and 2022 outbursts
Monthly Notices of the Royal Astronomical Society, 2025; 545(2): staf1983.

XXV A. Gnarini, S. Ravi, P. Kaaret, A. Bobrikova, J. Poutanen, S. V. Forsblom, F. Ursini, M.C. Baglio, S. Bianchi, F. Capitanio, et al.
Discovery of High X-Ray Polarization from the Neutron Star Low-Mass X-Ray Binary Cyg X-2 in the Horizontal Branch
The Astrophysical Journal, 2026; 997: 299.

XXVI M. A. Díaz Teodori, A. Bobrikova, A. Gnarini, F. Ursini, S. V. Forsblom, J. Poutanen, A. Salganik, S. Bianchi, F. Capitanio, M. Cocchi, et al.

X-Ray Polarization from the Atoll 4U 1735−44 Suggests a Low Inclination
The Astrophysical Journal, 2026; 1002: 143.

XXVII B. Dorsman, T. Salmi, A. L. Watts, M. Ng, A. Bobrikova, A. Di Marco, D. K. Galloway, S. Guillot, M. Hoogkamer, Y. Kini, et al.
Pulse profile modelling of the 2024 outburst of the accreting millisecond pulsar SRGA J144459.2−604207
Monthly Notices of the Royal Astronomical Society, 2026; 551(1): stag1340.

1 X-ray polarimetry

1.1 Polarimetric properties of light

Light is a wave, and light is a particle. In both approaches, a concept of polarization of light can be introduced.

Light is a transverse wave, i.e., a wave that oscillates in a direction perpendicular to the wave propagation. A light wave consists of coupled oscillating electric and magnetic fields. The geometrical orientation of the electric field vector oscillations is described by polarization. Alternatively, light can be viewed as a stream of photons, each of which has a spin, or a rotation direction with respect to the direction of travel. The polarization of light is then described by the superposition of the spins of all photons.

In order to properly describe polarimetric properties of light, let us now introduce mathematical formalism for the position of the electric field vector. If the wave propagates along the $\hat{z}$ axis with time t, the position of the electric vector on the $\hat{x}\hat{y}$ plane is described as:

$$\begin{aligned} \hat{\mathcal{E}}(z,t) &= \mathcal{E}_x\hat{x} + \mathcal{E}_y\hat{y}, \\ \mathcal{E}_x &= a_x \cos\left[\omega(t - \frac{z}{c}) + \varphi_x\right], \\ \mathcal{E}_y &= a_y \cos\left[\omega(t - \frac{z}{c}) + \varphi_y\right], \end{aligned} \tag{1}$$

where a_x and a_y are the amplitudes along the $\hat{x}$ and $\hat{y}$ axes, respectively, ω is the wave frequency, c is the wave propagation speed, and φ_x and φ_y are phases of the oscillations along the $\hat{x}$ and $\hat{y}$ axes, respectively.

Electric field vector traces an ellipse on the $\hat{x}\hat{y}$ plane. This general case is referred to as elliptical polarization. Two extreme cases are often discussed: linear polarization and circular polarization. In the case of linear polarization, the ellipse collapses into a line on the $\hat{x}\hat{y}$ plane, which can be achieved if either $a_x = 0$, $a_y = 0$, or $\varphi = \varphi_y - \varphi_x = 0$ or π. On the other hand, circular polarization is a case in which $a_x = a_y$ and $\varphi = \pm\pi/2$.

Thus, each wave has a polarization, but what about light itself? Natural light is not polarized: each light wave coming from the Sun has its own direction of electric field oscillation, so each wave train has a mixture of waves polarized in all possible

directions. Such light is called unpolarized. However, light can obtain polarization through interactions; for instance, reflection can align the oscillations of the electric field. It is important to note that polarization corresponds to a preferred orientation of the electric vector; light is considered polarized if some waves within a wave train are polarized in the same direction. If all waves have the same orientation of the electric field vector, the light is referred to as completely polarized.

The quantitative description of the polarimetric properties of elliptically polarized light is given using the Stokes four-vector, whose components are derived from Eq. (1) as follows:

$$\begin{aligned} I &= a_x^2 + a_y^2, \\ Q &= a_x^2 - a_y^2, \\ U &= 2a_x a_y \cos\varphi, \\ V &= 2a_x a_y \sin\varphi. \end{aligned} \tag{2}$$

Physically, I represents the total intensity of the radiation, Q and U describe the linear polarization, and V describes the circular polarization.

Eq. (2) describes the Stokes parameters of fully polarized light. In this case, $I^2 = Q^2 + U^2 + V^2$, while for partially polarized light this equation turns into an inequality, $I^2 > Q^2 + U^2 + V^2$, and Eq. (2) becomes slightly more complicated.

In the research presented in this dissertation, I worked with linear polarization, neglecting the Stokes parameter V. The main reason for omitting circular polarization lies, of course, in the absence of detectors capable of measuring circular polarization in the X-ray band. Furthermore, the emission and propagation mechanisms considered in this work are expected to produce predominantly linear polarization, while circular polarization is expected to be negligible. In principle, the circular polarization Stokes parameter V is affected by relativistic effects in the same way as the intensity I. Moreover, V is conserved along a photon trajectory in the absence of plasma effects; hence, omitting circular polarization does not affect the results obtained for the other Stokes parameters.

In the case of linear polarization, two standard polarimetric parameters are derived from the components of the Stokes vector: the polarization degree (PD) and the polarization angle (PA). The PD represents the fraction of light that has the same electric vector orientation,

$$\mathrm{PD} = \frac{\sqrt{Q^2 + U^2}}{I}, \tag{3}$$

while PA describes the orientation of the linear polarization vector on the $\hat{x}\hat{y}$ plane and is defined as

$$\mathrm{PA} = \frac{1}{2}\arctan\left(\frac{U}{Q}\right), \tag{4}$$

with appropriate quadrant corrections applied. The factor of one-half reflects the invariance of linear polarization under a rotation of 180°.

1.2 Thomson vs. Compton scattering

As mentioned above, natural light is not polarized, but several processes are known to introduce polarization. For instance, synchrotron radiation produced by charged particles spiraling along magnetic field lines is strongly polarized. In the presence of a very strong magnetic field, the vacuum birefringence effect also becomes important. However, since this doctoral research is focused on X-ray features of compact objects with weak magnetic field, the prime polarizing process of interest is scattering.

In classical electromagnetism, a process of elastic scattering of photons off free charged particles is referred to as Thomson scattering. Thomson scattering describes the case in which the photon energy is significantly lower than the rest-mass energy of the charged particle by which it is scattered. In Thomson scattering, a photon does not gain energy during the interaction; however, it becomes polarized with PD of

$$\mathrm{PD} = \frac{1 - \cos^2\theta}{1 + \cos^2\theta}, \tag{5}$$

where θ is the scattering angle.

In quantum electrodynamics, a similar but inelastic scattering process is referred to as Compton scattering. In this process, the photon energy changes after scattering. The Compton scattering cross-section for an unpolarized photon off a free electron at rest is described by the Klein-Nishina formula:

$$\frac{\mathrm{d}\sigma}{\mathrm{d}\Omega} = \frac{1}{2} r_\mathrm{e}^2 \frac{E'^2}{E^2} \left[\frac{E'}{E} + \frac{E}{E'} - \sin^2\theta \right], \tag{6}$$

where r_e is the classical electron radius, and E and E' are energies of the incident and scattered photons, respectively. For scattering off hot electrons, however, requires a more careful treatment. The polarization that photon gains through Compton scattering is also not so straightforward to calculate; in Nagirner & Poutanen (1994), a complete mathematical description of a single Compton scattering calculation is presented.

Thomson scattering is the low-energy limit of Compton scattering; when the difference between the wavelengths of the incident and scattered photons is negligibly small, the Klein-Nishina formula is reduced to the Thomson cross-section. The polarimetric picture is similar; Fig. 1 illustrates the PD calculated for scattering off electrons with different temperatures; here, PD resulting from inverse Compton scattering is considered. One can see that, while in the case of $kT_\mathrm{e} = 0$ the result coincides with Eq. 5, at higher electron energies the PD decreases, and the peak shifts from $\theta = 90°$ to smaller scattering angles.

All three processes, Thomson scattering, Compton scattering, and inverse Compton scattering, are relevant for studying various astrophysical phenomena. For some

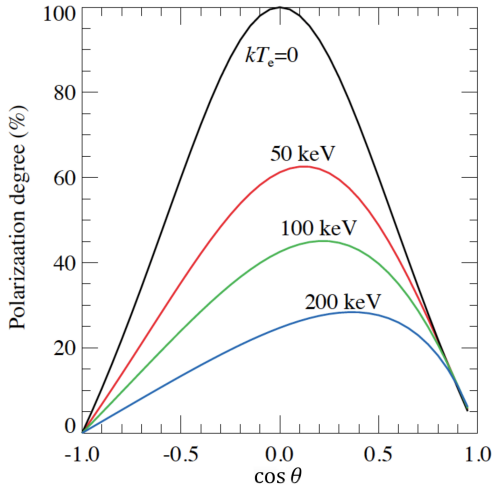


Figure 1. Photon PD as a function of a cosine of a scattering angle θ for scattering off electrons of different energy. Adapted from Poutanen (1994).

systems, Thomson scattering is a reasonable approximation, especially when the energies of the emitted photons and the scattering media are low; for instance, in Papers IV and V, we use the Thomson scattering approximation. On the other hand, the main motivation behind Paper I is the importance of exact Compton scattering calculations for polarimetric predictions in that particular case.

1.3 Imaging X-ray Polarimetry Explorer

Measuring the polarization of X-ray light is no easy task. Despite X-ray spectrometers orbiting Earth for decades, the first dedicated X-ray polarimetry mission, *Imaging X-ray Polarimetry Explorer (IXPE)*, was only launched in December 2021, and not for the lack of trying. Weisskopf (2018) and Costa (2024) review historic missions, instrumentation details, and the main challenges of X-ray polarimetry. The first efforts were made back in the 1970s with sounding rockets, and at least two orbital missions, *Orbiting Solar Observatory (OSO 8)* and *Ariel V*, had polarimeters on board. However, until the launch if *IXPE*, only a few polarimetric detections had been reported (see, for instance, Novick et al. 1972; Weisskopf et al. 1978; Long et al. 1980).

IXPE (Weisskopf et al. 2022) marked a new era of X-ray polarimetry. Since its launch, hundreds of discoveries were made using *IXPE* data and joint spectro-polarimetric campaigns. *IXPE* observations also stimulated theoretical research aimed at supporting data interpretation. For many classes of astronomical objects, it has changed our perspective on these objects and on the processes that form their emission. A joint project of National Aeronautics and Space Agency (NASA) and Italian

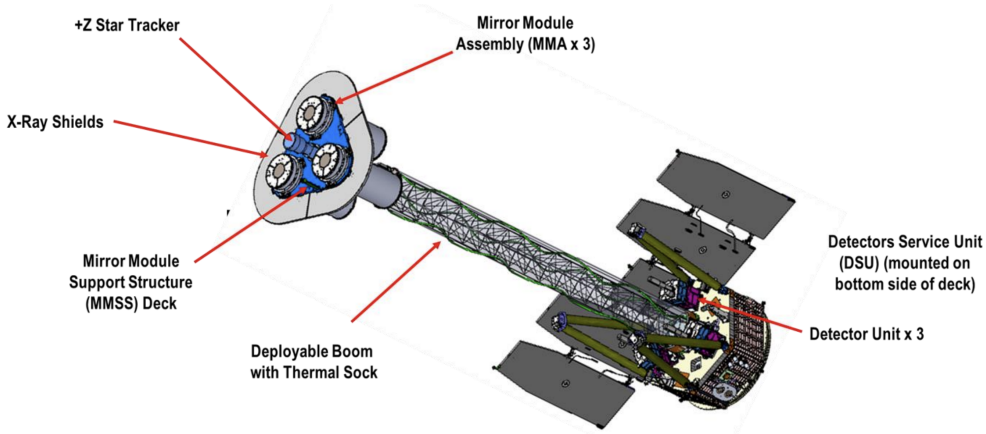


Figure 2. Scheme of the *IXPE* satellite. Key scientific payload elements are highlighted. From Weisskopf et al. (2022).

Space Agency (ASI), it was originally designed for a two-year scientific mission and has been extended for at least four more years of operation.

The main components of the *IXPE* satellite are marked in Fig 2. There are three identical instruments on board *IXPE*; each instrument consists of a gas pixel detector at the focus of a mirror module assembly. A 4-meter-long deployable boom separates the mirrors from the detectors, while two star trackers support the pointing of the instrument. The detectors are shielded from X-ray radiation that did not pass through the mirror modules by a combination of shields around the mirrors and a collimator on top of each detector. Although each telescope has a field of view of 11′, their overlapping field of view is 9′. *IXPE* detectors measure linear polarization in the energy range of $2 - 8$ keV.

The gas pixel detector units of *IXPE* are based on the photoelectric effect. A schematic image of the detector and an example of a detected track are shown in Fig. 3. An X-ray photon enters the detector unit and is absorbed by the gas (dimethyl ether); a photoelectron is then emitted. The photoelectron track is subsequently detected and analyzed. While the initial emission direction of the photoelectron is aligned with the X-ray polarization vector, both the initial interaction point and the total charge in the track contain information about the energy of the initial X-ray photon. For each detected photon, the detector units provide the position on the detector, energy, Stokes parameters describing linear polarization, and a time of arrival. An elaborate introduction to *IXPE* data analysis is provided in Di Marco (2026).

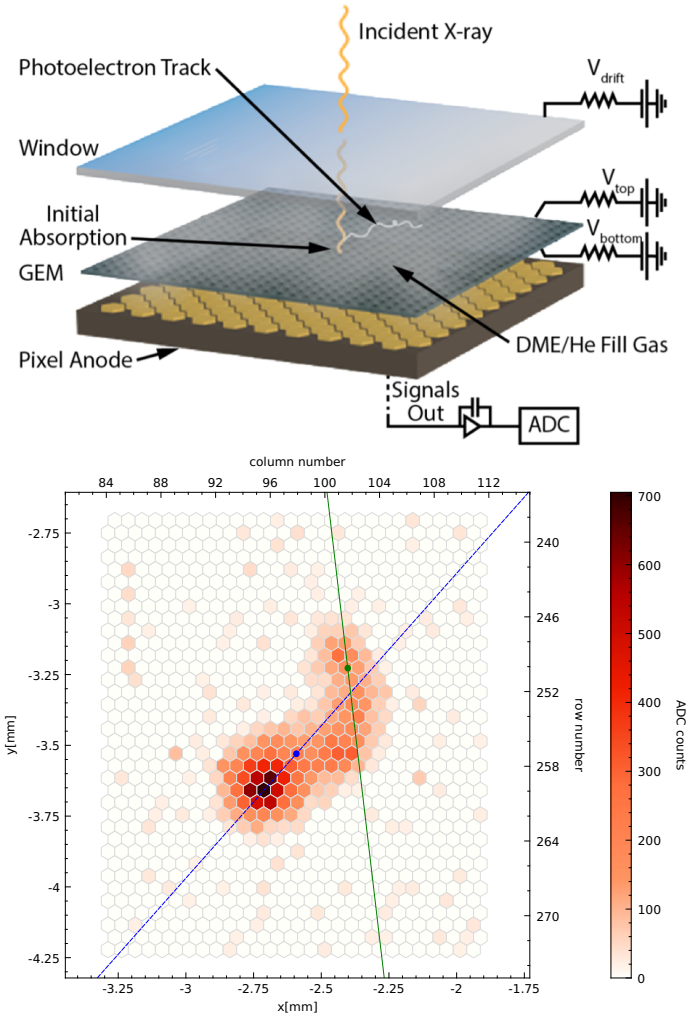


Figure 3. Left: schematic image of an *IXPE* detector unit. GEM stands from Gas Electron Multiplier, while DME stands for dimethyl ether. From Di Marco et al. (2022). Right: a real track from a 5.9 keV photon. The blue line and point mark the principal axis and the barycenter of the track, while the green line and point mark the estimate of the photoelectron direction and photon absorption point. From Baldini et al. (2021).

2 Neutron stars

2.1 Formation and main characteristics

Stars are powered by nuclear fusion and exist in a state of equilibrium between the radiative pressure caused by the nuclear fusion energy release and the gravitational pull. Nuclear fusion slowly builds the iron-rich core of the star; once the core has exhausted its fusion potential, radiative pressure can no longer balance gravity, so the core is supported by the degeneracy pressure alone. In massive stars ($M > 8\ M_\odot$), the increasing gravity forces the electrons and protons to form neutrons via electron capture, releasing neutrinos; electron degeneracy cannot support the core any further, leading to core collapse, while the outer layers of the star are ejected by the collapse shock. In very massive stars ($M > 25\ M_\odot$), this collapse leads to the formation of a black hole; however, in the stars with a mass between 8 and 25 $M_\odot$, the collapse is stopped by the neutron degeneracy pressure and strong repulsive force; this collapsed core is called a neutron star (NS).

Since a NS is born from the collapse of a massive star core, it inherits the star's angular momentum and magnetic field, which are strongly enhanced due to significantly reduced radius of the star. Young NSs rotate with a period of a few tens of milliseconds; their magnetic field is expected to be around 10^{12} G (for comparison, the magnetic field of the Sun is roughly 1 G). Despite the fact that no fusion is happening in NSs, their surface is still remarkably hot; for a newly born NS, the temperature is estimated at 10^9 K, and it rapidly decreases with time; for NSs aged $10^3 - 10^6$ yr, a characteristic temperature of 10^6 K is traditionally given (for the review on temperatures and cooling mechanisms, see Yakovlev & Pethick 2004).

The mass and radius of a NS are of key interest. From observation, the "canonical" NS mass of 1.4 $M_\odot$ was selected. Nowadays, masses have been measured for dozens of NSs, ranging from $1.174 \pm 0.004\ M_\odot$ for PSR J0453+1559 (Martinez et al. 2015) to $2.35 \pm 0.17\ M_\odot$ for PSR J0952−0607 (Romani et al. 2022). The radius of a NS is mostly calculated using various mass-radius equations for the extremely dense matter for a specific value of the NS mass; the "canonical" value is 12 km, while for a mass of 1.4 $M_\odot$, a range between 10.4 km and 12.9 km is traditionally cited (Steiner et al. 2013). Gravitational waves from a NS-NS binary merger also provide information about mass and radius, see, for instance, Abbott et al. (2018) for radius constraints from the GW170817 event, and Sect. VI B in Chatziioannou et al. (2025) for a review on mass constraints from 5 gravitational wave detections.

Whatever the exact values of the mass and radius may be, an object with a radius of 12 km and a mass exceeding that of the Sun is extremely dense, with a density exceeding that of an atomic nucleus. Such densities have never been reproduced on Earth, making NSs unique laboratories for dense matter studies.

2.2 Internal structure and the equation of state

NSs have layered structure. In literature, many ways of distinguishing the exact layers are reported; I adapt the structure presented in Burgio et al. (2021), where the outer crust, inner crust, and core are described. The outer crust (with density increasing from $\approx 10^4 \mathrm{g/cm^3}$ at the surface to $\approx 10^{11} \mathrm{g/cm^3}$) consists of a lattice of neutron-rich nuclei embedded in a degenerate electron gas; in the inner crust, where the density rises from $\approx 10^{11} \mathrm{g/cm^3}$ to $\approx 10^{14} \mathrm{g/cm^3}$, neutrons are released from the crystal lattice and form a gas around it. The whole crust is of only $1 - 2$ km thick and is solid, forming one of the strongest known materials in the universe. The core, with a density exceeding $10^{14} \mathrm{g/cm^3}$, is described as a homogeneous liquid, the exact composition of which is not known to this day. Over the years, many theories have been developed for the composition and properties of the NS core matter; however, since we cannot directly observe and probe this matter, definitively choosing the correct theory is a challenge. The EoS of the NS core is one of the fundamental open questions in astrophysics.

The pioneering work on the EoS was done by Oppenheimer and Volkoff shortly after the prediction of the existence of NSs. In Oppenheimer & Volkoff (1939), they constructed the first relativistic EoS in which they assumed that the entire NS consisted of a free neutron Fermi gas. This prediction gives a very soft EoS, with an upper limit on the NS mass of around 0.7 $M_\odot$, which is of course unrealistic. The predictions evolved with our understanding of elementary particle physics; once new particles were predicted and found, alternative compositions of the NS core were suggested (for a review see, for instance, Ji et al. 2025, and references therein). Based on the composition, all the modern models can be separated into:

- hadronic matter models assuming that the NSs are composed of nucleons, sometimes adding hyperons or meson condensates;
- quark matter models, in which the NSs (sometimes also referred to as strange stars) are composed of deconfined quarks;
- hybrid models that suggest a transition from hadronic matter to quark matter at a given density.

In terms of methodology, approaches to EoS construction can be divided into microscopic approaches, which are based on particle interactions and are created by solving the many-body problem; phenomenological approaches, which are based

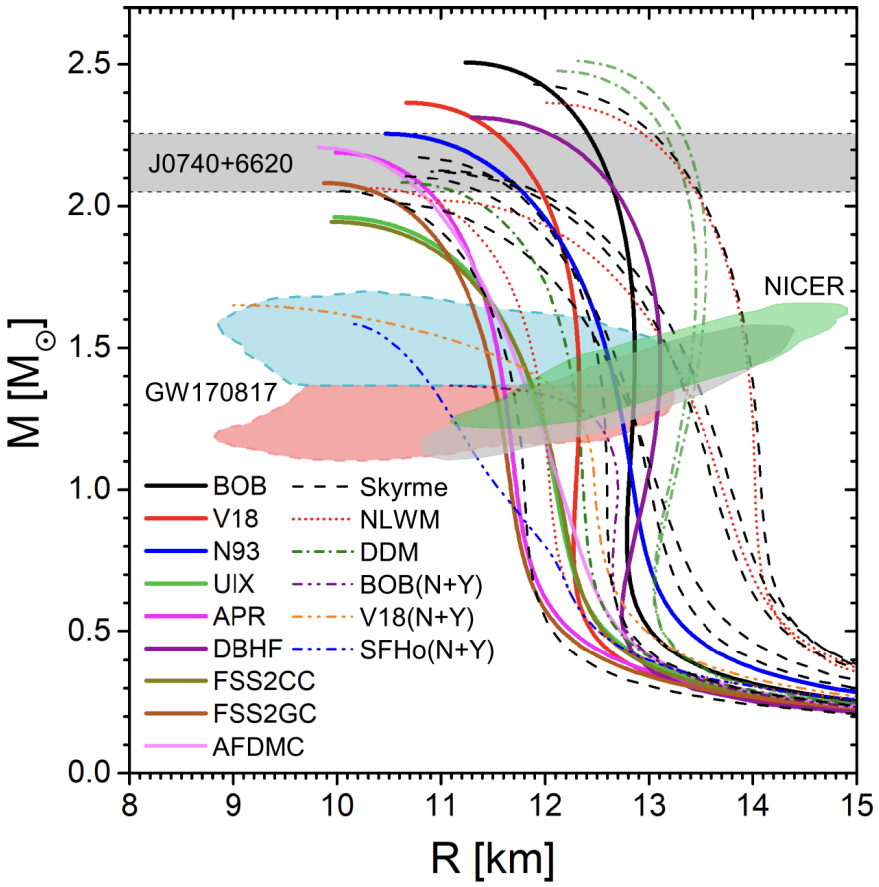


Figure 4. Mass-radius relations calculated with different equation of state (EoS) models. Microscopic models are shown with solid lines, and phenomenological models are shown with broken lines. Observational constraints from *NICER* observations of PSR J0030+0451 (Riley et al. 2019; Miller et al. 2019), the gravitational wave event GW170817 (Abbott et al. 2017), and a radio and optical campaign on PSR J0740+6620 (Cromartie et al. 2020) are labeled in the plot. From Burgio et al. (2021).

on fits to nuclear physics data; or models built by inference based on observationally provided constraints. These constraints come, for instance, from measuring the masses and radii of NSs, but also from tidal deformability that can be obtained from the gravitational-wave detections and from nuclear physics experiments.

An illustration of the ongoing process of creating new models and adding observational constraints is given in Fig. 4. There, mass-radius relations from various microscopic and phenomenological models are compared to mass and radius constraints from Neutron star Interior Composition ExploreR (NICER) observations of PSR J0030+0451 (Riley et al. 2019; Miller et al. 2019), the gravitational wave event GW170817 (Abbott et al. 2017), as well as a radio and optical campaign on PSR J0740+6620 (Cromartie et al. 2020). The exact details of the various EoS models are described in Burgio et al. (2021).

2.3 Neutron star zoo

Neutron stars come in a broad variety of flavors. Pulsating, transient, and persistent, visible in different energy ranges from radio to gamma-rays, bright and dim, they emit via different mechanisms and reside in very different environments. Each subclass is remarkable in its own way, and there are always unique objects that do not fit into any category and stand out. Most of the pulsating NSs can be placed on a $P - \dot{P}$ diagram, which illustrates the NS population diversity and common traits of different sub-classes. The characteristic age, $\tau_c = P/2\dot{P}$, and the magnetic field estimate $B \propto \sqrt{P\,\dot{P}}$ derived in the rotating magnetic dipole approximation (see, for instance, Di Salvo & Sanna 2022), are also indicated there.

There are many approaches to NS classification: for instance, isolated NSs can be separated from the ones located in binary systems, weakly magnetized ones can be separated from highly magnetized ones, young ones from old ones, etc. Here, I adopt a division by the mechanism powering the NS emission.

The first and most important powering mechanism for the work presented in this dissertation is accretion, an accumulation of matter by the gravitational pull. Several examples of sub-classes of accretion-powered NSs are:

- X-ray pulsars reside predominantly in high-mass X-ray binaries and accrete matter either from the strong radiation-driven wind surrounding their companion or from the decretion disk around a Be star. These systems exhibit spin-up and spin-down phases due to changing accretion regimes, hence, they cannot be placed on a $P - \dot{P}$ diagram. These NSs have magnetic fields of the order of 10^{12} G, and show rather slow pulsations with periods of $1 - 10^3$ s. Mushtukov & Tsygankov (2024) offer a modern review of this class of NSs.

- Non-pulsating weakly magnetized neutron stars (WMNSs) and accreting millisecond pulsars (AMPs) reside in low-mass X-ray binaries (LMXBs) and

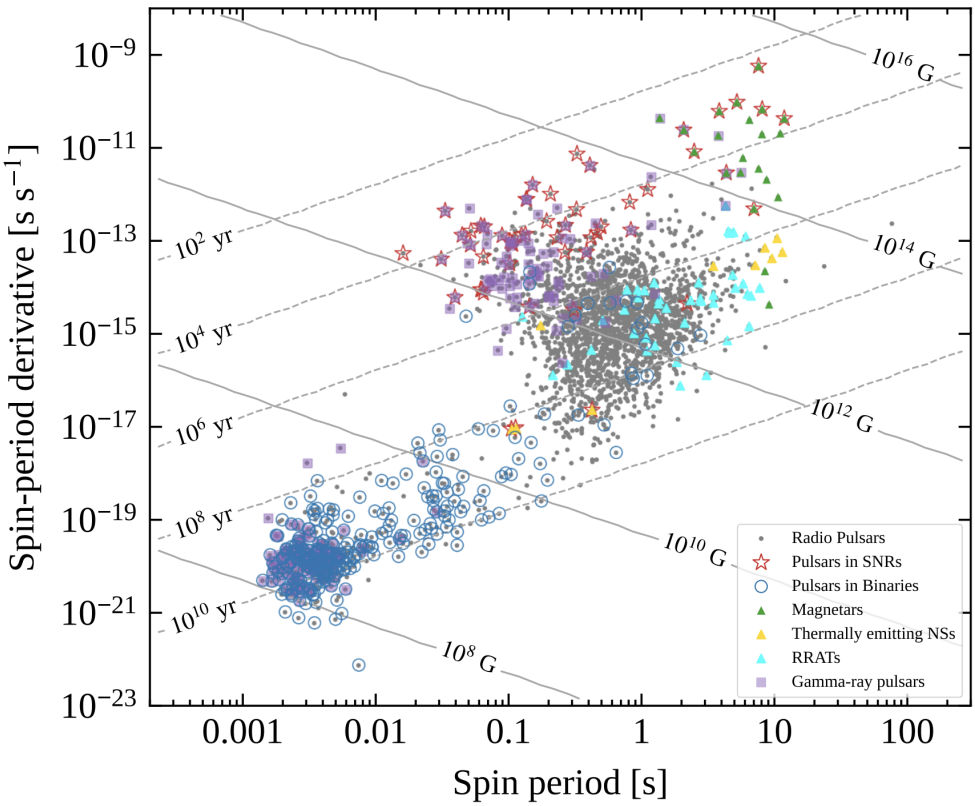


Figure 5. Pulsating NS population placed based on their spin period and spin period derivative. Gray solid lines show magnetic field strength, while gray dashed lines show characteristic age. From Borghese & Coti Zelati (2026).

accrete matter from their companion via gravitational overflow described in Sect. 2.4.2. These objects are the primary topic of this dissertation and are described in detail in the following chapters.

The vast majority of observed NSs are detected in radio; the emission of these systems is powered by the rapid rotation of these NSs. Here, two main sub-classes can be distinguished:

- Radio pulsars, a broad class with more than 3000 known sources; they are mainly observed in the radio band, and most of them are rapidly rotating (with periods of a few hundred milliseconds) and typically slow down at a rate of 10 microseconds per year (Borghese & Coti Zelati 2026). On the $P - \dot{P}$ diagram presented in Fig. 5, they occupy the upper-middle part and are noted in gray.

- Radio millisecond pulsars, also referred to as rotation-powered millisecond pulsars (RMPs). Compared to traditional radio pulsars, these systems have shorter periods (less than 100 ms) and smaller spin-down rates, with $\dot{P} < 10^{-17}$; these systems are also more often observed in binary systems (Manchester 2017). On the $P - \dot{P}$ diagram presented in Fig. 5, they occupy the lower-left part and are also noted in gray (notice the abundance of blue circles corresponding to pulsars in binaries in that part of the diagram). Within the RMPs, the particularly exotic subclass of the so-called spider pulsars is distinguished. These systems are known for their tight orbits and for the pulsar winds slowly ablating their very-low-mass companions (see Koljonen & Linares 2025, for a recent and detailed catalog of the spider pulsars).

In between these two groups lies a small class of transitional millisecond pulsars which switch from the rotation-powered regime to the accretion-powered regime and back (see, for instance, Papitto & Martino 2022, for a review on transitional millisecond pulsars).

Rotation-powered and accretion-powered systems make up the vast majority of the NS population. However, a few classes with different emission mechanisms are known. Among them, the most prominent examples are:

- Magnetars, also sometimes referred to as anomalous X-ray pulsars; remarkably magnetized, with magnetic fields of the order of $10^{14} - 10^{15}$ G, they have relatively long pulsation periods of seconds to tens of seconds. Around 30 magnetars are known today. In general, they exhibit luminosities that exceed their rotational energy loss rate; they are expected to be powered by magnetic field instabilities and decay; they are noted in green triangles in Fig. 5.

- Thermal isolated NSs, also known as the Magnificent Seven, are among the closest NSs to Earth. They were all detected in soft X-rays, but are not visible

in radio. They are believed to be rather young systems that emit thermal radiation as they are cooling (Turolla 2009). In Fig. 5, they are noted in yellow triangles.

- Central compact objects residing in young supernova remnants. Of a dozen known central compact objects, only three show pulsations and are confirmed to be NSs; for the others, some hints towards a NS with a weak magnetic field have been reported; even for the three pulsating objects, the magnetic field was small compared to other isolated NSs (Borghese & Coti Zelati 2026). The three pulsating central compact objects are noted in Fig. 5 by a combination of a yellow triangle and a red star.

2.4 Neutron stars in low-mass X-ray binaries

Binary systems are rather common; at least 30% of all stars are found in binary or multiple systems orbiting a common center of mass (see, e.g., Raghavan et al. 2010 for an estimation in solar-type stars; however, Boffin & Jones 2025, among many others, report higher values, around 50% for solar-mass stars with a fraction increasing with mass, up to 100% for massive stars). Neutron stars residing in LMXBs are the central objects of this doctoral research. Consisting of a neutron star and a companion with a mass not exceeding that of the Sun, these systems, often abbreviated as NS-LMXBs, exhibit a broad variety of phenomena across different stages of their evolution.

2.4.1 NS-LMXB evolution

In order to evolve into a NS-LMXB, the binary system must originally consist of two stars: one large enough to collapse into a neutron star, and another with a mass around or lower than that of the Sun. Of course, the more massive star will evolve faster and at some point will undergo a supernova phase. If the binary is disrupted in this process, which is quite a likely scenario, the neutron star will become an isolated radio pulsar. However, if the binary survives the supernova explosion and remains gravitationally bound, it will likely evolve according to the so-called recycling scenario (see, for instance, Bhattacharya & van den Heuvel 1991). Note that the recycling scenario is a schematic evolutionary framework rather than an exact sequence of observable classes through which every system must pass.

So, we begin with a young NS and a companion star that is in the main-sequence stage of its evolution. A young NSs is typically characterized by rather short rotational periods (tens to hundreds of milliseconds) and a magnetic field of order $\sim 10^{12}$ G; the Crab pulsar is a well-known example of a young, rapidly rotating NS (see, for instance, Lyne et al. 1993). As discussed above, the emission of such young

radio pulsar is powered by the loss of rotational energy and is primarily observed in the radio and gamma-ray ranges.

With time, the NS transforms so much of its rotational energy into emission that it slows down to a period of a few seconds and eventually is no longer visible in the radio sky (see, for instance, Lorimer 2008; Di Salvo & Sanna 2022, and references therein). At the same time, the magnetic field of a NS is decaying, probably due to ohmic dissipation, i.e. the resistive decay of magnetic fields within a NS's crust, or

Observational properties of the system change dramatically if the companion star fills its Roche lobe, either as a result of the donor's nuclear evolution and expansion or because orbital angular-momentum losses reduce the binary separation (Belloni & Schreiber 2023). Due to the so-called Roche Lobe overflow mechanism described below, the matter from the companion star can be transferred to the NS, typically forming an accretion disk around it. The matter flow creates ram pressure on the NS magnetosphere, pushing the magnetic field towards the NS; at sufficiently high mass accretion rates, the magnetospheric radius can approach the stellar surface. Matter accreted from a companion then falls onto the NS primarily in the equatorial region. Observational properties of such NS-LMXBs, usually referred to as non-pulsating WMNSs, are described in detail in Chapter 3.

In older systems, accretion process may slow down with time, while the NSs spin up due to angular momentum transfer. The ram pressure of the accreting matter decreases; in some systems, magnetic field reappears outside the NS surface. Accretion disk structure is also affected by the decreasing accretion rate, leading, among many possible scenarios, to alternating intervals of quiescence and outburst in the transient system. In the framework of the disk-instability model, the disk is expected to accumulate matter in a cool state until the local surface density reaches the critical value, triggering a thermal-viscous transition and a propagation of a heating front, leading to an accretion episode (see, e.g., Hameury 2020, for a recent review of the disk-instability model). In a subset of these rapidly rotating NS-LMXBs transients, the magnetic field is able to channel the accretion flow towards the mangetic poles, producing coherent millisecond pulsations. Such systems are observationally classified as AMPs; these objects are further described in Chapter 4.

As mass transfer decreases further or temporarily stops, the rotation-powered pulsar mechanism can again become active. Observationally, such objects are classified as RMPs. A few transitional millisecond pulsars have been observed; these systems, alternating between the accretion-powered and rotation-powered states, provide direct observational evidence for the strong connection between these two classes (see, for instance, Archibald et al. 2010; Papitto et al. 2013).

The subsequent binary evolution depends on the properties of the system. Among possible tracks for a recycled pulsar are, for instance, redbacks and black widow pulsars, subclasses of RMPs. These classes have been proposed to represent either two distinct populations (Chen et al. 2013) or different stages of a common evolutionary

process (Conrad-Burton et al. 2023; Misra et al. 2025). As these pulsars are known for their cannibalistic behavior, they are considered to be the last stage of an evolution of a NS binary with a low-mass companion; it is important to note, however, that not all the systems evolve into spider pulsars.

2.4.2 Accretion via Roche Lobe overflow

Accretion, a release of gravitational energy from infalling matter, is widely believed to be the main source of energy powering the emission of close binaries and active galactic nuclei (Frank et al. 2002). Accretion efficiency increases with compactness; for a standard NS, accretion releases roughly 10% of the rest mass in the form of electromagnetic radiation. This radiation, in turn, produces pressure that acts on the accreted matter flow. From the balance between the radiation pressure force and the gravitational force acting on the accreted particles, a limit on the accretion rate can be derived. As soon as the radiation pressure force exceeds the gravitational force, the accretion is inhibited. This limit is called the Eddington limit and is calculated as follows:

$$L_{\rm Edd} = \frac{4\pi G M c}{\kappa};\ \dot{M}_{\rm Edd} = \frac{L_{\rm Edd}}{\eta\, c^2}, \tag{7}$$

where $L_{\rm Edd}$ is the Eddington luminosity limit for a NS, G is the gravitational constant, M is the NS mass, c is the speed of light, and κ is the opacity of the stellar material. For ionized hydrogen, for instance, $\kappa = \sigma_{\rm T}/m_{\rm p} \approx 0.4$ cm^2/g, where $m_{\rm p}$ is the proton mass and $\sigma_{\rm T}$ is the Thomson scattering cross-section. $\dot{M}_{\rm Edd}$ is the Eddington mass-accretion rate, and η is the efficiency of converting mass into radiation. Eddington limits on luminosity and mass-accretion rate are actively used as units of luminosity or accretion rate when describing accretion-powered systems.

As mentioned above, in LMXBs, the accretion process begins when the outer layers of a companion star extends beyond its Roche lobe. The Roche lobe is a volume around a star in which the matter is gravitationally bound to this star, restricted by the gravitational equipotential surface. In a binary system, it has a teardrop-like shape, with an apex pointing towards the companion. Matter escaping the Roche Lobe surface is gravitationally driven towards the compact object. Due to the rotation of the binary system around its center of mass, matter passing from the companion star to the NS through the apex (also known as the inner Lagrangian point of the system) gains a large specific angular momentum that causes the inward spiraling motion of the matter via a thin disk rather than spherical accretion onto the compact object. The structure created in this process is usually called an accretion disk. Accreted plasma rotates around the compact object, slowly approaching it as the angular momentum is transferred outwards (Di Salvo & Sanna 2022). As the disk approaches the NS surface, it is either channeled towards the magnetic poles by the magneto-

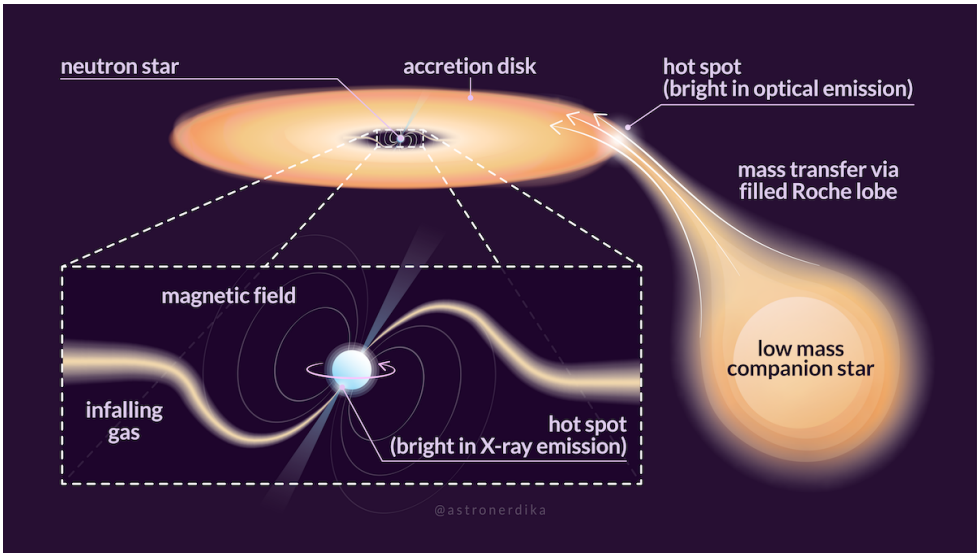


Figure 6. Schematic representation of an accretion flow geometry in an NS-LMXB. Image credit: Shanika Galaudage.

sphere or, if the accretion rate is high enough, accretes directly onto the NS surface in the equatorial region. The exact geometry of the accretion flow is one of the many open questions in NS-LMXB studies, but it is assumed to have a major impact on the X-ray emission. An example of a possible accretion flow geometry is shown in Fig. 6; here, the magnetic field is present and is sufficiently strong to channel the accretion flow towards the magnetic poles, corresponding to an AMP.

3 Non-pulsating weakly magnetized neutron stars

3.1 Main characteristics

Broadly represented, bright, and challenging, non-pulsating WMNS have been among the central objects of X-ray astronomy since the 1960s. One could say that the whole branch of X-ray astronomy began with a WMNS, when Riccardo Giacconi and his team launched a sounding rocket with Geiger counters on board and detected a strong X-ray source outside the solar system, which was later named Sco X-1 (Giacconi et al. (1962), 2002 Nobel Prize in Physics). Figure 7 illustrates both the first observation of Sco X-1 and the higher-resolution re-observation from Hill et al. (1968). In the upcoming years, significant efforts were made to investigate further the peculiarities of the galactic and extragalactic X-ray sources.

With WMNS, challenges begin with identifying the compact object. Since they are not pulsating, how can we know if there are NSs in these X-ray binaries? Observing the phenomena associated with the NS atmosphere would do the trick. For instance, many WMNS systems exhibit type I X-ray bursts, in which matter accreted from a companion star and accumulated on the NS surface ignites and fuses in a burst. These thermonuclear bursts usually peak in a few seconds and decay in tens to hundreds of seconds, releasing extreme amounts of energy, around 10^{39} erg, in this short time; see Galloway & Keek (2021) for a recent and detailed review. Another distinct NS binary phenomena are high-frequency quasi-periodic oscillations (QPOs). Observed in dozens of WMNSs (Méndez & Belloni 2021), these quasi-periodic peaks in the power spectra at kilohertz frequencies often occur in pairs and move together in correlation with the source state (Di Salvo et al. 2023); they are associated with the accretion flow variability in the close vicinity of the NS surface (see, for instance, Gilfanov et al. 2003; Revnivtsev et al. 2013; Abolmasov & Poutanen 2021). Alternatively, the nature of the compact object can be derived from the mass function measurement in a binary system. If the derived mass of the compact object exceeds the Tolman-Oppenheimer-Volkoff limit ($2.2 - 2.9\ M_\odot$ depending on the EoS, Kalogera & Baym 1996), it must be a black hole.

Apart from definitively confirming the nature of the compact object, pulsations in X-ray pulsars help constrain the magnetic field strength of the NS. In the absence of pulsations, different methods for constraining these key variables had to be intro-

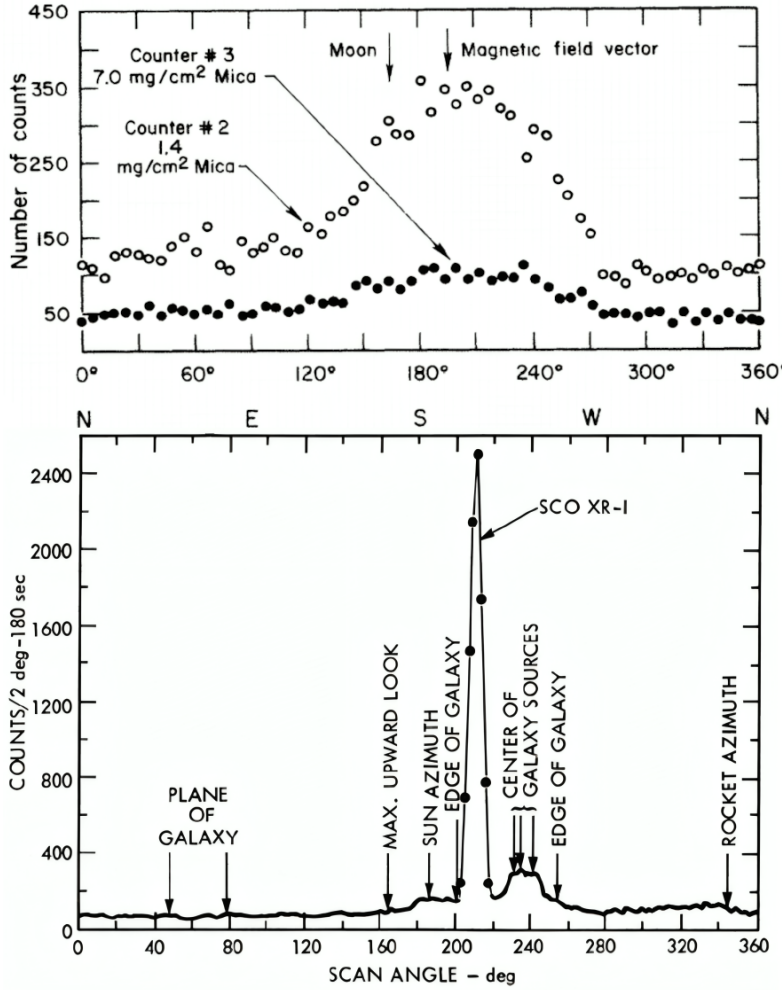


Figure 7. Top: first detection of an X-ray source outside the solar system. Scan of the sky with Geiger counters on board a sounding rocket. Adapted from Giacconi et al. (1962). Bottom: total count of two proportional counters on board of a sounding rocket. Adapted from Hill et al. (1968).

duced. For instance, either the NS radius or the inner disk radius could be used as an Alfven radius (see below for the disk truncation scenario and Bisnovatyi-Kogan 2017, for the estimation with a magnetosphere radius equal to that of a NS). The magnetic field can also be estimated from the processes contributing to the magnetic field decay. Shibazaki et al. (1989) studied the magnetic field decay by accretion, and Kar et al. (2025), for instance, used this approach to put an upper limit on the magnetic field of Sco X-1.

Because of their relatively weak magnetic field and their location mainly in the Galactic bulge and disk or in the globular clusters (see, for instance, Avakyan et al. 2023, for a recent catalogue), WMNSs are assumed to be old systems with an age of a few times 10^8 years (see, for instance, King & Ritter 1999, for Cyg X-2). Few exceptions are, for example, Sco X-1 with an estimated age of 7×10^6 years (Kar et al. 2025), and, most famously, Cir X-1 with an age not exceeding 5×10^3 years (Heinz et al. 2013). Their companion stars are primarily low-mass late-evolved stars like subgiants or giants (e.g. in Cyg X-2, Casares et al. 1998) and white dwarfs (e.g. in 4U 1820−303, Rappaport et al. 1987).

3.2 Spectral components

As briefly introduced in Sect. 2.4.2, the accretion flow in WMNSs comes very close to or even touches the NS surface, and the accretion happens onto the equatorial part of the NS. Since the innermost stable circular orbit of the accretion disk for these objects is smaller than the NS radius, no gap is expected between the accretion disk and the NS surface. A so-called boundary layer (BL) is formed in the region where the accretion disk touches the NS surface.

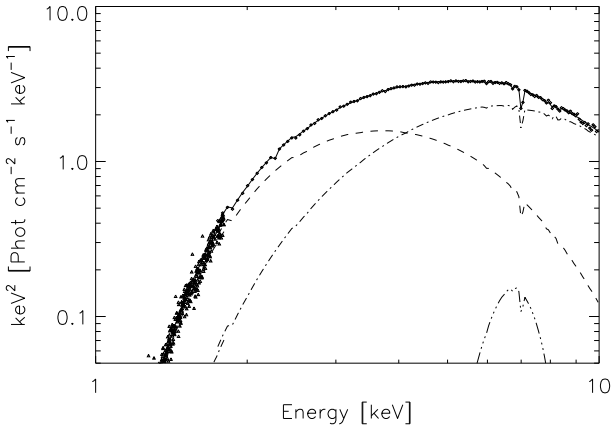


Figure 8. Unfolded spectrum of WMNS GX 13+1 measured by *XMM-Newton*. Solid line shows the full model; dashed line shows the contribution of the accretion disk; dot-dashed line shows the contribution of the Comptonized component; dot-dot-dashed line shows the combination of the emission line from reflection and absorption lines from the wind. From Díaz Trigo et al. (2012).

The spectrum of a WMNS has two main

components, traditionally associated with the thermal emission of an accretion disk (lower energies) and the Comptonized emission from the BL (higher energies). In addition, a reflection feature is present in many systems; normally, the assumption is that the Comptonized emission of a BL is partially reflected from the accretion disk, resulting in a Fe emission line around 6.5 keV and a "bump" above 10 keV. Finally, in some WMNSs, a wind above the accretion disk contributes to the total spectrum through absorption lines. Fig. 8 shows an example spectrum of a WMNS GX 13+1 with all four components present (Díaz Trigo et al. 2012).

Physics behind each of the spectral components has been extensively studied over the last decades. The accretion disk model was introduced in the 1960s, with a first complete astrophysical model presented in Pringle & Rees (1972), Shakura & Sunyaev (1973), and Lynden-Bell & Pringle (1974). Since then, the model has been developed and adjusted based on new observational results and modern physics approaches. For a review see, for instance, Frank et al. (2002) and Abramowicz & Fragile (2013). Reflection from the accretion disk has been reviewed, e.g., in Ludlam (2024), while winds above the accretion disk in X-ray binaries have been recently reviewed in Muñoz-Darias et al. (2026). Since the work presented in this dissertation focuses on the Comptonized component of the emission (coming, presumably, from the BL region), several possible geometrical configurations of the Comptonizing region are introduced here in more detail.

3.2.1 Boundary layer

BL, a relatively hot and turbulent region between the accretion disk and the surface of the compact object, is a feature characteristic not only of the WMNS systems. For instance, it has also been suggested and intensely studied in cataclysmic variables, X-ray binaries with a white dwarf (WD) as a compact object. The idea of a BL evolved naturally from studying the evolution of viscous disks in Lynden-Bell & Pringle (1974), where the BL in X-ray binaries was discussed among other phenomena. Further development of the model was initially driven by observations of WD binary and focused on these objects: Pringle (1977) and later Pringle & Savonije (1979) showed that the BL is

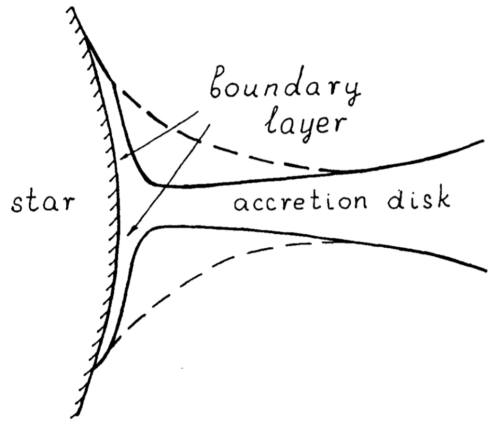


Figure 9. Schematic representation of an accretion flow geometry near the NS surface. Broadening of the inner part of the disk due to heating is shown with a dashed line. Not to scale. From Shakura & Sunyaev (1988).

capable of producing soft and, in shock,
hard X-rays, respectively, while Tylenda (1981) studied the viscous dissipation in the BL as another possible source of X-ray emission. Although not directly applicable to NSs, these works contributed to the model development and were later adapted for the NS studies.

The first study of the BL between the disk and the NS surface was reported in Shakura & Sunyaev (1988). They adapted the previously developed models for the WD binaries and discussed the challenges of calculating the accurate BL structure. Their BL was isothermal, and they used the method of successive approximation rather than exact solutions to the hydrodynamic and radiation transfer partial differential equations in the turbulent BL. The model was built under the assumption that in just one revolution around the NS, the matter slows down from the Keplerian velocity it had in the disk to the NS angular velocity, releasing a luminosity similar to that of the accretion disk. Later, Popham & Sunyaev (2001) studied the dependence of the BL structure and emission on mass accretion rate, spin of the NS, viscosity parameter, and viscosity prescription. The model developed in this paper did not include relativistic effects and ignored the vertical movement of the matter flow, focusing instead on the tangential component of the matter velocity.

The vertical movement, however, is a crucial component for calculating the exact behavior of the BL. Yet again, such a model was first developed for the WD binaries using a numerical approach in Popham & Narayan (1995). Babkovskaia et al. (2008) first performed a two-dimensional hydrodynamical simulation for the vertical extension of the BL. They did not account for the rotation of the star and considered a laminar flow, but their results inspired further simulations.

Although not all the processes in the BL are included in the current models or even completely understood, approximate models have been extensively used in spectroscopy. To mention a few:

- `compTT` model introduced in Titarchuk (1994) is a plasma-physics-driven model that accounts for the Comptonization of soft seed photons in a hot plasma;
- `compTB` model (Farinelli et al. 2008) is sometimes considered a descendant of the `compTT` model and includes not only thermal but also dynamical (bulk) Comptonization;
- `thcomp` (Zdziarski et al. 2020) is a more phenomenological convolution model that can Comptonize any seed photon distribution.

All these models include approximations and assumptions, yet, they are considered to be accurate enough for the currently available instrumentation.

3.2.2 Spreading layer

The so-called spreading layer (SL) is an extension of the BL on the surface of the NS. It was first introduced in Inogamov & Sunyaev (1999), where the authors assumed that the combination of radiation pressure and centrifugal forces would force the accreted matter to spread from the equatorial regions towards the NS poles, see Fig. 10. The matter in the accretion disk has, in this approximation, a local Keplerian velocity, which significantly exceeds the NS surface rotation rate; the deceleration of the accretion flow is expected to happen due to the viscous friction between the accreted matter and the NS surface. Due to the high accretion rate in WMNSs, this braking cannot happen in a narrow equatorial region, so the in-falling matter spreads towards the poles; the higher the mass-accretion rate, the broader the SL could be. In the model presented in Inogamov & Sunyaev (1999), the matter slowly decelerates while spreading towards the poles, with the most energy dissipation happening at the SL edges, making them the most luminous parts of the accretion flow.

The model introduced in Inogamov & Sunyaev (1999) was used as a foundation for further studies. Suleimanov & Poutanen (2006) and later Suleimanov et al. (2020) explored the spectrum of the SL, taking into account relativistic corrections and the chemical composition of the accreted matter; they also discussed possible constraints on the NS radius (and, consequently, on the EoS). The math presented in Suleimanov et al. (2020) together with the approach introduced in Inogamov & Sunyaev (1999) were the foundations of Paper IV and Paper V of this dissertation.

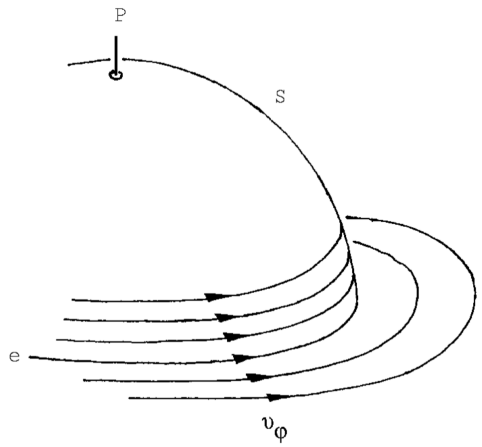


Figure 10. Schematic image of a SL. From Inogamov & Sunyaev (1999).

Modern approaches of hydrodynamic simulations have also been applied to the SL. For instance, Abolmasov et al. (2020) performed two-dimensional hydrodynamical spectral simulations. The goal of the research was to search for the possible origin of QPOs. As a result, they were able to reproduce the shear instabilities in the SL that could be responsible for the kHz pair QPOs observed in many WMNS systems. Rusakov et al. (2025) studied the SL flow evolution and observed an asymmetry between the two hemispheres by the end of their simulations; however, the question of whether this feature is stable remains open, since only the first seconds of the SL evolution have been simulated so far.

3.2.3 Accretion disk truncation

As mentioned above, the BL forms if the accretion rate is high enough to push the magnetosphere so that it remains only inside the NS. However, in the systems with less active accretion, it is still possible for the accretion disk to be truncated by the magnetosphere, albeit very close to the NS surface. Such a configuration is also possible when the system moves to a state with less active accretion, e.g. the hard state of atolls (see, for instance, Gierliński & Done 2002b; Sakurai et al. 2012). With the accretion disk truncated by the magnetosphere, the accretion flow is guided by the magnetic field lines, so the accretion would happen at higher latitudes rather than at the equatorial regions, as in the BL scenario. Such a configuration is not expected to significantly affect the spectrum; however, the inner radius of the accretion disk can be used to constrain the magnetic field in these systems (see, for instance, Ludlam et al. 2020, 2021; Mondal et al. 2022). This method should, however, be used with great care, since it is highly dependent on the model selected for the spectral fitting, and since such a geometrical configuration is not feasible for systems with a high accretion rate.

3.3 Classification and state transitions

From a bright, persistent, and flaring Sco X-1 to systems like XTE J1701−462, which are barely observable most of the time and only occasionally go into outburst, various objects constitute the WMNS class. Further classification of these systems can be done according to their spectral and temporal properties.

Based on their long-term X-ray variability, WMNS can be classified into transient and persistent sources. Transient sources are mostly found in a so-called quiescent state, with X-ray luminosities down to a few 10^{31} erg/s, which are sometimes alternated with outbursts, when their luminosity rather rapidly increases up to the Eddington limit. These outbursts, traditionally explained by the accretion disk instability, last from weeks to months, although a few systems are known with outbursts lasting longer that a year (Di Salvo et al. 2023). Persistent sources, on the other hand, show luminosity variability within an order of magnitude.

Alternatively, the systems can be classified based on their spectral hardness and luminosity and/or short-term X-ray variability. WMNS are traditionally divided into so-called Z-sources and atolls (van der Klis 1989). The main instruments in this classification are color-color diagram (CCD) and hardness-intensity diagram (HID), see Fig. 11. The CCD is constructed by tracing the variability of the soft color (a count rate ratio between a medium and soft energy ranges) and hard color (a count rate ratio between the hard and medium energy ranges) of the spectrum with time, while the HID reports the evolution of hardness (a count rate ratio between hard and soft energy ranges) and intensity of the source with time (Hasinger & van der Klis

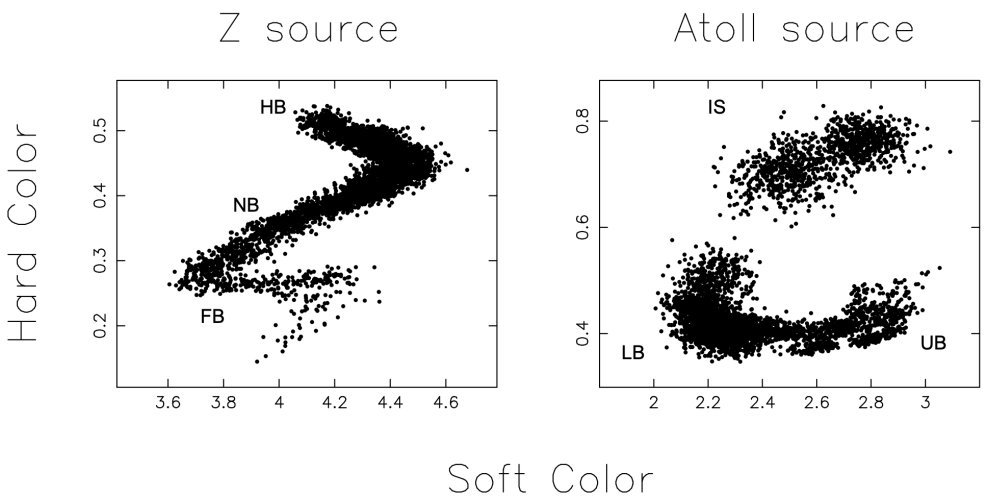


Figure 11. Typical CCDs of a Z-source (left) and an atoll source (right). Adapted from Wijnands (2001).

1989). WMNS are known to draw tracks on these diagrams, going there and back on time scales of days to weeks. The names of the sub-classes are associated with the shapes the sources track on the CCD: Z-sources draw a Z-shaped track, while the atolls draw an atoll-like structure.

CCD is mainly used to track the state transitions in WMNS systems. Different parts of the diagram correspond to different spectral states. In Z-sources, these different states are called, in order of tracing a Z-shape from top-left to bottom-right, a horizontal branch (HB), a normal branch (NB), and a flaring branch (FB). Sometimes, two extra sub-states are introduced, a hard apex (HA) between the HB and NB and a soft apex (SA) between the NB and FB. In atolls, island state (IS), lower banana (LB), and a upper banana (UB) are distinguished (van der Klis 1989). Apart from the different shapes, atolls and Z-sources also move along their tracks in different ways. While Z-sources draw a continuous track and do not exhibit any branch "jumping", atolls move continuously from UB to LB and back, but "jump" between the island and banana parts of their track. Z-sources move along the whole track in a matter of days, while atolls cover their track in weeks, moving particularly slowly in the IS (Muno et al. 2002).

Differences between the Z-sources and atolls are visible not only in the CCD, but also in, for instance, the power spectrum (Wijnands 2001). Fig. 12 illustrates power spectra of a typical Z-source and an atoll. The continuum in both classes consists of a power law and two noise components, very low frequency noise (VLFN) and high frequency noise (HFN) above 10 Hz. In Z-sources, the HB has an additional noise component, low frequency noise (LFN). For many years, the strong oscillations in the HB and NB, named respectively horizontal branch oscillations (HBOs) and

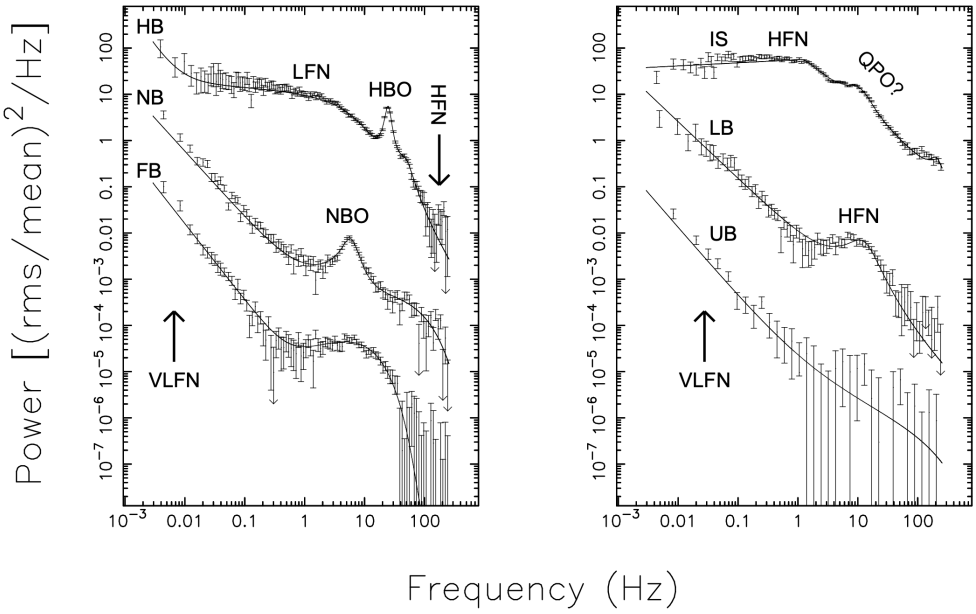


Figure 12. Typical power spectra observed in different spectral states of a Z-source (left) and an atoll source (right). From Wijnands (2001).

normal branch oscillations (NBOs), were considered the most prominent features of Z-sources. However, similar features were later observed in some atoll sources, as well (see Motta et al. 2017, for a review). Both classes also show kHz QPOs.

Apart from the CCD track shape, Fig. 11 illustrates the difference in the color variability of Z and atoll sources. Z-sources are known to be softer than atolls, while atolls typically show a wider range in color. Z-sources are also traditionally more luminous than atolls, with a typical luminosity of $\sim (0.5 - 1)\ L_{\rm Edd}$ for Z-sources and $\sim (10^{-3} - 0.5)\ L_{\rm Edd}$ for atolls. However, there is no clear boundary in terms of luminosity, and the luminosity itself cannot be a reason to classify a source (van der Klis 1989). Similarly, Z-sources have longer orbital periods (exceeding 10 hours), while atolls are often short-period systems (van der Klis 1992), but this is a common feature, not a classification criterion. Other common features of Z-sources include a stronger and more persistent radio emission, while atolls have fainter radio emission that only appears in the hard IS, and more luminous companion stars. It has also been suggested that Z-sources have stronger magnetic fields (van der Klis 1989, 1992) and do not exhibit type-I X-ray bursts (van der Klis 1989; Church et al. 2014), but these claims have not been confirmed observationally; while the magnetic field estimation for the strongly accreting Z-sources is a challenge, type-I bursts have been observed from at least two Z-sources (Muno et al. 2002).

Traditionally, only six sources are classified as Z-sources. They are divided into

two sub-groups based on their inclination and spectral state transitions; these groups are named after the most famous representatives of the groups (Hasinger & van der Klis 1989). So-called Sco-like sources (Sco X-1, GX 349+2, and GX 17+2) are thought to have lower inclination; they are rarely found in the HB, but their FB is prominent. On the other hand, the Cyg-like sources (Cyg X-2, GX 340+0, and GX 5−1) have higher inclination, are less likely to be observed in the FB, but their HB is prominent. A few dozens of sources are securely identified as atolls. Peculiarly, several sources are known to exhibit qualities of different classes at different times. Most famously, XTE J1701−462 behaved as a Z-source and then as an atoll later in the outburst (Lin et al. 2009). Another source transitioning from a Z-source to an atoll source during the outburst is 1A 1744−361 (Ng et al. 2024).

Shortly after the Z/atoll classification was introduced, the question was raised whether these are similar objects with different mass accretion rates, or whether there are any other principally different mechanisms at play (see, for instance, Hasinger & van der Klis 1989, for an early discussion). Wijnands (2001), while describing the differences between these two classes in their power spectra, stated that they are more similar than previously thought. Gierliński & Done (2002a) presented evidence of a topological similarity between the tracks of Z and atoll sources; however, they suggested that these classes have different mechanisms responsible for the disk truncation. In Ng et al. (2024), a unification theory was introduced based on the observations of class transitions in 1A 1744−361.

Physics behind the state transition in WMNS is still an open question. Over the years, various theories were suggested. For instance, in Gladstone et al. (2007), the authors speculated that the state transition in some of the atoll sources could be due to the magnetic field being able to emerge from the NS surface and mildly affecting the inner accretion flow geometry, however, further joint radio and X-ray observations are required to support this idea. The FB of the classical Z-sources is associated with unstable thermonuclear burning on the NS surface (Church et al. 2012), but the association is empirical and source-dependent rather than definitive. Transitions are often associated with the changes in mass accretion rate (see, for instance, the arrowed lines in Fig. 11), but the exact reasons behind color variability with the accretion rate are not yet definitively confirmed.

3.4 X-ray polarimetry of weakly magnetized neutron stars

3.4.1 Theoretical predictions

Persistent and bright, WMNSs were among the prime targets of X-ray polarimetric observations since the 1970s. These observations, in their turn, inspired extensive theoretical work that could support the data interpretation. For each of the spectral components, theoretical predictions of the polarimetric properties of the emitted light

have been made over the years.

X-ray polarization of the accretion disk has been studied primarily in black hole X-ray binaries. Although the gravity is not nearly as strong in NS-LMXBs, the results for black hole systems are applicable to WMNS with some corrections. The first polarimetric predictions for the accretion disk were presented in Rees (1975), where a Newtonian non-relativistic approach was used, and the polarimetric treatment was based on the model of an optically thick electron-scattering-dominated atmosphere (Chandrasekhar 1960). After that, many papers introduced corrections due to relativistic and other additional effects, both analytical and numerical (see, among many others, Stark & Connors 1977; Dovčiak et al. 2008; Loktev et al. 2022). Based on these works, for the accretion disk in a WMNS we expect the polarization in the *IXPE* energy range to not exceed 4% for the systems with the highest inclinations (80°), not exceed 2% for an inclination of 60°, and not exceed 0.5% for low-inclination systems. The emission is expected to be polarized along the accretion disk surface.

For the Comptonized emission component, the polarimetric properties of the emission strongly depend on the exact geometry of the Comptonizing region. In Sunyaev & Titarchuk (1985), predictions are given for the Comptonization in the disk, which could be used as an approximation for the BL that does not extend to the NS surface. On the other hand, in Lapidus & Sunyaev (1985), the opposite case is discussed, with radiation coming only from the SL-like belt in the equatorial area. These pioneering models were updated in the *IXPE* era: Gnarini et al. (2022) used a numerical approach, while in Farinelli et al. (2024) and in Paper IV, more precise and realistic analytical models were introduced. Relativistic corrections from the dynamical accretion flow, gravity, and anisotropy were added. In all the modern papers, the conclusion is that, while the polarization angle depends on the geometry (the polarization is aligned with the surface of the Comptonizing region), the expected polarization is low: in numerical simulations, for the most favorable parameter combination, a polarization of 4% is calculated, while in the analytical models, expectations barely exceed 1%. Finally, in Paper V, an asymmetric system was considered. Introducing obliquity to the model increased the expected polarization and added variety to the possible polarization directions.

Polarization of the light reflected from the disk was taken into account in Lapidus & Sunyaev (1985) and was studied in detail in Matt (1993) and Poutanen et al. (1996). While using different analytical methods to compute the polarization, these papers agree that the intrinsic polarization of the reflected component can be as high as 20%, depending on the inclination, while the total polarization from a system is expected to be a few percent, depending on the geometry of the Comptonizing region. The polarization direction is expected to be perpendicular to the disk plane, with some variability depending on the illumination pattern and the number of scatterings.

Scattering in the wind also contributes to the polarimetric picture. Tomaru et al.

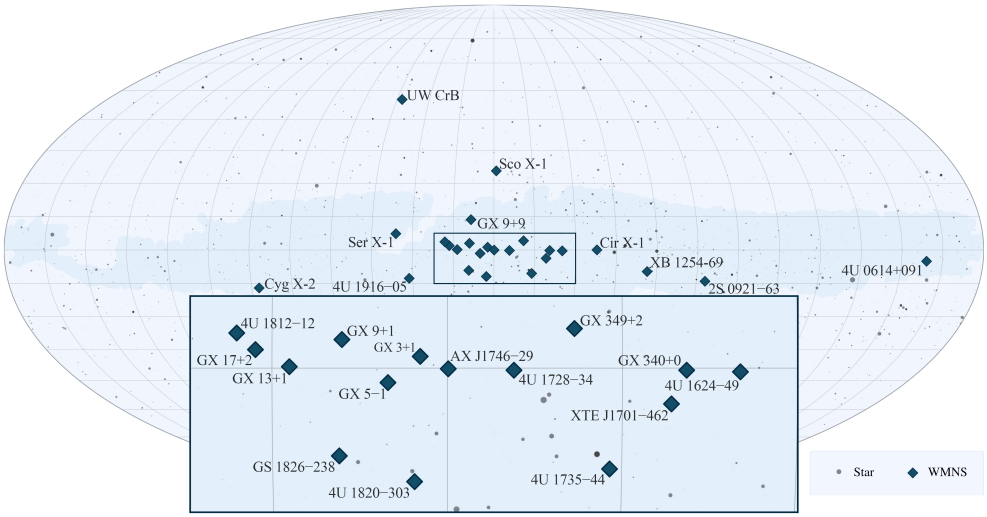


Figure 13. WMNS systems observed with *IXPE* in Galactic coordinates. The Milky Way and the brightest stars are added in the background. Created with `Starplot` (Berardi 2026).

(2024) used a numerical approach, while Nitindala et al. (2025) built a semi-analytical model. With different assumptions made about the geometry of the wind, these papers came to opposite conclusions: while in Tomaru et al. (2024), the thin-ish thermal-radiative wind is expected to depolarize the total emission, in Nitindala et al. (2025), an optically thick wind can dominate and increase the total polarization.

3.4.2 Observational results

The first polarimetric observations of WMNSs were performed with the *OSO 8*; Sco X-1 and Cyg X-2 were observed, although only the Sco X-1 observation results were published (Long et al. 1979), while for Cyg X-2, only a marginal detection was obtained (Long et al. 1980). Since the launch of *IXPE*, more than twenty WMNSs have been observed (see Fig. 13 for an overview).

With this many observations, dozens of papers have now been published. Some of the most comprehensive reviews include Ursini et al. (2024), Di Marco (2025), and Gnarini et al. (2025). The key conclusions were as follows:

- for most of the sources, harder emission dominated the polarization, with PD increasing with energy;
- for many sources, PD at higher energies significantly exceeded the theoretical predictions, rising higher than 10% at least in 4U 1820−303 and GX 340+0;
- for Z-sources, polarization was generally higher in the HB than in the NB

or FB, with GX 5−1, GX 340+0, and a transitional system XTE J1701−462 observed in both hard and soft states;

- on average, polarization was generally higher for Z-sources than for atolls;
- in several sources, variability and even rotation of PA with time were observed;
- for at least two sources, Cir X-1 and GX 13+1, obliquity between the rotational axis of the binary system and the NS rotational axis, was suggested as a possible explanation;
- in Cyg X-2, *IXPE* results were consistent with the marginal detection obtained with *OSO 8*; in Sco X-1, significant variability in the PA between the old and the new observations was observed;
- in Cyg X-2, polarization was aligned with the radio jet; however, in Cir X-1 and Sco X-1, PA was not aligned with the jet.

These trends are not universal or set in stone, there are exceptions and uncertainties for many of them. And even for the consistent trends, the explanation is somewhat lacking. X-ray polarimetry allowed us to study these systems in more detail than ever, draw some conclusions about the accretion flow geometry in some of the sources, and left us with more questions for others.

3.5 GX 13+1

Among the WMNSs, a few systems stand out. Sco X-1 is the brightest object on the X-ray sky except for the Sun, shining at 10−20 Crab, Cir X-1 is the youngest known galactic X-ray binary, with the age not exceeding 4 600 yr, and GX 13+1 is, to put it lightly, unnecessarily complicated.

GX 13+1 is a galactic X-ray burster with a late-evolved giant K5 III for a donor star located at a distance of 7 kpc from Earth (Bandyopadhyay et al. 1999). Of all the NS-LMXB, it has the longest orbital period of 24.5 d (Corbet et al. 2010). GX 13+1 is a dipping source, which put constraints on the system inclination at around 65° (Diaz Trigo et al. 2010; Iaria et al. 2014). GX 13+1 is a bright persistent source radiating at a level of $0.5L_{\rm Edd}$ (D'Aí et al. 2014), in between the Z-sources and atolls. Based on the track the source covers on the CCD, it has been classified both as atoll (see, among many others, Schnerr et al. 2003) and Z-source (Allen et al. 2018; Saavedra et al. 2023).

Spectrum of GX 13+1 show prominent features of the four main components discussed above, see Fig. 8 and Díaz Trigo et al. (2012) for the changes in the spectrum with state transitions. The reflection component is peculiar, since the Fe line is strong, but skewed (Maiolino et al. 2019). It is one of the three NS-LMXBs

with prominent narrow absorption features. Until recently, 7 main absorption lines were distinguished in the GX 13+1 spectrum, which reportedly came from different parts of a strong and complicated wind (Allen et al. 2018; Tomaru et al. 2020). GX 13+1 was one of the first targets for the *X-Ray Imaging and Spectroscopy Mission (XRISM)*, and the spectrum reported in Xrism Collaboration et al. (2025) inspired a new perspective on a level of complicated behavior of the wind in this system, suggesting a slow and highly ionized wind with a faster, even more highly ionized skin on its inner edge. As if it was not enough, in GX 13+1, a wind and a radio jet seem to coexist, and their launching mechanisms are not necessarily linked (Rogantini et al. 2025).

GX 13+1 was one of the *IXPE* targets during the baseline science mission time, first observed in October 2023. The discovery paper, Paper II, reported a highly peculiar polarimetric behavior of the source and inspired at least three more X-ray polarimetric observations of GX 13+1. The slow rotation of the polarization plane with time that we saw in the first observation did not appear in the second (Paper III) or third observation (Di Marco et al. 2025), but each and every observation had unique features, from rapid time PA and PD variability to changes in energy dependency of polarimetric features. Results for the GX 13+1 were re-analyzed using different statistical approaches, with Ravi et al. (2026) confirming the rotation of polarization plane in the first observation, while Li et al. (2025b) suggest that the bimodal distribution of PA is a better fit. Radio polarization was introduced in Kashyap et al. (2025), where the PA of the radio jet was obtained. More deep radio analysis, as well as the *IXPE* data analysis for the latest fourth observation of GX 13+1, is currently in progress. Combined efforts in spectroscopy and polarimetry will undoubtedly contribute to a deeper understanding of this challenging source and accretion mechanisms in X-ray binaries.

4 Accreting millisecond pulsars

4.1 Main characteristics

AMPs are transient sources that, during their outbursts, exhibit millisecond pulsations in the X-ray range. These systems are called "recycled pulsars", as they are very old binaries that have lived as radio pulsars and non-pulsating WMNSs (Patruno & Watts 2021; Di Salvo & Sanna 2022) and have nearly exhausted their companion during a long accretion process (see Sect. 2.4.1 for a recap of the NS-LMXB evolution scenario). They have relatively low magnetic fields of $10^8 - 10^9$ G and even during their outbursts remain quite faint, rarely exceeding 0.1 $L_{\rm Edd}$. AMPs are reviewed in detail in, for instance, Campana & Di Salvo (2018), Patruno & Watts (2021), Papitto & Martino (2022), and Di Salvo & Sanna (2022). Here, a quick recap of these reviews is given.

The first AMP was discovered in 1998 (SAX J1808.4−3658, Wijnands & van der Klis 1998), when the system was observed with the *Rossi X-ray Timing Explorer (RXTE)* telescope; the discovery was met with great enthusiasm, since their existence had been theoretically predicted for decades, and they were considered the "missing link" of the recycling scenario. Nowadays, out of hundreds of known NS-LMXBs, only around 25 are AMPs. It is a small but versatile group of objects, with very few characteristics common to all the members of the class.

Take, for instance, the outbursts: all the AMPs are transients, but while some systems (for instance, SAX J1808.4−3658, SAX J1748.9−2021) go into outbursts more or less regularly every few years, others have only showed one outburst since the beginning of monitoring (or, like NGC 6440 X-2, showed a series of outbursts between 2009 and 2011 and then returned to quiescence). For most of the systems, outbursts last from a few weeks to a few months, but several sources has longer-than-one-year outbursts, with the longest known 10-year-long outburst observed in HETE J1900.1−2455.

Another prominent characteristic of AMPs is, of course, their pulsations. The AMP spin frequencies are distributed roughly uniformly before an apparent cut-off at 700 Hz, which is explained by the balance between accretion torques and magnetic torques, disk–magnetosphere coupling, and possibly gravitational-wave losses (see, for instance, Patruno et al. 2017, and references therein). Apart from the spin frequencies, consistency among the class representatives is lacking here, too. AMPs

have low pulsation amplitudes, with the majority of the sources showing 0.2–10% amplitude variability, but there are exceptions, like XTE J1807−294 that showed a fractional amplitude of 27% in the energy range of 2.5−30 keV (Patruno et al. 2010), and IGR J17379−3747 that showed variability in amplitude from 10% to 70% during a single outburst (Bult et al. 2019). Another peculiar feature of the pulsations in AMPs is the intermittence of pulsations. While for some systems pulsations are present throughout the whole outburst and in every observed outburst, other show pulsations that appear and disappear at different times during outbursts. For instance, in HETE J1900.1−2455, the pulsations appeared at the beginning of the outburst, and then disappeared and kept reappearing and disappearing for the next 2.5 years. In Aql X-1, the pulsations were observed only for 150 s during one outburst in 1998 (Casella et al. 2008). Aql X-1 goes into outburst every 0.5−1 yr, and many of these outbursts were carefully observed, but the 1998 one remains the only one with pulsations present. Aql X-1 is now referred to as an intermittent AMP.

Approximately half of the AMP population consists of ultra-compact X-ray binaries; most of AMPs have an orbital period from 30 min to a few hours, with only Aql X-1 being an exception with an orbital period of 18.5 h. Their companions are mostly brown dwarfs, WDs, or main sequence stars with predominantly very low masses, with only a few sources having a companion more massive than 0.5 $M_\odot$.

The accretion flow geometry in AMPs during an outburst is presented in Fig. 6. The accretion disk is truncated by the magnetosphere, and the accreted matter is channeled towards the poles of the magnetic field. In the most basic approximation, the magnetic field is dipolar, so the matter is channeled towards two antipodal spots on the NS surface. However, since these systems have rather weak magnetic field, the accretion disk is truncated close to the NS surface, where not only the dipole component, but also higher components of the magnetic field can affect the accretion flow. In the AMP spectrum in the soft X-ray range, the main contribution comes from the hotspots' emission. The accretion disk and reflection from it also contribute to the continuum (see, for instance, Gierliński et al. 2002; Gierliński & Poutanen 2005; Dorsman et al. 2026a, for detailed studies of the spectral decomposition of AMPs).

Similar to WMNSs, AMPs exhibit X-ray bursts and kHz QPOs associated with the region of accretion disk truncation. Interestingly, in some systems, pulsations are observed during the X-ray bursts. In some cases, the pulsations during the bursts are synchronized in phase with the regular pulsations outside the burst, suggesting that the thermonuclear burning on the NS surface happens around the hotspot and does not cover the whole NS surface.

4.2 Pulse profile

Pulse profile, the light curve folded by the pulsation period, is the key observable characteristic of any pulsar. In a rapidly rotating AMP, the pulse profile encodes

information not only about the magnetic field geometry, but also, through relativistic effects, about the compactness and radius of the NS.

The magnetic field channels the accreted matter and defines the hotspot positions, which, in their turn, shape the pulse profile. Consequently, when studying a pulse profile, one can see hints towards the magnetic field structure and behavior. For instance, a double-peaked, sinusoidal pulse profile is usually a sign of a dipole field with two antipodal spots. If the pulse profile is more complicated and has strong high-harmonic content, the magnetic field is expected to be more complicated as well. Evolution of a pulse profile with time is a sign of a complex interaction between the disk and the magnetosphere.

Relativistic effects are also visible in the pulse profile shape, as illustrated in Fig. 14. Gravitational light-bending reduces the amplitude of the pulsation, while Doppler shift and aberration skew the profile. Time delay, a minor correction coming from the different travel times of emitted photons to the observer, also contributes to the total shape. When all these effects are properly accounted for, one can reconstruct the NS spin frequency and the velocity of the hotspot from the Doppler effect, which allows us to derive an estimate of the radius. Gravitational light-bending depends on the compactness, and with a known radius, one can also derive constraints on the mass and, consequently, on the EoS.

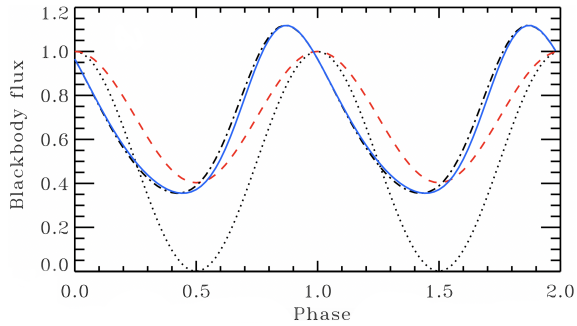


Figure 14. The bolometric flux as a function of the observed phase. Analytical simulation for one blackbody-emitting hotspot at a colatitude $\theta = 45°$ observed at an inclination $i = 45°$. Dotted black line: slowly rotating star without any relativistic effects; dashed red line: accounting for the gravitational light bending; dot-dashed black line: accounting also for the Doppler shift and aberration for a NS rotating with a frequency of 600 Hz; solid blue line: accounting also for the time delays. Adapted from Poutanen (2006).

However great in theory, it is a challenge to properly extract the relativistic effects from the observed pulse profile. Firstly, a significant amount of parameters impact the pulse profile shape, including the geometry of the system, atmospheric parameters, and magnetic field configuration. With that many parameters, degeneracy is inevitable, and it is impossible to constrain them all from the pulse profile. Secondly, pulses of AMPs are short and rather weak, so several hundred thousand pulses need to be folded and averaged to get a pulse profile, which introduces additional noise. Moreover, the pulses are not as stable as in radio pulsars, so it is particularly difficult to establish a fiducial point on which to base timing analysis. The coherent timing

technique reviewed in Patruno & Watts (2021) helps to track the spin changes and account for them. This method also allows us to correctly convert the observed pulse frequency to the actual NS spin frequency.

Pulse profile modeling is a challenging, but rewarding task. The first analytical model was presented in Poutanen & Gierliński (2003). Later, the formalism was adapted to include the oblateness of the star (Morsink et al. 2007) and disk occultation (Ibragimov & Poutanen 2009; Poutanen et al. 2009). In Salmi et al. (2018), a Bayesian method for constraining NS mass and radius from the pulse profiles was introduced. The most recent updates include introducing the X-ray Pulse Simulation and Inference code (X-PSI, Riley et al. 2023) and applying it to AMPs in Dorsman et al. (2025) and Dorsman et al. (2026a).

4.3 X-ray polarimetry of accreting millisecond pulsars

One of the key problems of the pulse profile studies is the large number of parameters that affect the pulse profile shape. It was shown in Viironen & Poutanen (2004) that at least the system inclination i and hotspot colatitude θ, which are degenerate in spectroscopy, can be disentangled using polarimetry (see Fig. 15).

Before *IXPE*, it was not possible to observe the X-ray polarimetric properties of the emission from AMPs. However, in preparation for the *IXPE* launch, existing pulse profile models were expanded to include X-ray polarimetry. First, in Poutanen (2020), a relativistic rotating vector model (RVM) was introduced to account for the rapid rotation of AMPs. This paper also included an analytical formalism for the calculation of polarimetric properties. In Loktev et al. (2020), the relativistic RVM was further modified accounting for the oblateness of the NS due to rapid rotation. In Salmi et al. (2021), polarimetry and oblateness were added to the Bayesian method for deriving parameter constraints from pulse profiles developed in Salmi et al. (2018). In Paper I, the model was further developed, replacing the Thomson scattering routine with the exact Compton scattering formalism, since these two processes affect

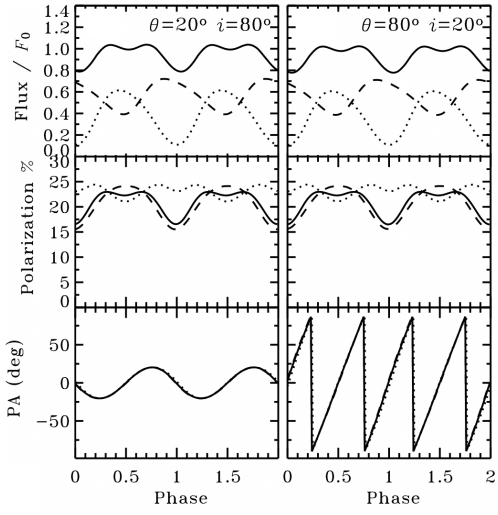


Figure 15. Pulse profiles of the flux, PD, and PA for different geometrical configurations of the AMP. Dashed, dotted, and solid lines correspond to the the primary spot flux, secondary spot flux, and total flux, respectively. Adapted from Viironen & Poutanen (2004).

polarimetric properties in different ways (see Sect. 1.2 for a recap). Replacing the scattering model led to a decrease in the expected polarization; for the parameter set inspired by the most famous AMP, SAX J1808.4−3658, the expected PD dropped from more than 5% in Salmi et al. (2021) to barely 2% in Paper I. However, some favorable parameter combinations were discussed, and the preparation for *IXPE* observations of AMPs continued. The model from Paper I was later incorporated into the X-PSI code and applied to fitting synthetic *IXPE* data in Salmi et al. (2025); there, variability of the hotspot shape was added to the model.

IXPE performed its first observation of an AMP in February 2024, the target was a newly discovered SRGA J144459.2−604207 (Papitto et al. 2025). An average PD of 2.3% ± 0.4% was observed in the 2−8 keV energy range; energy-resolved analysis showed that the emission between 3 and 6 keV is more highly polarized than below 3 keV (4.0% ± 0.5% vs. an upper limit of 1.5%, respectively). Phase-resolved analysis showed Stokes parameters compatible with a constant function, despite the fact that the source showed a rather stable pulse profile with an amplitude of ∼ 5% throughout most of the observation. A relativistic RVM was applied to constrain the geometry of the system, obtaining a rather high inclination of 74° ± 6°, consistent with optical observations, and two almost antipodal spots at colatitudes of 12° and 173°. Applying the more advanced pulse profile modeling to the *IXPE* and NICER observations of SRGA J144459.2−604207 is reported in Dorsman et al. (2026b).

5 Future prospects

5.1 New X-ray polarimetric instruments

With the launch of *IXPE*, a new era in X-ray polarimetry has begun. Dozens of objects have been observed for the first time, and many more observations are anticipated. While observational papers are usually published shortly after the data become available, hidden gems are constantly discovered years after the observation, leaving plenty of space for re-analyzing the data.

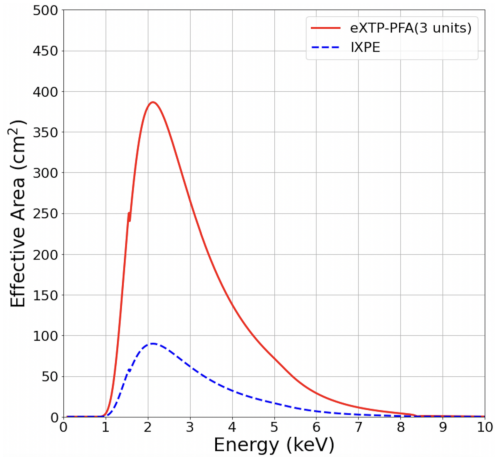


Figure 16. Effective area of *IXPE* (blue) and eXTP polarimetry focusing array (PFA) instruments (red). From Zhang et al. (2025).

With the upcoming launch of *enhanced X-ray Timing and Polarimetry (eXTP)* mission (Zhang et al. 2025) and the *Globe Orbiting Soft X-ray (GOSoX)* polarimeter (Marshall et al. 2021), new horizons are opening for X-ray polarimetry. *eXTP*, with its large effective area (see Fig. 16), wide field monitor instruments, and remarkable timing capabilities, is expected to provide tighter constraints on the EoS by measuring polarized pulse profiles and, consequently, masses and radii of pulsars. Moreover, it is expected to study the phenomena associated with the accretion disk dynamics, such as kHz QPOs and relativistic Fe line profiles (Li et al. 2025a), which will help constrain the geometry of the accretion flow.

GOSoX, in turn, is a recently selected soft X-ray mission with an expected energy range from 165 eV to 400 eV, below those of both *IXPE* and *eXTP*. Since some RMPs are observable below 1 keV, *GOSoX* offers a unique opportunity to study the polarimetric properties of their radiation.

5.2 Weakly magnetized neutron stars

Despite the significant theoretical efforts and a multitude of *IXPE* observations of various WMNS systems, many questions are currently left without an answer, requiring further investigation.

In the first years of *IXPE* mission, dozens of WMNSs have been observed, and rarely the observation results met the theoretical predictions. For instance, in many sources, we saw a relatively high polarization at higher energies (see, e.g., Gnarini et al. 2025, for a review), suggesting that either the BL/SL region, where the harder spectral component is expected to originate, should emit highly-polarized light, or the scattering in the wind and/or reflection from the disk should have major contribution to the flux. While for some systems it seems to be true, in many we still do not have a clear explanation for their higher-than-expected polarization (see, e.g., Di Marco et al. 2023; La Monaca et al. 2024). We also regularly see a hard-to-justify variability of polarimetric properties with time and energy (see, e.g., Fabiani et al. (2024), Paper II). Moreover, plenty of suggestions in the observational papers are not yet quantitatively confirmed. All these unanswered questions require further studies.

In order to simplify and qualitatively change the data interpretation, a complete model for WMNS systems is needed. At this point, significant achievements have been reported for calculating the emission of specific regions of the binary system, and first attempts at creating a numerical spectropolarimetric model for a combination of an accretion disk and a BL have been recently introduced in Farinelli & Cocchi (2025). Yet, there is a place for further improvements, such as accounting for reflection and scattering, or including the possibility of misalignment in the system.

Last but not least, one of the key open questions of the WMNS studies, the physics behind the state transition, is yet without an answer. For this, a long and consistent observation of a single source is required. In December 2025 – January 2026, such a campaign happened for the first time with the Cyg X-2 system, and hopefully, the results of this campaign will provide us with insights regarding the polarimetric variability along the Z-track of this source. Cyg X-2 is a well-known benchmark Z-source, bright, persistent, and with a systematical evolution of the spectral parameters along the Z-track (Di Salvo et al. 2002; Farinelli et al. 2009). I believe that only after understanding the principal mechanism of the state transition in such a system would we be able to explain and fully understand challenging behavior of enigmatic systems like GX 13+1.

5.3 Accretion millisecond pulsars

Improving theoretical models is a never-ending process. Salmi et al. (2021) introduced polarization into a Thomson-scattering-based model of the AMP atmosphere. In Paper I, we replaced the Thomson scattering approximation with exact Compton

scattering calculations, but the model development did not end there. For instance, Salmi et al. (2025) and Dorsman et al. (2025) report the results of implementing the model from Paper I into the X-PSI code (Riley et al. 2023). Salmi et al. (2025) focused on hotspot shapes and constraints on the mass and radius derived from polarimetric data, while Dorsman et al. (2025) applied a disk and atmosphere model to the analysis of NICER data.

Applying the model to experimental data comes with its challenges, but the work in this direction is ongoing. At the time of writing, two AMPs has been observed by *IXPE*: SRGA J144459.2−604207 in February 2024 (Papitto et al. 2025) and SAX J1808.4−3658 in September 2025 (analysis in progress). In the discovery paper (Papitto et al. 2025), only the standard RVM was applied to the data, while Dorsman et al. (2026b) present the results of the first attempt to fit the *IXPE* and NICER data simultaneously with the most modern model we have. They were able to fit the data, suggest the shape and location of the hotspots, and even provide weak constraints on mass and radius of the source. However, they strongly encourage further investigation.

Another promising direction of the future research in AMP modeling is the application of modern plasma astrophysics approaches. Global three-dimensional relativistic magnetohydrodynamic simulations have recently been applied to AMPs in Das et al. (2025), introducing significant broadband variability to the pulse profiles and leaving space for further model improvements. On the other hand, particle-in-cell (PIC) simulations have so far been applied only to radio pulsars (Philippov et al. 2020; Chernoglazov et al. 2024), not to AMPs. These simulations have provided new insights into the origin of X-ray pulsar emission. It would be interesting to explore how these methods could be applied to AMP to further investigate the spectropolarimetric picture.

6 Summary of the original publications

I Polarized radiation from an accretion shock in accreting millisecond pulsars using exact Compton scattering formalism

In this paper, we introduce a new analytical model for calculating the polarized pulse profiles of AMPs. The emission was assumed to become polarized via Compton scattering in an accretion shock above the NS surface, which we approximated as a plane parallel electron-dominated isothermal slab. We solved the radiative transfer equation using the iterative scattering method, replacing the previously used Thomson scattering routine, which lead to decrease in expected polarization. We calculated the Stokes parameters as functions of photon energy and zenith angle for almost 14 000 combinations of the main atmospheric parameters. We then developed a routine to calculate the pulse profiles and to fit the synthetic *IXPE* data with our model. We estimated the possible constraints on the geometric and atmospheric parameters that could be derived from *IXPE* data.

II Discovery of a strong rotation of the X-ray polarization angle in the galactic burster GX 13+1

The paper reports the first *IXPE* observation of GX 13+1, a bright persistent WMNS system. A 100 ks spectropolarimetric observation allowed us to study not only the overall polarization of the source (PD = 1.4% ± 0.3%, PA = −2° ± 6°), but also the time, intensity, and energy dependence of polarimetric properties. Because of the dip in the light curve, we separated the observation into three segments (pre-dip, dip, and post-dip) and learned that in all three segments, both PD and PA behaved differently. Most importantly, we reported a strong rotation of PA with time, slowly and persistently changing by 70° during the observation. To estimate the state of the source, a complimentary observation with *XMM-Newton* was organized. The results of the observation reported in this paper inspired at least three more X-ray polarimetric observational campaigns on GX 13+1.

III New polarimetric study of the galactic burster GX 13+1

The second observation of GX 13+1 with *IXPE* is reported in the paper. During this 90 ks spectropolarimetric observation, *IXPE* observed an overall PD = 2.6% ± 0.5% and PA = 23° ± 5°, different from the first observation, despite the source being in a similar spectral state. Most peculiarly, we did not see the previously discovered rotation of PA with time. We compared the observational results in detail and provided possible explanations for the polarimetric properties. This observation was accompanied by a *Swift* spectroscopic observation to track the state of the source.

IV Polarized radiation from the spreading layer of weakly magnetized neutron stars

In this paper, we introduce an analytical model that allowed us to calculate the estimated polarimetric properties of the light coming from a SL of a WMNS. Since the magnetosphere of WMNS is not strong enough to direct the accretion flow, the matter from an accretion disk falls onto the NS surface, and a SL is a possible geometrical configuration of the accretion flow near the surface. In the paper, we studied the impact of various SL parameters on the polarimetric properties. We concluded that SL emission is primarily polarized in the plane perpendicular to the accretion disk, while the PD does not exceed 1.5% in any of the reported simulations. We discussed the application of the model to *IXPE* observations analysis and compared the derived expectations to the already existing observational results.

V Breaking the symmetry: X-ray polarization from a spreading layer on a tilted weakly magnetized neutron star

Several *IXPE* observations have shown hints toward a possible misalignment between the rotational axis of the NS and the binary rotation axis. We developed an analytical model for a SL polarization in a misaligned WMNS system. In the paper, we studied the effects of the new parameters on the polarimetric properties of the SL emission. We concluded that a SL on a tilted WMNS produce PD higher than the aligned one, reaching 2–3%, and that the PA strongly depend on the misalignment parameters. We discussed the possibility for a misalignment to serve as an explanation for some of the observational results.

The author's contribution to the publications

Paper I: The research presented in the paper is based on the theoretical work on the AMP atmosphere modeling of V. Loktev, as well as the pulse profile modeling of T. Salmi presented in Salmi et al. (2021). The author is responsible for combining these techniques, performing the parameter study and the synthetic data fitting, as well as deriving the conclusions and predictions for the future *IXPE* observations. The author is also responsible for writing 80% of the manuscript. The contribution covers approximately 50% of the total amount of work. The article was used in the doctoral thesis of V. Loktev.

Paper II: The author lead the work of the large team behind the manuscript. The author planned the paper, coordinated the data analysis, worked on the interpretation of the results, and wrote most of the manuscript. The author also applied for and obtained the complimentary *XMM-Newton* data used in the paper.

Paper III: The author coordinated the data analysis, worked on the interpretation of the results, and wrote most of the manuscript. The author also applied for and obtained the complimentary *Swift* data used in the paper.

Paper IV: The author contributed to planning the research. The author performed the majority of the theoretical and practical work and wrote the manuscript.

Paper V: The author contributed to planning the research. The author performed the majority of the theoretical work and conducted the practical part. The author also wrote the manuscript.

List of References

Abbott, B. P., Abbott, R., Abbott, T. D., et al. 2017, Phys. Rev. Lett., 119, 161101
Abbott, B. P., Abbott, R., Abbott, T. D., et al. 2018, Phys. Rev. Lett., 121, 161101
Abolmasov, P., Nättilä, J., & Poutanen, J. 2020, A&A, 638, A142
Abolmasov, P. & Poutanen, J. 2021, A&A, 647, A45
Abramowicz, M. A. & Fragile, P. C. 2013, Living Reviews in Relativity, 16, 1
Allen, J. L., Schulz, N. S., Homan, J., et al. 2018, ApJ, 861, 26
Archibald, A. M., Kaspi, V. M., Bogdanov, S., et al. 2010, ApJ, 722, 88
Avakyan, A., Neumann, M., Zainab, A., et al. 2023, A&A, 675, A199
Babkovskaia, N., Brandenburg, A., & Poutanen, J. 2008, MNRAS, 386, 1038
Baldini, L., Barbanera, M., Bellazzini, R., et al. 2021, Astroparticle Physics, 133, 102628
Bandyopadhyay, R. M., Shahbaz, T., Charles, P. A., & Naylor, T. 1999, MNRAS, 306, 417
Belloni, D. & Schreiber, M. R. 2023, in Handbook of X-ray and Gamma-ray Astrophysics, 129
Berardi, S. 2026, Starplot
Bhattacharya, D. & van den Heuvel, E. P. J. 1991, Phys. Rep., 203, 1
Bisnovatyi-Kogan, G. 2017, in XII Multifrequency Behaviour of High Energy Cosmic Sources Workshop (MULTIF2017), 37
Boffin, H. M. J. & Jones, D. 2025, Contributions of the Astronomical Observatory Skalnate Pleso, 55, 21
Borghese, A. & Coti Zelati, F. 2026, in Encyclopedia of Astrophysics, Volume 3, Vol. 3, 145–159
Bult, P., Markwardt, C. B., Altamirano, D., et al. 2019, ApJ, 877, 70
Burgio, G. F., Schulze, H.-J., Vidaña, I., & Wei, J.-B. 2021, Progress in Particle and Nuclear Physics, 120, 103879
Campana, S. & Di Salvo, T. 2018, in Astrophysics and Space Science Library, Vol. 457, Astrophysics and Space Science Library, ed. L. Rezzolla, P. Pizzochero, D. I. Jones, N. Rea, & I. Vidaña, 149
Casares, J., Charles, P., & Kuulkers, E. 1998, ApJ, 493, L39
Casella, P., Altamirano, D., Patruno, A., Wijnands, R., & van der Klis, M. 2008, ApJ, 674, L41
Chandrasekhar, S. 1960, Radiative transfer (New York: Dover)
Chatziioannou, K., Cromartie, H. T., Gandolfi, S., et al. 2025, Reviews of Modern Physics, 97, 045007
Chen, H.-L., Chen, X., Tauris, T. M., & Han, Z. 2013, The Astrophysical Journal, 775, 27
Chernoglazov, A., Philippov, A., & Timokhin, A. 2024, ApJ, 974, L32
Church, M. J., Gibiec, A., & Bałucińska-Church, M. 2014, MNRAS, 438, 2784
Church, M. J., Gibiec, A., Bałucińska-Church, M., & Jackson, N. K. 2012, A&A, 546, A35
Conrad-Burton, J., Shabi, A., & Ginzburg, S. 2023, MNRAS, 525, 2708
Corbet, R. H. D., Pearlman, A. B., Buxton, M., & Levine, A. M. 2010, ApJ, 719, 979
Costa, E. 2024, in Handbook of X-ray and Gamma-ray Astrophysics, ed. C. Bambi & A. Santangelo (Singapore: Springer), 5663–5682
Cromartie, H. T., Fonseca, E., Ransom, S. M., et al. 2020, Nature Astronomy, 4, 72
D'Aí, A., Iaria, R., Di Salvo, T., et al. 2014, A&A, 564, A62
Das, P., Salmi, T., Davelaar, J., Porth, O., & Watts, A. 2025, ApJ, 987, 34
Di Marco, A. 2025, Astronomische Nachrichten, 346, e20240126
Di Marco, A. 2026, arXiv e-prints, arXiv:2604.03366
Di Marco, A., Fabiani, S., La Monaca, F., et al. 2022, AJ, 164, 103

Di Marco, A., La Monaca, F., Bobrikova, A., et al. 2025, ApJ, 979, L47
Di Marco, A., La Monaca, F., Poutanen, J., et al. 2023, ApJ, 953, L22
Di Salvo, T., Farinelli, R., Burderi, L., et al. 2002, A&A, 386, 535
Di Salvo, T., Papitto, A., Marino, A., Iaria, R., & Burderi, L. 2023, in Handbook of X-ray and Gamma-ray Astrophysics, 147
Di Salvo, T. & Sanna, A. 2022, in ASSL, Vol. 465, Millisecond Pulsars, ed. S. Bhattacharyya, A. Papitto, & D. Bhattacharya, 87–124
Díaz Trigo, M., Sidoli, L., Boirin, L., & Parmar, A. N. 2012, A&A, 543, A50
Diaz Trigo, M., Sidoli, L., Parmar, A., & Boirin, L. 2010, in AIP Conf. Ser., Vol. 1248, X-ray Astronomy 2009; Present Status, Multi-Wavelength Approach and Future Perspectives, ed. A. Comastri, L. Angelini, & M. Cappi (AIP), 153–154
Dorsman, B., Salmi, T., Watts, A. L., et al. 2026a, MNRAS, 545, staf1983
Dorsman, B., Salmi, T., Watts, A. L., et al. 2026b, MNRAS, 551, stag1340
Dorsman, B., Salmi, T., Watts, A. L., et al. 2025, MNRAS, 538, 2853
Dovčiak, M., Muleri, F., Goosmann, R. W., Karas, V., & Matt, G. 2008, MNRAS, 391, 32
Fabiani, S., Capitanio, F., Iaria, R., et al. 2024, A&A, 684, A137
Farinelli, R. & Cocchi, M. 2025, A&A, 702, A272
Farinelli, R., Paizis, A., Landi, R., & Titarchuk, L. 2009, A&A, 498, 509
Farinelli, R., Titarchuk, L., Paizis, A., & Frontera, F. 2008, ApJ, 680, 602
Farinelli, R., Waghmare, A., Ducci, L., & Santangelo, A. 2024, A&A, 684, A62
Frank, J., King, A., & Raine, D. J. 2002, Accretion Power in Astrophysics: Third Edition
Galloway, D. K. & Keek, L. 2021, in ASSL, Vol. 461, Timing Neutron Stars: Pulsations, Oscillations and Explosions, ed. T. M. Belloni, M. Méndez, & C. Zhang, 209–262
Giacconi, R., Gursky, H., Paolini, F. R., & Rossi, B. B. 1962, Phys. Rev. Lett., 9, 439
Gierliński, M. & Done, C. 2002a, MNRAS, 331, L47
Gierliński, M. & Done, C. 2002b, MNRAS, 337, 1373
Gierliński, M., Done, C., & Barret, D. 2002, MNRAS, 331, 141
Gierliński, M. & Poutanen, J. 2005, MNRAS, 359, 1261
Gilfanov, M., Revnivtsev, M., & Molkov, S. 2003, A&A, 410, 217
Gladstone, J., Done, C., & Gierliński, M. 2007, MNRAS, 378, 13
Gnarini, A., Ursini, F., Matt, G., et al. 2025, A&A, 699, A230
Gnarini, A., Ursini, F., Matt, G., et al. 2022, MNRAS, 514, 2561
Hameury, J. M. 2020, Advances in Space Research, 66, 1004
Hasinger, G. & van der Klis, M. 1989, A&A, 225, 79
Heinz, S., Sell, P., Fender, R. P., et al. 2013, ApJ, 779, 171
Hill, R. W., Grader, R. J., & Seward, F. D. 1968, ApJ, 154, 655
Iaria, R., Di Salvo, T., Burderi, L., et al. 2014, A&A, 561, A99
Ibragimov, A. & Poutanen, J. 2009, MNRAS, 400, 492
Inogamov, N. A. & Sunyaev, R. A. 1999, Astronomy Letters, 25, 269
Ji, Z., Chen, J., & Chen, Y. 2025, arXiv e-prints, arXiv:2505.05241
Kalogera, V. & Baym, G. 1996, ApJ, 470, L61
Kar, A., Ojha, P., & Bhattacharyya, S. 2025, ApJ, 980, 51
Kashyap, U., Maccarone, T. J., Pattie, E. C., et al. 2025, ApJ, 992, 66
King, A. R. & Ritter, H. 1999, MNRAS, 309, 253
Koljonen, K. I. I. & Linares, M. 2025, ApJ, 994, 8
La Monaca, F., Di Marco, A., Ludlam, R. M., et al. 2024, A&A, 691, A253
Lapidus, I. I. & Sunyaev, R. A. 1985, MNRAS, 217, 291
Li, A., Watts, A. L., Zhang, G., et al. 2025a, Science China Physics, Mechanics, and Astronomy, 68, 119503
Li, H., Zhao, Q.-C., Feng, H., Tao, L., & Tsygankov, S. S. 2025b, ApJ, 994, 41
Lin, D., Remillard, R. A., & Homan, J. 2009, ApJ, 696, 1257
Loktev, V., Salmi, T., Nättilä, J., & Poutanen, J. 2020, A&A, 643, A84

Loktev, V., Veledina, A., & Poutanen, J. 2022, A&A, 660, A25
Long, K. S., Chanan, G. A., Ku, W. H.-M., & Novick, R. 1979, ApJ, 232, L107
Long, K. S., Chanan, G. A., & Novick, R. 1980, ApJ, 238, 710
Lorimer, D. R. 2008, Living Reviews in Relativity, 11, 8
Ludlam, R. M. 2024, Ap&SS, 369, 16
Ludlam, R. M., Cackett, E. M., García, J. A., et al. 2020, ApJ, 895, 45
Ludlam, R. M., Jaodand, A. D., García, J. A., et al. 2021, ApJ, 911, 123
Lynden-Bell, D. & Pringle, J. E. 1974, MNRAS, 168, 603
Lyne, A. G., Pritchard, R. S., & Graham Smith, F. 1993, MNRAS, 265, 1003
Maiolino, T., Laurent, P., Titarchuk, L., Orlandini, M., & Frontera, F. 2019, A&A, 625, A8
Manchester, R. N. 2017, Journal of Astrophysics and Astronomy, 38, 42
Marshall, H. L., Heine, S. N. T., Davidson, R., et al. 2021, in Proc. SPIE, Vol. 11822, Optics for EUV, X-Ray, and Gamma-Ray Astronomy X, ed. S. L. O'Dell, J. A. Gaskin, & G. Pareschi, 118220O
Martinez, J. G., Stovall, K., Freire, P. C. C., et al. 2015, ApJ, 812, 143
Matt, G. 1993, MNRAS, 260, 663
Méndez, M. & Belloni, T. M. 2021, in ASSL, Vol. 461, Timing Neutron Stars: Pulsations, Oscillations and Explosions, ed. T. M. Belloni, M. Méndez, & C. Zhang, 263–331
Miller, M. C., Lamb, F. K., Dittmann, A. J., et al. 2019, ApJ, 887, L24
Misra, D., Linares, M., & Ye, C. S. 2025, A&A, 693, A314
Mondal, A. S., Raychaudhuri, B., Dewangan, G. C., & Beri, A. 2022, MNRAS, 516, 1256
Morsink, S. M., Leahy, D. A., Cadeau, C., & Braga, J. 2007, ApJ, 663, 1244
Motta, S. E., Rouco Escorial, A., Kuulkers, E., Muñoz-Darias, T., & Sanna, A. 2017, MNRAS, 468, 2311
Muñoz-Darias, T., Díaz Trigo, M., Done, C., Ponti, G., & Tomaru, R. 2026, Space Sci. Rev., 222, 39
Muno, M. P., Remillard, R. A., & Chakrabarty, D. 2002, ApJ, 568, L35
Mushtukov, A. & Tsygankov, S. 2024, in Handbook of X-ray and Gamma-ray Astrophysics, ed. C. Bambi & A. Santangelo (Singapore: Springer), 4105–4176
Nagirner, D. I. & Poutanen, J. 1994, Astrophysics and Space Physics Reviews, 9, 1
Ng, M., Hughes, A. K., Homan, J., et al. 2024, ApJ, 966, 232
Nitindala, A. P., Veledina, A., & Poutanen, J. 2025, A&A, 694, A230
Novick, R., Weisskopf, M. C., Berthelsdorf, R., Linke, R., & Wolff, R. S. 1972, ApJ, 174, L1
Oppenheimer, J. R. & Volkoff, G. M. 1939, Physical Review, 55, 374
Papitto, A., Di Marco, A., Poutanen, J., et al. 2025, A&A, 694, A37
Papitto, A., Ferrigno, C., Bozzo, E., et al. 2013, Nature, 501, 517
Papitto, A. & Martino, D. d. 2022, Transitional Millisecond Pulsars, ed. S. Bhattacharyya, A. Papitto, & D. Bhattacharya (Cham: Springer International Publishing), 157–200
Patruno, A., Hartman, J. M., Wijnands, R., Chakrabarty, D., & van der Klis, M. 2010, ApJ, 717, 1253
Patruno, A., Haskell, B., & Andersson, N. 2017, ApJ, 850, 106
Patruno, A. & Watts, A. L. 2021, in ASSL, Vol. 461, Timing Neutron Stars: Pulsations, Oscillations and Explosions, ed. T. M. Belloni, M. Méndez, & C. Zhang, 143–208
Philippov, A., Timokhin, A., & Spitkovsky, A. 2020, Phys. Rev. Lett., 124, 245101
Popham, R. & Narayan, R. 1995, ApJ, 442, 337
Popham, R. & Sunyaev, R. 2001, ApJ, 547, 355
Poutanen, J. 1994, ApJS, 92, 607
Poutanen, J. 2006, Advances in Space Research, 38, 2697
Poutanen, J. 2020, A&A, 641, A166
Poutanen, J. & Gierliński, M. 2003, MNRAS, 343, 1301
Poutanen, J., Ibragimov, A., & Annala, M. 2009, ApJ, 706, L129
Poutanen, J., Nagendra, K. N., & Svensson, R. 1996, MNRAS, 283, 892
Pringle, J. E. 1977, MNRAS, 178, 195
Pringle, J. E. & Rees, M. J. 1972, A&A, 21, 1
Pringle, J. E. & Savonije, G. J. 1979, MNRAS, 187, 777

Raghavan, D., McAlister, H. A., Henry, T. J., et al. 2010, ApJS, 190, 1
Rappaport, S., Nelson, L. A., Ma, C. P., & Joss, P. C. 1987, ApJ, 322, 842
Ravi, S., Ng, M., Marshall, H. L., & Gnarini, A. 2026, ApJ, 997, 60
Rees, M. J. 1975, MNRAS, 171, 457
Revnivtsev, M. G., Suleimanov, V. F., & Poutanen, J. 2013, MNRAS, 434, 2355
Riley, T. E., Choudhury, D., Salmi, T., et al. 2023, The Journal of Open Source Software, 8, 4977
Riley, T. E., Watts, A. L., Bogdanov, S., et al. 2019, ApJ, 887, L21
Rogantini, D., Homan, J., Plotkin, R. M., et al. 2025, ApJ, 986, 41
Romani, R. W., Kandel, D., Filippenko, A. V., Brink, T. G., & Zheng, W. 2022, ApJ, 934, L17
Rusakov, A., Abolmasov, P., & Bromberg, O. 2025, ApJ, 991, 29
Saavedra, E. A., García, F., Fogantini, F. A., et al. 2023, MNRAS, 522, 3367
Sakurai, S., Yamada, S., Torii, S., et al. 2012, PASJ, 64, 72
Salmi, T., Dorsman, B., Watts, A. L., et al. 2025, MNRAS, 538, 2562
Salmi, T., Loktev, V., Korsman, K., et al. 2021, A&A, 646, A23
Salmi, T., Nättilä, J., & Poutanen, J. 2018, A&A, 618, A161
Schnerr, R. S., Reerink, T., van der Klis, M., et al. 2003, A&A, 406, 221
Shakura, N. I. & Sunyaev, R. A. 1973, A&A, 500, 33
Shakura, N. I. & Sunyaev, R. A. 1988, Adv. Space Res., 8, 135
Shibazaki, N., Murakami, T., Shaham, J., & Nomoto, K. 1989, Nature, 342, 656
Stark, R. F. & Connors, P. A. 1977, Nature, 266, 429
Steiner, A. W., Lattimer, J. M., & Brown, E. F. 2013, ApJ, 765, L5
Suleimanov, V. & Poutanen, J. 2006, MNRAS, 369, 2036
Suleimanov, V. F., Poutanen, J., & Werner, K. 2020, A&A, 639, A33
Sunyaev, R. A. & Titarchuk, L. G. 1985, A&A, 143, 374
Titarchuk, L. 1994, ApJ, 434, 570
Tomaru, R., Done, C., & Odaka, H. 2024, MNRAS, 527, 7047
Tomaru, R., Done, C., Ohsuga, K., Odaka, H., & Takahashi, T. 2020, MNRAS, 497, 4970
Turolla, R. 2009, in Astrophysics and Space Science Library, Vol. 357, Astrophysics and Space Science Library, ed. W. Becker, 141
Tylenda, R. 1981, Acta Astron., 31, 267
Ursini, F., Gnarini, A., Capitanio, F., et al. 2024, Galaxies, 12, 43
van der Klis, M. 1989, in ESA Special Publication, Vol. 1, Two Topics in X-Ray Astronomy, Volume 1: X Ray Binaries. Volume 2: AGN and the X Ray Background, ed. J. Hunt & B. Battrick, 203
van der Klis, M. 1992, in NATO Advanced Study Institute (ASI) Series C, Vol. 377, X-Ray Binaries and Recycled Pulsars, ed. E. P. J. van den Heuvel & S. A. Rappaport, 49–59
Viironen, K. & Poutanen, J. 2004, A&A, 426, 985
Weisskopf, M. 2018, Galaxies, 6, 33
Weisskopf, M. C., Silver, E. H., Kestenbaum, H. L., Long, K. S., & Novick, R. 1978, ApJ, 220, L117
Weisskopf, M. C., Soffitta, P., Baldini, L., et al. 2022, J. Astron. Telesc. Instrum. Syst., 8, 026002
Wijnands, R. 2001, Advances in Space Research, 28, 469
Wijnands, R. & van der Klis, M. 1998, Nature, 394, 344
Xrism Collaboration, Audard, M., Awaki, H., et al. 2025, Nature, 646, 57
Yakovlev, D. G. & Pethick, C. J. 2004, ARA&A, 42, 169
Zdziarski, A. A., Szanecki, M., Poutanen, J., Gierliński, M., & Biernacki, P. 2020, MNRAS, 492, 5234
Zhang, S.-N., Santangelo, A., Xu, Y., et al. 2025, Science China Physics, Mechanics, and Astronomy, 68, 119502

Original Publications

A. Bobrikova, V. Loktev, T. Salmi, J. Poutanen
Polarized radiation from an accretion shock in accreting millisecond pulsars using exact Compton scattering formalism

Astronomy & Astrophysics, 2023; 678: A99

I

A&A 678, A99 (2023)
https://doi.org/10.1051/0004-6361/202346833
© The Authors 2023

Astronomy & Astrophysics

Polarized radiation from an accretion shock in accreting millisecond pulsars using exact Compton scattering formalism

Anna Bobrikova[1], Vladislav Loktev[1], Tuomo Salmi[2,1], and Juri Poutanen[1]

[1] Tuorla Observatory, Department of Physics and Astronomy, University of Turku, 20014 Turku, Finland
e-mail: anna.a.bobrikova@utu.fi
[2] Anton Pannekoek Institute for Astronomy, University of Amsterdam, Science Park 904, 1098 XH Amsterdam, The Netherlands

Received 8 May 2023 / Accepted 11 August 2023

ABSTRACT

Pulse profiles of accreting millisecond pulsars can be used to determine neutron star (NS) parameters, such as their masses and radii, and therefore provide constraints on the equation of state of cold dense matter. Information obtained by the Imaging X-ray Polarimetry Explorer (IXPE) can be used to decipher pulsar inclination and magnetic obliquity, providing ever tighter constraints on other parameters. In this paper, we develop a new emission model for accretion-powered millisecond pulsars based on thermal Comptonization in an accretion shock above the NS surface. The shock structure was approximated by an isothermal plane-parallel slab and the Stokes parameters of the emergent radiation were computed as a function of the zenith angle and energy for different values of the electron temperature, the Thomson optical depth of the slab, and the temperature of the seed blackbody photons. We show that our Compton scattering model leads to a significantly lower polarization degree of the emitted radiation compared to the previously used Thomson scattering model. We computed a large grid of shock models, which can be combined with pulse profile modeling techniques both with and without polarization included. In this work, we used the relativistic rotating vector model for the oblate NS in order to produce the observed Stokes parameters as a function of the pulsar phase. Furthermore, we simulated the data to be produced by IXPE and obtained constraints on model parameters using nested sampling. The developed methods can also be used in the analysis of the data from future satellites, such as the enhanced X-ray Timing and Polarimetry mission.

Key words. methods: numerical – polarization – stars: neutron – techniques: polarimetric – X-rays: binaries

1. Introduction

Rapidly rotating accreting neutron stars (NSs) can be used to study the properties of the extremely dense matter inside their cores. Some of these are accretion-powered millisecond pulsars (AMPs), which show X-ray pulsations at the stellar spin frequency. Their emission profiles can be modeled, accounting for light bending and other relativistic effects, and from these profiles, the information about the mass and radius of the NS can be extracted (see e.g., Pechenick et al. 1983; Miller & Lamb 1998; Poutanen & Gierliński 2003; Poutanen & Beloborodov 2006; Morsink et al. 2007; Lo et al. 2013; Watts et al. 2016; Salmi et al. 2018; Bogdanov et al. 2019). The mass and radius constraints can be translated to the equation of state (EOS) constraints for matter inside the NS core (e.g., see Lindblom 1992; Lattimer 2012; Hebeler et al. 2013; Baym et al. 2018).

This technique was recently applied to the case of rotation-powered millisecond pulsars using data from the Neutron Star Interior Composition Explorer (NICER; Miller et al. 2019, 2021; Riley et al. 2019, 2021; Salmi et al. 2022). In these sources, the hot regions on the NS surface are heated by a magnetospheric return current and the emission escaping the NS surface can be computed using self-consistent atmosphere models (see e.g., Zavlin et al. 1996; Ho & Lai 2001; Heinke et al. 2006; Ho & Heinke 2009; Haakonsen et al. 2012; Salmi et al. 2020). For AMPs, these models are not adequate because the emitted radiation is Comptonized in an accretion "shock" formed above the hot region. In reality, a standard gasdynamical shock might not exist at all, but the kinetic energy of incoming particles is released in the surface layer through Coulomb collisions and plasma instabilities (Zel'dovich & Shakura 1969; Suleimanov et al. 2018; Salmi et al. 2020). Comptonization of soft photons generated within the layer as well as by the underlying NS surface is then responsible for the power-law spectra extending up to 100 keV as observed from AMPs (Poutanen & Gierliński 2003; Gierliński & Poutanen 2005; Falanga et al. 2005a,b, 2007, 2011, 2012). Electron scattering also causes the radiation to be significantly polarized. Variations of polarization with pulsar phase can be used to determine geometrical parameters such as inclination angle and magnetic obliquity (Viironen & Poutanen 2004), which in their turn allow us to improve constraints on the NS mass and radius.

Previously, polarized emission models for AMPs used the Thomson scattering approximation in an optically thin NS atmosphere (see Sunyaev & Titarchuk 1985; Viironen & Poutanen 2004; Salmi et al. 2021). However, the polarization degree due to Compton scattering on hot electrons strongly depends on the electron temperature (Nagirner & Poutanen 1994; Poutanen 1994); for example, for 100 keV electrons, polarization is less than 50% of that for Thomson scattering. On the other hand, the models for nonpolarized radiation – in the context of pulse profile modeling – typically employ approximate formulas for the anisotropy of the radiation and empirical models for the Comptonized spectra (see e.g., Poutanen & Gierliński 2003; Leahy et al. 2008; Steiner et al. 2009; Salmi et al. 2018). Self-consistent accretion-heated atmosphere models have also been developed (see e.g., Zampieri et al. 1995; Deufel et al. 2001;

Open Access article, published by EDP Sciences, under the terms of the Creative Commons Attribution License (https://creativecommons.org/licenses/by/4.0), which permits unrestricted use, distribution, and reproduction in any medium, provided the original work is properly cited.
This article is published in open access under the Subscribe to Open model. Subscribe to A&A to support open access publication.

Suleimanov et al. 2018), although these are relatively computationally expensive and have a large number of free parameters.

In this work, we applied the formalism for Compton scattering in a hot slab (Nagirner & Poutanen 1993; Poutanen & Svensson 1996) to compute the Stokes parameters of the emergent radiation as a function of energy and emission angle using only three model parameters: the electron temperature and optical depth of the hot slab on top of the NS surface, and the temperature of the seed blackbody photons coming from the NS. By employing pulse profile modeling for polarized radiation from rapidly rotating oblate NSs (Poutanen 2020; Loktev et al. 2020), we also simulated data for the Imaging X-ray Polarimeter Explorer (IXPE; Weisskopf et al. 2022) and updated the NS geometry parameter constraints previously predicted in Salmi et al. (2021) using the Thomson scattering model. These methods can also be applied when analyzing the observations from IXPE[1] or from future X-ray polarimetric missions such as the enhanced X-ray Timing and Polarimetry mission (eXTP; Zhang et al. 2019; Watts et al. 2019). The atmosphere look-up tables produced here can also be combined with any AMP pulse profile modeling codes[2].

The remainder of this paper is structured as follows. In Sect. 2, we present the theory that describes the formation of polarized radiation in a Comptonizing slab above the NS surface. We then apply this theory to obtain the intensity and polarization of the radiation escaping from the slab. We then describe the method to obtain pulse profiles using our new radiation model. We compare our resulting spectra and pulse profiles to those obtained using previous models. We also discuss pulse profiles obtained for different NS parameters. In Sect. 3, we generate synthetic data and apply our fitting routine to determine the NS parameters from the data. We discuss the applications of our model and predictions for the upcoming observations in Sect. 4. In Sect. 5, we conclude and summarize our findings.

2. Emission model

2.1. Radiative transfer equation

We consider a simple NS atmosphere model in which the atmosphere is a plane parallel slab consisting of electrons and lying above an optically thick source that radiates as a blackbody. The hot slab has the Thomson optical depth $\tau_{\rm T} = \sigma_{\rm T} n_{\rm e} H$, where H is the vertical height, $\sigma_{\rm T}$ is the Thomson cross section, and $n_{\rm e}$ is the electron concentration. The electron gas in the atmosphere is considered to be isotropic and isothermal with the electron temperature $T_{\rm e}$. The momentum distribution of electrons is given by relativistic Maxwellian distribution characterized by the dimensionless temperature $\Theta_{\rm e} = kT_{\rm e}/m_{\rm e}c^2$:

$$f_{\rm M}(\gamma) = \frac{{\rm e}^{-\gamma/\Theta_{\rm e}}}{4\pi\Theta_{\rm e} K_2(1/\Theta_{\rm e})}, \tag{1}$$

where γ is the electron Lorentz factor and K_2 is the modified Bessel function of the second kind. This distribution is normalized to unity:

$$\int_0^\infty f_{\rm M}(\gamma){\rm d}^3p = 4\pi\int_0^\infty f_{\rm M}(\gamma)p^2{\rm d}p = 1, \tag{2}$$

where $p = \sqrt{\gamma^2-1}$ is the electron dimensionless momentum. The radiation field can be described by the Stokes vector $\boldsymbol{I}(\tau, x, \mu)$, where μ is the cosine of the zenith angle, an angle between the normal to the slab and the direction of photon propagation, and $x = E/m_{\rm e}c^2$ is the photon energy measured in the units of the electron rest mass.

The Stokes vector usually contains four components I, Q, U, and V, but because of the azimuthal symmetry and the absence of sources of circular polarization, the latter two are equal to zero. We therefore use just two Stokes parameters $\boldsymbol{I}(\tau, x, \mu) = (I, Q)^{\rm T}$, where superscript T denotes the transposed vector.

The photon distribution at the bottom of the slab is considered to be Planckian of the temperature $T_{\rm bb}$. The incident radiation (for zeroth scattering order, $n = 0$) at the bottom of the slab is given by the Stokes vector

$$\boldsymbol{I}_{n=0}(\tau = 0, x, \mu) = \frac{2m_{\rm e}^4c^6}{h^3}\frac{x^3}{{\rm e}^{x/\Theta_{\rm bb}}-1}\begin{pmatrix}1\\0\end{pmatrix}, \tag{3}$$

where $\Theta_{\rm bb} = kT_{\rm bb}/m_{\rm e}c^2$. In order to describe the propagation of polarized radiation through the hot electron slab, we solve the radiative transfer equation (RTE; Nagirner & Poutanen 1994; Poutanen & Svensson 1996):

$$\mu\frac{{\rm d}\boldsymbol{I}(\tau, x, \mu)}{{\rm d}\tau} = -\sigma(x)\boldsymbol{I}(\tau, x, \mu) + \boldsymbol{S}(\tau, x, \mu), \tag{4}$$

where ${\rm d}\tau = \sigma_{\rm T} n_{\rm e}{\rm d}z$ is the Thomson optical depth, $\boldsymbol{S}$ is the source function (also a Stokes vector), and $\sigma(x)$ is the dimensionless Compton scattering cross-section (in units of the Thomson cross-section $\sigma_{\rm T}$). We solve the RTE using the iterative scattering method of Poutanen & Svensson (1996), where the intensity is represented as a series expansion in scattering orders. The Stokes vector of unscattered radiation at all optical depths is

$$\boldsymbol{I}_{n=0}(\tau, x, \mu) = \boldsymbol{I}_{n=0}(0, x, \mu)\,{\rm e}^{-\sigma(x)\tau/\mu}. \tag{5}$$

From the known Stokes vector at the nth scattering order, we find the source function for the following scattering order as

$$\boldsymbol{S}_{n+1}(\tau, x, \mu) = x^2\int_0^\infty\frac{{\rm d}x_1}{x_1^2}\int_{-1}^1{\rm d}\mu_1\,\hat{\boldsymbol{R}}(x, \mu; x_1, \mu_1)\boldsymbol{I}_n(\tau, x_1, \mu_1), \tag{6}$$

where $\hat{\boldsymbol{R}}$ is the 2×2 azimuth averaged redistribution matrix describing Compton scattering by isotropic electrons (see Appendix A.1 in Poutanen & Svensson 1996). If the source function is known, the Stokes vector is found via the formal solution of the RTE:

$$\boldsymbol{I}_{n+1}(\tau, x, \mu) = \begin{cases}\displaystyle\int_0^\tau\frac{{\rm d}\tau'}{\mu}\,\boldsymbol{S}_{n+1}(\tau', x, \mu)\,{\rm e}^{-(\tau-\tau')\sigma(x)/\mu}, & \mu > 0,\\ \displaystyle\int_\tau^{\tau_{\rm T}}\frac{{\rm d}\tau'}{(-\mu)}\,\boldsymbol{S}_{n+1}(\tau', x, \mu)\,{\rm e}^{-(\tau'-\tau)\sigma(x)/(-\mu)}, & \mu < 0.\end{cases} \tag{7}$$

Iterations proceed until the required accuracy of the total Stokes vector $\boldsymbol{I} = \sum_n \boldsymbol{I}_n$ is achieved so that the maximal contribution of the next scattering is less than 1% of the total spectrum in all energies and angles.

Finally, we can compute the polarization degree (PD) of the emergent radiation as

$$P(x, \mu) = 100\%\frac{Q(\tau_{\rm T}, x, \mu)}{I(\tau_{\rm T}, x, \mu)}. \tag{8}$$

[1] IXPE was launched in December 2021, but has not yet been able to observe an AMP in outburst.

[2] The tables are available at https://github.com/AnnaBobrikova/ComptonSlabTables

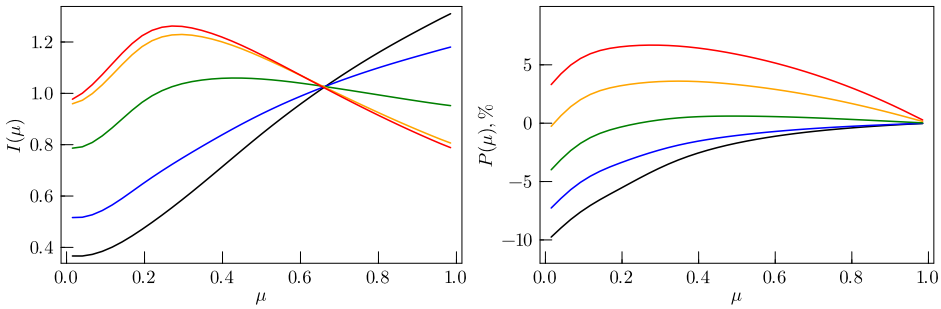


Fig. 1. Intensity of the emergent radiation (left) and the PD (right) as functions of the cosine of the zenith angle. The atmosphere parameters are $\tau_T = 1.0$, electron temperature $T_e = 50$ keV, and seed photon temperature $T_{bb} = 1$ keV. Black, blue, green, orange, and red solid lines show the model for photon energies of 2, 5, 8, 12, and 18 keV, respectively. The angular dependence of the intensity is normalized so that $\int_0^1 \mu I(\mu) d\mu = 1/2$.

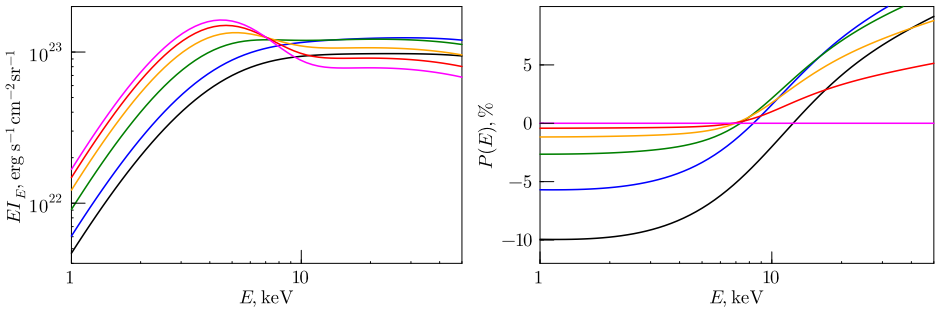


Fig. 2. Intensity of emergent radiation (left) and the PD (right) as functions of photon energy. The same atmosphere parameters are used as in Fig. 1. Black, blue, green, orange, red, and magenta solid lines show the model for $\mu = 0.0$, 0.2, 0.4, 0.6, 0.8, and 1.0 respectively.

The positive values of P imply that the polarization vector lies in the meridional plane defined by the slab normal and the photon momentum, while for the negative values, the polarization vector is perpendicular to that plane, as in the case of optically thick electron scattering atmosphere (Chandrasekhar 1960; Sobolev 1963).

2.2. Spectro-polarimetric properties of accretion shocks

We can now apply the derived formalism to predict the beaming patterns, energy spectra, and polarization of the accretion shock at the NS surface. We take as a fiducial set of parameters: $\tau_T = 1$, $T_e = 50$ keV, $T_{bb} = 1$ keV. Figures 1 and 2 show the spectrum and the PD as functions of the cosine of the zenith angle and energy, respectively, for this set of parameters. The parameters of the source are the same as those used in the Thomson model of Salmi et al. (2021; see their Figs. 1 and 2), and so these figures can be used to illustrate the impact of using an exact Compton scattering description instead of the Thomson scattering model in the slab of hot electrons.

When comparing our results with those of Salmi et al. (2021), we note that the PD differs significantly while the spectrum remains mainly unchanged. This effect is most obviously seen in the angular dependence of the PD. The absolute values of the PD are reduced by a factor of two for the photon energies of 2, 5, and 8 keV, and increased at higher energies. For Compton scattering, the PD changes the sign already at the photon energy of 8 keV and is positive at higher values, while for Thomson scattering the sign changes at photon energies above 18 keV. Last but not least, the maximum in the absolute value of the PD for the photon energies higher than 8 keV has shifted from $\mu = 0$ to higher values of the cosine of the zenith angle. Keeping in mind the energy range of the IXPE satellite (2–8 keV), we can say that compared to the previously developed model for AMPs that used Thomson scattering, the Compton scattering model predicts a lower PD. This result is in agreement with our expectations, as for hot electrons the relativistic aberration becomes important (Poutanen 1994). In the case of cold electrons, the PD of the Thomson singly scattered radiation is highly dependent on the scattering angle, reaching 100% at 90°. For relativistic electrons (but still in the Thomson scattering regime), the same happens in the electron rest frame; however, because of the relativistic motion of the electron, the photon in the external frame is preferentially scattered in the direction of the electron motion, resulting in zero final PD independent of the scattering angle (Bonometto et al. 1970; Nagirner & Poutanen 1993). In our case of 50 keV electrons, the electrons are not yet relativistic and the maximum PD is reduced to 60% from the Thomson case. We

can predict here that with the higher electron temperature, the PD will decrease further. This will be examined in the following section.

2.3. Grid of models

The model we consider for the accretion shock has three parameters: the optical depth of the Comptonizing plasma τ_T, the dimensionless electron temperature Θ_e, and the dimensionless characteristic photon temperature Θ_{bb} (associated with T_e and T_{bb}, respectively). To determine these parameters from the upcoming IXPE data, we need a dense grid of models. For the optical depth of the shock τ_T, we chose the lower and higher value of 0.5 and 3.5, respectively, and varied the parameter in steps of 0.1. For the electron temperature, we varied Θ_e from 0.04 to 0.2 (i.e., T_e from ∼20 to 100 keV) with a step of 0.004 (i.e., ∼2 keV). For the seed photon temperature, the dimensionless Θ_{bb} was varied in the interval $(1–3)\times10^{-3}$ (i.e., T_{bb} = 0.5–1.5 keV) in steps of 2×10^{-4} (i.e., ∼0.1 keV). Altogether, we computed 13 981 models.

The impact of the NS atmosphere parameters on the PD can be seen in Fig. 3. For the electron temperature, we see the expected decrease in the PD with T_e as electrons become more relativistic. For the two other parameters, the main feature is that with increasing the parameter value, the change of sign of the PD happens at higher energies. Within the mentioned intervals of parameter values, the impact is most significant with increasing the optical depth of the atmosphere and least significant with changes to the seed photon energy. For the IXPE observational range of 2–8 keV, this means that, in general, PD increases with the increase in these parameters.

In order to use the calculated Stokes parameters more effectively, we wrote a 3D interpolation routine over this grid of parameters, so that for any arbitrary combination of these parameters within the intervals mentioned, we can obtain the intensity and PD of the emission as functions of energy and zenith angle. We tested that the results of this interpolation match the direct calculation results for any combination of the parameters within the grid to within 8% (within 1% in the IXPE energy range).

2.4. Pulse profiles and polarization

We calculated the pulse profiles from the known beaming pattern and PD exactly as in Salmi et al. (2021). After obtaining the beaming pattern and PD of the emission on top of the NS atmosphere, we transport them from the hot emitting regions of the star (called hot spots) to the observer following the formalism described in Morsink et al. (2007), AlGendy & Morsink (2014), Poutanen (2020), and Loktev et al. (2020). We consider an oblate, rapidly rotating star in the Schwarzschild metric (hence, the effects of rotation on space-time are neglected). Gravitational redshift and the light-bending effect, as well as the effect of the fast rotation of the star, are accounted for in the polarization angle (PA) transfer. The only difference in approach is the reference radius used in time-delay calculation. While Loktev et al. (2020) use the exact radius of the star at the center of the spot, we follow the path described in Poutanen & Beloborodov (2006) and applied in Salmi et al. (2021) and use the equatorial radius as a reference radius.

We again return to the results from Salmi et al. (2021) and compare the pulse profiles coming from the model with Compton scattering in the atmosphere with previously obtained ones using Thomson scattering. Figure 4 presents this comparison for the case of two antipodal spots, both combined and individually from each spot, for the NS with atmospheric parameters from the fiducial set (inclination $i = 60°$ and magnetic co-latitude $\theta = 20°$ as in Salmi et al. 2021). We see that the flux does not change significantly, which is in agreement with the beaming patterns not changing either. The PD is now decreasing from 2 to 5 keV and then slowly increasing towards 8 keV. From inspection of the corresponding lines in Fig. 1, and accounting for the gravitational redshift, it is clear that the PD is following the same pattern for the corresponding energies of the emitted photons. The 'jump' by 90° in the PA for the 8 keV photons comes from the PD changing sign.

The main conclusion here is that we expect a significant drop in the observed PD compared to that predicted by Salmi et al. (2021). The impact of this reduction in PD on the possibility of observing the AMPs is further discussed in Sects. 3 and 4.

3. Synthetic data and their analysis

3.1. Generating the synthetic data

The developed model can be further used to analyze the data. Polarimetric measurements of the AMPs are yet to be carried out. In the absence of observations, we used the IXPEOBSSIM framework (Baldini et al. 2022; version 16) with the PCUBE algorithm to generate several samples of synthetic data imitating the data to be obtained from the IXPE observations of an AMP. We substituted the source with the model described above and obtained the event list for a specified observing time of 600 ks for a source with a flux of 100 mCrab. In this part of our study, we do not investigate the energy dependency of PD, and collect all the data in one energy bin. These data sets are in exactly the same form as publicly available IXPE data products, so we will be able to apply the developed routines to the real data as soon as they become available.

As mentioned above, applying the Compton scattering formalism reduces the expected PD as compared to the previous studies where Thomson scattering in the NS atmosphere was considered. We synthesized the data for the same parameter set as used in Fig. 4 (see Table 1, Model 1) and compared the PD to the so-called minimal detectable polarization (MDP) at 99% significance (see Weisskopf et al. 2010 for a definition of the MDP and Kislat et al. 2015 for further details) values for the corresponding phase bins. Figure 5a illustrates that the obtained values of the PD are below the MDP. According to Weisskopf et al. (2010), this means that we cannot have a proper measurement of the PD in this case. From this point, there are three main ways to improve the quality of the potential measurement: (i) we can increase the number of counts to reduce the MDP values, (ii) study different energy bands to see if the PD values are higher there, and/or (iii) choose a more promising source, which in terms of simulated data means selecting different source parameters.

Increasing the number of counts by prolonging the exposure time is impossible with AMPs, as they are transient sources observable only during the outbursts, which typically last for a few weeks (see e.g., Patruno & Watts 2021). Also, observations lasting longer than 600 ks are unrealistic for scheduling reasons. The two other options are explored below.

Studying different energy bands is relevant as, according to our predictions from Sect. 2.1, the PD changes sign within the 2–8 energy band. This means that averaging over all energies decreases the total PD value. Figure 5b illustrates the results of analyzing the 2–5 keV energy band instead of the 2–8 keV represented in Fig. 5a. The blue line corresponding to the model prediction is now significantly higher and closer to the MDP values.

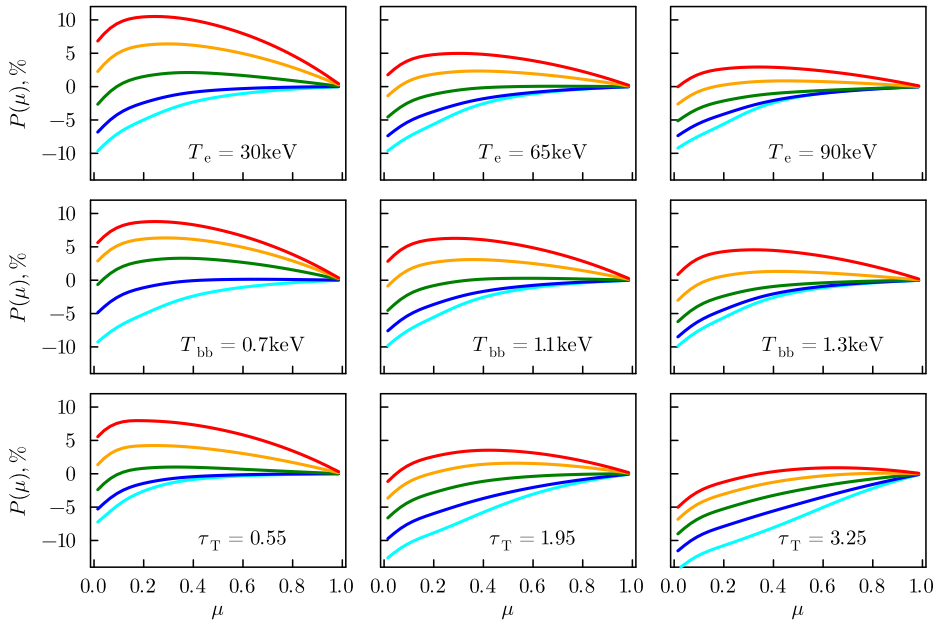


Fig. 3. Angular dependency of the PD for different atmosphere parameters. For each plot, we vary only one parameter (marked on the plot) while other parameters are from the fiducial set ($\tau_T = 1$, $T_e = 50$ keV, $T_{bb} = 1$ keV). Cyan, blue, green, orange, and red solid lines show the PD on photon energies of 2, 5, 8, 12, and 18 keV, respectively.

However, the improvement is slight, and we note that the PD values are still below the MDP values in this case.

In our search for a more optimistic (from the point of view of potential observations) yet still valid set of both geometrical and atmosphere parameters, we aimed to reproduce the known spectra of the AMPs with the parameters that, coming from our previous investigations, are expected to give a higher PD of the emission. From Fig. 3, we see that the optical depth affects the PD strongest from all the atmosphere parameters, and so we aimed to increase it but preserve the overall spectrum behavior presented in Poutanen & Gierliński (2003). We also attempted to increase the electron temperature to match the predictions in Poutanen & Gierliński (2003), but the scenario proposed there gives PD values below the MDP values, and so we chose not to continue with it. We developed two possible adjustments to the fiducial scenario (Model 1): we can choose the geometry such that the angle between the inclination and co-latitude of the spot is almost 90° (as in Model 2) or use 'more promising' atmosphere parameters (as in Model 3). We can also combine these two (Model 4). The parameter values for these four models are given in the left part of Table 1 in the columns labeled correspondingly 1–4. Figure 5c shows that for Model 4, the PD now exceeds the MDP values. We also checked this for Models 2 and 3, and for Model 2 the PD is slightly higher than the MDP values, while for Model 3 the PD is similar to MDP. In all the models, we only calculated the emission coming from one spot on the surface of the NS.

In addition, we attempted to improve the quality of the results for Model 1 illustrated in Fig. 5a,b by reducing the number of phase bins, as the PD varies less in these cases compared to other models. We find that for Model 1, case a, only reducing the number of bins to one gives us the PD value that barely exceeds the MDP, meaning that we can detect something from such a source, but we would lose the phase variability completely. For Model 1, case b, we can obtain a detection with three phase bins, but only for the bin that includes the peak (in Fig. 5b the corresponding phase shift is 0.5), and again, the PD barely exceeds the MDP. We conclude that reducing the number of bins can support the observations with barely measurable PD, but its impact is not sufficient for us to rely upon it in cases where the source is otherwise unobservable with IXPE.

Nevertheless, the most recent development of the IXPE data analysis shows that for multiple-point observations (i.e., observations split in different phase bins), information about polarization can be extracted even from the data points where PD values do not exceed MDP (González-Caniulef et al. 2023; Suleimanov et al. 2023). As IXPE measures the Stokes parameters q and u rather than PD, we can fit these parameters directly and obtain some constraints on the geometry of the source. This approach is further explored in the following section.

3.2. Fitting the data

After synthesizing the data, we applied the MULTINEST (Feroz et al. 2009) multimodal nested sampling algorithm (specifically, the PYMULTINEST package, see Buchner et al. 2014) to obtain new constraints on both the geometrical and atmosphere parameters of the source. As in Salmi et al. (2021), we fit the geometrical parameters, such as inclination,

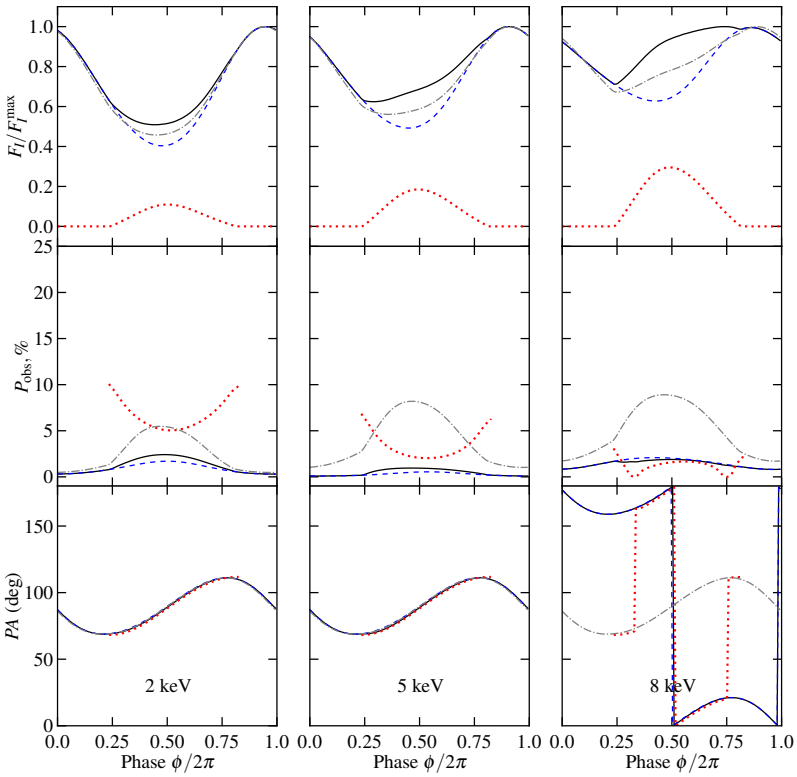


Fig. 4. Pulse profiles of the observed flux, PD, and PA for two antipodal spots shown for three different energies (2, 5, 8 keV). The solid black curves correspond to the total flux (PD, PA), the dashed blue lines correspond to the contribution from the primary spot, and the dotted red lines are for the secondary spot. The dash-dotted gray lines correspond to the Thomson model from Salmi et al. (2021; combined from two spots). The NS parameters in both models are those shown in Table 1 of Salmi et al. (2021).

Table 1. Parameter sets for all the computed models and the most probable values obtained in the fitting.

Parameter	Injected values				Fitting results					
	1	2	3	4	1a [a]	1b [b]	2	3a [a]	3b [b]	4
i [deg]	60	10	60	10	25^{+17}_{-12}	40^{+18}_{-11}	10^{+4}_{-3}	49^{+15}_{-12}	54^{+15}_{-10}	9^{+3}_{-3}
θ [deg]	20	105	20	105	21^{+16}_{-12}	15^{+7}_{-5}	101^{+6}_{-6}	20^{+7}_{-6}	17^{+4}_{-3}	104^{+4}_{-6}
χ[deg]	0	0	0	0	-2^{+33}_{-30}	-7^{+9}_{-9}	-6^{+14}_{-14}	2^{+8}_{-41}	-3^{+3}_{-3}	-7^{+11}_{-11}
$\Delta\phi/2\pi$	0.0	0.0	0.0	0.0	$0.01^{+0.22}_{-0.24}$	$-0.02^{+0.13}_{-0.11}$	$-0.02^{+0.04}_{-0.04}$	$0.03^{+0.05}_{-0.05}$	$-0.02^{+0.03}_{-0.03}$	$-0.02^{+0.03}_{-0.03}$
$T_{\rm e}$ [keV]	50	50	50	50	58^{+27}_{-24}	62^{+26}_{-26}	59^{+28}_{-25}	63^{+26}_{-27}	65^{+24}_{-27}	64^{+24}_{-26}
$T_{\rm bb}$ [keV]	1.0	1.0	1.0	1.0	$1.0^{+0.3}_{-0.3}$	$1.0^{+0.3}_{-0.3}$	$0.9^{+0.4}_{-0.3}$	$1.0^{+0.3}_{-0.3}$	$1.1^{+0.3}_{-0.3}$	$0.9^{+0.4}_{-0.3}$
$\tau_{\rm T}$	1.0	1.0	1.6	1.6	$1.4^{+1.1}_{-0.6}$	$1.9^{+1.0}_{-0.8}$	$1.6^{+0.9}_{-0.6}$	$2.0^{+0.9}_{-0.8}$	$2.2^{+0.8}_{-0.9}$	$2.1^{+0.8}_{-0.7}$

Notes. NS mass, radius, and spin frequency are fixed at $M = 1.4\,M_\odot$, $R = 12$ km, $\nu = 401$ Hz. These parameters, as well as Model 1 parameters, are selected based on the SAX J1808.4−3658 pulsar and expected values for canonical NSs. The errors represent the 68% credible interval. Additional parameters χ and $\Delta\phi$ are the position angle of the pulsar rotation axis and the phase shift, respectively. As before, i is inclination, θ is co-latitude of the spot, $T_{\rm e}$ and $T_{\rm bb}$ are the temperatures of the electron in the slab and seed photons, respectively, and $\tau_{\rm T}$ is the Thomson optical depth of the slab. Values are averaged over two data realizations for each scenario. [a]Columns labeled 1a and 3a correspond to fitting the whole energy band of IXPE, 2–8 keV. [b]Columns labeled 1b and 3b correspond to the data realization generated and fitted in the 2–5 keV energy band.

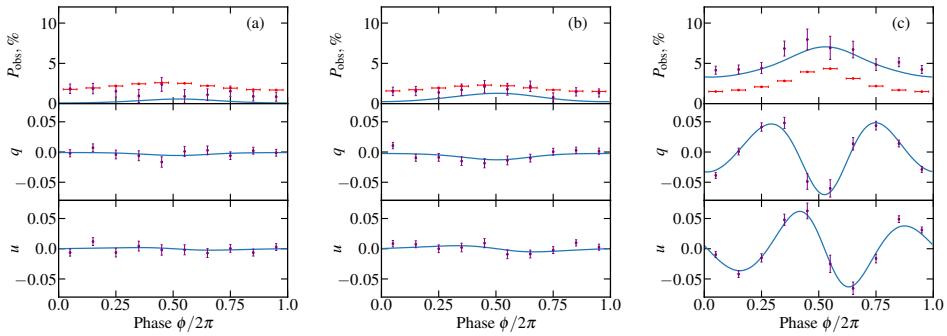


Fig. 5. Simulated PD and normalized Stokes q and u profiles for the NS parameter set 1 (panels a and b are for the 2–8 keV and 2–5 keV energy range, respectively) and set 4 (panel c) from Table 1. The exposure time is 600 ks in all three cases. The blue lines show the theoretical model, the purple dots are the synthesized observed data, and the red dots are the MDP values for the corresponding phase bins.

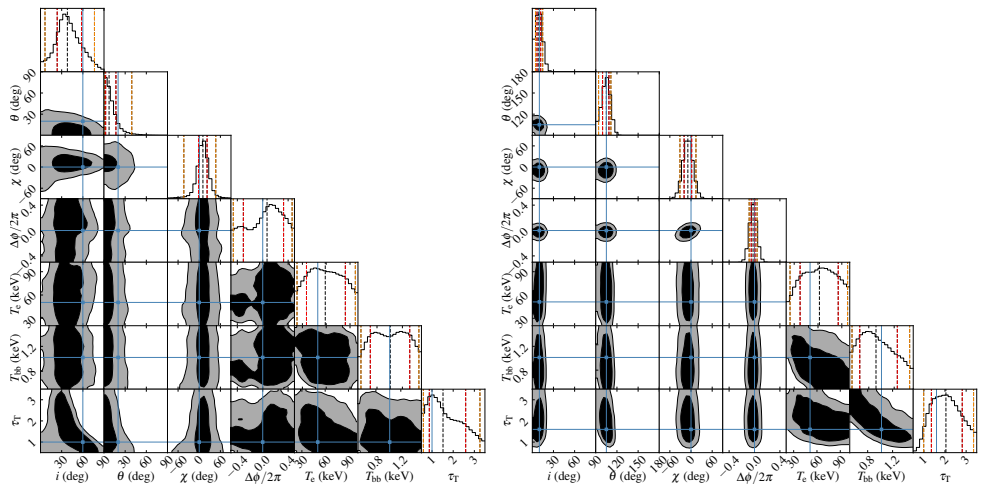


Fig. 6. Posterior probability distributions for NS parameters for Model 1a (left panels) and Model 4 (right panels) from Table 1 using one data realization. The two-dimensional contours correspond to 68% and 95% credible regions with the corresponding regions colored black and gray. The histograms show the normalized one-dimensional distribution for a given parameter derived from the posterior samples. The mean value and the 68% and 95% credible levels for the parameters are shown by the vertical dashed black, red, and orange lines, respectively. Blue lines indicate the true values of the parameters that were used for the data simulations.

co-latitude, phase shift, and position angle, but unlike there, we also perform a simultaneous fit over the parameters of the atmosphere, such as characteristic photon temperature, electron temperature, and optical depth of the thermalization layer. Table 1 presents the most probable values and 68% credible intervals for these parameters. Figure 6 shows the results of the fitting presented for the fiducial set of parameters (Model 1) and for a 'more promising' scenario (Model 4). In both cases, the full energy band of IXPE (2–8 keV) is considered, and the exposure time is 600 ks.

Figure 6 clearly illustrates the improvement of the fitting results if comparing the data synthesized from the Model 1-type of source (left) and the data coming from the Model 4-type of source (right). As we use the uniform prior for all our fittings, in the former case, the constraints originate from our direct fitting of the q and u Stokes parameters. This illustrates the possibility to extract some information even when the MDP values are not reached. In the latter case, we can clearly see the significant constraints coming from the PD values exceeding the MDP by approximately a factor of two.

We can also conclude that the constraints on the atmospheric parameters are notably less restrictive than the ones on the geometrical parameters of the NS. The main reason for obtaining such broad constraints on atmospheric parameters lies in the energy range of the IXPE satellite, as we are unable to detect the whole spectrum and fit it correctly. A solution to this issue could

be to use the observational results from several missions simultaneously; for instance, fitting the *NuSTAR* data in its higher energy range to determine the electron temperature (and consequently the optical depth through the spectral slope). Then, using the values obtained, we can fit the IXPE data with the fixed (or constrained) atmospheric parameters. However, we see that even with large uncertainties on these parameters, we are able to derive constraints on the geometry of the source from the IXPE data only.

Table 1 also shows that the constraints from the Model 3 data are less restrictive than the ones from Model 2, and so we can conclude that the atmospheric parameters are less important in our search for the 'promising' source than the geometric parameters of the NS. We also attempted to improve the constraints by reducing the number of simultaneously fitted parameters (e.g., we fixed the atmospheric parameters and only fitted the geometrical parameters). Decreasing the number of fitted parameters reduces the calculation time, but the credible intervals for the fitted parameters remain the same.

In the fittings presented here, we fixed the mass and radius of the NS. This is done for the simplicity of the calculations, as they are quite time-consuming. Moreover, we only fit the normalized Stokes q and u parameters, and they are not particularly sensitive to the mass or radius. We could also fit the Stokes I parameter (i.e., flux) as well and add mass and radius as free parameters. Adding two more parameters would increase the computational time significantly, but we do not expect any significant impact of this on the credible intervals of other parameters.

4. Discussion

Our fiducial set of NS parameters is based on the SAX J1808.4−3658, and Fig. 4 shows that, for the parameters selected, our predictions for the PD of the SAX J1808.4−3658-like source are low. However, with the uncertainties we still have on both the geometry and the atmospheric parameters of the source, there is still a possibility to observe a higher PD. Furthermore, with about 20 AMPs discovered, we can put forward several conclusions about the perspective of observing measurable PD from this class of sources.

It is known that the product of the electron temperature and optical depth for the AMPs is almost invariant (Poutanen 2006). Nevertheless, we have learned that all the atmospheric parameters have their own contribution to the PD values; see Fig. 3. Optical depth is the most important parameter here; we are searching for a source with an atmosphere that is sufficiently optically thick for many Compton scattering events to occur, yet not so thick that the pulsation pattern is excessively influenced by these scatterings. In this sense, objects such as IGR J17591−2342 and IGR J17511−3057 are promising. The former has an estimated optical depth of 1.59–2.3 and a pulsed fraction of the emission of 10%–17% (Kuiper et al. 2020; Manca et al. 2023). The latter has a lower optical depth of 1.34, but higher electron and seed photons temperatures (T_e = 51 keV, T_{bb} = 1.36 keV) and a pulsed fraction of 14% (Papitto et al. 2010). Constraints on the geometrical parameters of the AMPs are among the goals of the polarimetric observations. So far our main source of information on the possible geometry is the amplitude of the pulsation, which depends approximately on the product of the sines of the inclination and the magnetic co-latitude (Poutanen & Beloborodov 2006). Moreover, while for the inclination we usually have some constraints, little is known about the geometrical configuration of the magnetic field of the AMP. From the emission patterns shown in Fig. 1, the highest PD is received when the line of sight and the normal to the emitting area are orthogonal. One of the most interesting objects to study is Swift J1749.4−2807, for which the inclination is well-constrained, $74.4^\circ < i < 77.3^\circ$, and the co-latitude is estimated to be $\theta \approx 50^\circ$ (Altamirano et al. 2010). In this case, we can expect high polarization and we can test whether the inclination obtained from the polarimetry actually matches the orbital one.

We performed all our fittings with 600 ks of exposure time. It is typical for AMPs to go into outburst for a couple of weeks, and so in order to collect enough photons we need either a rather soft spectrum of emission or a very bright source. We can exclude hard sources such as IGR J18245−2452 with a photon index of $\Gamma \approx 1.4$ (Papitto et al. 2013).

Figure 4 illustrates an additional feature of the PD behavior we expect to observe: the observed PD is different between cases where the secondary spot is invisible (e.g., the very beginning of the outburst) and where it is visible (at the later stages of the outburst). In order to get additional information about the geometry of the source, it is crucial to observe the outburst from the earliest to the latest possible stages.

We purposely focused on phase-resolved analysis and did not investigate the possibilities that energy-resolved analysis could open up. IXPE has an energy resolution of 0.57 keV (at 2 keV; Ramsey et al. 2021), and so with sufficient statistics it is possible to study the behavior of PD with energy and obtain more information about the geometry and atmospheric properties of the source.

The model presented in this paper can be improved further. For instance, the isothermal (static) slab approximation of the accretion shock can be replaced with a more physical model where the dynamics of the accreting gas is computed self-consistently with the electron temperature. Also, the model for seed soft photons can be modified to account more accurately for the reprocessing of the hard X-rays at the NS surface, accounting for the polarization properties of this radiation. We intend to work on these developments in the future.

5. Summary

We present a new model to compute the flux and polarization of the emission coming from the accretion-powered millisecond pulsars. We used the formalism for Compton scattering in a plane-parallel isothermal hot slab to describe the propagation of photons in the accretion shock above the NS surface. Figures 1 and 2 show the result of such calculations for the fiducial set of parameters taken from Salmi et al. (2021). Comparing our results with the previous studies using Thomson scattering formalism shows that, at least for the same NS parameters, our model predicts lower PD values.

We calculated the Stokes parameters of the radiation as a function of two variables, the zenith angle of the emitted photon and its energy, for almost 14 000 combinations of three parameters: electron temperature, the temperature of the seed blackbody photons, and the Thomson optical depth of the slab. The tables of the spectral energy distribution of the Stokes parameters for all the parameters can now be used for further analysis of the accretion-powered millisecond pulsars, both in studying the pulse profiles and the polarimetric properties of the emerged radiation. Figure 3 illustrates one of the ways to use this new data set. We can understand the impact of the NS atmosphere parameters on the angular dependency of the PD from this particular study.

We then used the relativistic rotating vector model for the oblate NS to produce observed Stokes parameters as a function of the pulsar phase. Figure 4 shows the observed fluxes coming from the two antipodal spots of an AMP and the combined total flux as calculated using our model and a total flux calculated using a previously developed Thomson model. A significant drop in the PD between these two models is again present here.

We used the developed model of the AMP emission to generate the synthetic data sets imitating the one that the IXPE satellite could produce after observing an AMP. We note that the NS with the parameters from our fiducial set would emit the light with PD values below the MDP values of IXPE (which still does not exclude the possibility to extract information about the geometry of the source); however, for a different set of NS parameters, the PD is high enough to be detectable by IXPE, as shown in Fig. 5. We then applied the multimodal nested sampling technique to fit the simulated data with our model and obtain constraints on both the geometrical and atmospheric parameters of the NS. The results of the fitting are presented in Fig. 6. The main conclusion of this study is that we can obtain reasonably good constraints on the geometrical parameters from the IXPE data for some of the AMPs; however, the parameters of the atmosphere of the NS need to be constrained from the supporting observations by other X-ray missions such as *NuSTAR*.

Our findings contribute to the advancement of understanding AMPs and have significant implications for future research in this field. We are waiting for the AMPs to be observed by IXPE so that we may apply the developed formalism to analyze the resulting data. We also hope to see the eXTP mission observing the AMPs, as it would solve several of the issues discussed in this article: the larger effective area will lower the MDP, and so the fainter sources will become observable; the broader energy range will allow us to develop better constraints on the atmospheric parameters; and finally, the wide field instrument of eXTP will be able to catch the transients, such as AMPs, and observe the outbursts from their very beginning.

Acknowledgements. This research was supported by the Academy of Finland grant 333112 and by the Finnish Cultural Foundation grant 00220175 (AB). TS acknowledges support from ERC Consolidator Grant (CoG) No. 865768 AEONS (PI: A. Watts). The computer resources of the Finnish IT Center for Science (CSC) and the FGCI project (Finland) are acknowledged. We thank Anna Watts, Bas Dorsman, Alessandro Di Marco, and John Rankin for discussions and testing our models.

References

AlGendy, M., & Morsink, S. M. 2014, ApJ, 791, 78
Altamirano, D., Cavecchi, Y., Patruno, A., et al. 2010, ApJ, 727, L18
Baldini, L., Bucciantini, N., Lalla, N. D., et al. 2022, SoftwareX, 19, 101194
Baym, G., Hatsuda, T., Kojo, T., et al. 2018, Rep. Prog. Phys., 81, 056902
Bogdanov, S., Lamb, F. K., Mahmoodifar, S., et al. 2019, ApJ, 887, L26
Bonometto, S., Cazzola, P., & Saggion, A. 1970, A&A, 7, 292
Buchner, J., Georgakakis, A., Nandra, K., et al. 2014, A&A, 564, A125
Chandrasekhar, S. 1960, Radiative Transfer (New York: Dover)
Deufel, B., Dullemond, C. P., & Spruit, H. C. 2001, A&A, 377, 955
Falanga, M., Bonnet-Bidaud, J. M., Poutanen, J., et al. 2005a, A&A, 436, 647
Falanga, M., Kuiper, L., Poutanen, J., et al. 2005b, A&A, 444, 15
Falanga, M., Poutanen, J., Bonning, E. W., et al. 2007, A&A, 464, 1069
Falanga, M., Kuiper, L., Poutanen, J., et al. 2011, A&A, 529, A68
Falanga, M., Kuiper, L., Poutanen, J., et al. 2012, A&A, 545, A26
Feroz, F., Hobson, M. P., & Bridges, M. 2009, MNRAS, 398, 1601
Gierliński, M., & Poutanen, J. 2005, MNRAS, 359, 1261
González-Caniulef, D., Caiazzo, I., & Heyl, J. 2023, MNRAS, 519, 5902
Haakonsen, C. B., Turner, M. L., Tacik, N. A., & Rutledge, R. E. 2012, ApJ, 749, 52
Hebeler, K., Lattimer, J. M., Pethick, C. J., & Schwenk, A. 2013, ApJ, 773, 11
Heinke, C. O., Rybicki, G. B., Narayan, R., & Grindlay, J. E. 2006, ApJ, 644, 1090
Ho, W. C. G., & Heinke, C. O. 2009, Nature, 462, 71
Ho, W. C. G., & Lai, D. 2001, MNRAS, 327, 1081
Kislat, F., Clark, B., Beilicke, M., & Krawczynski, H. 2015, Astropart. Phys., 68, 45
Kuiper, L., Tsygankov, S. S., Falanga, M., et al. 2020, A&A, 641, A37
Lattimer, J. M. 2012, Annu. Rev. Nucl. Part. Sci., 62, 485
Leahy, D. A., Morsink, S. M., & Cadeau, C. 2008, ApJ, 672, 1119
Lindblom, L. 1992, ApJ, 398, 569
Lo, K. H., Miller, M. C., Bhattacharyya, S., & Lamb, F. K. 2013, ApJ, 776, 19
Loktev, V., Salmi, T., Nättilä, J., & Poutanen, J. 2020, A&A, 643, A84
Manca, A., Gambino, A. F., Sanna, A., et al. 2023, MNRAS, 519, 2309
Miller, M. C., & Lamb, F. K. 1998, ApJ, 499, L37
Miller, M. C., Lamb, F. K., Dittmann, A. J., et al. 2019, ApJ, 887, L24
Miller, M. C., Lamb, F. K., Dittmann, A. J., et al. 2021, ApJ, 918, L28
Morsink, S. M., Leahy, D. A., Cadeau, C., & Braga, J. 2007, ApJ, 663, 1244
Nagirner, D. I., & Poutanen, J. 1993, A&A, 275, 325
Nagirner, D. I., & Poutanen, J. 1994, Astrophys. Space. Phys. Rev., 9, 1
Papitto, A., Riggio, A., Di Salvo, T., et al. 2010, MNRAS, 407, 2575
Papitto, A., Ferrigno, C., Bozzo, E., et al. 2013, Nature, 501, 517
Patruno, A., & Watts, A. L. 2021, Astrophys. Space Sci. Lib., 461, 143
Pechenick, K. R., Ftaclas, C., & Cohen, J. M. 1983, ApJ, 274, 846
Poutanen, J. 1994, ApJS, 92, 607
Poutanen, J. 2006, AdSpR, 38, 2697
Poutanen, J. 2020, A&A, 641, A166
Poutanen, J., & Beloborodov, A. M. 2006, MNRAS, 373, 836
Poutanen, J., & Gierliński, M. 2003, MNRAS, 343, 1301
Poutanen, J., & Svensson, R. 1996, ApJ, 470, 249
Ramsey, B. D., Attina, P., Baldini, L., et al. 2021, Proc. SPIE, 11821, 118210M
Riley, T. E., Watts, A. L., Bogdanov, S., et al. 2019, ApJ, 887, L21
Riley, T. E., Watts, A. L., Ray, P. S., et al. 2021, ApJ, 918, L27
Salmi, T., Nättilä, J., & Poutanen, J. 2018, A&A, 618, A161
Salmi, T., Suleimanov, V. F., Nättilä, J., & Poutanen, J. 2020, A&A, 641, A15
Salmi, T., Loktev, V., Korsman, K., et al. 2021, A&A, 646, A23
Salmi, T., Vinciguerra, S., Choudhury, D., et al. 2022, ApJ, 941, 150
Sobolev, V. V. 1963, A Treatise on Radiative Transfer (Princeton: Van Nostrand)
Steiner, J. F., Narayan, R., McClintock, J. E., & Ebisawa, K. 2009, PASP, 121, 1279
Suleimanov, V. F., Poutanen, J., & Werner, K. 2018, A&A, 619, A114
Suleimanov, V. F., Forsblom, S. V., Tsygankov, S. S., et al. 2023, A&A, in press, https://doi.org/10.1051/0004-6361/202346994
Sunyaev, R. A., & Titarchuk, L. G. 1985, A&A, 143, 374
Viironen, K., & Poutanen, J. 2004, A&A, 426, 985
Watts, A. L., Andersson, N., Chakrabarty, D., et al. 2016, Rev. Mod. Phys., 88, 021001
Watts, A. L., Yu, W., Poutanen, J., et al. 2019, Sci. China Phys. Mech. Astron., 62, 29503
Weisskopf, M. C., Elsner, R. F., & O'Dell, S. L. 2010, Proc. SPIE, 7732, 77320E
Weisskopf, M. C., Soffitta, P., Baldini, L., et al. 2022, J. Astron. Telesc. Instrum. Syst., 8, 026002
Zampieri, L., Turolla, R., Zane, S., & Treves, A. 1995, ApJ, 439, 849
Zavlin, V. E., Pavlov, G. G., & Shibanov, Y. A. 1996, A&A, 315, 141
Zel'dovich, Y. B., & Shakura, N. I. 1969, Soviet Ast., 13, 175
Zhang, S., Santangelo, A., Feroci, M., et al. 2019, Sci. China Phys. Mech. Astron., 62, 29502

A. Bobrikova, S. V. Forsblom, F. La Monaca, A. Di Marco, J. Poutanen, M. Ng, S. Ravi, V. Loktev, J. J. E. Kajava, F. Ursini, et al. (IXPE collaboration)
Discovery of a strong rotation of the X-ray polarization angle in the galactic burster GX 13+1

Astronomy & Astrophysics, 2024; 688: A170

II

A&A, 688, A170 (2024)
https://doi.org/10.1051/0004-6361/202449318
© The Authors 2024

Astronomy & Astrophysics

Discovery of a strong rotation of the X-ray polarization angle in the galactic burster GX 13+1

Anna Bobrikova[1], Sofia V. Forsblom[1], Alessandro Di Marco[2], Fabio La Monaca[2,3,4], Juri Poutanen[1], Mason Ng[5], Swati Ravi[5], Vladislav Loktev[1], Jari J. E. Kajava[6], Francesco Ursini[7], Alexandra Veledina[1,8], Daniele Rogantini[5], Tuomo Salmi[9], Stefano Bianchi[7], Fiamma Capitanio[2], Chris Done[10,11], Sergio Fabiani[2], Andrea Gnarini[7], Jeremy Heyl[12], Philip Kaaret[13], Giorgio Matt[7], Fabio Muleri[2], Anagha P. Nitindala[1], John Rankin[2], Martin C. Weisskopf[13], Iván Agudo[14], Lucio A. Antonelli[15,16], Matteo Bachetti[17], Luca Baldini[18,19], Wayne H. Baumgartner[13], Ronaldo Bellazzini[18], Stephen D. Bongiorno[13], Raffaella Bonino[20,21], Alessandro Brez[18], Niccolò Bucciantini[22,23,24], Simone Castellano[18], Elisabetta Cavazzuti[25], Chien-Ting Chen[26], Stefano Ciprini[27,16], Enrico Costa[2], Alessandra De Rosa[2], Ettore Del Monte[2], Laura Di Gesu[25], Niccolò Di Lalla[28], Immacolata Donnarumma[25], Victor Doroshenko[29], Michal Dovčiak[30], Steven R. Ehlert[13], Teruaki Enoto[31], Yuri Evangelista[2], Riccardo Ferrazzoli[2], Javier A. García[32], Shuichi Gunji[33], Kiyoshi Hayashida[34], Wataru Iwakiri[35], Svetlana G. Jorstad[36,37], Vladimir Karas[30], Fabian Kislat[38], Takao Kitaguchi[31], Jeffery J. Kolodziejczak[13], Henric Krawczynski[39], Luca Latronico[20], Ioannis Liodakis[13], Simone Maldera[20], Alberto Manfreda[40], Frédéric Marin[41], Andrea Marinucci[25], Alan P. Marscher[36], Herman L. Marshall[5], Francesco Massaro[20,21], Ikuyuki Mitsuishi[42], Tsunefumi Mizuno[43], Michela Negro[44], Chi-Yung Ng[45], Stephen L. O'Dell[13], Nicola Omodei[28], Chiara Oppedisano[20], Alessandro Papitto[15], George G. Pavlov[46], Abel L. Peirson[28], Matteo Perri[16,15], Melissa Pesce-Rollins[18], Pierre-Olivier Petrucci[47], Maura Pilia[17], Andrea Possenti[17], Simonetta Puccetti[16], Brian D. Ramsey[13], Ajay Ratheesh[2], Oliver J. Roberts[26], Roger W. Romani[28], Carmelo Sgrò[18], Patrick Slane[48], Paolo Soffitta[2], Gloria Spandre[18], Douglas A. Swartz[26], Toru Tamagawa[31], Fabrizio Tavecchio[49], Roberto Taverna[50], Yuzuru Tawara[42], Allyn F. Tennant[13], Nicholas E. Thomas[13], Francesco Tombesi[3,27,51], Alessio Trois[17], Sergey S. Tsygankov[1], Roberto Turolla[50,52], Jacco Vink[9], Kinwah Wu[52], Fei Xie[53,2], and Silvia Zane[52]

(Affiliations can be found after the references)

Received 23 January 2024 / Accepted 3 May 2024

ABSTRACT

Weakly magnetized neutron stars in X-ray binaries show a complex phenomenology with several spectral components that can be associated with the accretion disk, the boundary, and/or a spreading layer, a corona, and a wind. Spectroscopic information alone, however, is not enough to distinguish these components. The analysis of the timing data revealed that most of the variability, and in particular, kilohertz quasi-period oscillations, are associated with the high-energy component that corresponds to the boundary and/or spreading layer. Additional information about the nature of the spectral components, and in particular, about the geometry of the emission region, can be provided by X-ray polarimetry. One of the objects of the class, a bright, persistent, and rather peculiar galactic Type I X-ray burster GX 13+1, was observed with the *Imaging X-ray Polarimetry Explorer* (IXPE) and the *XMM–Newton*. Using the *XMM–Newton* data, we obtained the best-fit values for the continuum spectral parameters and detected strong absorption lines associated with the accretion disk wind. IXPE data showed the source to be significantly polarized in the 2–8 keV energy band, with an overall polarization degree (PD) of 1.4% ± 0.3% at a polarization angle (PA) of −2° ± 6° (errors at the 68% confidence level). During the two-day long observation, we detected rotation of the PA by about 70° with the corresponding changes in the PD from 2% to nondetectable and then up to 5%. These variations in polarization properties are not accompanied by visible spectral state changes of the source. The energy-resolved polarimetric analysis showed a significant change in polarization, from being strongly dependent on energy at the beginning of the observation to being almost constant with energy in the later parts of the observation. As a possible interpretation, we suggest a constant polarization component, strong wind scattering, or a different polarization of the two main spectral components with an individually peculiar behavior. The rotation of the PA suggests a misalignment of the neutron star spin from the orbital axis.

Key words. accretion, accretion disks – polarization – stars: neutron – X-rays: binaries

1. Introduction

Weakly magnetized neutron stars (WMNSs) reside in low-mass X-ray binary (LMXB) systems and accrete material from companion stars via an accretion disk. With their luminosity ranging in the 10^{36}–10^{38} erg s^{-1}, they are among the brightest X-ray sources in the sky. WMNSs can be classified as *Z*- or atoll-sources, based on the shape of their tracks in the X-ray hardness-intensity (HID) diagram or in the color-color diagram (CCD), their timing proprieties in the 1–10 keV band, their radio emission, and their luminosity and mass-accretion rate. WMNSs are also known for their fast X-ray variability:

Open Access article, published by EDP Sciences, under the terms of the Creative Commons Attribution License (https://creativecommons.org/licenses/by/4.0), which permits unrestricted use, distribution, and reproduction in any medium, provided the original work is properly cited.
This article is published in open access under the Subscribe to Open model. Subscribe to A&A to support open access publication.

The quasi-periodic oscillations in the ranges seconds and milliseconds that were observed from many sources of the class (van der Klis 1989, 2000; Méndez & Belloni 2021) are associated with a harder spectral component (Gilfanov et al. 2003; Revnivtsev & Gilfanov 2006; Revnivtsev et al. 2013) close to the neutron star (NS) surface.

In the absence of a strong magnetic field surrounding the NS in these systems, the matter from the accretion disk falls onto the equator of the star via the boundary layer (BL, see e.g. Shakura & Sunyaev 1988) and further spreads throughout the NS surface, where it forms the so-called spreading layer (SL, see e.g. Lapidus & Sunyaev 1985; Inogamov & Sunyaev 1999). The geometry and physics of the processes that occur within these layers both affect the emission of WMNSs and their polarization (see e.g. Lapidus & Sunyaev 1985; Gnarini et al. 2022). The emission of WMNSs in the X-ray band has two main components: a soft thermal emission, which can be blackbody-like emission from the NS surface or a multicolor emission from the disk, and a harder component associated with the Comptonization in the BL or SL. In addition to these two main components, signs of reflection of the SL emission from the accretion disk (usually a broad emission line around 6.4 keV) and a set of absorption lines are sometimes visible, which indicates that the radiation interacts in the wind above the disk. A contribution of the hot corona is also possible, as is a contribution of the hot flow in the hard state.

Polarimetry is a useful tool for understanding the geometry of the source and the emission mechanisms by studying the two additional variables it provides: the polarization degree (PD), and polarization angle (PA). The Imaging X-ray Polarimetry Explorer (IXPE; Weisskopf et al. 2022), launched in December 2021, is a pathfinder that gives us the unique opportunity to measure the X-ray polarimetric properties of WMNSs with high precision. In the last two years, nine objects of the class were observed (see Capitanio et al. 2023; Farinelli et al. 2023; Cocchi et al. 2023; Ursini et al. 2023; Di Marco et al. 2023a; Rankin et al. 2024; La Monaca et al. 2024; Saade et al. 2024; Fabiani et al. 2024). These observations shed new light on the emission mechanisms of these sources, as well as on the changes in PD and PA while the source changes its spectral state. We aim to add another important piece of evidence to the global picture.

GX 13+1 is a peculiar source with a unique position between atolls and Z-sources. It is located at a distance of 7 ± 1 kpc in a binary system and has a late-evolved K5 III giant as a companion (Bandyopadhyay et al. 1999). The source shows several features that have traditionally been associated with Z-sources: It shines almost as brightly as Z-sources (up to $0.5L_{\rm Edd}$, D'Aí et al. 2014), it has persistent radio emission (Grindlay & Seaquist 1986), and it shows 57–69 Hz quasi-periodic oscillations (Homan et al. 1998). The path it draws on the CCD, however, is closer to the path normally observed from the atolls (Schnerr et al. 2003). However, even the CCD of the source has recently been interpreted as if GX 13+1 were a Z-source (Saavedra et al. 2023; Allen et al. 2018). Another unique property of GX 13+1 is the complex spectrum (e.g., Díaz Trigo et al. 2012). In addition to the common softer accretion disk and harder Comptonized components, a sign of reflection of the Comptonized emission from the disk is present, as well as seven absorption features caused by the interaction of the radiation in the wind above the disk. Allen et al. (2018) showed that these absorption features could not be produced by a single absorbing region, which indicates a complicated structure of the wind. GX 13+1 also exhibits periodic variations in the emission with a period of 24.5 d (Corbet et al. 2010). These modulations are associated with the orbital movement of the source, making GX 13+1 the NS–LMXB with the longest orbital period. Short dips of ≈1 ks in the X-ray spectrum are associated with this orbital movement (Diaz Trigo et al. 2010; Iaria et al. 2014), but they are occasional events and are not present in every orbit. These dips are traditionally interpreted as an indication of the high source inclination (60°−75°). They come from the interaction of the emission of the NS with the mostly neutral accretion bulge located in the outer parts of the disk (White & Holt 1982; D'Aí et al. 2014).

The wind above the accretion disk of GX 13+1 has been studied with several observatories. For instance, using *Chandra* data, Tomaru et al. (2020) gave constraints on the radial and azimuthal velocity of the wind, and Allen et al. (2018) constrained the wind-launching radius, showing that the radiation pressure likely launches the wind. Maiolino et al. (2019) developed a nonrelativistic framework capable of fitting and interpreting the asymmetric Kα lines in *XMM–Newton* data and reported that this nonrelativistic approach performs as well as the known relativistic framework. This adds an alternative explanation of the red-skewed Fe line in the spectrum of GX 13+1. Saavedra et al. (2023) used *NuSTAR* data to estimate the distance between the source and the ionized absorbing material of $(4–40) \times 10^5$ km, constrained the magnetic field at $B \lesssim 1.8 \times 10^8$ G, and pointed out the overabundance of Fe and Ni in the source. GX 13+1 is also in the list of targets for the recently launched *X-ray Imaging and Spectroscopy Mission* (*XRISM*; XRISM Science Team 2022). The aim of our project is to obtain constraints on the source geometry and radiation mechanisms using the polarimetric capabilities of IXPE.

The remainder of the paper is structured as follows. We introduce the observations performed with IXPE and the *XMM–Newton* observatories in Sect. 2. In Sect. 3 we present the data analysis. We provide an interpretation of the results in Sect. 4 and summarize in Sect. 5.

2. Observations

2.1. IXPE

The IXPE was launched on 2021 December 9 as a result of joint efforts of NASA and the Italian Space Agency. It has three identical grazing-incidence telescopes on board, each of which comprises an X-ray mirror assembly and a polarization-sensitive detector unit (DU) equipped with a gas-pixel detector (Soffitta et al. 2021; Baldini et al. 2021). IXPE is capable of performing imaging polarimetry over the 2–8 keV energy band with a time resolution of about 10 μs. A detailed description of the observatory and its performance is given in Weisskopf et al. (2022).

IXPE observed GX 13+1 on 2023 October 17–19 with a total effective exposure of ≃100 ks for each of the three telescopes (see Table 1). For the data analysis, we used the IXPEOBSSIM software, version 30.6.3 (Baldini et al. 2022), and the HEASOFT package, version 6.31.1 (NASA High Energy Astrophysics Science Archive Research Center (HEASARC)). We used the latest version of the IXPE response matrices, released at the HEASARC CALDB on 2023 June 16. We extracted the I, Q, and U spectra from a region with a radius of 80″. Following Di Marco et al. (2023b), we did not perform background subtraction or rejection, as GX 13+1 is sufficiently bright for the background to be negligible. The polarimetric analysis was performed using the formalism of Kislat et al. (2015) implemented in the IXPEOBSSIM package (Baldini et al. 2022) under the `pcube` algorithm in the `xpbin` tool. We used IXPEOBSSIM to investigate the time-dependence of the normalized Stokes parameters $q = Q/I$ and $u = U/I$, as well

Table 1. Observations of GX 13+1 presented in the paper.

Observatory	Dates	ObsID	Instrument	Duration (s)
IXPE	2023 Oct. 17–19	02006801	DU1	98 204
			DU2	98 299
			DU3	98 299
XMM–Newton	2023 Oct. 16	0932390601	EPIC/PN	11 336

as the PD = $\sqrt{q^2+u^2}$ and PA = $\frac{1}{2}\arctan(u/q)$ (see Figs. 1a–d). We applied the unweighted analysis implemented in the IXPEOBSSIM. For the spectral and spectropolarimetric analysis, we used XSPEC, version 12.13.0c (Arnaud 1996), and applied a weighted analysis as introduced in Di Marco et al. (2022). For the spectral analysis, the data were binned to have at least 30 counts in each energy bin. For the spectropolarimetric analysis, we applied a constant energy binning of 80 eV for the three Stokes parameters.

2.2. XMM–Newton

XMM–Newton observed GX 13+1 on 2023 October 16 (see Table 1). This observation could not be scheduled simultaneously with IXPE because the visibility window for GX 13+1 with *XMM–Newton* closed on October 16. As GX 13+1 is very bright, EPIC/PN was operated in timing mode. The thick filter was used to reduce the count rate, which was about 690 cnt s^{-1} on average during the observation. The EPIC/MOS instruments were not used, and their telemetry was allocated to EPIC/PN. Despite this effort, PN nevertheless suffered from telemetry gaps as the science buffer was full throughout the observation. For this reason, the data are not suitable for a timing analysis, but are still useful for measuring the spectral shape and the known wind lines in the 6–9 keV range (Díaz Trigo et al. 2012).

The data were reduced using XMM–SAS v.21 with the latest calibration files as of October 2023. The clean event files were generated from the ODF files with the `epchain` tool. They were filtered further using the #XMMEA_EP and PATTERN==0 flags in the 0.3–12 keV range. No soft proton flares were seen in the light curves above 10 keV, giving us a total effective exposure of ≃10 ks. To extract the source spectrum, we selected events from a 9-pixel wide box around the RAWX column with the highest count rate. We also extracted a background spectrum from RAWX columns 3–5, but as expected for such a bright target, these columns were still dominated by the source itself, and thus, we did not subtract the background at all. The ancillary response file and the redistribution matrix were generated using the tools `arfgen` and `rmfgen`, respectively. Finally, we grouped the data to have at least 20 counts per channel and added 1% systematic errors in quadrature to each channel using the `grppha` tool.

3. Data analysis

3.1. Model-independent polarimetric analysis

The light curve of GX 13+1 is shown in Fig. 1f. The source showed some variations, with the count rate dropping by almost a factor of two in the wide dip, but some more rapid dips are noticeable. The hardness ratio (Fig. 1e) changes with time by only a small margin; the largest increase slightly after MJD 60236 coincides with the wide dip in the light curve and is ≈10%.

The significant variability of the Stokes parameters is immediately obvious. This variability is reflected in the changes in PD and PA in Figs. 1c,d. While the PA slowly increases throughout the observation, the PD changes significantly and without an obvious pattern.

The HID presented in Fig. 2 illustrates a lack of state variability within the more than two days of IXPE observation. From the data publicly available in the MAXI (Matsuoka et al. 2009) archive[1] of the most recent observations, we calculated the CCD from the ratio of fluxes $F_{10-20\,\mathrm{keV}}/F_{4-10\,\mathrm{keV}}$ against the ratio $F_{4-10\,\mathrm{keV}}/F_{2-4\,\mathrm{keV}}$. We then estimated the position of the points corresponding to the observation days on the CCD and concluded that the source during the IXPE observation was in the so-called lower left banana (LLB) state, a soft state common for the atoll sources. In the two days of IXPE observation, GX 13+1 moved in the lower left part of the CCD, but the uncertainties are too high to conclude about the state variability. Polarimetric analysis of the averaged data in the 2–8 keV energy band resulted in low PD values of 1.4% ± 0.3% and a PA of −2° ± 6° (from here onward, the errors are given at the 68% confidence level, CL) with the significance of the detection exceeding 99.99% (see Fig. 3 and Table 2).

As the HID does not show any significant change of state, we decided to perform a more detailed study of different parts of the observation based on the light curve. We separated the dip state (highlighted in yellow in Fig. 1f) from the nondip states and divided the observation into three unequal parts: the pre-dip (before t = 6.05 d), the dip (6.05 < t < 6.30 d), and the post-dip (t > 6.30 d), with the times t given relative to MJD 60230. The results are gathered in Fig. 4. The PD in the dip state is 2.2% ± 1.1%, and the PA is −49° ± 14° at 68% CL. Due to the lack of statistics, we chose not to perform an energy-resolved analysis of this part of the observation.

However, the pre- and post-dip parts show an interesting and completely different behavior (see Table 2). The energy-resolved PA and PD for these parts are presented in Fig. 5, and the corresponding Stokes q and u parameters are shown in Fig. 6. We also additionally studied the dip core, one specific bin in Fig. 1 at t = 6.15 d that falls out of the patterns in Figs. 1a and b. This bin lies in the middle of the hardening in Fig. 1e and of the dip in Fig. 1f, which makes it particularly interesting. As mentioned in Table 2, the PD there exceeds 7%, and the PA is below −50° with a significance of the detection higher than 99%.

The change in PD behavior is noticeable. In the pre-dip part, the PD strongly depended on energy and increased from an upper limit of 1.7% at 2σ CL in the 2–3 keV bin to a strong detection of 5.5% in the 5.5–8 keV bin. In the post-dip part, however, the PD was almost constant with energy and averaged at about 5.3%, exceeding 7% in the 5.5–8 keV bin. No significant PA dependence on energy is observed in either part of the observation, but the value of the angle shifts by almost 60° between the pre-dip and post-dip parts. This complete change in the behavior between the two parts of the observation is also visible in the

[1] https://maxi.riken.jp/v7l3h/J1814-171/index.html

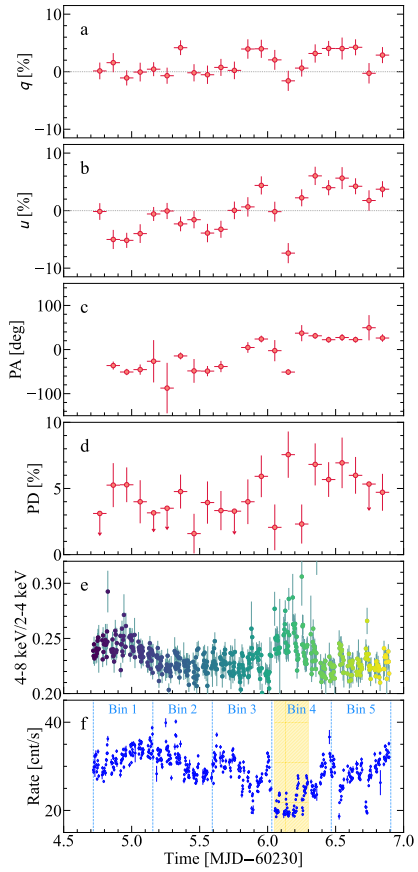


Fig. 1. Normalized Stokes q (a) and u (b) parameters, PA (c), PD (d), hardness ratio (e) with the same colors as in Fig. 2, and the count rate (f) as functions of time as observed by IXPE (all three detectors combined in the energy range 2–8 keV). The light curve is binned in ≈200 s. The dashed vertical blue lines separate the observation into five equal time bins of 10.5 h (Bins 1–5). The region highlighted in yellow corresponds to the dip in the light curve (see Sect. 3.1). Uncertainties are reported at the 68% CL.

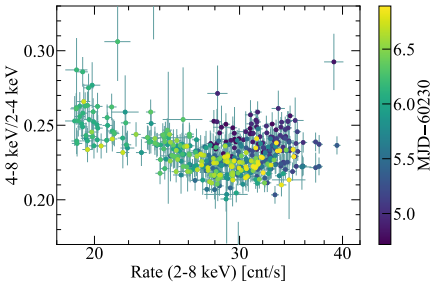


Fig. 2. Hardness-intensity diagram derived from the IXPE data in time bins of 200 s. The colors correspond to the evolution of the data with time, from dark blue at the beginning of the observation to yellow at the end of the observation.

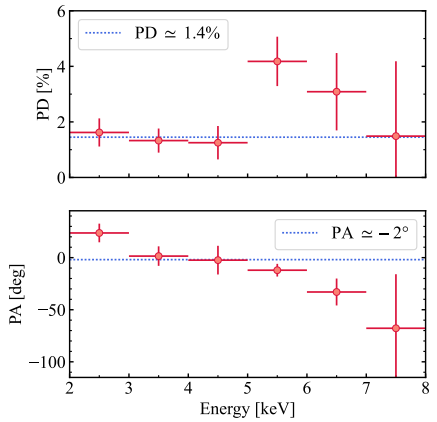


Fig. 3. Energy-resolved PD and PA averaged over all the IXPE observation, obtained with the pcube algorithm. The data are divided into six 1-keV wide energy bins. Uncertainties are reported at the 68% CL.

Stokes $q - u$ plane (see Fig. 6): The polarization vector changes in amplitude and direction.

To study the separation of the observation in even more detail, we split it into five equal parts of 10.5 h each (bins 1–5 are defined with vertical dashed blue lines in Fig. 1f). The results are shown in Fig. 7 and Table 2. We performed a fit of the five PA values with a straight line (see Fig. 8) and confirmed the clear rotation of the PA with time with a slope of 1°.64 per hour and a total rotation angle exceeding 70°. We also note that the PD is relatively high at the beginning and end of the observation. We note here that the polarization in bins 2, 3, and 4 in Fig. 7 is consistent with zero within the error bars at 99% CL. Thus, as three individual measurements, they are not significant, but as a part of the trend, they are still meaningful. The important conclusion we make here is that the dip does not fully cause the variability in the polarimetric properties. As can be concluded from the data presented in Table 2, the drop in PD already occurred in bin 2, while the dip occurs around bin 4. The PA rotates throughout the whole observation. The anomalies in the PA and PD occur around the time corresponding to the dip in the light curve in Fig. 1, but the general trend for PA and PD is not directly correlated with the dip.

Last but not least, we attempted to divide the observation into two parts by the count rate: below and above 25 cnt s^{-1}. Data below the threshold fall into one of the many dips in the light curve. In the brighter state (above 25 cnt s^{-1}), we saw a PD of ≈1.6% and PA of ≈2°, which is similar to that shown in Fig. 3 and in Table 2 for the overall polarization. The dimmer state (below 25 cnt s^{-1}) showed PD ≈ 1.3% and PA ≈ −36°, which is in between the wide dip state of the previous analysis (between MJD−60230=6.05 and 6.30, as shown in Fig. 1f) and

Table 2. Results of the `pcube` analysis performed with various approaches to separate the data.

Part of the observation	PD (%)	PA (deg)
Overall	1.4 ± 0.3	−2 ± 6
Pre-dip	1.8 ± 0.4	−29 ± 6
Dip	2.2 ± 1.1	−49 ± 14
Post-dip	5.3 ± 0.6	26 ± 3
Dip-core	7.5 ± 1.7	−51 ± 7
Bin 1	3.2 ± 0.7	−44 ± 6
Bin 2	1.5 ± 0.7	−21 ± 13
Bin 3	1.6 ± 0.7	4 ± 13
Bin 4	1.6 ± 0.7	12 ± 13
Bin 5	5.0 ± 0.7	26 ± 4
Dimmer state, <25 cnt s^{-1}	1.3 ± 0.9	−36 ± 18
Brighter state, >25 cnt s^{-1}	1.6 ± 0.3	2 ± 6

Notes. The errors are at 68% CL. The results are presented for the overall polarization during the observation, separation by the light curve into pre-dip, dip, and post-dip parts with a special mention of the dip-core, one bin at ≈6.15 d in Fig. 1, separation into five equal time bins, and separation by the count rate into dimmer and brighter states.

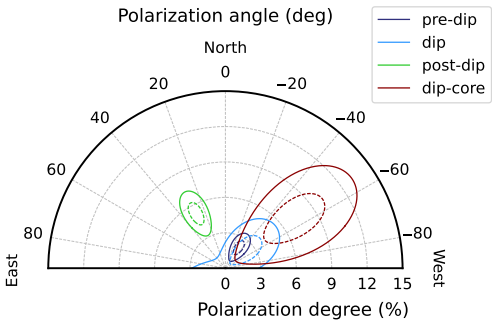


Fig. 4. Polar plot of the PD and PA in the 2–8 keV energy band for the three parts of the observation (pre-dip, dip, and post-dip) and the dip core. Contours are at the 68% CL (dashed lines) and 99% CL (solid lines).

the overall polarization. Thus, adding the data obtained from the times corresponding to all the minor dips smoothed the difference between the anomalous polarimetric behavior during the dip and the general trend that we observed. It shifted the dimmer state PA and PD closer to the overall states than those of the wide dip. The polarimetric properties of the minor dips are then different from those of the wide dip, which means that the nature of the wide dip is different from the nature of all other dips in the light curve we observed.

3.2. Spectroscopic analysis

3.2.1. *XMM–Newton*

In the *XMM–Newton* data, below 2 keV, the count rate drops significantly due to the high interstellar absorption. We observe a significant excess below 2 keV with any continuum model combination. High residuals are also seen near the instrumental edges. In combination with our inability to subtract the background, this led us to discard these low-energy data. After all, they do not affect the modeling at higher energies.

Thus, we modeled the spectrum of the *XMM–Newton* observation in the 2–10 keV range. As we traditionally expect two continuum components to be present in the spectrum of a WMNS with some additional reflection and absorption features, we performed a fit with a `tbabs*(diskbb+bbodyrad+gaussian)` model modified by four Gaussian absorption lines, `gabs`, and two interstellar dust absorption edges, `edge`. The results are shown in Table 3 and in Fig. 9. To properly resolve the absorption features in the 6–9 keV energy range, we fixed the parameters of the `gaussian` corresponding to the broad emission line.

The resulting fit illustrates that the spectrum of GX 13+1 is dominated by the disk. The harder component is modeled with the blackbody (as suggested in Schnerr et al. 2003; Díaz Trigo et al. 2012; Revnivtsev et al. 2013) and dominates at energies higher than 7 keV. Four strong absorption lines at 6.90, 7.18, 8.10, and 8.48 keV are also visible. These lines are identified with the Fe XXV Heα resonant line at 6.700 keV, Fe XXVI Lyα doublet at 6.966 keV, Ni XXVII Heα resonant line at 7.806 keV, and Ni XXVIII Lyα doublet at 8.092 keV, and they are well known in the source (see, e.g., Tomaru et al. 2020); three other known lines are not resolved in our fit. Compared with the previous results, the energies of the lines we obtain are higher than in Díaz Trigo et al. (2012) and correspond to a very high blueshift, $z = -0.03$ for the Fe lines and even higher for the Ni lines (although the latter are known to be blended with Fe Heβ lines) and might come from the full science buffer of the *XMM–Newton* during our observation. It is known that in this source, the wind is complex, very structured, and highly variable, and we therefore avoid interpreting this nominal blueshift without a much more detailed analysis of the absorption features, which is well beyond the scope of this paper. However, we do not expect this issue to significantly affect the continuum parameters in which we are mostly interested. We also note the anomalously high equivalent hydrogen column density parameter $N_{\rm H}$ of the absorption component.

Additionally, we tried to model the *XMM–Newton* spectrum with only one continuum component. That is, we removed the `bbodyrad` component, and fit the whole continuum using a single `diskbb` component with high $kT_{\rm dbb} \approx 1.9$ keV, resulting in a bad χ^2/d.o.f.= 2058/1485 corresponding to a null-hypothesis probability $<10^{-3}$% with respect to the 34% achieved from the fit reported in Table 3.

3.2.2. IXPE

As the HID obtained from the IXPE data in Fig. 2 has rather large uncertainties and was obtained over a small energy range, it is not the most informative representation of the spectral variation in the data with time. We used XSPEC to fit the I spectrum obtained by IXPE. For this study, we chose the same five equal time bins as for the `pcube` analysis presented in Fig. 7. All five spectra were fit with the same model `tbabs*(diskbb+bbodyrad)`. Considering the spectral capabilities of IXPE and the small effective area above 6 keV, we did not attempt to add the `gabs` or `gaussian` components that were prominent in the *XMM–Newton* spectrum. We multiplied the model by the `constant` component to scale the data from the three detectors of IXPE. We also fixed the value of the equivalent hydrogen column density $N_{\rm H}$, as IXPE does not have the capability to estimate it, and the temperature of the `bbodyrad` component to the best-fit values obtained with the *XMM–Newton*.

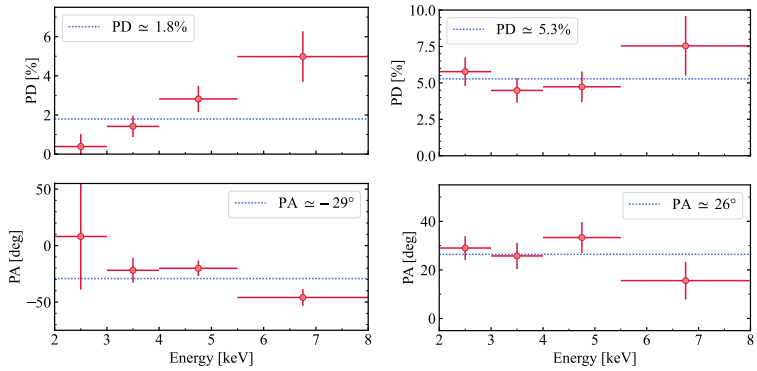


Fig. 5. Energy dependence of the PD and PA obtained by the `pcube` algorithm. Left: Pre-dip part of the observation. Right: Post-dip part of the observation. The data are divided into four energy bins: 2–3, 3–4, 4–5.5, and 5.5–8 keV. Uncertainties are reported at 68% CL.

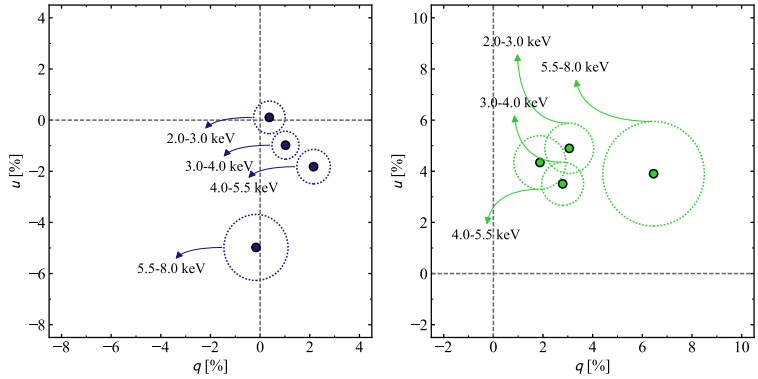


Fig. 6. Same as Fig. 5, but for the normalized Stokes parameters q and u. Arrows only indicate the label of the energy band. Uncertainties are reported at 68% CL.

We applied the weighted analysis introduced in Di Marco et al. (2023b). The results are presented in Table 4 and Fig. 10.

We note the lack of a change in the spectral parameters with time. The temperature of the disk does not vary with time, and only the normalization of the continuum components decreases toward the end of the observation, which could be consistent with increased absorption or scattering in the disk wind during the last part of the observation. In bin 5 of the observation, the contribution of the blackbody component also drops by a factor of two (however, the normalizations of all the blackbody components are compatible with each other within a 1σ error). Bin 4 almost coincides with the broad dip and has a lower flux, and this is shown in Fig. 10.

3.3. Spectropolarimetric analysis

For the spectropolarimetric analysis, we used the results of the model-independent polarimetric analysis and the spectroscopic analysis as a driver. As we learned that both spectral and polarimetric properties are rather similar in bins 2–4 (see Tables 2 and 4), we combined these three in one larger time bin. Our aim was to obtain a stronger detection in this part of the observation, as in the polarimetric analysis we obtained the results that are only meaningful as a part of the trend for bins 2–4. We studied bins 1 and 5 separately. Instead of studying the polarization of each spectral component independently, we applied the `polconst` model to the entire continuum, as the data quality did not allow us to determine the polarization of the two spectral components. For bin 1, we also attempted to apply the `pollin` polarimetric model, as we previously saw the dependence of PD on energy at the beginning of the observation (see Fig. 5, left). We again fixed the hydrogen column density $N_{\rm H}$ and the blackbody temperature. The results are presented in Table 5, and the fit of three Stokes parameters, I, Q, and U, performed for the bin 1 data with the `pollin` model is shown in Fig. 11. The distribution of the residuals for all the three parameters illustrates the quality of the fit, which was found to be good.

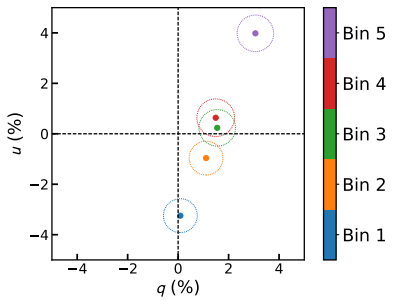


Fig. 7. Time dependence of the normalized Stokes parameters q and u obtained by the `pcube` algorithm using the data separation into five equal time bins. Uncertainties are reported at the 68% CL.

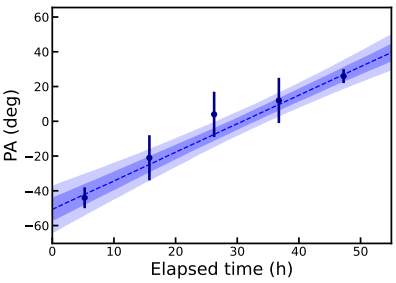


Fig. 8. Linear fit of the PA obtained for time bins 1–5 in Fig. 1f. The plot illustrates the rotation of the polarization plane with time. Uncertainties are reported at the 68% CL.

We note that for bins 1 and 5, the spectral and polarimetric properties obtained in the spectropolarimetric analysis agree with the previous results presented in Tables 2 and 4. As we do not have strong detection for the polarimetric properties of bins 2–4, we decided not to present the spectropolarimetric analysis of these bins independently in Table 5, as this does not improve the quality of our results. In bin 1, due to the strong dependency of PD on energy, we applied the `pollin` model with a constant PA, which gives an improvement by $\Delta\chi^2 = 9$ compared to the fit with the `polconst` model (which has one parameter less). This improvement corresponds to an F-test probability of $\approx 3 \times 10^{-3}$.

4. Discussion

4.1. Correlation of the polarimetric behavior with the dip in the light curve

The data analysis presented in Sect. 3 provided us with several significant insights that require interpretation and further reflection. To begin with, we observed significant and anomalous variation in the light curve: the broad dip closer to the end of the observation is not correlated with the regular dips known in the source, as the folding of the MAXI data using the formulae from Iaria et al. (2014) suggests that our observation was made one week before the regular dip. During the dip, we also observed a slight increase in the hardness ratio. It would be natural to expect that polarimetric properties, as hardness and the count rate, have some variations around 6.1–6.3 [MJD–60230]. However, the behavior of the polarimetric properties is not aligned

Table 3. Best-fit parameters of GX 13+1 spectrum from *XMM–Newton* data.

Parameter		Value
`tbabs`	$N_{\rm H}$ (10^{22} cm^{-2})	$5.94^{+0.06}_{-0.07}$
`diskbb`	kT (keV)	$1.39^{+0.12}_{-0.06}$
	norm	130^{+20}_{-30}
`bbodyrad`	kT (keV)	$2.0^{+0.3}_{-0.1}$
	norm	20.08 ± 0.03
	$R_{\rm bb}$ (km)	3.13 ± 0.02
`gaussian`	E (keV)	6.6 (frozen)
	σ (keV)	0.8 (frozen)
	norm	$0.0048^{+0.0009}_{-0.0007}$
`gabs`	E (keV)	$8.476^{+0.005}_{-0.009}$
	σ (keV)	0.05 (frozen)
	Depth (keV)	0.067 ± 0.004
`gabs`	E (keV)	8.10 ± 0.01
	σ (keV)	0.05 (frozen)
	Depth (keV)	0.040 ± 0.003
`gabs`	E (keV)	$7.180^{+0.006}_{-0.004}$
	σ (keV)	0.05 (frozen)
	Depth (keV)	0.040 ± 0.001
`gabs`	E (keV)	6.90 ± 0.01
	σ (keV)	0.050 (frozen)
	Depth (keV)	$0.0150^{+0.0017}_{-0.0013}$
`edge`	E (keV)	8.83 (frozen)
	τ	0.20 ± 0.01
`edge`	E (keV)	9.28 (frozen)
	τ	0.08 ± 0.01
	χ^2/d.o.f.	1504/1483

Notes. The errors are at 68% CL. $R_{\rm bb}$ is calculated from the normalization of the `bbodyrad` component, assuming a distance to the source of 7 kpc.

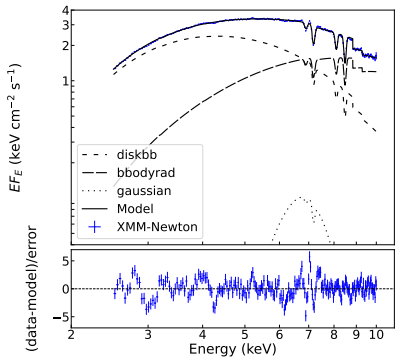


Fig. 9. Spectral energy distribution of GX 13+1 in EF_E representation. The blue crosses show the data from *XMM–Newton*. The different spectral model components are reported as black lines for `diskbb` (short dashed), `bbodyrad` (long dashed), and `gaussian` (dotted). The total model is shown with a solid black line. The bottom panel shows the residuals between the data and the best fit. The data are rebinned only for plotting purposes.

Table 4. Best-fit parameters of GX 13+1 spectrum from IXPE data divided into five equal time bins.

Component	Parameter (units)	Bin 1	Bin 2	Bin 3	Bin 4	Bin 5
tbabs	$N_{\rm H}$ (10^{22} cm^{-2})	5.9 (frozen)	5.9 (frozen)	5.9 (frozen)	5.9 (frozen)	5.9 (frozen)
diskbb	$kT_{\rm in}$ (keV)	$1.49^{+0.03}_{-0.05}$	$1.44^{+0.04}_{-0.03}$	1.45±0.04	$1.57^{+0.06}_{-0.07}$	1.55±0.06
	norm	131^{+14}_{-8}	142^{+13}_{-12}	130^{+10}_{-11}	79^{+10}_{-8}	102^{+10}_{-7}
bbodyrad	kT (keV)	2.0 (frozen)	2.0 (frozen)	2.0 (frozen)	2.0 (frozen)	2.0 (frozen)
	norm	14±4	14^{+2}_{-5}	14±3	10±4	8^{+4}_{-5}
	$R_{\rm bb}$ (km)	2.6±0.4	$2.6^{+0.2}_{-0.5}$	2.6 ± 0.3	2.2 ± 0.4	$2.0^{+0.5}_{-0.6}$
constant	DU1	1 (frozen)	1 (frozen)	1 (frozen)	1 (frozen)	1 (frozen)
	DU2	0.951 ± 0.004	0.956 ± 0.004	0.948 ± 0.004	0.951 ± 0.004	0.950 ± 0.006
	DU3	0.908 ± 0.003	0.910 ± 0.004	0.904 ± 0.004	0.912 ± 0.004	0.911 ± 0.005
	χ^2/d.o.f.	392/420	415/416	389/411	420/411	403/409
$\rm Flux_{2\text{-}8\,keV}$ (10^{-9} erg s^{-1} cm^{-2})		6.42	5.98	5.77	4.96	5.65
$\rm Flux_{diskbb}/Flux_{2-8\,keV}$		0.82	0.83	0.81	0.81	0.91
$\rm Flux_{bbodyrad}/Flux_{2-8\,keV}$		0.18	0.17	0.19	0.19	0.09

Notes. The errors are at the 68% CL. A gain slope of ≈0.96 and gain offsets ≈2–80 eV for the three DUs were needed to obtain a good reduced χ^2. $R_{\rm bb}$ is calculated from the normalization of the bbodyrad component, assuming the distance to the source of 7 kpc.

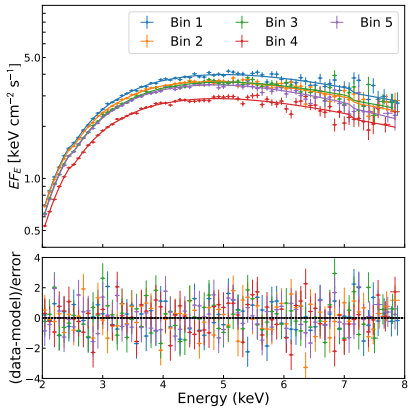


Fig. 10. Spectral energy distribution of the source in $EF_{\rm E}$ representation during five equal parts of the observation. Here, only IXPE DU1 is reported as an example, and the data are rebinned for plotting purposes.

with this variation time-wise. There is a polarimetric anomaly during the dip core state, but the overall trend in PA and PD is not correlated with the dip. PA increases slowly throughout the whole observation, and PD decreases already in bin 2 and then increases in bin 5 without a direct correlation to the dip in the light curve. The inconsistency in the behavior of the spectral and polarimetric properties invites us to search for an explanation for the PA and PD variation outside the regular hardness/intensity changes.

The results of the previous IXPE observations of the X-ray binaries showed that the concept of a rapid and significant change in the PA is not new to this class of objects. The high luminosity of GX 13+1 allowed us to separate the observation into smaller parts and see the slow monotonous rotation of the polarization plane, but the results presented in Fig. 5 are similar to several results that were obtained previously. It is tempting to assume that similar mechanisms might cause the polarimetric behavior of GX 13+1 and that a slow rotation similar to the one presented in Fig. 7 has not been observed previously just due to the lack of statistics or a different approach used in the data analysis. For instance, in Sco X-1, La Monaca et al. (2024) reported that the rotation of the PA with respect to the previous observations (Long et al. 1979) and the jet position angle was around 54°, and the authors explained it with the precession of the jet or with the change in the corona geometry with the transition between the states. However, no sign of an X-ray color variability in GX 13+1 could be associated with these state changes. In the case of Cir X-1 (Rankin et al. 2024), the PA changed by 60° between the two parts of a single observation, but in this case, a clear sign of a corresponding state transition was observed. The difference of 60° between the PA of the hard and soft components of the observation was explained by a switch from the BL to the SL in a tilted NS, as Cir X-1 is a young system (Heinz et al. 2013). GX 13+1, on the other hand, is an older stable system (as is suggested by the companion being a late-evolved K5 III giant) with a high accretion rate; the chances for the rotation axis of the NS to be significantly misaligned relative to the orbital axis are smaller. The results are in many ways also very similar to the polarization that is commonly seen in black hole X-ray binaries (see, e.g., Fig. S6 in Krawczynski et al. 2022 in comparison with Fig. 5). As for Cyg X-1, in GX 13+1 we see the PD during a higher flux rising with energy, while the PD at a (slightly) lower flux is constant. The PA is constant with energy in both cases, but the change in the PA by 60° between the two cases presented in Fig. 5 is significantly different from that in black holes. The rotation of the PA with time was seen recently in the blazar Mrk 421 (Di Gesu et al. 2023). They explained it by the helical magnetic structure in the jet illuminated in the X-rays by a localized shock propagating along this helix. Unfortunately, jets have only been observed in GX 13+1 in the hard state (Allen et al. 2018), and we observed the source in the soft state. It is therefore challenging to imagine that a similar geometry and physics cause the PA rotation in GX 13+1 as in the Mrk 421. In X-ray pulsars, the rotation of the PA with the pulsar phase is routinely observed (Doroshenko et al. 2022, 2023; Tsygankov et al. 2022, 2023), but GX 13+1 is not a pulsar. We conclude that we need to search for a new mechanism that causes the polarimetric behavior of GX 13+1.

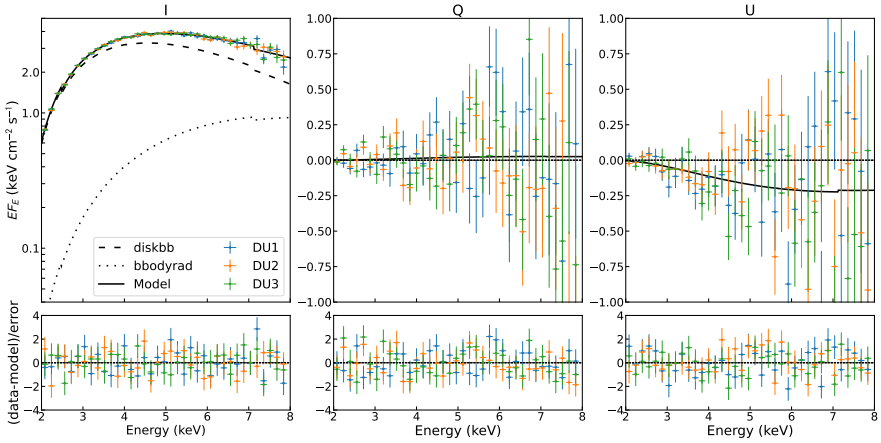


Fig. 11. Spectral energy distribution of GX 13+1 in EF_E representation as observed by IXPE in bin 1. The left, middle, and right panels show the Stokes parameters I, Q, and U, respectively. The fit is performed in the 2–8 keV energy band using the three IXPE detectors and applying the model `tbabs*pollin*(diskbb+bbodyrad)`. The total model is shown with the solid black line, and `diskbb` and `bbodyrad` are shown with the dashed and dotted lines, respectively. The lower subpanels show the residuals between the data and the best fit. The data are rebinned only for plotting purposes.

Table 5. Best-fit parameters of the spectropolarimetric model for GX 13+1.

Component	Parameter (units)	Bin 1, `polconst`	Bin 1, `pollin`	Bin 2–4	Bin 5
`tbabs`	$N_{\rm H}$ (10^{22} cm^{-2})	5.9 (frozen)	5.9 (frozen)	5.9 (frozen)	5.9 (frozen)
`diskbb`	$kT_{\rm in}$ (keV)	$1.51^{+0.05}_{-0.04}$	$1.51^{+0.05}_{-0.04}$	$1.50^{+0.02}_{-0.03}$	$1.58^{+0.05}_{-0.06}$
	norm	120 ± 11	120 ± 11	106^{+6}_{-5}	92 ± 10
`bbodyrad`	kT (keV)	2.0 (frozen)	2.0 (frozen)	2.0 (frozen)	2.0 (frozen)
	norm	13^{+6}_{-3}	13^{+4}_{-3}	12 ± 2	<14
	$R_{\rm bb}$ (km)	$2.5^{+0.6}_{-0.3}$	$2.5^{+0.4}_{-0.3}$	2.4 ± 0.2	<2.6
`polconst`	A (%)	3.0 ± 0.5	–	1.2 ± 0.3	4.5 ± 0.5
	ψ (deg)	-42 ± 5	–	7 ± 7	32 ± 3
`pollin`	A_1 (%)	–	-0.75 ± 1.4	–	–
	$A_{\rm slope}$ (% keV^{-1})	–	1.3 ± 0.5	–	–
	ψ_1 (deg)	–	-42 ± 4	–	–
	$\psi_{\rm slope}$ (deg keV^{-1})	–	0 (frozen)	–	–
`constant`	DU1	1 (frozen)	1 (frozen)	1 (frozen)	1 (frozen)
	DU2	0.953 ± 0.004	0.953 ± 0.004	0.956 ± 0.002	0.950 ± 0.004
	DU3	0.910 ± 0.004	0.910 ± 0.004	0.910 ± 0.002	0.909 ± 0.004
	χ^2/d.o.f.	634/653	626/652	600/653	630/653

Notes. IXPE I, Q, and U spectra are divided into five equal time bins and regrouped based on their spectral and polarimetric behavior. The errors are at the 68% CL. A gain slope of ≈0.97 and gain offsets ≈130–200 eV for the three DUs were needed to obtain a good reduced χ^2. $R_{\rm bb}$ is calculated from the normalization of the `bbodyrad` component, assuming the distance to the source of 7 kpc.

4.2. Additional polarimetric component

Figure 7 showed that the source evolves in a straight line (within the uncertainties) in the $q - u$ plane shifted from the origin. Considering this, we tried to decompose the polarized flux into different components with different polarization orientations. It would be problematic to interpret the emission in bins 1 and 5 as coming from two distinct components that differ in PA by 70°, with the rest representing a transitional phase, because a transition like this is unlikely to result in a straight-line trajectory in the $q - u$ plane, particularly given that the flux during bin 4 is lower than during bins 1 and 5. We therefore suggest alternatively that the polarization nature in bins 1 and 5 is predominantly the same, and that the misaligned polarization component is observed in between. A similar model that involves a constant polarized component has previously been proposed to interpret X-ray polarization data from the bright X-ray pulsars LS V +44 17/RX J0440.9+4431 (Doroshenko et al. 2023) and Swift J0243.6+6124 (Poutanen et al. 2024).

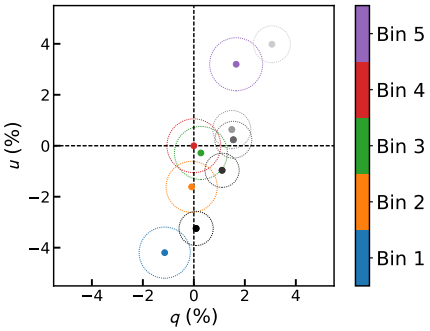


Fig. 12. Same as Fig. 7, but the (absolute) Stokes parameters corresponding to bin 4 are subtracted. The gray points are the same as in Fig. 7.

We define a constant component corresponding to bin 4 (a period nearly overlapping with the dip, as shown in Fig. 1f). Thus, we subtract absolute Stokes parameters corresponding to bin 4 from the absolute Stokes parameters of each time bin. The resulting normalized Stokes parameters are shown in Fig. 12 with colored points, and the originally observed values are shown with gray points. Their positions are still consistent with a straight line that is now located near the origin. In this scenario, the polarization vectors during bins 1 and 5 are essentially perpendicular to each other (since they lie on the same line in the $q - u$ plane at different sides around the origin), and the radiation observed in bins 2 and 3 appears to be statistically consistent with being unpolarized.

The picture we see after the subtraction is physically meaningful. A difference of 90° in PAs of bins 1 and 5 could be attributed to changes in the geometry of the scattering or reflecting medium, changes in the scattering optical depth, and the relative brightness changes in the accretion disk, the BL, and the SL. The PA of the permanent component of the polarization (in our assumption, similar to that of bin 4) differs from the PA of the varying component (which we see after the subtraction in Fig. 12) by ≈30°, as clearly visible in the $q-u$ plane. However, as technically, we could have associated the permanent component with any other bin, it is impossible to constrain the angle. The main conclusion here is that this angle is nonzero. To provide this misalignment of the PA between the components associated with the different emission regions within the source, a misalignment in the geometry of the system should be introduced.

4.3. Influence of the variations in the wind

One other possible explanation for the rotation of the polarization plane with time could be the impact of the orbital movement on the polarization arising from the scattering in the accretion bulge. With the high accretion rate known in GX 13+1, some asymmetry in the accretion disk surrounding the NS can be expected. However, GX 13+1 is recognized for having the largest disk in terms of gravitational radius of all observed LMXBs (Tomaru et al. 2020). If a bulge exists, it is therefore probably quite distant from the source. Moreover, we observed a rotation of the polarization plane by ≈70° in the two days of observation. The orbital period of GX 13+1 is 24.5 d. The unknown mechanism that causes the rotation of the polarization plane would need to operate on a shorter timescale.

GX 13+1 is known to have a strong and rapidly changing wind, and evidence for the absorption in the wind comes from the *XMM–Newton* observation. Scattering in the equatorial wind can produce different polarization patterns in theory, and with this mechanism and with the high inclination of the source, relatively high polarization can be produced easily (see Sunyaev & Titarchuk 1985; Tomaru et al. 2024; Nitindala et al., in prep.). The nature of the polarization variability could be that the observed emission is scattered in the different parts of the wind above the accretion disk. As different absorption features are assumed to come from several distinct parts of the wind with various physical, optical, and geometrical properties, we expect significant differences in the polarimetric behavior. If the line of sight passes close to the edge of the wind, then small variations in the wind opening angle would lead to large variations in the contribution of the scattered component and the polarization degree. We hope to study the correlation between the behavior of the wind and polarimetric properties in the future with simultaneous and IXPE observations.

4.4. Spectral features

All the studies we performed on the spectra of GX 13+1 confirmed the original results from the HID: according to (however limited) IXPE data, there are no significant changes in the spectral behavior with time during the IXPE observation. The study of the radius of the blackbody component $R_{\rm bb}$ showed no variation in the geometry throughout the observation, with only a slight decrease in the last two bins. In bin 5, the contribution of this component to the total flux also dropped. This adds a challenge to the data interpretation. When we assume that in bin 5, the polarization is produced by the dominating softer disk component, we need to find a way for the disk emission to be polarized at the detected level. The PD coming from the disk is estimated at up to 4% for an inclination of 80° and up to only 1.5% for an inclination of 60° (Loktev et al. 2022) assuming a semi-infinite atmosphere dominated by electron scattering (Chandrasekhar 1960). This means that some scattering in the wind above the disk might need to be introduced. The spectrum contains strong absorption features and GX 13+1 is known to have a strong wind with several absorbing areas. We therefore assume that the wind adds to the polarization of this component. For the harder component, it is more likely to be produced by the BL than the SL. The SL can produce PD up to 1.5% (Bobrikova et al., in prep.), which is not sufficient to explain the high PD we see for higher energies (see Fig. 5). We also expect the polarization from the SL to be orthogonal to the polarization from the disk. We do not see this behavior: all the changes in PA with energy in Fig. 5 and especially in Fig. 3 come from the averaging over time.

We also explored the possibility that the two continua components (`diskbb` and `bbodyrad`) each have different polarization properties by fitting the data with the XSPEC model `tbabs*(polconst*diskbb+polconst*bbodyrad)*const`. We only attempted to apply this model to bin 1 because in this alone, the PD strongly depends on energy, so that it would be easier to resolve the two components. The fit suggested that the `diskbb` component is almost unpolarized (no significant polarization with the PD < 2.9% is obtained at 99% CL), and the `bbodyrad` component has a PD of 10% and a PA of −42°. However interesting, this suggestion makes it even harder to understand the relatively high polarization in bin 5, where the

disk completely dominates the spectrum. The results of the observation are promising and exciting. They require further study supported by the modeling of the emission from different components and the emission that is scattered in the wind above the disk.

5. Summary

We reported the highly significant detection of polarization from GX 13+1 obtained by IXPE. We performed the polarimetric, spectroscopic, and spectropolarimetric analysis of the IXPE data. The two main components of the spectrum, the soft disk emission and the harder Comptonized component, were described by the `diskbb` and `bbodyrad` models, respectively. The spectral analysis was supported by a nonsimultaneous observation performed by *XMM–Newton*. Due to the high energy resolution of *XMM–Newton*, we added the `gaussian` component to describe the broad emission line corresponding to the reflection of the NS surface emission from the disk, four Gaussian absorption lines, `gabs`, and two edges, `edge`. For the different parts of the observation, we used the `polconst` and `pollin` models for the polarimetric properties. The overall PD of the IXPE data was measured at 1.4% at $>5\sigma$ CL, and the PA at $-2°$.

From the in-depth study of the time variability of the polarimetric properties, we reported the strong rotation of the PA by 70° during the two observation days. The PD varied from 3.2% to the nondetectable and then up to 5.0%. Moreover, we reported the change in the dependence of the PD on energy. At the beginning of the observation, we detected polarization that depended linearly on energy, while in the middle and at the end of the observation, the PD was constant with energy. Some of the previous studies of the WMNSs with IXPE reported a rapid switch of the PA by up to 60°, but the persistent rotation of the polarization plane was presented here for the first time.

We suggested several ways to interpret the results of the data analysis. We studied the correlation of the dip in the light curve with the polarimetric properties and concluded that although the dip corresponds to the anomaly in the PA and PD behavior in the dip-core part of the observation, it is not correlated with the general trends of the polarimetric behavior. We defined a constant polarized component and subtracted it from all the observations. We concluded that the second, time-variable component then is expected to switch the sign of the PD (i.e., the PA rotates by 90°) in the middle of the observation. We also discussed the possible impact of the wind and the unusual state in which we found the source. The observed variations in the PA likely imply a misalignment between the NS spin and the orbital axis. Future polarimetric observations will help us to uncover the nature of this unique phenomenon.

Acknowledgements. The Imaging X-ray Polarimetry Explorer (IXPE) is a joint US and Italian mission. The US contribution is supported by the National Aeronautics and Space Administration (NASA) and led and managed by its Marshall Space Flight Center (MSFC), with industry partner Ball Aerospace (contract NNM15AA18C). The Italian contribution is supported by the Italian Space Agency (Agenzia Spaziale Italiana, ASI) through contract ASI-OHBI-2022-13-I.0, agreements ASI-INAF-2022-19-HH.0 and ASI-INFN-2017.13-H0, and its Space Science Data Center (SSDC) with agreements ASI-INAF-2022-14-HH.0 and ASI-INFN 2021-43-HH.0, and by the Istituto Nazionale di Astrofisica (INAF) and the Istituto Nazionale di Fisica Nucleare (INFN) in Italy. This research used data products provided by the IXPE Team (MSFC, SSDC, INAF, and INFN) and distributed with additional software tools by the High-Energy Astrophysics Science Archive Research Center (HEASARC), at NASA Goddard Space Flight Center (GSFC). We thank the *XMM–Newton* Project Scientist for approving our DDT request to observe GX 13+1. The research leading to these results has received funding from the European Union's Horizon 2020 Programme under the AHEAD2020 project (grant agreement 871158). This research has been supported by the Academy of Finland grants 333112, 349144, and 355672 (AB, SVF, JP, VL, AV, APN, SST) and the German Academic Exchange Service (DAAD) travel grant 57525212 (VD). ADM, FLM, SF, FMu, ECo, RF, and PSo are partially supported by MAECI with grant CN24GR08 "GRBAXP: Guangxi-Rome Bilateral Agreement for X-ray Polarimetry in Astrophysics". This research was also supported by the INAF grant 1.05.23.05.06: "Spin and Geometry in accreting X-ray binaries: The first multifrequency spectro-polarimetric campaign". IL was supported by the NASA Postdoctoral Program at the Marshall Space Flight Center, administered by Oak Ridge Associated Universities under contract with NASA.

References

Allen, J. L., Schulz, N. S., Homan, J., et al. 2018, ApJ, 861, 26
Arnaud, K. A. 1996, ASP Conf. Ser., 101, 17
Baldini, L., Barbanera, M., Bellazzini, R., et al. 2021, Astropart. Phys., 133, 102628
Baldini, L., Bucciantini, N., Di Lalla, N., et al. 2022, SoftwareX, 19, 101194
Bandyopadhyay, R. M., Shahbaz, T., Charles, P. A., & Naylor, T. 1999, MNRAS, 306, 417
Capitanio, F., Fabiani, S., Gnarini, A., et al. 2023, ApJ, 943, 129
Chandrasekhar, S. 1960, Radiative Transfer (New York: Dover)
Cocchi, M., Gnarini, A., Fabiani, S., et al. 2023, A&A, 674, L10
Corbet, R. H. D., Pearlman, A. B., Buxton, M., & Levine, A. M. 2010, ApJ, 719, 979
D'Aí, A., Iaria, R., Di Salvo, T., et al. 2014, A&A, 564, A62
Diaz Trigo, M., Sidoli, L., Parmar, A., & Boirin, L. 2010, AIP Conf. Ser., 1248, 153
Díaz Trigo, M., Sidoli, L., Boirin, L., & Parmar, A. N. 2012, A&A, 543, A50
Di Gesu, L., Marshall, H. L., Ehlert, S. R., et al. 2023, Nat. Astron., 7, 1245
Di Marco, A., Costa, E., Muleri, F., et al. 2022, AJ, 163, 170
Di Marco, A., La Monaca, F., Poutanen, J., et al. 2023a, ApJ, 953, L22
Di Marco, A., Soffitta, P., Costa, E., et al. 2023b, AJ, 165, 143
Doroshenko, V., Poutanen, J., Tsygankov, S. S., et al. 2022, Nat. Astron., 6, 1433
Doroshenko, V., Poutanen, J., Heyl, J., et al. 2023, A&A, 677, A57
Fabiani, S., Capitanio, F., Iaria, R., et al. 2024, A&A, 684, A137
Farinelli, R., Fabiani, S., Poutanen, J., et al. 2023, MNRAS, 519, 3681
Gilfanov, M., Revnivtsev, M., & Molkov, S. 2003, A&A, 410, 217
Gnarini, A., Ursini, F., Matt, G., et al. 2022, MNRAS, 514, 2561
Grindlay, J. E., & Seaquist, E. R. 1986, ApJ, 310, 172
Heinz, S., Sell, P., Fender, R. P., et al. 2013, ApJ, 779, 171
Homan, J., van der Klis, M., Wijnands, R., Vaughan, B., & Kuulkers, E. 1998, ApJ, 499, L41
Iaria, R., Di Salvo, T., Burderi, L., et al. 2014, A&A, 561, A99
Inogamov, N. A., & Sunyaev, R. A. 1999, Astron. Lett., 25, 269
Kislat, F., Clark, B., Beilicke, M., & Krawczynski, H. 2015, Astropart. Phys., 68, 45
Krawczynski, H., Muleri, F., Dovčiak, M., et al. 2022, Science, 378, 650
La Monaca, F., Di Marco, A., Poutanen, J., et al. 2024, ApJ, 960, L11
Lapidus, I. I., & Sunyaev, R. A. 1985, MNRAS, 217, 291
Loktev, V., Veledina, A., & Poutanen, J. 2022, A&A, 660, A25
Long, K. S., Chanan, G. A., Ku, W. H. M., & Novick, R. 1979, ApJ, 232, L107
Maiolino, T., Laurent, P., Titarchuk, L., Orlandini, M., & Frontera, F. 2019, A&A, 625, A8
Matsuoka, M., Kawasaki, K., Ueno, S., et al. 2009, PASJ, 61, 999
Méndez, M., & Belloni, T. M. 2021, Astrophys. Space Sci. Lib., 461, 263
NASA High Energy Astrophysics Science Archive Research Center (HEASARC) 2014, Astrophysics Source Code Library [record ascl:1408.004]
Poutanen, J., Tsygankov, S. S., Doroshenko, V., et al. 2024, A&A, submitted [arXiv:2405.08107]
Rankin, J., La Monaca, F., Di Marco, A., et al. 2024, ApJ, 961, L8
Revnivtsev, M. G., & Gilfanov, M. R. 2006, A&A, 453, 253
Revnivtsev, M. G., Suleimanov, V. F., & Poutanen, J. 2013, MNRAS, 434, 2355
Saade, M. L., Kaaret, P., Gnarini, A., et al. 2024, ApJ, 963, 133
Saavedra, E. A., García, F., Fogantini, F. A., et al. 2023, MNRAS, 522, 3367
Schnerr, R. S., Reerink, T., van der Klis, M., et al. 2003, A&A, 406, 221
Shakura, N. I., & Sunyaev, R. A. 1988, Adv. Space Res., 8, 135
Soffitta, P., Baldini, L., Bellazzini, R., et al. 2021, AJ, 162, 208
Sunyaev, R. A., & Titarchuk, L. G. 1985, A&A, 143, 374
Tomaru, R., Done, C., Ohsuga, K., Odaka, H., & Takahashi, T. 2020, MNRAS, 497, 4970
Tomaru, R., Done, C., & Odaka, H. 2024, MNRAS, 527, 7047
Tsygankov, S. S., Doroshenko, V., Poutanen, J., et al. 2022, ApJ, 941, L14
Tsygankov, S. S., Doroshenko, V., Mushtukov, A. A., et al. 2023, A&A, 675, A48

Ursini, F., Farinelli, R., Gnarini, A., et al. 2023, A&A, 676, A20
van der Klis, M. 1989, ARA&A, 27, 517
van der Klis, M. 2000, ARA&A, 38, 717
Weisskopf, M. C., Soffitta, P., Baldini, L., et al. 2022, JATIS, 8, 026002
White, N. E., & Holt, S. S. 1982, ApJ, 257, 318
XRISM Science Team 2022, arXiv e-prints [arXiv:2202.05399]

[1] Department of Physics and Astronomy, 20014 University of Turku, Finland
e-mail: anna.a.bobrikova@utu.fi
[2] INAF Istituto di Astrofisica e Planetologia Spaziali, Via del Fosso del Cavaliere 100, 00133 Roma, Italy
[3] Dipartimento di Fisica, Università degli Studi di Roma "Tor Vergata", Via della Ricerca Scientifica 1, 00133 Roma, Italy
[4] Dipartimento di Fisica, Università degli Studi di Roma "La Sapienza", Piazzale Aldo Moro 5, 00185 Roma, Italy
[5] MIT Kavli Institute for Astrophysics and Space Research, Massachusetts Institute of Technology, 77 Massachusetts Avenue, Cambridge, MA 02139, USA
[6] Serco for the European Space Agency (ESA), European Space Astronomy Centre, Camino Bajo del Castillo s/n, 28692 Villanueva de la Cañada, Madrid, Spain
[7] Dipartimento di Matematica e Fisica, Università degli Studi Roma Tre, Via della Vasca Navale 84, 00146, Roma, Italy
[8] Nordita, KTH Royal Institute of Technology and Stockholm University, Hannes Alfvéns väg 12, 106 91, Stockholm, Sweden
[9] Anton Pannekoek Institute for Astronomy & GRAPPA, University of Amsterdam, Science Park 904, 1098 XH Amsterdam, The Netherlands
[10] Centre for Extragalactic Astronomy, Department of Physics, Durham University, South Road, Durham DH1 3LE, UK
[11] Kavli Institute for Physics and Mathematics of the Universe (WPI), University of Tokyo, Kashiwa, Chiba 277-8583, Japan
[12] University of British Columbia, Vancouver, BC V6T 1Z4, Canada
[13] NASA Marshall Space Flight Center, Huntsville, AL 35812, USA
[14] Instituto de Astrofísica de Andalucía – CSIC, Glorieta de la Astronomía s/n, 18008 Granada, Spain
[15] INAF Osservatorio Astronomico di Roma, Via Frascati 33, 00040 Monte Porzio Catone, (RM), Italy
[16] Space Science Data Center, Agenzia Spaziale Italiana, Via del Politecnico snc, 00133 Roma, Italy
[17] INAF Osservatorio Astronomico di Cagliari, Via della Scienza 5, 09047 Selargius (CA), Italy
[18] Istituto Nazionale di Fisica Nucleare, Sezione di Pisa, Largo B. Pontecorvo 3, 56127 Pisa, Italy
[19] Dipartimento di Fisica, Università di Pisa, Largo B. Pontecorvo 3, 56127 Pisa, Italy
[20] Istituto Nazionale di Fisica Nucleare, Sezione di Torino, Via Pietro Giuria 1, 10125 Torino, Italy
[21] Dipartimento di Fisica, Università degli Studi di Torino, Via Pietro Giuria 1, 10125 Torino, Italy
[22] INAF Osservatorio Astrofisico di Arcetri, Largo Enrico Fermi 5, 50125 Firenze, Italy
[23] Dipartimento di Fisica e Astronomia, Università degli Studi di Firenze, Via Sansone 1, 50019 Sesto Fiorentino (FI), Italy
[24] Istituto Nazionale di Fisica Nucleare, Sezione di Firenze, Via Sansone 1, 50019 Sesto Fiorentino (FI), Italy
[25] Agenzia Spaziale Italiana, Via del Politecnico snc, 00133 Roma, Italy
[26] Science and Technology Institute, Universities Space Research Association, Huntsville, AL 35805, USA
[27] Istituto Nazionale di Fisica Nucleare, Sezione di Roma "Tor Vergata", Via della Ricerca Scientifica 1, 00133 Roma, Italy
[28] Department of Physics and Kavli Institute for Particle Astrophysics and Cosmology, Stanford University, Stanford, California 94305, USA
[29] Institut für Astronomie und Astrophysik, Universität Tübingen, Sand 1, 72076 Tübingen, Germany
[30] Astronomical Institute of the Czech Academy of Sciences, Boční II 1401/1, 14100 Praha 4, Czech Republic
[31] RIKEN Cluster for Pioneering Research, 2-1 Hirosawa, Wako, Saitama 351-0198, Japan
[32] X-ray Astrophysics Laboratory, NASA Goddard Space Flight Center, Greenbelt, MD 20771, USA
[33] Yamagata University, 1-4-12 Kojirakawa-machi, Yamagata-shi 990-8560, Japan
[34] Osaka University, 1-1 Yamadaoka, Suita, Osaka 565-0871, Japan
[35] International Center for Hadron Astrophysics, Chiba University, Chiba 263-8522, Japan
[36] Institute for Astrophysical Research, Boston University, 725 Commonwealth Avenue, Boston, MA 02215, USA
[37] Department of Astrophysics, St. Petersburg State University, Universitetsky pr. 28, Petrodvoretz 198504 St. Petersburg, Russia
[38] Department of Physics and Astronomy and Space Science Center, University of New Hampshire, Durham, NH 03824, USA
[39] Physics Department and McDonnell Center for the Space Sciences, Washington University in St. Louis, St. Louis, MO 63130, USA
[40] Istituto Nazionale di Fisica Nucleare, Sezione di Napoli, Strada Comunale Cinthia, 80126 Napoli, Italy
[41] Université de Strasbourg, CNRS, Observatoire Astronomique de Strasbourg, UMR 7550, 67000 Strasbourg, France
[42] Graduate School of Science, Division of Particle and Astrophysical Science, Nagoya University, Furo-cho, Chikusa-ku, Nagoya, Aichi 464-8602, Japan
[43] Hiroshima Astrophysical Science Center, Hiroshima University, 1-3-1 Kagamiyama, Higashi-Hiroshima, Hiroshima 739-8526, Japan
[44] Department of Physics and Astronomy, Louisiana State University, Baton Rouge, LA 70803, USA
[45] Department of Physics, University of Hong Kong, Pokfulam, Hong Kong
[46] Department of Astronomy and Astrophysics, Pennsylvania State University, University Park, PA 16801, USA
[47] Université Grenoble Alpes, CNRS, IPAG, 38000 Grenoble, France
[48] Center for Astrophysics, Harvard & Smithsonian, 60 Garden St, Cambridge, MA 02138, USA
[49] INAF Osservatorio Astronomico di Brera, Via E. Bianchi 46, 23807 Merate (LC), Italy
[50] Dipartimento di Fisica e Astronomia, Università degli Studi di Padova, Via Marzolo 8, 35131 Padova, Italy
[51] Department of Astronomy, University of Maryland, College Park, Maryland 20742, USA
[52] Mullard Space Science Laboratory, University College London, Holmbury St Mary, Dorking, Surrey RH5 6NT, UK
[53] Guangxi Key Laboratory for Relativistic Astrophysics, School of Physical Science and Technology, Guangxi University, Nanning 530004, PR China

A. Bobrikova, A. Di Marco, F. La Monaca, J. Poutanen, S. V. Forsblom, V. Loktev
New polarimetric study of the galactic burster GX 13+1

Astronomy & Astrophysics, 2024; 688: A217

III

A&A, 688, A217 (2024)
https://doi.org/10.1051/0004-6361/202450207
© The Authors 2024

Astronomy & Astrophysics

New polarimetric study of the galactic X-ray burster GX 13+1

Anna Bobrikova[1], Alessandro Di Marco[2], Fabio La Monaca[2,3,4], Juri Poutanen[1], Sofia V. Forsblom[1], and Vladislav Loktev[1]

[1] Department of Physics and Astronomy, University of Turku, 20014 Turku, Finland
e-mail: anna.a.bobrikova@utu.fi
[2] INAF Istituto di Astrofisica e Planetologia Spaziali, Via del Fosso del Cavaliere 100, 00133 Roma, Italy
[3] Dipartimento di Fisica, Università degli Studi di Roma "Tor Vergata", Via della Ricerca Scientifica 1, 00133 Roma, Italy
[4] Dipartimento di Fisica, Università degli Studi di Roma "La Sapienza", Piazzale Aldo Moro 5, 00185 Roma, Italy

Received 2 April 2024 / Accepted 17 May 2024

ABSTRACT

Weakly magnetized neutron stars (WMNSs) are complex astrophysical objects with challenging phenomenology. For decades, they have been studied via spectrometry and timing analyses. It is well established that the spectrum of WMNSs consists of several components traditionally associated with the accretion disk, the boundary or spreading layer, and the wind, along with their interactions. Since 2022, WMNSs have been actively observed using the Imaging X-ray Polarimetry Explorer (IXPE). Polarimetric studies have provided new information about the behavior and geometry of these sources. One of the most enigmatic sources in this category, the galactic X-ray burster GX 13+1, was first observed with IXPE in October 2023. A highly variable polarization at levels of 2–5% was detected, with the source showing a rotation of the polarization angle (PA), suggestive of misalignment within the system. A second observation was performed in February 2024, complemented by observations from *Swift*/XRT. IXPE measured an overall polarization degree (PD) of 2.5% and a PA of 24°, while *Swift*/XRT data helped us evaluate the galactic absorption and fit the continuum. Here, we study the similarities and differences in the polarimetric properties of the source during the two observations. Our findings confirm the expected misalignment in the system and the assignment of the harder component to the boundary layer. We also emphasize the significance of the wind in the system. Additionally, we observe notable differences in the variation of polarimetric properties with energy and over time.

Key words. accretion, accretion disks – polarization – stars: neutron – X-rays: binaries

1. Introduction

Although weakly magnetized neutron stars (WMNSs) do not show pulsation or strong orbital variation, they present a complex phenomenology that requires further studies and observations to be explained. The broad class of WMNSs includes sources with a magnetic field on the order of 10^7–10^9 G. These neutron stars accrete matter from their companions via the Roche lobe. If the accretion rate is high enough to overpower the relatively weak magnetic field, the matter from the accretion disk falls directly onto the equator of the neutron star.

Non-pulsating WMNSs are traditionally classified into two main groups, Z and atolls, based on the patterns they show on the color-color diagram (CCD) or hardness-intensity diagram (HID). Although the classification is completely phenomenological, objects of these two classes have many other characteristic behavioral properties. For instance, atolls are known to be less bright than the Z sources: the typical luminosity of the atolls is in the range of 10^{36}–10^{37} erg s^{-1}, while Z sources are among the brightest objects in the X-ray sky, with luminosities on the order of 10^{38} erg s^{-1}. However, many features are known to be present in both classes. For example, quasi-periodic oscillations (QPOs) in the hertz and kilohertz ranges were observed from both Z and atoll sources (van der Klis 1989, 2000). Sources of both classes are observed in both hard and soft states, and the main components of their spectrum are expected to be the same. The spectrum is generally well described by the two main components (see, e.g., Revnivtsev et al. 2013). The soft component can be approximated by the multicolor blackbody emission of temperature <1 keV associated with the accretion disk. The harder component is probably caused by Comptonization in a relatively cool plasma (2–3 keV), either a boundary layer between the accretion disk and the surface of the neutron star (Shakura & Sunyaev 1988) or the spreading layer at the neutron star surface (Inogamov & Sunyaev 1999; Suleimanov & Poutanen 2006). Additional features known to the spectrum are the broad Fe emission line associated with the reflection of the spreading layer emission from the accretion disk and sharp absorption lines caused by the absorption of the emission in the wind above the disk.

However, the geometry of the WMNSs cannot be fully understood from spectroscopic and time-resolved observations alone. Information obtained from variability, and specifically from the QPOs, revealed that the strongest variability is associated with a harder spectral component (Gilfanov et al. 2003; Revnivtsev & Gilfanov 2006; Revnivtsev et al. 2013) originating close to the neutron star surface. Polarimetry brought a new perspective to the problem. For instance, it became possible to distinguish between the boundary and spreading layer emission based on the polarimetric properties of the emission, while spectroscopically, they are identical. The boundary layer is expected to have a polarization similar to that of the accretion disk, with the polarization vector lying in the plane of the disk (Chandrasekhar 1960; Loktev et al. 2022), while the polarization of the spreading layer is expected to be perpendicular to the accretion disk (Farinelli et al. 2024). For example, the

Open Access article, published by EDP Sciences, under the terms of the Creative Commons Attribution License (https://creativecommons.org/licenses/by/4.0), which permits unrestricted use, distribution, and reproduction in any medium, provided the original work is properly cited.
This article is published in open access under the Subscribe to Open model. Subscribe to A&A to support open access publication.

polarization angle (PA) of the bright Z-source Cyg X-2 (Farinelli et al. 2023) turned out to be consistent with the position angle of the radio jet (which is likely perpendicular to the accretion disk), implying the polarization originated in the spreading layer or from scattering in the accretion disk wind (Tomaru et al. 2024; Nitindala et al., in prep.). In La Monaca et al. (2024), on the other hand, a significant difference between the jet position angle and the PA for Sco X-1 has been observed, which implies a more complicated geometry of the source. In the peculiar case of Cir X-1 (Rankin et al. 2024), the variability of the PA with time and hardness supports the idea of a misalignment between the angular momentum of the neutron star and the binary orbital axis. In Z-sources XTE J1701−462 (Cocchi et al. 2023) and GX 5−1 (Fabiani et al. 2024), a significant variation in the polarization between observations in the hard and soft states suggested a change in geometry between states. In atoll sources GX 9+9 (Ursini et al. 2023), 4U 1820−303 (Di Marco et al. 2023a), and 4U 1624−49 (Saade et al. 2024), the strong dependence of the polarization degree (PD) on energy supports the separation of the spectrum into two components with the different PAs. These discoveries demonstrate the usefulness of using polarimetric observations to study these sources.

The galactic X-ray burster GX 13+1 was first observed by Imaging X-ray Polarimetry Explorer (IXPE) on 2023 October 17–19 (Bobrikova et al. 2024, hereafter B24). This source is known for the strong wind above the large disk being responsible for several absorption lines (Díaz Trigo et al. 2012), a brightness of 0.5 $L_{\rm Edd}$ (D'Aí et al. 2014), and an orbital period of 24.5 d, which is very long for a low-mass X-ray binary (Corbet et al. 2010). GX 13+1 presents a classification challenge: it is still debatable whether it is a Z (see, e.g., Saavedra et al. 2023) or an atoll source (see, e.g., Schnerr et al. 2003).

During the first IXPE observation, GX 13+1 presented an enigmatic behavior: the polarimetric properties varied significantly during the observation, while the spectral properties remained almost unchanged. Moreover, GX 13+1 shows a peculiar continuous rotation of the PA by 70° in the two days of observations, together with a change in the pattern of dependence of PD on energy. These two peculiar behaviors left some space for further investigation. Here, we aim to answer some of the open questions and bring a new perspective to the study of GX 13+1.

The remainder of the paper is structured as follows: we introduce the observations performed with the IXPE and *Swift*/XRT observatories in Sect. 2. In Sect. 3, we present our data analysis. We provide possible interpretations of the results in Sect. 4 and a summary in Sect. 5.

2. Observations

2.1. IXPE

IXPE is a joint mission of the National Aeronautics and Space Administration (NASA) and the Italian Space Agency (Agenzia Spaziale Italiana, ASI) that was launched on 2021 December 9. The observatory comprises three grazing-incidence mirror assembly modules, each of which has a polarization-sensitive X-ray detector unit (DU) in the focal plane (Costa et al. 2001; Baldini et al. 2021). A description of the mission and of the instrument on board is given in Soffitta et al. (2021) and Weisskopf et al. (2022).

IXPE observed GX 13+1 twice: the first observation was conducted in October 2023, as reported in B24, and the second took place from 2024 February 25, at 13:34 UTC to 2024 February 27, at 12:59 UTC, with a total exposure time of approximately 90 ks for each DU (see Table 1 and the light curve in Fig. 1). Data were processed for model-independent polarimetric analysis using the IXPEOBSSIM package version 30.2.1 (Baldini et al. 2022). Spectral and spectropolarimetric analysis was performed using HEASOFT version 6.33 and the standard FTOOLS (Nasa High Energy Astrophysics Science Archive Research Center (Heasarc) 2014), with the IXPE Calibration Database (CALDB) that was released on 2024 February 28. Source photons were selected in a circular region with a radius of 100″ centered at the source position. As recommended by Di Marco et al. (2023b), given the brightness of the source, the background was not subtracted. The unweighted analysis was performed with IXPEOBSSIM, while the weighted analysis was adopted for the spectropolarimetric analysis, as suggested by Di Marco et al. (2022a).

2.2. Swift/XRT

Carrying three instruments on board, the *Neil Gehrels Swift* Observatory (Gehrels et al. 2004) enables the most detailed observations of gamma-ray bursts to date; the X-ray Telescope (XRT), one of the instruments on board, is based on a sensitive, flexible, autonomous X-ray CCD imaging spectrometer. *Swift*/XRT-coordinated observations with IXPE for GX 13+1 were performed, and used to monitor the status of the source and obtain spectral information during IXPE observations. Given the source brightness, the *Swift*/XRT observations were performed in windowed timing (WT) mode. Ten *Swift*/XRT pointings covered the IXPE observation, as reported in Table 1 and Fig. 1. *Swift*/XRT data were extracted using HEASOFT v6.33 and standard FTOOLS (Nasa High Energy Astrophysics Science Archive Research Center (Heasarc) 2014). Source and background extractions were performed using *Swift*/XRT imaging capabilities in an annulus with an inner radius of about 5″ and an outer radius of about 60″ to avoid possible pile-up effects (Romano et al. 2006). The *Swift*/XRT data were fitted in the energy band 0.7−8 keV to ensure sufficient statistics in the spectral fits and grouped to have at least 50 counts bin^{-1}. Response matrices released in the HEASARC CALDB on 2023 July 25, were applied in this analysis.

3. Data analysis

IXPE observed GX 13+1 for ∼90 ks. During the observation, as shown in Fig. 1 (top panel), the source rate was rather stable, with a slight increase at the end of the observation. The source hardness in the IXPE data appears to have no strong variations, showing only a slight decrease with the count rate increase toward the end of the observation; this contrasts with the previous IXPE observation reported in B24, where a dip corresponding to a slight hardening was present. Figure 2, which reports the HID obtained from the IXPE data, shows that hardness did not change by more than 10%.

Consisting of short snapshots during the IXPE observation, the *Swift*/XRT pointings enable us to monitor the spectral state of the source. Previous studies of GX 13+1 have shown that its spectrum can be well described, as is typical for atoll and Z sources, by a soft `diskbb` component representing disk emission and a `bbodyrad` component representing Comptonization emission from the spreading and/or boundary layer (Díaz Trigo et al. 2012). More detailed modeling of the hard Comptonization component, such as using `compTT` or `compTB`, is not possible due to the limited energy bands of IXPE and *Swift*/XRT. Literature

Table 1. List of IXPE and *Swift*/XRT observations.

Observatory	ObsID	Start – Stop	Instrument	Exposure time (s)
Swift	00036688042	2024-02-26T05:05–2024-02-26T05:27	XRT	1366
	00036688043	2024-02-25T13:14–2024-02-25T17:59		892
	00036688044	2024-02-26T13:07–2024-02-26T14:52		1249
	00036688045	2024-02-25T22:53–2024-02-26T00:35		1395
	00036688046	2024-02-26T17:56–2024-02-26T19:30		1311
	00036688047	2024-02-26T08:22–2024-02-26T10:12		1429
	00036688048	2024-02-25T19:28–2024-02-25T21:32		1321
	00036688049	2024-02-26T22:24–2024-02-26T23:59		771
	00036688050	2024-02-27T03:22–2024-02-27T05:14		507
	00036688051	2024-02-27T11:05–2024-02-27T11:29		1443
IXPE	03001101	2024-02-25T13:34–2024-02-27T12:59	DU1	90 670
			DU2	90 819
			DU3	90 799

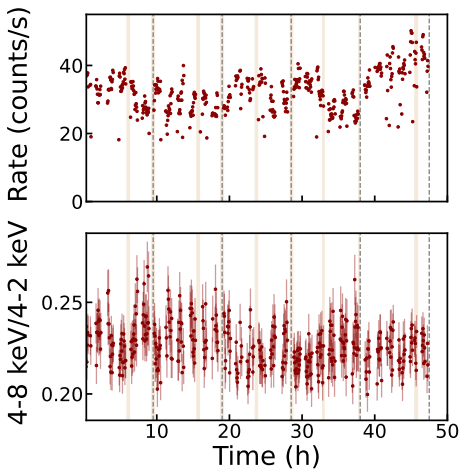


Fig. 1. IXPE light curve obtained by combining the three DUs (top panel) and the corresponding hardness ratio as a function of time (bottom panel). The data are binned in 200 s. Shaded regions indicate the *Swift*/XRT observation periods. Dashed vertical lines indicate the separation of the observation into five equal 9.5 h time bins.

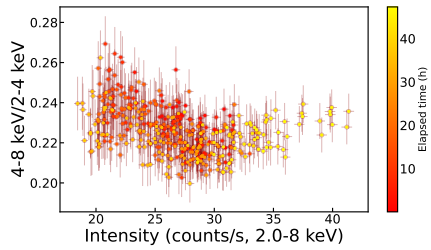


Fig. 2. Hardness-intensity diagram obtained from IXPE data. The data are binned in 200 s.

on *XMM-Newton* spectra of GX 13+1 reports wind and reflection features (Díaz Trigo et al. 2012), but neither IXPE nor *Swift*/XRT allows us to study these features. Therefore, in the following analysis, we will apply the simplified spectral model, `tbabs*(diskbb+bbodyrad)`.

3.1. Spectroscopy

Given its superior spectral capabilities, we used *Swift*/XRT data as the primary source for spectral modeling and to monitor spectral variations. The analysis was conducted in the 0.7−8 keV energy band, with best-fit values reported for each observation in Table 2, including uncertainties at the 68% confidence level (CL). Observation IDs are ordered by observation date to illustrate the time evolution of the spectral model.

In the spectral analysis, the *Swift*/XRT data were fitted using the `tbabs*(diskbb+bbodyrad)` model. Across the different pointings, the absorption column density was on average $\sim 4.7 \times 10^{22}\,\mathrm{cm}^{-2}$, while the disk temperature ranged between 0.7 and 1.1 keV. Regarding the `bbodyrad` component – which in our case is used to describe a Comptonization emission from the boundary layer – the temperature ranged from ∼1.3−1.8 keV. The flux was typically in the range of $\sim(4\text{–}6) \times 10^{-9}\,\mathrm{erg\,cm^{-2}\,s^{-1}}$, except in the final pointing, where it reached the highest value of $\sim 8 \times 10^{-9}\,\mathrm{erg\,cm^{-2}\,s^{-1}}$. The hardness (see Table 2) defined as

$$\mathrm{Hardness} = \frac{\mathrm{Flux}_{3-8\,\mathrm{keV}} - \mathrm{Flux}_{0.7-3\,\mathrm{keV}}}{\mathrm{Flux}_{0.7-8\,\mathrm{keV}}} \quad (1)$$

has an almost constant value, except for Observation ID 00036688045, where the flux was minimal and the hardness maximal. However, this *Swift*/XRT observation (third snapshot) was conducted mainly during an IXPE occultation period. Thus, the IXPE data are not affected by this slight hardening, and the other snapshots confirm the IXPE result of an almost constant hardness ratio during the observation. In the following analysis for the spectropolarimetric study, this Observation ID is excluded, and the others are used in the joint fit with the IXPE data.

Considering the entire IXPE observation and the *Swift*/XRT spectra, except the Observation ID 00036688045, we obtain a good joint spectrum model. The best-fit parameters are reported in Table 3 and Fig. 3. To account for the calibration uncertainties

Table 2. Best-fit parameters for the `tbabs*(diskbb+bbodyrad)` spectral model as obtained by the different *Swift*/XRT spectra.

ObsID	`tbabs`	`diskbb`		`bbodyrad`		χ^2/d.o.f.	$\mathrm{Flux}_{2-8\,\mathrm{keV}}$	Hardness
	N_H (10^{22} cm^{-2})	kT_in (keV)	norm	kT_bb (keV)	norm		(10^{-9} erg cm^{-2} s^{-1})	
00036688043	$4.54^{+0.18}_{-0.14}$	$1.1^{+0.6}_{-0.2}$	250^{+260}_{-160}	$1.5^{+0.6}_{-0.1}$	100^{+60}_{-90}	0.93	6.0	0.35
00036688048	4.52 ± 0.10	[1.0]	290 ± 19	1.52 ± 0.04	120 ± 12	0.91	5.9	0.37
00036688045	5.71 ± 0.19	0.67 ± 0.05	1100 ± 400	1.57 ± 0.04	100 ± 10	1.13	4.1	0.45
00036688042	5.0 ± 0.2	$0.70^{+0.10}_{-0.07}$	1000^{+700}_{-400}	$1.41^{+0.06}_{-0.04}$	150 ± 30	1.06	5.9	0.38
00036688047	$4.62^{+0.14}_{-0.18}$	$0.88^{+0.38}_{-0.10}$	500 ± 300	$1.38^{+0.18}_{-0.05}$	200^{+40}_{-100}	1.12	6.0	0.36
00036688044	$4.67^{+0.17}_{-0.15}$	$0.98^{+0.39}_{-0.15}$	400^{+300}_{-200}	$1.46^{+0.31}_{-0.09}$	130^{+60}_{-100}	1.04	5.9	0.33
00036688046	$4.9^{+0.3}_{-0.2}$	$0.70^{+0.11}_{-0.08}$	1100^{+900}_{-600}	$1.29^{+0.06}_{-0.04}$	230^{+40}_{-50}	1.10	5.0	0.33
00036688049	4.3 ± 0.3	$1.0^{+0.6}_{-0.2}$	320^{+630}_{-260}	$1.7^{+1.3}_{-0.1}$	80^{+65}_{-75}	1.16	5.4	0.34
00036688050	5.7 ± 0.4	$0.66^{+0.12}_{-0.09}$	1800^{+2000}_{-1000}	$1.46^{+0.11}_{-0.08}$	130 ± 40	0.92	4.7	0.36
00036688051	$4.70^{+0.12}_{-0.09}$	$1.13^{+0.19}_{-0.16}$	310^{+200}_{-120}	$1.77^{+0.28}_{-0.17}$	80^{+50}_{-40}	1.16	7.9	0.35

Notes. The fits are performed in the energy band 0.7–8.0 keV. Errors correspond to the 68% CL. The reported flux has a typical uncertainty on the order of 0.3×10^{-9}. The hardness is defined as in Eq. (1).

Table 3. Best-fit parameters of the `const*tbabs* (diskbb+bbodyrad)` model for the joint *Swift*/XRT and IXPE spectra.

Model	Parameter	Value
`tbabs`	N_H (10^{22} cm^{-2})	$4.45^{+1.00}_{-0.05}$
`diskbb`	kT_in (keV)	$0.88^{+0.10}_{-0.07}$
	norm	390^{+140}_{-130}
`bbodyrad`	kT_bb (keV)	$1.33^{+0.13}_{-0.14}$
	norm	228^{+20}_{-8}
`const`	*Swift*/XRT/XRT	[1]
	IXPE-DU1	0.722 ± 0.003
	IXPE-DU2	0.686 ± 0.003
	IXPE-DU3	0.658 ± 0.003
χ^2/d.o.f.	991/956 = 1.04	
Flux (10^{-9} erg cm^{-2} s^{-1})		
2–8 keV		6.0
`diskbb`		1.3
`bbodyrad`		4.7

Notes. Errors correspond to the 68% CL.

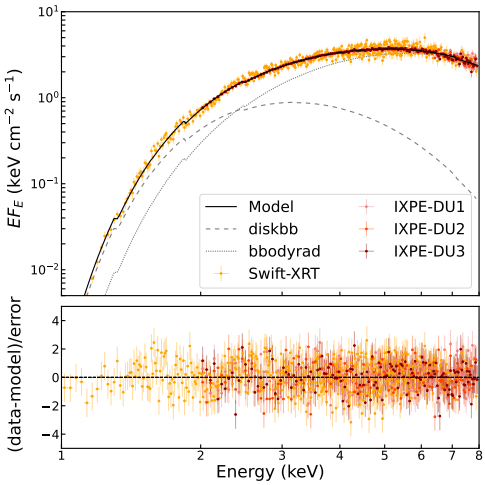


Fig. 3. Joint spectral fit of *Swift*/XRT and IXPE data in the 1–8 keV energy range. In the top panel, the spectra of each telescope are reported in EF_E units; residuals are shown in the bottom panel.

in the IXPE data (see, e.g., Di Marco et al. 2022b), we allowed the gain slope and offset of the IXPE DUs to vary freely.

The joint fit confirms the expected result for the average model from several *Swift*/XRT snapshots. In the following spectropolarimetric analysis, the spectral model is fixed to the present one. The IXPE gain correction is at a level of 0.95 for the slope in all three DUs, with the offset in the range of 70–100 eV.

3.2. Polarimetry

The spectroscopy reveals that neither the light curve nor the hardness has strong dips or features that would suggest the observation should be separated into several parts to be studied independently. To study the time variability of the polarimetric properties, we followed the same approach as in B24 and split this new IXPE observation into five equal time bins spanning 9.5 h. The results are reported in Fig. 4.

The time dependence of the polarimetric properties shows a hint of variability in PD, completely different from the rotation we observed in the first IXPE observation. We found it useful to proceed with analyzing the observation as a whole since there are no clear trends. Next, we studied the dependence of the polarimetric properties on energy; the results are reported in Fig. 5. The polarization shows a hint of energy dependence, but the significance of this trend is less than 2σ, as seen later in the spectropolarimetric analysis. The average in energy and time polarization during this observation is PD = 2.6% ± 0.5% with

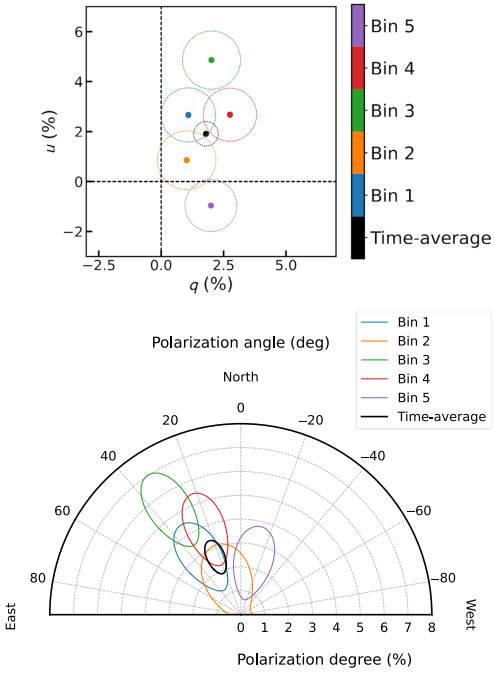


Fig. 4. Time dependence of the normalized Stokes parameters q and u (top), and of the PD and PA (bottom) obtained by the `pcube` algorithm using the data separated into 9.5 h time bins. Confidence regions are reported at 68%.

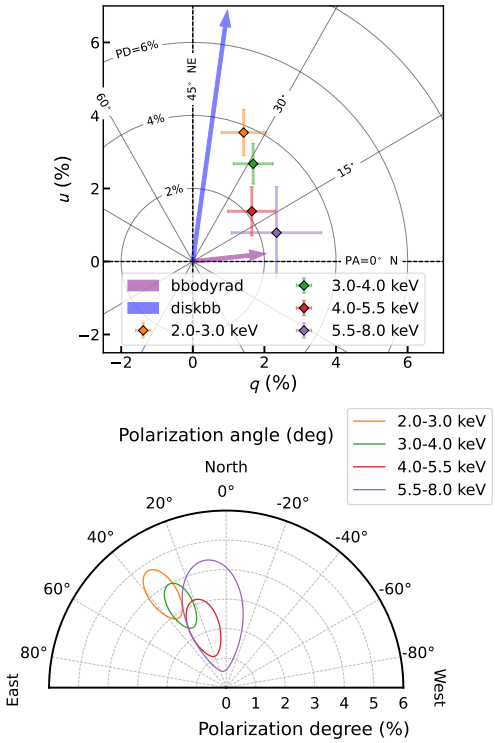


Fig. 5. Energy-resolved normalized Stokes parameters q and u (top), and PD and PA (bottom) obtained by the `pcube` algorithm using the reported energy bins for time-averaged data. The confidence regions are reported at 68% CL. The vectors correspond to the best-fit polarization parameters of the `diskbb` and `bbodyrad` components, respectively, as obtained using spectropolarimetric analysis and reported in Table 4.

the PA = 23° ± 5° at a significance level of 5.2σ, corresponding to a secure detection at CL > 99.9999%.

3.3. Spectropolarimetry

To study the polarization of the different spectral components, we used the results from the spectral analysis to freeze the spectral model in the spectropolarimetric analysis. First, instead of studying the polarization of each spectral component independently, we applied the `polconst` model to the entire continuum model to confirm the model-independent analysis. The result is an average PD of 2.4%±0.3% with the PA of 28°±3°, fully compatible with the model-independent analysis. We then replaced the `polconst` model with `pollin` to obtain a quantitative estimation of the dependence of polarization on energy. We obtained nonzero slopes for PA and PD, but they were compatible with zero within a 2σ level. Finally, we applied a model with different polarizations for each spectral component, obtaining a PD of 6.1%±1.6% and a PA of 41°±7° for the `diskbb` component, and a PD of 1.6%±0.9% with a PA of 6°±10° for the `bbodyrad` component. The results of the spectropolarimetric analysis are summarized in Table 4; the best-fit plots for the spectropolarimetric analysis are reported for the I, Q, and U Stokes parameters in Fig. 6.

4. Discussion

Although intriguing on its own, the observation reported in this article yields the most insight when compared to the results of the October 2023 observations reported in B24, when we measured an overall PD of ∼1.4% and a PA of ∼−2°, significantly different from the current results. However, the reason for the depolarization in the first observation was fast variability in the PA. In B24, the observation was separated into the pre-dip, dip, and post-dip states. The results for the dip were poorly constrained, but the other two are presented in Fig. 7 and compared to the results of the current observation. We note that the current observation is similar in PA to the post-dip state of B24, but the PD is lower probably due to the averaging over time and energy. Bin 3 in Fig. 4, for instance, shows a polarization within errors similar to the one measured after the dip in B24.

Both the HID and the shape of the spectrum confirm that GX 13+1 was in a soft state throughout the observation. We do not see any significant change of state in the IXPE and *Swift*/XRT energy bands, although, in the last part of the

Table 4. IXPE spectropolarimetric fit of the Stokes parameters I, Q, and U using the spectral model from Table 3.

Model	PD/A_1 (%)	$A_{\rm slope}$ (% keV^{-1})	PA/ψ_1 (deg)	$\psi_{\rm slope}$ (deg keV^{-1})	χ^2/d.o.f.
`tbabs*(diskbb+bbodyrad)*polconst`	2.4 ± 0.3	–	28 ± 3	–	243/250 = 0.97
`tbabs*(diskbb+bbodyrad)*pollin`	3.8 ± 0.8	-0.5 ± 0.3	28 ± 3	-8 ± 4	234/248 = 0.94
`tbabs*(diskbb*polconst`	6.5 ± 1.6	–	41 ± 7	–	235/248 = 0.95
`+bbodyrad*polconst)`	1.6 ± 0.7	–	3 ± 13	–	

Notes. Errors correspond to 68% CL.

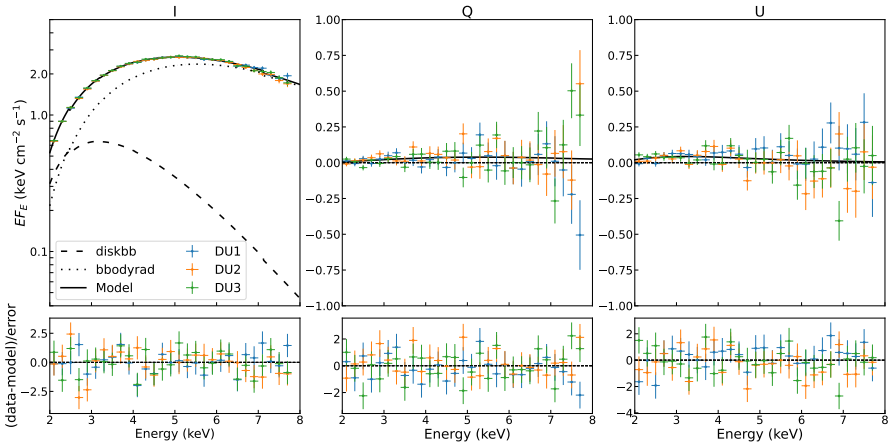


Fig. 6. Spectral energy distribution of GX 13+1 in EF_E representation as observed by IXPE. The left, middle, and right panels are for the Stokes parameters I, Q, and U, respectively. The fit is performed in the 2−8 keV energy band using the three IXPE detectors and applying the `tbabs*(diskbb*polconst+bbodyrad*polconst)` model. The total model is shown with the solid black line, while `diskbb` and `bbodyrad` are indicated with the dashed and dotted lines, respectively. The lower subpanels show the residuals between the data and the best fit. In the joint spectral fit, we applied a rebinning to obtain at least 50 counts per bin as in *Swift*/XRT, while for the spectropolarimetric analysis, a constant grouping was applied to have energy bins of 200 eV.

observation, the flux rises, which is a sign of the source going into an even softer state. If we look at the HID of the source in the October observation (Fig. 2 in B24), we see that the source is almost in the same state, except for the dipping period. During the new observation period, the spectral modeling and decomposition into two main components are better determined, since simultaneous *Swift*/XRT observations offer a better spectral capability than IXPE, thereby allowing for a better spectropolarimetric analysis.

The light curve does not show any peculiar variability: unlike the one from the October observation, the current one has no strong dips or rapid changes, and neither does the hardness ratio. Despite this constant hardness, we attempted to study the possible variation in 9.5 h equal time bins similar to B24. This analysis suggests possible variation in PD in Fig. 4; in particular, it is interesting to note that in Bin 5, corresponding to a softening of GX 13+1, there is lower polarization and an indication of a possible rotation with respect to the other four time bins. The clear rotation of the PA observed during the first observation is not present this time, but the PA appears to have remained aligned with the post-dip polarization measured in B24. If we compare the positions of the points on the (q, u) plane with those obtained from the October 2023 observation (Fig. 7 in B24), we see a different pattern; however, the points are still in the I or IV quadrant. The most significant difference lies in the pattern: in October, we observed the points following a straight line path, whereas here, the variability exhibits a different pattern.

Because of the almost constant hardness and flux, we decided to examine the observation as a whole and study the polarization as a function of energy. As presented in Table 4, the slopes of the `pollin` model are consistent with zero at the 2σ level, indicating only a weakly significant dependence of PA and PD on energy. However, it is interesting to note that the spectropolarimetric analysis assigned very different PAs to the two main continuum components. Figure 5 (top) illustrates this decomposition: while the PD of the disk is rather high, the contribution of the disk to the total spectrum is low, and it becomes even lower with increasing energy, as the Comptonized component becomes increasingly dominant. The most interesting part here is the unusual difference in PA of the two components of 30°–40°. This indication can be seen in the energy-resolved analysis, with the 2−3 keV bin near the arrow corresponding to the DISKBB component polarization, and the 5.5−8.0 keV energy bin approaching the arrow, which represents the polarization of the `bbodyrad` component.

From the aligned systems, we expect the polarization vectors of the emission coming from the disk and the Comptonized component to be either nearly parallel or perpendicular to each other.

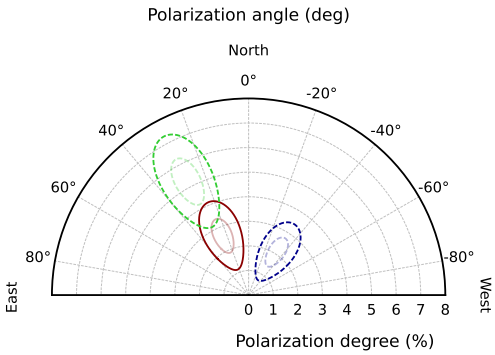


Fig. 7. Average polarization in the 2−8 keV energy band for the pre-dip (dashed blue lines) and post-dip (dashed green lines) of the first observation of GX 13+1, and for the new observation (solid dark red lines). Contours correspond to the 68% and 99% CLs. A significant detection of polarization at 5.2σ is obtained in the new observation with the PA aligned with the post-dip reported in B24.

Hence, we expect some misalignment in the system that would account for this difference in the PA. Additionally, it is important to note the exceptionally high PD of the disk component. As stated by Loktev et al. (2022), polarization exceeding 4% in the IXPE energy range is not anticipated, even at the highest inclination. This value is compatible with the spectropolarimetric results at 90% CL. However, knowing that the source is likely to have an inclination lower than 80° (Díaz Trigo et al. 2012; Tomaru et al. 2020), we need to add the scattering of the disk emission in the wind to reach a PD of 6.5%. We assumed that the Comptonized component comes from the boundary layer, as it is expected to align in PA with the disk emission. The observed difference in PAs is less than 45°.

In search of a source of misalignment, we examined previous observations by IXPE. It is possible, though unexpected, that the rotation axis of the neutron star is slightly misaligned from the rotation axis of the binary system, similar to the Cir X-1 (Rankin et al. 2024). In such a scenario, the boundary layer could be dragged out of the disk plane by the motion of the star. Another potential explanation is the peculiar geometry of the wind within the system.

Finally, we wish to address the significant difference between the two observations of GX 13+1. Although the object was in the same spectral state, it was observed half an orbit away from the previous observation, during which the source clearly exhibited a rotation of the PA over time. However, in February 2024, there was no evident monotonic change in the PA, despite ongoing variations. One possibility is that the mechanism responsible for the dip in the light curve during the first observation also caused the rotation of the PA. However, this mechanism remains unidentified. Notably, the recent observation suggests that the PA remained aligned with that observed at the end of the previous observation. As the flux increased and the source transitioned to a softer state at the end of the present IXPE pointing, the PD decreased and rotated to a PA similar to that observed in October before the dip. This pattern might indicate, as observed in Cir X-1, a variation in the PA corresponding to the state of the source. This implies a potential variation in the geometry of the hot region across different states. This hypothesis is supported by the October 2023 observation, where the energy dependence of the polarization shifted from an energy-dependent behavior, as seen in 4U 1820−30 (Di Marco et al. 2023a), to a constant polarization with energy, as observed, for example, in Sco X-1 in La Monaca et al. (2024). While current data do not allow for a definitive conclusion, we hope that future observations will provide sufficient significance for a detailed analysis of the polarization across different states of atoll and Z sources.

Additionally, the role of the wind remains an open question. Given our lack of knowledge regarding wind behavior during both observations, it is plausible that the wind could contribute to the observed differences in polarimetric properties, although we currently have no means to substantiate this hypothesis.

5. Summary

We analyzed the observation of GX 13+1 carried out simultaneously by IXPE and *Swift*/XRT. In this article, we report the highly significant detection of polarization from this source in the soft state. Spectroscopic analysis shows that the spectrum is close to that in Díaz Trigo et al. (2012), and the hardness of the emission confirms the lower left banana state, as well as the further softening of the spectrum at the end of this new observation. We used a `diskbb` model for the softer disk emission, and the `bbodyrad` model to approximate the harder component associated with the spreading or boundary layer. The polarimetric analysis provided the overall PD of 2.5% at $>5\sigma$ CL and a PA of 24°. We also see a marginally significant decrease in PD and PA with energy. The same trend was confirmed by the spectropolarimetric analysis, which showed that the softer component was more strongly polarized than the harder component, with the PA differing by ∼40°. The results of the spectropolarimetric analysis using XSPEC performed under the assumption of one overall polarization model were in agreement with the `pcube` polarimetric results.

We studied the differences and similarities between the first (B24) and the second observations of GX 13+1 by IXPE. Our main conclusion is that the overall polarization is significantly higher in the second observation despite the source being in the same state during the two observations. Depolarization was caused by the variability in polarimetric properties, which was larger during the first observation. We have discussed possible reasons for the different polarimetric behavior in the two observations.

Acknowledgements. This research used data products provided by the IXPE Team (MSFC, SSDC, INAF, and INFN) and distributed with additional software tools by the High-Energy Astrophysics Science Archive Research Center (HEASARC), at NASA Goddard Space Flight Center (GSFC). The Imaging X-ray Polarimetry Explorer (IXPE) is a joint US and Italian mission. The Italian contribution is supported by the Italian Space Agency (Agenzia Spaziale Italiana, ASI) through contract ASI-OHBI-2022-13-I.0, agreements ASI-INAF-2022-19-HH.0 and ASI-INFN-2017.13-H0, and its Space Science Data Center (SSDC) with agreements ASI-INAF-2022-14-HH.0 and ASI-INFN 2021-43-HH.0, and by the Istituto Nazionale di Astrofisica (INAF) and the Istituto Nazionale di Fisica Nucleare (INFN) in Italy. We thank the *Swift* Project Scientists for approving our DDT request to observe GX 13+1. This research has been supported by the Finnish Cultural Foundation grant 00240328 (AB) and the Academy of Finland grant 333112 (AB, JP, SVF, VL). ADM, FLM are partially supported by MAECI with grant CN24GR08 "GRBAXP: Guangxi-Rome Bilateral Agreement for X-ray Polarimetry in Astrophysics".

References

Baldini, L., Barbanera, M., Bellazzini, R., et al. 2021, Astropart. Phys., 133, 102628

Baldini, L., Bucciantini, N., Di Lalla, N., et al. 2022, SoftwareX, 19, 101194
Bobrikova, A., Forsblom, S. V., Di Marco, A., et al. 2024, A&A, 688, A170
Chandrasekhar, S. 1960, Radiative Transfer (New York: Dover)
Cocchi, M., Gnarini, A., Fabiani, S., et al. 2023, A&A, 674, L10
Corbet, R. H. D., Pearlman, A. B., Buxton, M., & Levine, A. M. 2010, ApJ, 719, 979
Costa, E., Soffitta, P., Bellazzini, R., et al. 2001, Nature, 411, 662
D'Aí, A., Iaria, R., Di Salvo, T., et al. 2014, A&A, 564, A62
Di Marco, A., Costa, E., Muleri, F., et al. 2022a, AJ, 163, 170
Di Marco, A., Muleri, F., Fabiani, S., et al. 2022b, Proc. SPIE, 12181, 121811C
Di Marco, A., La Monaca, F., Poutanen, J., et al. 2023a, ApJ, 953, L22
Di Marco, A., Soffitta, P., Costa, E., et al. 2023b, AJ, 165, 143
Díaz Trigo, M., Sidoli, L., Boirin, L., & Parmar, A. N. 2012, A&A, 543, A50
Fabiani, S., Capitanio, F., Iaria, R., et al. 2024, A&A, 684, A137
Farinelli, R., Fabiani, S., Poutanen, J., et al. 2023, MNRAS, 519, 3681
Farinelli, R., Waghmare, A., Ducci, L., & Santangelo, A. 2024, A&A, 684, A62
Gehrels, N., Chincarini, G., Giommi, P., et al. 2004, ApJ, 611, 1005
Gilfanov, M., Revnivtsev, M., & Molkov, S. 2003, A&A, 410, 217
Inogamov, N. A., & Sunyaev, R. A. 1999, Astron. Lett., 25, 269
La Monaca, F., Di Marco, A., Poutanen, J., et al. 2024, ApJ, 960, L11
Loktev, V., Veledina, A., & Poutanen, J. 2022, A&A, 660, A25
Nasa High Energy Astrophysics Science Archive Research Center (Heasarc) 2014, Astrophysics Source Code Library [record ascl:1408.004]
Rankin, J., La Monaca, F., Di Marco, A., et al. 2024, ApJ, 961, L8
Revnivtsev, M. G., & Gilfanov, M. R. 2006, A&A, 453, 253
Revnivtsev, M. G., Suleimanov, V. F., & Poutanen, J. 2013, MNRAS, 434, 2355
Romano, P., Campana, S., Chincarini, G., et al. 2006, A&A, 456, 917
Saade, M. L., Kaaret, P., Gnarini, A., et al. 2024, ApJ, 963, 133
Saavedra, E. A., García, F., Fogantini, F. A., et al. 2023, MNRAS, 522, 3367
Schnerr, R. S., Reerink, T., van der Klis, M., et al. 2003, A&A, 406, 221
Shakura, N. I., & Sunyaev, R. A. 1988, Adv. Space Res., 8, 135
Soffitta, P., Baldini, L., Bellazzini, R., et al. 2021, AJ, 162, 208
Suleimanov, V., & Poutanen, J. 2006, MNRAS, 369, 2036
Tomaru, R., Done, C., Ohsuga, K., Odaka, H., & Takahashi, T. 2020, MNRAS, 497, 4970
Tomaru, R., Done, C., & Odaka, H. 2024, MNRAS, 527, 7047
Ursini, F., Farinelli, R., Gnarini, A., et al. 2023, A&A, 676, A20
van der Klis, M. 1989, ARA&A, 27, 517
van der Klis, M. 2000, ARA&A, 38, 717
Weisskopf, M. C., Soffitta, P., Baldini, L., et al. 2022, JATIS, 8, 026002

A. Bobrikova, J. Poutanen, V. Loktev
Polarized radiation from the spreading layer of weakly magnetized neutron stars

Astronomy & Astrophysics, 2025; 696: A181

IV

A&A, 696, A181 (2025)
https://doi.org/10.1051/0004-6361/202452358
© The Authors 2025

Astronomy & Astrophysics

Polarized radiation from the spreading layer of weakly magnetized neutron stars

Anna Bobrikova[1,⋆], Juri Poutanen[1], and Vladislav Loktev[1,2]

[1] Department of Physics and Astronomy, 20014 University of Turku, Finland
[2] Department of Physics, P.O. Box 64, 00014 University of Helsinki, Finland

Received 24 September 2024 / Accepted 6 March 2025

ABSTRACT

Observations show that the X-ray emission of the accreting weakly magnetized neutron stars is polarized. We developed a theoretical model for polarized radiation from the spreading layer, which is the extension of the accretion flow boundary layer onto the neutron star surface. We calculated the Stokes parameters of the radiation and accounted for relativistic aberration and gravitational light bending in the Schwarzschild metric. We show that regardless of the geometry, the polarization degree of the spreading layer does not exceed 1.5%. Our results have implications with regard to the understanding of the X-ray polarization from weakly magnetized neutron stars observed with the Imaging X-ray Polarimetry Explorer and the future enhanced X-ray Timing and Polarimetry mission.

Key words. accretion, accretion disks – polarization – methods: analytical – stars: neutron – X-rays: binaries

1. Introduction

Weakly magnetized neutron stars (WMNSs) in low-mass X-ray binary systems (LMXBs) are among the brightest X-ray sources. The neutron stars (NSs) in these systems emit mostly by accretion of matter that leaks from the companion star that fills its Roche lobe. The emission of these sources is highly variable due to the outbursts and rapid changes in the geometry of the system and is a subject of thorough research.

The emission mechanism of WMNSs has been studied for decades. Spectroscopic results obtained in X-ray and radio bands allowed scientists to conclude that the emission mostly comes from the accretion disk that formed around the NS and from a Comptonized component, which can be associated with a boundary layer (BL) between the disk and the NS surface (Shakura & Sunyaev 1988) or a spreading layer (SL), which is a layer of accreted matter at the NS surface (see, e.g., Lapidus & Sunyaev 1985; Inogamov & Sunyaev 1999). Timing observations added more information about the QPOs in these systems. Observable both at Hz and kHz frequencies (van der Klis 1989, 2000), they are currently associated with the events that occur near the NS surface. However, the exact geometry of the sources remains unknown.

Polarimetric studies add two more measurable variables to the data sets we obtain from the sources. With the launch of the Imaging X-ray Polarimetry Explorer (IXPE; Weisskopf et al. 2022) in December 2021, we are capable for the first time of measuring the polarization degree (PD) and polarization angle (PA) of the WMNS X-ray emission with high precision. These new observables can shed new light on the emission mechanisms, the geometry of the source, and the interactions of the light on the way from the emitting region to the observer.

Fifteen WMNSs have been observed with IXPE in the three years of operation (see Ursini et al. 2024, for a recent review), each providing answers and new questions. From an upper limit in GS 1826−238 (Capitanio et al. 2023) to a 10σ polarization detection in GX 340+0 (La Monaca et al. 2024a; Bhargava et al. 2024), we saw a broad variety of complex phenomena in all the sources. For some of the sources, we were able to compare the recent observations with previous results: in Cyg X-2 (Farinelli et al. 2023), the agreement between IXPE and Orbiting Solar Observatory 8 (OSO-8; Weisskopf et al. 1976; Long et al. 1980) was reported, while in Sco X-1 (La Monaca et al. 2024b), a discrepancy between the archive and recent observations was observed. The PD increased with energy in GX 9+9 (Ursini et al. 2023), 4U 1624−49 (Saade et al. 2024), and 4U 1820−303 (Di Marco et al. 2023), and the PD increases from the soft to the hard state in XTE 1701−462 (Cocchi et al. 2023) and GX 5−1 (Fabiani et al. 2024). Significant variability of the PA with time and/or energy was observed in Cir X-1 (Rankin et al. 2024) and GX 13+1 (Bobrikova et al. 2024a,b; Di Marco et al. 2025). Various interpretations, such as scattering in the disk wind, tilted rotating NS, and precession of the rotation axis, were suggested for all these phenomena. Further investigation is still required, however.

To understand the polarimetric data, we need to have expectations regarding the PA and PD values of the emission coming from different parts of the source, such as the accretion disk, the BL, and the SL. The polarization of the disk emission was studied in detail (see, e.g., Dovčiak et al. 2008; Li et al. 2009; Loktev et al. 2022). Lapidus & Sunyaev (1985) estimated the SL emission and its polarization.

In the current article, we present a detailed study of the polarized emission coming from the SL. We calculate the emission of the rapidly rotating SL accounting for relativistic aberration and light bending in the Schwarzschild metric. We account for rotation of the polarization plane due to relativistic effects (Poutanen 2020). Unlike Lapidus & Sunyaev (1985), we account for the rapid motion of the matter in the SL and consider various geometries of the SL.

⋆ Corresponding author; anna.a.bobrikova@utu.fi

Open Access article, published by EDP Sciences, under the terms of the Creative Commons Attribution License (https://creativecommons.org/licenses/by/4.0), which permits unrestricted use, distribution, and reproduction in any medium, provided the original work is properly cited.
This article is published in open access under the Subscribe to Open model. Subscribe to A&A to support open access publication.

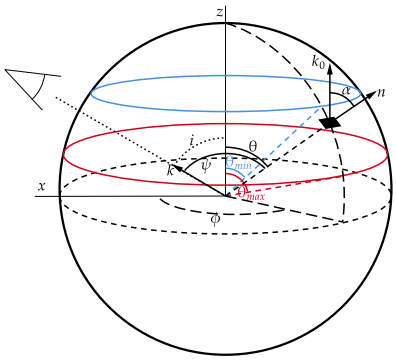


Fig. 1. Geometry of the problem. The SL is confined between the two circles with the colatitude $\theta_{\rm min}$ and $\theta_{\rm max}$, plotted in blue and red, respectively.

The more recent studies that were inspired by IXPE observations, such as the study by Gnarini et al. (2022), applied relativistic Monte Carlo codes to simulate the polarimetric properties of the emission regions of various geometries. We present a semi-analytical approach to the problem, similar to that of Farinelli et al. (2024). However, we study a broader range of parameters, use a more realistic approach to the properties of the layer such as velocity and temperature, and investigate the dependence of the polarization on energy.

The remainder of the paper is organized as follows. In Sect. 2, we present the model that describes the formation of polarized radiation in a SL at the NS surface. In Sect. 3, we apply the formalism to different geometrical configurations of the SL and evaluate the polarimetric properties of the emitted radiation. In Sect. 4, we study the effect of varying the emission model. We compare our results to the existing observations of the WMNS by IXPE in Sect. 5. We conclude in Sect. 6.

2. Emission model

We considered a spherical NS of radius, R, and mass, M, with a SL covering part of the NS surface. We defined the layer as a belt located between the minimum and maximum colatitude, $\theta_{\rm min}$ and $\theta_{\rm max}$ (see Fig. 1). The coordinate system was chosen such that the z-axis was aligned with the rotation axis of the NS, and the disk lay in the xy-plane. As we assumed the accretion disk to be geometrically thin and optically thick, we only considered the emission from the upper half of the NS surface. We considered the direct emission from the SL and neglected the components corresponding to the reflection of the SL emission from the accretion disk surface or scattering off the wind above the disk.

We first calculated the observed flux to estimate the polarization of the emission from the SL. For completeness, we repeated (with some adjustments for the SL geometry) the method that was used to compute the observed flux (see also Poutanen & Beloborodov 2006; Salmi et al. 2018; Bogdanov et al. 2019; Suleimanov et al. 2020) and then extended it to the description of the polarization following Poutanen (2020).

To obtain the emission from the whole SL, we started by calculating the emission from a small surface element with colatitude θ and azimuthal angle ϕ. Then, we integrated over the whole visible area of the layer in the nonrotating frame.

We chose the static coordinate system so that the unit vector in the direction of the observer was $\hat{\boldsymbol{k}} = (\sin i, 0, \cos i)$, where i is the inclination of the spin axis to the line of sight (see Fig. 1 for the geometry). The unit vector of the normal to the surface element (which is parallel to the radius vector of the emission point in the case of a spherical star) is $\hat{\boldsymbol{n}} = (\sin\theta\cos\phi, \sin\theta\sin\phi, \cos\theta)$. Thus, the angle between the surface element radius vector and the line of sight is given by

$$\cos\psi \equiv \hat{\boldsymbol{k}}\cdot\hat{\boldsymbol{n}} = \cos i\ \cos\theta + \sin i\ \sin\theta\ \cos\phi. \tag{1}$$

Because photon trajectories in the Schwarzschild metric are planar, the unit vector of the photon momentum close to the surface can be obtained as a linear combination:

$$\hat{\boldsymbol{k}}_0 = \frac{\sin\alpha\,\hat{\boldsymbol{k}} + \sin(\psi-\alpha)\,\hat{\boldsymbol{n}}}{\sin\psi}, \tag{2}$$

where α is the angle between the surface normal and the photon momentum,

$$\cos\alpha = \hat{\boldsymbol{k}}_0\cdot\hat{\boldsymbol{n}}. \tag{3}$$

For our calculations, we used the approximate analytical formula for the light bending $\alpha(\psi)$ as suggested by Beloborodov (2002),

$$\cos\alpha \approx 1-(1-u)(1-\cos\psi), \tag{4}$$

where $u = R_{\rm S}/R$ is the NS compactness, with $R_{\rm S} = 2GM/c^2$ being the Schwarzschild radius.

The material in the SL moves with a velocity v in the direction defined by the unit vector $\hat{\boldsymbol{v}} = (-\sin\phi, \cos\phi, 0)$. For most of the models, we assumed a solid-body-like rotation profile in which the equatorial velocity is a fraction β_0 of the Keplerian velocity,

$$\beta(\theta) = \beta_{\rm eq}\sin\theta = \beta_0\frac{v_{\rm Kepl}}{c}\sin\theta = \beta_0\sqrt{\frac{u}{2(1-u)}}\sin\theta. \tag{5}$$

The angle between the velocity vector and the photon direction is then

$$\cos\xi = \hat{\boldsymbol{v}}\cdot\hat{\boldsymbol{k}}_0 = \frac{\sin\alpha}{\sin\psi}\,\hat{\boldsymbol{v}}\cdot\hat{\boldsymbol{k}} = -\frac{\sin\alpha}{\sin\psi}\sin i\ \sin\phi. \tag{6}$$

The observed flux at energy E from the surface element is

$$\mathrm{d}F_E = I_E\mathrm{d}\Omega_{\rm obs}, \tag{7}$$

where

$$\mathrm{d}\Omega_{\rm obs} = \mathcal{D}\cos\alpha\frac{\mathrm{d}S}{D^2} \tag{8}$$

is the solid angle of the surface element as observed from the distance D, with the layer element area $dS = R^2 d\cos\theta\, d\phi$ and the lensing factor

$$\mathcal{D} = \frac{1}{1-u}\frac{d\cos\alpha}{d\cos\psi} \tag{9}$$

being equal to unity in the Beloborodov approximation. The observed specific intensity can be related to the intensity measured in the corotating frame as

$$I_E = \left(\frac{E}{E'}\right)^3 I'_{E'}(\alpha',\theta), \tag{10}$$

where α' is the angle of the photon momentum to the surface normal as measured in the corotating frame of the surface element, and all the quantities in the corotating frame are labeled with a prime. The ratio of the energies combines gravitational redshift and the Doppler effect,

$$\frac{E}{E'} = \delta\sqrt{1-u}. \tag{11}$$

The Doppler factor

$$\delta = \frac{1}{\gamma(1-\beta\cos\xi)} \tag{12}$$

depends on the SL velocity at this colatitude relative to the external nonrotating frame, and the Lorentz factor is

$$\gamma(\theta) = \frac{1}{\sqrt{1-\beta^2(\theta)}}. \tag{13}$$

The angle α' is related to the analogous angle measured in the static frame as (Poutanen & Gierliński 2003)

$$\cos\alpha' = \delta\cos\alpha. \tag{14}$$

Assuming that radiation from the SL can be described by electron-scattering dominated semi-infinite atmosphere (Chandrasekhar 1960; Sobolev 1963), we approximated the energy and angular distribution of the specific intensity as (Suleimanov et al. 2020)

$$I'_{E'}(\mu,\theta) = \frac{1}{f_c^4} B_{E'}(f_c T_{\rm eff}) a_{\rm es}(\mu), \tag{15}$$

where $a_{\rm es}(\mu) \approx 0.421 + 0.868\mu$, $\mu = \cos\alpha'$, B_E is the Planck function, $T_{\rm eff}$ is the effective temperature, which can be a function of colatitude θ, and the color correction f_c is assumed to be latitude-independent. We finally obtained the observed flux from the surface element

$$\mathrm{d}F_E = \frac{R^2}{D^2}\cos\alpha\,\mathcal{D}\left(\delta\sqrt{1-u}\right)^3 I'_{E'}(\alpha',\theta)\,\mathrm{d}\cos\theta\,\mathrm{d}\phi. \tag{16}$$

To describe the polarimetric properties of the emission from a surface element, we introduced the Stokes vector,

$$\mathrm{d}\boldsymbol{F}(E) = \begin{pmatrix} \mathrm{d}F_I(E) \\ \mathrm{d}F_Q(E) \\ \mathrm{d}F_U(E) \end{pmatrix} = \mathrm{d}F_E \begin{pmatrix} 1 \\ P\cos 2\chi \\ P\sin 2\chi \end{pmatrix}, \tag{17}$$

where P is the observed PD, and χ is the observed PA, both of which depend on energy. The fourth component of the Stokes vector describing circular polarization was removed from consideration, as circular polarization is conserved along the photon trajectory in the absence of the plasma effects and is not observable with IXPE or eXTP. Because the linear PD is also conserved along the photon trajectory, we set P to be equal to the PD of the emitted radiation at the NS surface, corresponding to the optically thick electron-scattering-dominated plane-parallel atmosphere (Chandrasekhar 1960; Viironen & Poutanen 2004),

$$P_{\rm es}(\mu) = -\frac{1-\mu}{1+3.582\mu}\,0.1171. \tag{18}$$

The corresponding PA χ was calculated as in Poutanen (2020),

$$\tan\chi = \frac{\sin\theta\sin\phi + \beta A}{-\sin i\cos\theta + \cos i\sin\theta\cos\phi - \beta\sin\phi\, C}, \tag{19}$$

where

$$\begin{aligned} A &= \frac{\sin\psi}{\sin\alpha}B + \frac{\cos\alpha-\cos\psi}{\sin\alpha\sin\psi}(\cos\phi - B\cos\psi), \\ B &= \sin i\sin\theta + \cos i\cos\theta\cos\phi, \\ C &= \frac{\sin\psi}{\sin\alpha}\cos\theta + \frac{\cos\alpha-\cos\psi}{\sin\alpha\sin\psi}(\cos i - \cos\theta\cos\psi). \end{aligned} \tag{20}$$

Finally, to obtain the polarized emission from the whole SL, we integrated over its visible area as defined by the visibility condition $\cos\alpha > 0$ (Suleimanov et al. 2020),

$$\begin{aligned} \boldsymbol{F}(E) = \begin{pmatrix} F_I(E) \\ F_Q(E) \\ F_U(E) \end{pmatrix} = \frac{R^2}{D^2}\iint\limits_{\cos\alpha>0} \cos\alpha\,\mathcal{D}\left(\delta\sqrt{1-u}\right)^3 \\ \times I'_{E'}(\cos\alpha',\theta)\begin{pmatrix} 1 \\ P_{\rm es}(\cos\alpha')\cos 2\chi \\ P_{\rm es}(\cos\alpha')\sin 2\chi \end{pmatrix}\mathrm{d}\cos\theta\,\mathrm{d}\phi. \end{aligned} \tag{21}$$

Both the PD ($P_{\rm es}$) and PA (χ) in this equation depend on the coordinates of the surface element (θ,ϕ). For the whole SL emission, the observed PD and PA at every energy were computed via

$$P_{\rm obs} = \frac{\sqrt{F_Q^2 + F_U^2}}{F_I} \tag{22}$$

and

$$\cos(2\chi_{\rm obs}) = F_Q/(P_{\rm obs}F_I), \quad \sin(2\chi_{\rm obs}) = F_U/(P_{\rm obs}F_I). \tag{23}$$

3. Results for various geometries

The formalism derived in Sect. 2 was applied to the various geometries of the SL. The resulting polarimetric characteristics were expressed as a function of the dimensionless photon energy

$$x = \frac{E}{f_c k_{\rm B} T_*}, \tag{24}$$

where $k_{\rm B}$ is the Boltzmann constant and T_* is a characteristic effective temperature $T_{\rm eff}$ of the SL. By scaling Eq. (21) for the observed flux EF_E by the typical flux at the NS surface $\sigma_{\rm SB}T_*^4$, we introduced the dimensionless luminosity (Stokes vector) as

$$\begin{aligned} x\boldsymbol{I}_x = \frac{D^2}{\Delta R^2}\frac{E\boldsymbol{F}_E}{\sigma_{\rm SB}T_*^4} = \frac{15}{\pi^5}\iint_S \cos\alpha\,\mathcal{D}\left(\delta\sqrt{1-u}\right)^4 a_{\rm es}(\cos\alpha') \\ \times \frac{x'^4}{\mathrm{e}^{x' T_*/T_{\rm eff}(\theta)}-1}\begin{pmatrix} 1 \\ P_{\rm es}(\cos\alpha')\cos 2\chi \\ P_{\rm es}(\cos\alpha')\sin 2\chi \end{pmatrix}\mathrm{d}\cos\theta\,\mathrm{d}\phi. \end{aligned} \tag{25}$$

Here, Δ is the fraction of the NS surface occupied by the SL, and $x' = x/(\delta\sqrt{1-u})$. The dependences of the dimensionless luminosity xI_x, PD, and PA on dimensionless energy x for various SL models are shown in Figs. 2–6. We note that for an isothermal ($T_{\rm eff}(\theta) = T_*$) nonrotating NS surface, Eq. (25) is reduced to

$$x\boldsymbol{I}_x = \frac{15}{\pi^4}(1-u)^{-1}\frac{x^4}{\mathrm{e}^{x/\sqrt{1-u}}-1}\begin{pmatrix}1\\0\\0\end{pmatrix}. \tag{26}$$

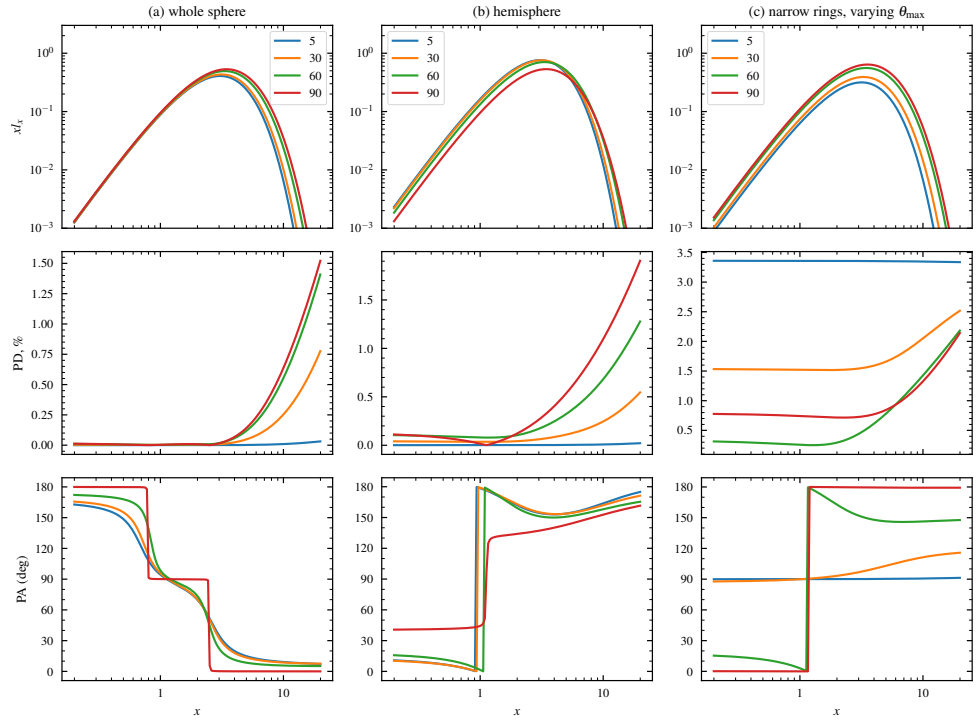


Fig. 2. Dimensionless luminosity xI_x, PA, and PD as functions of the dimensionless photon energy, $x = E/f_c k_B T_{eff}$. For all the cases presented, $\beta = 0.35$. Results for the whole sphere (column a) and upper hemisphere (column b), observed at inclinations of 5°, 30°, 60°, and 90° are shown with blue, orange, green, and red lines, respectively. Results for 1°-wide rings observed at an inclination 90° are shown in column (c) with blue, orange, green, and red lines for ring colatitude of 5°, 30°, 60°, and 90°, respectively.

3.1. Basic geometries: Sphere, hemisphere, and one-degree rings

We started with the most basic geometrical models and explored the emission from a SL that is shaped as a sphere, hemisphere, and a narrow ring of 1° width. We also assumed that the effective temperature is constant over the SL. Studying these basic cases can support our general understanding of the SL emission and its polarization. The equatorial velocity of the plasma flow in the SL β_{eq} was fixed at the value of 0.35, which corresponds to $\beta_0 = 0.68$ for a NS with a radius $R = 12$ km and a mass $M = 1.4\,M_\odot$.

We first studied the emission from the whole sphere (Fig. 2a) for different inclination angles noted in the plot. Except for the energies above the peak in the luminosity, the emission is almost not polarized, regardless of the inclination, because the problem is nearly symmetric. The increase in PD is connected to the exponential cutoff in the spectrum of the SL and the Doppler effect. The rotation of the SL increases the observed energy of the light from the part of the SL in which the matter flows toward the observer. As the light from that part of the SL is polarized, the PD increases. This pattern is also more visible for higher inclinations because the direction of the matter flow is parallel to the NS equator. The variation in the PA with energy is most peculiar: in the extreme case of an inclination $i = 90°$ (red lines), three steps appear, and for the lower inclinations, the pattern is smoothed. These steps also appear due to the Doppler effect: at lower energies, the emission from the part of the sphere that moves away from the observer dominates, and the light from this area is polarized perpendicular to the disk plane, so that PA = 0° (or 180°). For medium energies, the flux is dominated by the observed middle section of the NS from the poles to the equator. This light is polarized in the disk plane, so that PA = 90°. At higher energies, the emission from the part of the sphere where matter flows toward the observer is observed. The polarization is again perpendicular to the disk plane, and the PA is zero.

A hemisphere is a good approximation for the presence of the accretion disk because it covers half of the NS (Fig. 2b). In this case, PD is nonzero even at the lowest photon energies. The most significant change between the two cases is in the PA. We again examine the edge-on case (red lines). In general, the polarization from the electron-scattering-dominated optically thick cold slab is parallel to the surface of the slab. For the whole sphere and counterclockwise rotation of the matter, the left half of the sphere is brighter because of the Doppler effect. As this case is otherwise symmetric, the overall polarization is expected

to be dominated by the PD of the brighter part and perpendicular to the disk plane for any energies, so that PA is zero (or 180°). For the hemisphere case, however, the quarter of the sphere now dominates the overall picture. At lower energies, the emission is therefore dominated by the right part of the star, so that the PA shifts toward 45°. Moreover, PA rotates rapidly close to the energy $x \approx 1$ (i.e., $E \approx kT_{\rm eff} f_{\rm c}$). At higher energies, the PA rotates toward ≈140° (which is equivalent to $\approx -40°$), and PD rises because the emission is now is dominated by Doppler boosting of a smaller portion on the left part of the star, where the matter moves toward to the observer.

For the last column of the figure, we considered a narrow ring with a width of 1° at different colatitudes and report the value of the colatitude of the lower edge of the ring, $\theta_{\rm max}$ (Fig. 2c). With the inclination fixed at 90°, the PD decreases with the colatitude of the ring (except for the case of the ring at $\theta_{\rm max} = 60°$, which is discussed below). This occurs because the emission observed from the normal to the surface is not polarized. For instance, the observer at an inclination of 90° sees the radiation from the polar ring polarized (practically) horizontally. At the equator, on the other hand, the emission that arrives at the observer from the part of the ring in which the azimuthal angle is close to the angle of the observer is not polarized at all, and the light from this part of the SL contributes to a further decrease in the overall observed PD. This trend of a decrease in the PD with colatitude of the ring, however, breaks for the higher colatitudes because the PD from the ring at the equator exceeds the PD from the ring at a colatitude of 60°. This is because the PA of the light from the ring observed at this intermediate angle varies with the azimuthal angle (i.e., the light is not horizontally polarized, like at the pole, nor vertically, like at the equator), leading to partial cancellation of the overall PD. This is also reflected in the PA-dependence plot.

3.2. Narrow one-degree rings: Detailed study

We explored the emission from rings of 1° width in detail. Unless specified otherwise, our fiducial set of parameters was $\theta_{\rm max} = 30°$, $i = 60°$, and $\beta_{\rm eq} = 0.35$. As we understood the results of the simple cases shown in Fig. 2, with the more complicated cases, we relied on the results of the simulations and switched to the description and interpretation rather than an explanation of the phenomena presented in the plots.

Figure 3a illustrates the differences in the spectra for different inclinations. As in the case considered in Fig. 2c, an increase in the angle between the normal to the surface and the direction to the observer increases the PD. Additionally, unpolarized emission is observed when the observer is close to the pole because the entire ring is seen and the problem becomes (almost) azimuthally symmetric around the direction to the observer. The change in the inclination does not affect the PA in this case. The differences only occur at higher energies because of the Doppler effect.

The effect of varying the colatitude of the ring is shown in Fig. 3b. The Doppler effect again affects the spectrum of the ring more prominently when the ring is closer to the equator, where the gas moves with the highest velocities. We also note that the lowest PD is expected from the ring at the colatitude $\theta_{\rm max} = 60°$, which coincides with the inclination in this scenario, as PD turns to zero when the emitting region is observed along the normal.

For the cases presented in Fig. 3c, we changed the equatorial velocity. In the nonrotating case (blue line), PD and PA do not depend on energy. A slight decrease in the PD with increasing velocity is observed at lower energies, while an increase is seen at higher energies. In all three considered cases of a rotating SL, the rotation of the PA reached 30°.

3.3. Wide spreading layer

For the next step of our simulations, we broadened the 1° ring into a wider layer. Unless specified otherwise, we consider in this section an isothermal SL with $\theta_{\rm min} = 30°$, $\theta_{\rm max} = 90°$, $i = 60°$, and $\beta_{\rm eq} = 0.35$. Similar to Fig. 3, we took for Fig. 4a the fiducial set and examined the influence of the inclination on the observed emission for different inclinations between 5° and 90°. We again observe that the PD is the highest for $i = 90°$. Observing the system virtually from the pole ($i = 5°$) shows the lowest PD, as the SL appears nearly axially symmetric around the direction to the observer. For the case shown in Fig. 4b, we investigated the dependence on the width of the SL by changing the $\theta_{\rm min}$ from 5° to the values mentioned in the plot. Our dimensionless luminosity was normalized by the surface area of the emitting region, so that the observed flux did not change much with the width of the layer. However, the PD decreased when the SL changed from a narrow belt to a hemisphere. Finally, we changed in Fig. 4c the value of the equatorial velocity of the plasma in the SL. The change in this parameter predominantly affected the flux at the highest energies. The difference in the PD and PA between a nonrotating case (blue line) and rotating at the Keplerian velocity case (red line) is significant. In all three cases presented in Fig. 4, we obtained a change of up to 40° in the PA.

4. Results for various physical configurations

In the previous section, we considered various geometrical configurations of both SL and the binary system. To do this, we kept the surface temperature, the velocity of the relativistic flow, and the polarization calculations as simple as possible. However, a homogeneous effective surface temperature across the whole accretion flow is not realistic, and neither is the weak dependence of the velocity on θ presented in Sect. 2. Chandrasekhar's limit on the polarization from an infinitely thick slab can also be replaced with exact Thomson scattering calculations. We searched for alternative models and tested the polarimetric properties of these SLs.

4.1. Inogamov-Sunyaev spreading layer

Inogamov & Sunyaev (1999) introduced the concept of a SL that is most luminous at the edge of the layer, where it reaches the surface of the NS, decelerates, and emits, rather than at the stellar equator, where the gas levitates because its velocity is close to the Keplerian velocity. To match the suggested flux profile (as shown in Fig. 8 in Inogamov & Sunyaev 1999), we introduced the dependence of the effective temperature on colatitude,

$$T_{\rm IS}^4(\theta) = H(\theta - \theta_{\rm peak}) \left\{ T_{\rm min}^4 + T_*^4 \exp\left[-\frac{(\theta - \theta_{\rm peak})^2}{2\sigma^2} \right] \right\}, \qquad (27)$$

where H is the Heaviside step function, $T_{\rm min}$ is the temperature of the SL off-peak, T_* is a characteristic temperature impacting the height of the peak, and σ parameterizes the width of the peak. This dependence is illustrated in the left panel in Fig. 5. We assumed a Gaussian peak at $\theta_{\rm peak} = 30°$ with a full width at half maximum of 20° (=2.355σ), $T_{\rm min} = 1$ keV, and $T_* = 2$ keV.

As the gas at the equator was assumed to levitate with a velocity corresponding to that of the accretion disk and to slow

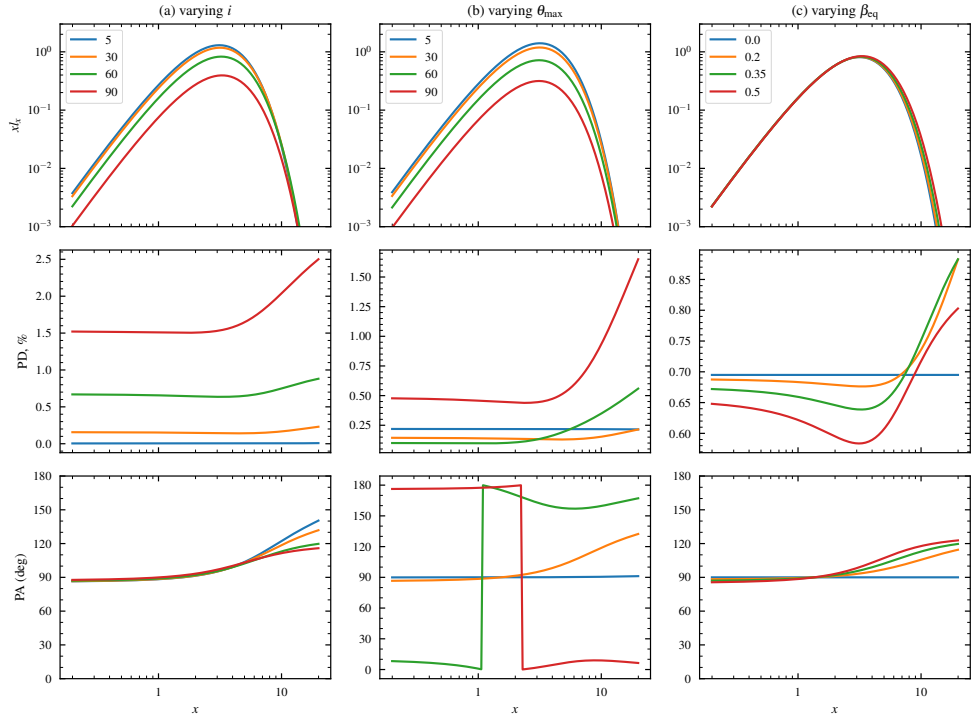


Fig. 3. Dimensionless luminosity xI_x, PA, and PD as functions of the dimensionless photon energy, $x = E/f_c k_B T_{\rm eff}$ for emission from the 1°-wide rings with the fiducial parameter set $\theta_{\max} = 30°$, $i = 60°$, and $\beta_{\rm eq} = 0.35$. Column (a) shows the results for various inclinations with other parameters from the fiducial set. The blue, orange, green, and red lines correspond to $i = 5°$, 30°, 60°, and 90°, respectively. Column (b) shows the results for various ring colatitudes with other parameters from the fiducial set. The blue, orange, green, and red lines correspond to $\theta_{\max} = 5°$, 30°, 60°, and 90°, respectively. Column (c) shows the results for various equatorial velocities with other parameters from the fiducial set. The blue, orange, green, and red lines correspond to $\beta_{\rm eq} = 0.0$, 0.2, 0.35, and 0.5, respectively. The PA is zero for vertical polarization and is measured counterclockwise.

down closer to the edge of the SL, we also introduced a stronger dependence of the velocity on colatitude,

$$\beta_{\rm IS}(\theta) = \left(\beta_{\rm eq} - \frac{\cos\theta}{\cos\theta_{\rm peak}}\,(\beta_{\rm eq} - \beta_{\rm r})\right)\sin\theta, \tag{28}$$

where $\beta_{\rm eq}$ is the velocity of the SL surface at the equator of the NS, and $\beta_{\rm r}\sin\theta_{\rm peak}$ is the velocity of the SL surface at the edge of the SL that is associated with the rotation of the NS. This dependence is illustrated in the right panel in Fig. 5. When these dependences are taken into account, the dimensionless luminosity given in Eq. (25) changes accordingly.

The results are presented in Fig. 6. We varied the parameters of the SL in the same way as for Figs. 3 and 4. Overall, the behavior is quite similar to the one shown in Fig. 4. The PD follows the same trends with the energy and varied parameters. The PA is ≈0° at lower energies and decreasing with energy. We note a stronger dependence of the PA on energy in this case. The most significant difference from Fig. 4 is in Column (c), where we study the impact of varying the SL velocity on the polarimetric properties. In the case of $\beta_{\rm eq} = 0$, the vertical polarization at lower energies changes to horizontal polarization at higher energies. This occurs because the temperature of the layer is a function of colatitude. The emission from the colatitudes above ≈45° has an effective temperature of 1 keV, while the emission from lower colatitudes is hotter, with $T_{\rm eff}$ exceeding 2 keV at the SL edge. The light from these parts of the SL is observed in different energy ranges: emission from $\theta > 45°$ is seen at lower energies, and the emission of the SL edge is in the higher-energy range. As we already noted in Sect. 3 and especially Column (b) of Fig. 3, the polarization from the rings close to the equator is vertical, while the polarization from the lower colatitudes, for instance, $\theta \approx 30°$, is horizontal. The increased velocity of the SL causes the energy dependence of the PD to become smoother, but the decrease in PD associated with the fast rotation of the PA is still visible.

4.2. Optically thin spreading layer

In the previous examples, we assumed the SL to be optically thick and used Eq. (18) for the PD as a function of emis-

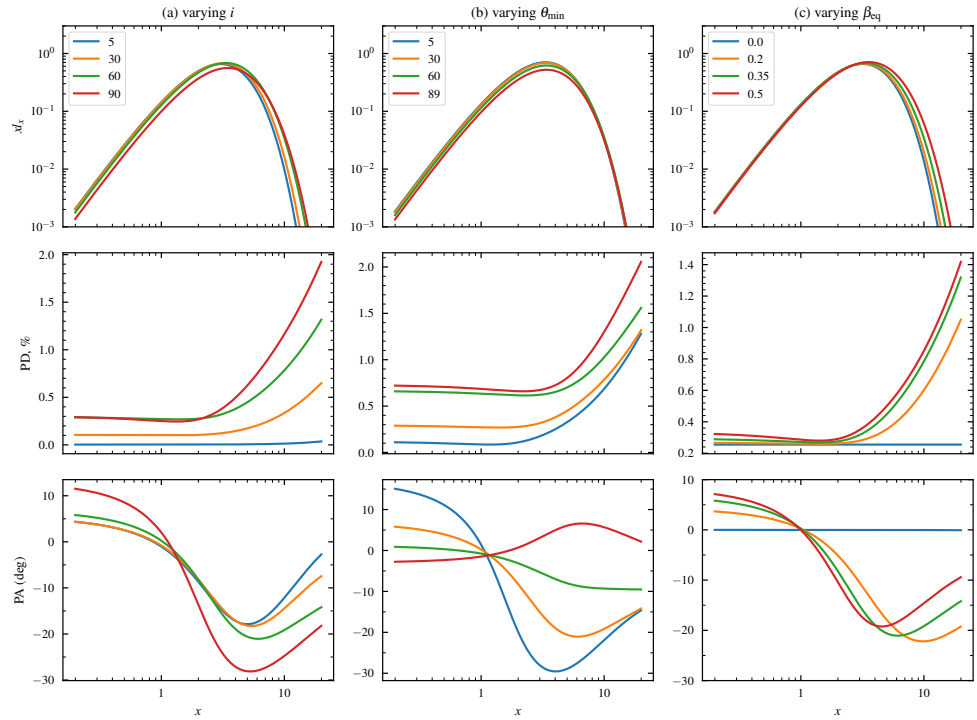


Fig. 4. Same as Fig. 3, but for emission from the broad SL. The fiducial set of parameters is $\theta_{\rm min} = 30°$, $\theta_{\rm max} = 90°$, $i = 60°$, and $\beta_{\rm eq} = 0.35$.

sion angle. We can instead assume that the SL is optically thin and perform the exact calculation of the Thomson scattering in the SL to estimate the polarization of the emission. The formalism for calculating the polarization from the Thomson scattering was discussed in Sunyaev & Titarchuk (1985) and Viironen & Poutanen (2004). From our calculations, we learned that the PD as a function of emission angle barely depends on the optical thickness of the layer. Emission is still polarized in the plane of the SL surface, and the effects of the first few scatterings cancel out, leading to depolarization, as shown in Fig. 7.

High polarization from Compton scattering is expected if we were only to observe the photons after they have experienced many scatterings. This is the case in hot Comptonizing regions, where cool seed photons are upscattered to the X-ray range, and we only see multiple scattered photons in the IXPE range 2–8 keV. This is not the case for the WMNSs, as we expect the SL to be at a low temperature of 2–3 keV. In this case, we observe all the photons in the same energy range, regardless of the number of scatterings they experience. As is shown, for instance, in Fig. 2 of Viironen & Poutanen (2004), the PD of the photon changes sign (i.e. PA rotates by 90°) depending on the number of scatterings it experienced. When we see them all in the same energy range, we therefore expect an overall low polarization regardless of the optical depth.

5. Applications

In the past two years, IXPE has observed a dozen WMNSs. The model presented in this paper gave valuable insights that supported the interpretation of the observation results. First, we learned from the simulations that the emission of the SL is polarized perpendicular to the accretion disk, while for the optically thick electron-scattering-dominated disk, the polarization vector lies in the disk plane. In the spectrum of the WMNSs, we usually see two main components, the softer of which is interpreted as the emission from the disk, while the harder component comes from the BL or the SL. Thus, if a source presents a strong dependence of the PA on energy, we assumed that the harder component of the spectrum comes from the SL rather than the BL, which produces polarization similar to that of the disk. This was the case, for instance, in the IXPE data on Cyg X-2 (Farinelli et al. 2023). However, in this source, the estimated PD from the harder component was about 4%, which is much higher than the PD in our simulations. Similarly, in 4U 1820−303 (Di Marco et al. 2023), the shift by 90° in the PA suggests the presence of a SL, but PD at the higher energies reaches 10%, which is far above our predictions.

On the other hand, in the cases of Sco X-1 (La Monaca et al. 2024b) or GX 13+1 (Bobrikova et al. 2024a,b), a clear absence of PA rotation with energy suggested that the SL, at least in our model, cannot produce the harder component of the spectrum.

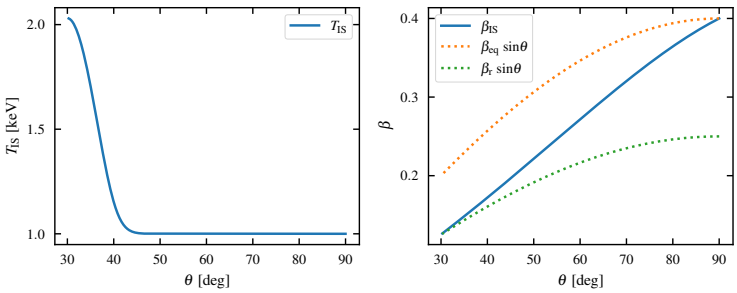


Fig. 5. Effective temperature (left panel) and velocity of the matter flow (right panel) for the Inogamov-Sunyaev SL as functions of the colatitude. The parameters are $\theta_{peak} = 30°$, $\beta_r = 0.25$, and $\beta_{eq} = 0.4$.

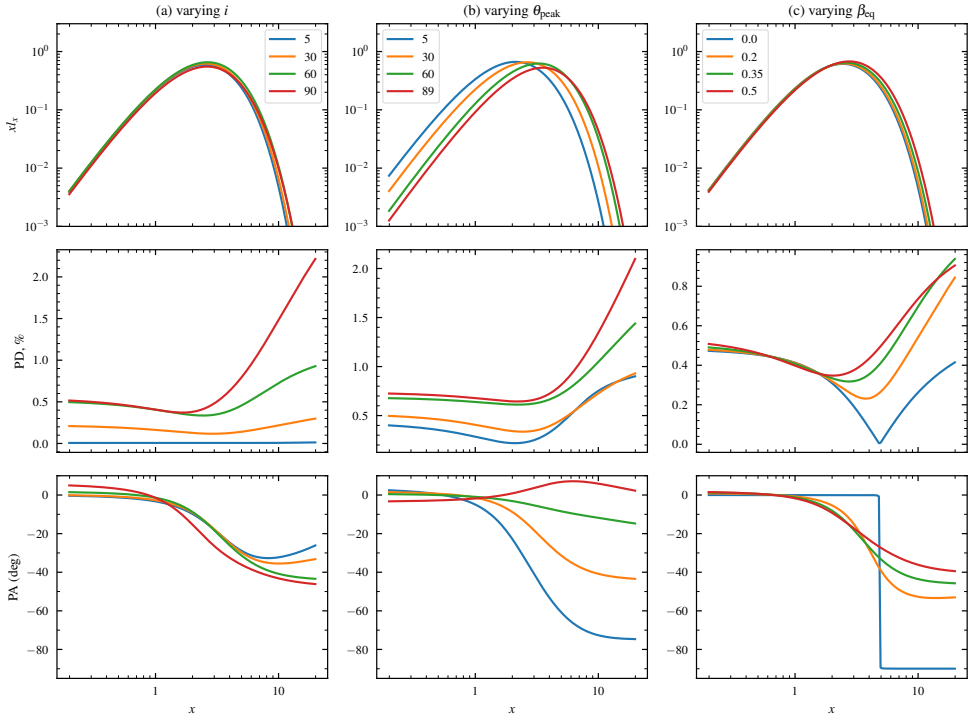


Fig. 6. Spectropolarimetric characteristic of the Inogamov-Sunyaev SL model. The upper panels show the dimensionless luminosity xI_x, and the middle and lower panels show the PD and PA as functions of the dimensionless photon energy $x = E/f_c k_B T_*$. The fiducial parameter set is $\theta_{peak} = 30°$, $i = 60°$, $\beta_r = 0.25$, and $\beta_{eq} = 0.4$. Column (a) shows the results for various inclinations. The blue, orange, green, and red lines correspond to $i = 5°$, 30°, 60°, and 90°, respectively. Column (b) shows the results for various colatitudes of the peak θ_{peak}. The blue, orange, green, and red lines correspond to $\theta_{peak} = 5°$, 30°, 60°, and 89°, respectively. Column (c) shows the results for various equatorial velocities. The blue, orange, green, and red lines correspond to $\beta_{eq} = 0$, 0.2, 0.35, and 0.5, respectively. In this case, the edge velocity was fixed at $\beta_r = 0.5\beta_{eq}$.

The most peculiar case of the Cir X-1 (Rankin et al. 2024) required a complicated explanation of the observed phenomena, but the authors concluded that the Comptonized component of the spectrum might come from the SL in the hard state of the source, while in the soft state, the Comptonized emission might come from the BL. In sources GX 9+9 (Ursini et al. 2023),

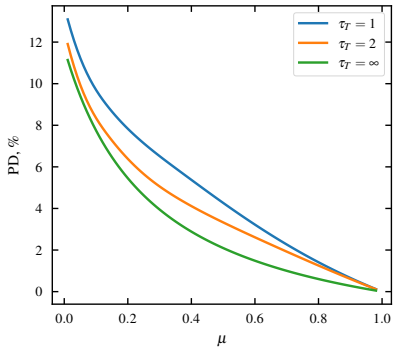


Fig. 7. PD as a function of emission angle $\mu = \cos\alpha'$ for various SL optical thicknesses.

GX 5−1 (Fabiani et al. 2024), and XTE J1701−462 (Cocchi et al. 2023), a misalignment in the PA of the two components was found, but the statistics did not allow us to properly constrain the shift in the PA. There is no clear conclusion about the geometry of these sources.

The model supports the data interpretation, but it is not fully capable of explaining the observed phenomena, even when an assumption about the presence of the SL in the source is made. Thus, additional sources of polarized emission are needed. For example, radiation produced close to the NS surface can be further scattered in the wind above the disk (Tomaru et al. 2024; Nitindala et al. 2025) or be reflected from the disk (Lapidus & Sunyaev 1985), which could lead to a higher PD of the emission. Observational results leave much space for further improvements to the current SL model.

6. Summary

We developed a theoretical model for the emission from the SL of the WMNS. We derived exact analytic expressions for the Stokes parameters of the emission. We accounted for the special relativistic effects and light bending when calculating the PA.

We computed the emission from the source with various geometries of the SL, and we accounted for the velocity of matter. We studied the impact of the inclination, matter velocity, and the geometrical configuration of the SL on the polarization of the observed emission. We calculated the polarization from the Inogamov-Sunyaev SL, where both the velocity of the matter and the intensity of the emission are functions of colatitude.

We showed that for all the tested scenarios, the PD of the emission does not exceed 1.5%. Recent observations of the IXPE satellite showed that WMNSs emit light with stronger polarization, especially at higher energies. Hence, the SL, at least the current model, cannot be the only mechanism to explain the data. A higher polarization of the harder component of the WMNS spectrum can come from the reflection of the SL emission from the disk, scattering of the SL emission in the wind above the accretion disk, the emission from the jet, and others. Developing the emission models for these processes is the next step for further investigation of WMNSs. We also note the significant variability of the PA with energy that is observed in the emission of the SL.

The developed model can support the IXPE data analysis, and it was successfully used to interpret the already existing results of IXPE. Combined with other tools and methods, it can shed new light on the geometry of the WMNSs and their emission mechanisms.

Acknowledgements. This research was supported by the Academy of Finland grant 333112, and the grants 002200175 and 00240328 of the Finnish Cultural Foundation (AB). We thank the referee for their useful suggestions.

References

Beloborodov, A. M. 2002, ApJ, 566, L85
Bhargava, Y., Ng, M., Zhang, L., et al. 2024, ApJ, submitted [arXiv:2405.19324]
Bobrikova, A., Forsblom, S. V., Di Marco, A., et al. 2024a, A&A, 688, A170
Bobrikova, A., Di Marco, A., La Monaca, F., et al. 2024b, A&A, 688, A217
Bogdanov, S., Lamb, F. K., Mahmoodifar, S., et al. 2019, ApJ, 887, L26
Capitanio, F., Fabiani, S., Gnarini, A., et al. 2023, ApJ, 943, 129
Chandrasekhar, S. 1960, Radiative Transfer (New York: Dover)
Cocchi, M., Gnarini, A., Fabiani, S., et al. 2023, A&A, 674, L10
Di Marco, A., La Monaca, F., Poutanen, J., et al. 2023, ApJ, 953, L22
Di Marco, A., La Monaca, F., Bobrikova, A., et al. 2025, ApJ, 979, L47
Dovčiak, M., Muleri, F., Goosmann, R. W., Karas, V., & Matt, G. 2008, MNRAS, 391, 32
Fabiani, S., Capitanio, F., Iaria, R., et al. 2024, A&A, 684, A137
Farinelli, R., Fabiani, S., Poutanen, J., et al. 2023, MNRAS, 519, 3681
Farinelli, R., Waghmare, A., Ducci, L., & Santangelo, A. 2024, A&A, 684, A62
Gnarini, A., Ursini, F., Matt, G., et al. 2022, MNRAS, 514, 2561
Inogamov, N. A., & Sunyaev, R. A. 1999, Astron. Lett., 25, 269
La Monaca, F., Di Marco, A., Ludlam, R. M., et al. 2024a, A&A, 691, A253
La Monaca, F., Di Marco, A., Poutanen, J., et al. 2024b, ApJ, 960, L11
Lapidus, I. I., & Sunyaev, R. A. 1985, MNRAS, 217, 291
Li, L.-X., Narayan, R., & McClintock, J. E. 2009, ApJ, 691, 847
Loktev, V., Veledina, A., & Poutanen, J. 2022, A&A, 660, A25
Long, K. S., Chanan, G. A., & Novick, R. 1980, ApJ, 238, 710
Nitindala, A. P., Veledina, A., & Poutanen, J. 2025, A&A, 694, A230
Poutanen, J. 2020, A&A, 639, A33
Poutanen, J., & Beloborodov, A. M. 2006, MNRAS, 373, 836
Poutanen, J., & Gierliński, M. 2003, MNRAS, 343, 1301
Rankin, J., La Monaca, F., Di Marco, A., et al. 2024, ApJ, 961, L8
Saade, M. L., Kaaret, P., Gnarini, A., et al. 2024, ApJ, 963, 133
Salmi, T., Nättilä, J., & Poutanen, J. 2018, A&A, 618, A161
Shakura, N. I., & Sunyaev, R. A. 1988, Adv. Space Res., 8, 135
Sobolev, V. V. 1963, A Treatise on Radiative Transfer (Princeton: Van Nostrand)
Suleimanov, V. F., Poutanen, J., & Werner, K. 2020, A&A, 639, A33
Sunyaev, R. A., & Titarchuk, L. G. 1985, A&A, 143, 374
Tomaru, R., Done, C., & Odaka, H. 2024, MNRAS, 527, 7047
Ursini, F., Farinelli, R., Gnarini, A., et al. 2023, A&A, 676, A20
Ursini, F., Gnarini, A., Capitanio, F., et al. 2024, Galaxies, 12, 43
van der Klis, M. 1989, ARA&A, 27, 517
van der Klis, M. 2000, ARA&A, 38, 717
Viironen, K., & Poutanen, J. 2004, A&A, 426, 985
Weisskopf, M. C., Kestenbaum, H. L., Long, K. S., et al. 1976, BAAS, 8, 493
Weisskopf, M. C., Soffitta, P., Baldini, L., et al. 2022, JATIS, 8, 026002

A. Bobrikova, A. Veledina, J. Poutanen, V. Loktev
Breaking the symmetry: X-ray polarization from a spreading layer on a tilted weakly magnetized neutron star

Astronomy & Astrophysics, submitted

V

Astronomy & Astrophysics manuscript no. output
September 8, 2026
©ESO 2026

Breaking the symmetry: X-ray polarization from a spreading layer on a tilted weakly magnetized neutron star

Anna Bobrikova[1]★, Alexandra Veledina[1,2], Juri Poutanen[1], and Vladislav Loktev[3]

[1] Department of Physics and Astronomy, FIN-20014 University of Turku, Finland
[2] Nordita, Stockholm University and KTH Royal Institute of Technology, Hannes Alfvéns väg 12, SE-10691 Stockholm, Sweden
[3] School of Mathematics, Statistics, and Physics, Newcastle University, Newcastle upon Tyne NE1 7RU, UK

September 8, 2026

ABSTRACT

When modeling the emission from an X-ray binary system, we often assume that the rotational axis of the compact object is aligned with that of the binary system. While often considered irrelevant for spectroscopic observations, the orientation of the binary system is crucial for polarimetric properties. With the recent advent of X-ray polarimetric observations enabled by the *Imaging X-ray Polarimetry Explorer* (*IXPE*), indications of a possible misalignment of the neutron star rotational axis with respect to the binary axis have been reported. Following these indications, we present an analytical model for the polarimetric properties of emission arising from a spreading layer on an inclined weakly magnetized neutron star (WMNS). We discuss the expected polarimetric properties and study the impact of geometrical parameters of the system on the polarization of WMNS emission. We compare our results with those for aligned systems. Finally, we discuss applications of the model to recent and upcoming X-ray polarimetric observations with *IXPE* and mention the suggestions for further development of the model.

Key words. methods: analytical – polarization – stars: neutron – X-rays: binaries

1. Introduction

In an X-ray binary with a weakly magnetized neutron star (WMNS), the accretion flow is barely affected by the magnetosphere of the neutron star (NS) and is instead shaped by gravity. Once the companion star fills its Roche lobe, matter from the outer layers of the companion star is transferred from the companion star and is driven towards the NS. The matter transferred through the inner Lagrangian point carries a high specific angular momentum; it circulates around the NS, forming an accretion disk (Shakura & Sunyaev 1973). In WMNS systems, the mass accretion rate is so high that the accretion disk can push the magnetosphere towards the NS surface or even burying it beneath the NS surface. Consequently, the accretion disk is either mildly affected by the magnetosphere or reaches the NS surface unaffected by the magnetic field; in either scenario, matter accretes onto the equatorial region of the NS rather than onto the magnetic field poles as in pulsars. As the accretion disk reaches the NS surface, the matter is forced to decelerate rapidly from near-Keplerian velocities in the accretion disk to the rotational velocity of the NS surface before settling onto the NS. A so-called boundary layer (BL; see, e.g., Shakura & Sunyaev 1988) is formed. The accreted matter can subsequently spread over the NS surface, forming a spreading layer (SL, Inogamov & Sunyaev 1999).[1]

The spectrum of WMNS systems is traditionally decomposed into two main components: the softer disk emission and the harder emission from the BL/SL. Additional spectral features include reflection of the harder component from the disk and scattering of the emission in the wind above the disk. In spectroscopy, the disk and BL/SL components are often hard to distinguish. Timing analysis helps distinguish these components, since BL/SL emission is expected to vary on much faster timescales. For instance, quasi-periodic oscillations (QPOs) have been shown to be associated with the BL/SL region (Gilfanov et al. 2003; Revnivtsev & Gilfanov 2006). However, timing cannot determine the exact geometry of the accretion flow or distinguish between the BL and SL configurations.

Polarimetry holds promise to investigate the geometry of binary systems. With the launch of the *Imaging X-ray Polarimetry Explorer* (*IXPE*; Weisskopf et al. 2022) in December 2021, it became possible, for the first time, to measure with high precision the polarization degree (PD) and polarization angle (PA) of WMNS X-ray emission. In addition to providing information on the geometrical configuration of the system, polarimetric properties carry information about the processes affecting the emission as it travels from the source to the observer, since X-ray emission becomes polarized through scattering, reflection, or interaction with the magnetic field. In recent years, more than twenty WMNS systems have been observed with *IXPE*, and observations of many of these systems have provided constraints on the source geometry.

Since the early stages of X-ray astronomy, various theoretical models for the expected polarized emission of binary systems have been developed in preparation for X-ray polarimetric observations. For instance, the polarimetric properties of accretion disks were studied in Rees (1975) based on pioneering work of Chandrasekhar (1960) and Sobolev (1963), under the assumption of electron-scattering-dominated disk atmospheres. Relativistic effects were later incorporated into the model by, e.g.,

★ Corresponding author: anna.a.bobrikova@utu.fi

[1] We note here that the terms BL and SL have been conflated in the literature; in this paper, we use BL to denote the boundary region between the accretion disk and the NS surface, and SL for the extension of the accretion flow onto the NS surface.

Connors et al. (1980), Dovčiak et al. (2008), and Loktev et al. (2022). Currently, for linear polarization in the *IXPE* energy range, the expected PD is 2% for moderate inclination, rising to 6% for $i = 80°$ (Loktev et al. 2022). Polarization is expected to be aligned with the accretion disk plane.

For the BL/SL, polarimetric expectations strongly depend on the geometry of the region. Both pioneering analytical works (Sunyaev & Titarchuk 1985; Lapidus & Sunyaev 1985) and modern numerical simulations, e.g., Gnarini et al. (2022), predict that emission arising from a BL configuration of the accretion flow is polarized in the plane of the accretion disk, whereas for the SL configuration, the emission is expected to be polarized perpendicular to the disk plane. In recent analytical modeling, Bobrikova et al. (2025, hereafter B25) calculated that the PD of the SL is not expected to exceed 1.5% and that the emission is polarized in the plane perpendicular to the accretion disk, with minor variations depending on the energy and geometrical configuration of the system. Similar conclusions are presented in Farinelli et al. (2024).

Both scattering in the wind (Nitindala et al. 2025) and reflection from the accretion disk (Lapidus & Sunyaev 1985; Matt 1993; Poutanen et al. 1996) are expected to boost the total polarization of the WMNS emission. However, the contributions of reflection component to the total flux are usually small, and the scattered fraction is low for the systems observed from low and medium inclinations Nitindala et al. (2025), so the general expected PD of WMNS systems remains relatively low.

However, recent *IXPE* observations have shown that for many sources the observed PD values significantly exceed theoretical expectations (see, e.g., Ursini et al. 2024; Di Marco 2025; Gnarini et al. 2025, for reviews). In several cases, at higher energies, where the Comptonized component is expected to dominate the flux, the PD exceeded 10%. Among possible explanations for the high PD, scattering in the wind and reflection from the disk are usually mentioned (see, among many others, Gnarini et al. 2025); however, not all the systems are known to have strong winds or to show signs of reflection. For instance, GX 5−1 is known for a lack of reflection features (Homan et al. 2018) and does not show signs of a strong wind in X-ray spectroscopy, yet the observed PD exceeds 4% at higher energies (Fabiani et al. 2024). One possible explanation for the unexpectedly high PD in these systems is a breaking of the axial symmetry.

Another known issue is the PA of the continuum components: although theoretically the PA of the Comptonized component is expected to be aligned with or orthogonal to that of the disk, for several sources, a PA difference of about 60° has been observed. Notably, the young X-ray binary Cir X-1 was one such source, and in this source, a misalignment between the rotational axis of the NS and the binary axis was suggested as a possible explanation (Rankin et al. 2024), since hints of misalignment such as precession of the accretion disk and twisted jets had already been observed in this system (Coriat et al. 2019; Cowie et al. 2025).

Here, we introduce an analytical model of polarized SL emission from a misaligned NS. In Sect. 2 we present the model, describing the physical properties of the SL emission, its propagation, and the geometrical configuration of the system. In Sect. 3 we present the results of our study of the impact of various system parameters on the observed emission. We discuss the application of our model to previous *IXPE* observations in Sect. 4. Finally, we conclude in Sect. 5.

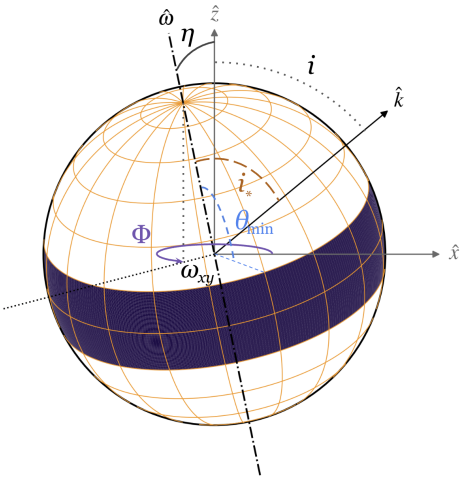


Fig. 1. Geometry of the problem. The rotational axis of the NS ω is misaligned relative to the rotational axis of the binary system (z) by an angle η. The rotational axis of the NS forms the azimuthal angle Φ (marked with a purple solid line) with the direction to the observer ($\hat{\boldsymbol{k}}$). The inclinations of the binary system, i, and of the NS, i_*, are indicated by black dotted and brown dashed lines, respectively. The SL is shown in dark purple and is confined between co-latitudes $\theta_{\rm min}$ (marked with a blue dashed line) and $\theta_{\rm max} = 180° - \theta_{\rm min}$. The accretion disk lies in the xy plane; it is omitted from the sketch for clarity.

2. Model setup

The geometry of the system is shown in Fig. 1. We consider a spherical NS of radius R and mass M with a SL centered at the NS equator and extending between the co-latitudes of the SL edges, $\theta_{\rm min}$ and $\theta_{\rm max} = 180° - \theta_{\rm min}$. The matter in the SL flows counterclockwise with the equatorial velocity $\beta_{\rm eq}$ and the velocity decreasing towards the poles as described in Eq. (A.4). The SL emission is assumed to correspond to the constant effective temperature $T_{\rm eff}$ and is modeled as a semi-infinite electron-scattering-dominated plane-parallel slab.

We assume that the rotation axis of the binary system is aligned with the z-coordinate axis, and the accretion disk lies in the xy-coordinate plane. The coordinates are chosen so that the vector in the direction of the observer $\hat{\boldsymbol{k}}$ lies in the xz plane and makes an angle i with the binary rotation axis, giving

$$\hat{\boldsymbol{k}} = (\sin i, 0, \cos i). \tag{1}$$

We assume that the NS rotational axis $\hat{\boldsymbol{\omega}}$ is misaligned with respect to the rotational axis of the binary system by an angle η and to form an azimuthal angle Φ with the direction to the observer $\hat{\boldsymbol{k}}$ in the xy-plane:

$$\hat{\boldsymbol{\omega}} = (\sin\eta\cos\Phi, \sin\eta\sin\Phi, \cos\eta). \tag{2}$$

The NS inclination i_*, defined as the angle between the direction to the observer and the NS rotational axis $\hat{\boldsymbol{\omega}}$, is given by

$$\cos i_* = \hat{\boldsymbol{k}} \cdot \hat{\boldsymbol{\omega}} = \cos i\ \cos\eta + \sin i \sin\eta \cos\Phi. \tag{3}$$

To relate the current model to the axisymmetric case presented in B25, where the NS rotation axis was aligned with the orbital axis, we move to the coordinate system associated with the NS. We then define all the necessary vectors in that new coordinate system, which we refer to as the "NS frame", and denote their coordinates with the subscript *. Here, z_* is aligned with the NS rotational axis $\hat{\boldsymbol{\omega}} = (0,0,1)_*$ and we define the coordinate axes as follows:

$$\begin{aligned}\hat{\boldsymbol{x}}_* &= \hat{\boldsymbol{y}}_* \times \hat{\boldsymbol{\omega}} = (\hat{\boldsymbol{k}} - \hat{\boldsymbol{\omega}}\cos i_*)/\sin i_*,\\ \hat{\boldsymbol{y}}_* &= \hat{\boldsymbol{\omega}} \times \hat{\boldsymbol{k}}/\sin i_*,\\ \hat{\boldsymbol{z}}_* &= \hat{\boldsymbol{\omega}}.\end{aligned} \tag{4}$$

The direction to the observer in this system is

$$\hat{\boldsymbol{k}} = (\sin i_*, 0, \cos i_*)_*. \tag{5}$$

Introducing the co-latitude θ and the azimuthal angle ϕ, which specify a point on the NS surface in that coordinate system, we can define the normal to the surface element:

$$\hat{\boldsymbol{n}} = (\sin\theta\cos\phi, \sin\theta\sin\phi, \cos\theta)_*. \tag{6}$$

This geometry is used to calculate the polarized emission from the SL on an aligned NS using the formalism presented in Suleimanov et al. (2020) and B25. For completeness, we provide the necessary formulae in Appendix A. We assume that the spectrum of the local emission can be described by a diluted blackbody

$$I'_{E'}(\alpha') = a_{\rm es}(\alpha')\frac{1}{f_{\rm c}^4}B_{E'}(f_{\rm c}T_{\rm eff}), \tag{7}$$

where $B_{E'}$ is the Planck function, $f_{\rm c}$ is the color correction factor, and $a_{\rm es}(\alpha') = 0.421 + 0.868\cos\alpha'$ is an approximation to the angular distribution of radiation intensity from a semi-infinite, electron-scattering-dominated atmosphere (Chandrasekhar & Breen 1947) as a function of the zenith angle α' in the local comoving frame of the gas. The Stokes vector (flux) produced by a SL surface element $\mathrm{d}S$ is given by

$$\mathrm{d}\boldsymbol{F}(E) = \begin{pmatrix} \mathrm{d}F_I(E)\\ \mathrm{d}F_Q(E)\\ \mathrm{d}F_U(E)\end{pmatrix} = \mathrm{d}F_E\begin{pmatrix} 1\\ P(\alpha')\cos 2\chi\\ P(\alpha')\sin 2\chi\end{pmatrix}, \tag{8}$$

where P is the PD at the zenith angle α', calculated using the approximation (Chandrasekhar 1960) for a semi-infinite electron-scattering-dominated atmosphere. The PA χ is calculated using the formula derived in Poutanen (2020b) that accounts for corrections caused by the relativistic motion of the SL matter and light bending in the Schwarzschild metric.

The misalignment must be included in the PA calculation. The PA is measured counterclockwise with respect to the orbital axis as $\chi_{\rm tot} = \chi + \chi_{\rm m}$, where the angle $\chi_{\rm m}$ is the position angle of the NS rotational axis measured eastward (i.e. counterclockwise) from the projection of the orbital axis onto the sky. To compute $\chi_{\rm m}$, we introduce the polarization basis related to the orbital coordinate system:

$$\hat{\boldsymbol{e}}^z_x = \frac{\hat{\boldsymbol{z}} - \hat{\boldsymbol{k}}\cos i}{\sin i} = (-\cos i, 0, \sin i), \tag{9}$$

$$\hat{\boldsymbol{e}}^z_y = \frac{\hat{\boldsymbol{k}} \times \hat{\boldsymbol{z}}}{\sin i} = (0, -1, 0). \tag{10}$$

The polarization basis related to the coordinate system of the misaligned NS is similarly defined as

$$\hat{\boldsymbol{e}}^*_x = \frac{\hat{\boldsymbol{\omega}} - \hat{\boldsymbol{k}}\cos i_*}{\sin i_*} = \frac{1}{\sin i_*}\begin{pmatrix}\sin\eta\cos\Phi - \sin i\cos i_*\\ \sin\eta\sin\Phi\\ \cos\eta - \cos i\cos i_*\end{pmatrix}, \tag{11}$$

$$\hat{\boldsymbol{e}}^*_y = \frac{\hat{\boldsymbol{k}} \times \hat{\boldsymbol{\omega}}}{\sin i_*}. \tag{12}$$

Then, we calculate $\chi_{\rm m}$ using

$$\cos\chi_{\rm m} = \hat{\boldsymbol{e}}^*_x \cdot \hat{\boldsymbol{e}}^z_x = \frac{\cos\eta\sin i - \sin\eta\cos i\cos\Phi}{\sin i_*}, \tag{13}$$

$$\sin\chi_{\rm m} = \hat{\boldsymbol{e}}^*_x \cdot \hat{\boldsymbol{e}}^z_y = -\frac{\sin\eta\sin\Phi}{\sin i_*},$$

or

$$\tan\chi_{\rm m} = \frac{\sin\eta\sin\Phi}{\sin\eta\cos i\cos\Phi - \cos\eta\sin i}. \tag{14}$$

Once the Stokes flux produced by a surface element is estimated, we can then integrate over the whole SL. To account for light bending, we introduce the visibility condition for the surface element $\cos\alpha > 0$, as in Suleimanov et al. (2020) (see Appendix A). The misalignment of the NS rotational axis with the accretion disk axis requires one more visibility condition. The observer cannot see the parts of the NS covered by the accretion disk, which is mathematically expressed as the inequality $\hat{\boldsymbol{n}} \cdot \hat{\boldsymbol{z}} > 0$. Since $\hat{\boldsymbol{n}}$ is defined in the coordinate system associated with the NS, we need $\hat{\boldsymbol{z}}$ in the same coordinate system:

$$\hat{\boldsymbol{z}} = (\hat{\boldsymbol{x}}_* \cdot \hat{\boldsymbol{z}}, \hat{\boldsymbol{y}}_* \cdot \hat{\boldsymbol{z}}, \hat{\boldsymbol{z}}_* \cdot \hat{\boldsymbol{z}}) = \begin{pmatrix}(\cos i - \cos\eta\cos i_*)/\sin i_*\\ -\sin i\sin\eta\sin\Phi/\sin i_*\\ \cos\eta\end{pmatrix}_*. \tag{15}$$

The second visibility condition $\hat{\boldsymbol{n}} \cdot \hat{\boldsymbol{z}} > 0$ then takes the form

$$\cos\eta\cos\theta + \sin\eta\sin\theta\cos(\Phi_* - \phi) > 0, \tag{16}$$

where Φ_* is the azimuth of the orbital angular momentum vector in the NS frame and

$$\begin{aligned}\cos\Phi_* &= (\sin\eta\cos i - \cos\eta\sin i\cos\Phi)/\sin i_*,\\ \sin\Phi_* &= -\sin i\sin\Phi/\sin i_*.\end{aligned} \tag{17}$$

Thus, for $\theta < \pi/2 - \eta$, an element is visible for any ϕ, whereas for $\theta > \pi/2 + \eta$ it is invisible. In the intermediate regime, $\pi/2 - \eta < \theta < \pi/2 + \eta$, the visibility condition reads $\cos(\Phi_* - \phi) > -\cot\theta\cot\eta$, which is equivalent to $|\Phi_* - \phi| < \phi_0 \equiv \pi - \arccos(\cot\theta\cot\eta)$.

The total polarized flux from the SL is then calculated as follows:

$$\begin{aligned}\boldsymbol{F}(E) &= \begin{pmatrix}F_I(E)\\ F_Q(E)\\ F_U(E)\end{pmatrix} = \frac{R^2}{D^2}\iint\limits_{\substack{\cos\alpha>0\\ \hat{\boldsymbol{n}}\cdot\hat{\boldsymbol{z}}>0}} \cos\alpha\,\mathcal{D}\left(\delta\sqrt{1-u}\right)^3 \\ &\times I'_{E'}(\alpha',\theta)\begin{pmatrix}1\\ P(\alpha')\cos 2\chi_{\rm tot}\\ P(\alpha')\sin 2\chi_{\rm tot}\end{pmatrix}\mathrm{d}\cos\theta\,\mathrm{d}\phi.\end{aligned} \tag{18}$$

Here $u = R_{\rm S}/R$ is the NS compactness, $R_{\rm S} = 2GM/c^2$ is the Schwarzschild radius, $\mathcal{D}$ is the lensing factor, $I'_{E'}$ is the intensity of escaping radiation in the comoving frame, and D is the distance to the source. Finally, we obtain the polarimetric properties of the SL emission:

$$P_{\rm obs} = \frac{\sqrt{F_Q^2 + F_U^2}}{F_I} \tag{19}$$

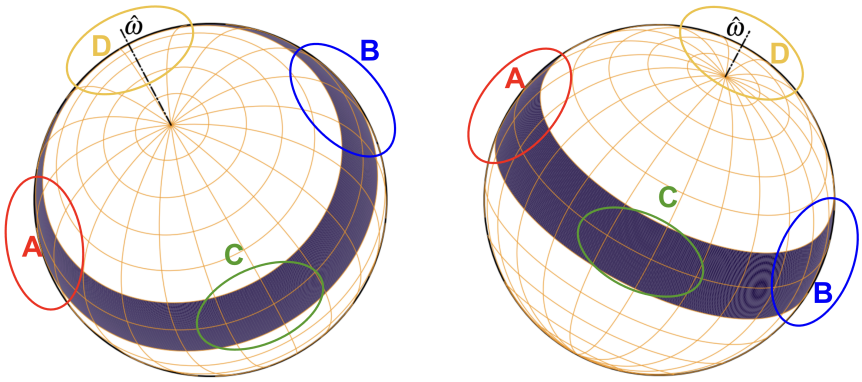


Fig. 2. A sketch of a SL on the surface of a NS with compactness $u = 0.34$ as seen by a distant observer. The matter in the SL flows counterclockwise. The main regions of the SL are shown in different colors: red (zone A) is the flank of the SL with approaching flow; blue (zone B) is the flank of the SL with receding flow; green (zone C) is the main body of the SL; and yellow (zone D) is the back of the SL that is visible in some geometrical configurations due to light bending around the NS. For clarity, the accretion disk is omitted from the sketch.

and

$$\cos(2\chi_{\rm obs}) = F_Q/(P_{\rm obs}F_I), \quad \sin(2\chi_{\rm obs}) = F_U/(P_{\rm obs}F_I). \tag{20}$$

3. Results

We applied the formalism developed in Sect. 2 to study the effects of the misalignment in the system on the observed spectral and polarimetric properties. We use dimensionless variables, such as the photon energy:

$$x = \frac{E}{f_{\rm c} k_{\rm B} T_{\rm eff}}, \tag{21}$$

where $k_{\rm B}$ is the Boltzmann constant. We scaled the observed flux to the typical flux at the NS surface $\sigma_{\rm SB} T_{\rm eff}^4$ and the ratio of the distance squared to the emitting area, to introduce the dimensionless luminosity (Stokes vector):

$$\begin{aligned} x\,\boldsymbol{l}_x &= \frac{D^2}{\Delta R^2}\frac{E\boldsymbol{F}_E}{\sigma_{\rm SB}T_{\rm eff}^4} = \frac{15}{\pi^5}\iint_S \cos\alpha\ \mathcal{D}\ \left(\delta\sqrt{1-u}\right)^4 a_{\rm es}(\alpha') \\ &\times \frac{x'^4}{{\rm e}^{x'}-1}\begin{pmatrix} 1 \\ P(\alpha')\cos 2\chi_{\rm tot} \\ P(\alpha')\sin 2\chi_{\rm tot} \end{pmatrix} {\rm d}\cos\theta\,{\rm d}\phi, \end{aligned} \tag{22}$$

where Δ is the fraction of the NS surface covered by the SL and $x' = x/(\delta\sqrt{1-u})$ is the dimensionless photon energy in the comoving frame (see Appendix A for details).

The results are sensitive to several parameters: the azimuthal angle Φ, the obliquity angle η, the orbital inclination i, the colatitude of the SL edge $\theta_{\rm min}$, the dimensionless equatorial velocity $\beta_{\rm eq}$ (see Appendix A), and the photon energy x. The parameter combinations used in the simulations presented in this section are listed in Table 1.

In Fig. 2, a sketch of a SL on the surface of an misaligned WMNS with compactness $u = 0.34$ is shown. The main regions of the SL are marked in different colors. These regions make significantly different contributions to both the luminosity and the polarimetric properties of the SL emission. Regarding the luminosity, Zone C accounts for the majority of the emission, Zone A contributes at higher energies, Zone B contributes at lower energies, and Zone D is only visible in some cases. For a plane-parallel slab, the polarimetric properties depend on the angle between the slab surface normal and the direction to the observer: the larger this angle, the larger the PD. This means that Zones A (approaching flow on the flank of the SL) and B (receding flow on the other flank of the SL) emit more strongly polarized light in the direction of the observer than Zone C (main body of the SL), whereas emission from Zone C is mostly unpolarized. Zone D (back of the SL) has a PD similar to those of Zones A and B, although the PA is different: since the emission from a plane-parallel slab is polarized in the plane of the slab surface, the PA of the emission from Zone D is almost orthogonal to those of Zones A and B.

Table 1. List of parameters used in the simulations presented in this section.

Figure	Φ (deg)	η (deg)	i (deg)	$\theta_{\rm min}$ (deg)
Fig. 3 (a)	0	v	75	60
Fig. 3 (b)	45	v	75	60
Fig. 3 (c)	90	v	75	60
Fig. 4 (a)	45	15	v	75
Fig. 4 (b)	45	15	75	v
Fig. 4 (c)	v	15	75	75
Fig. 5 (a)	–	–	30	$90-\eta$
Fig. 5 (b)	–	–	50	$90-\eta$
Fig. 5 (c)	–	–	70	$90-\eta$
Fig. 6 (a)	–	15	–	75
Fig. 6 (b)	–	30	–	60

Notes. Parameters varied along the plot axes are indicated by a "–" sign. The letter "v" indicates that multiple values of the parameter are used and specified in the corresponding plot legend. The equatorial velocity is fixed at $\beta_{\rm eq} = 0.35$ for all studies presented in this section. The energy is fixed at $E = 5$ keV for Figs. 5 and 6.

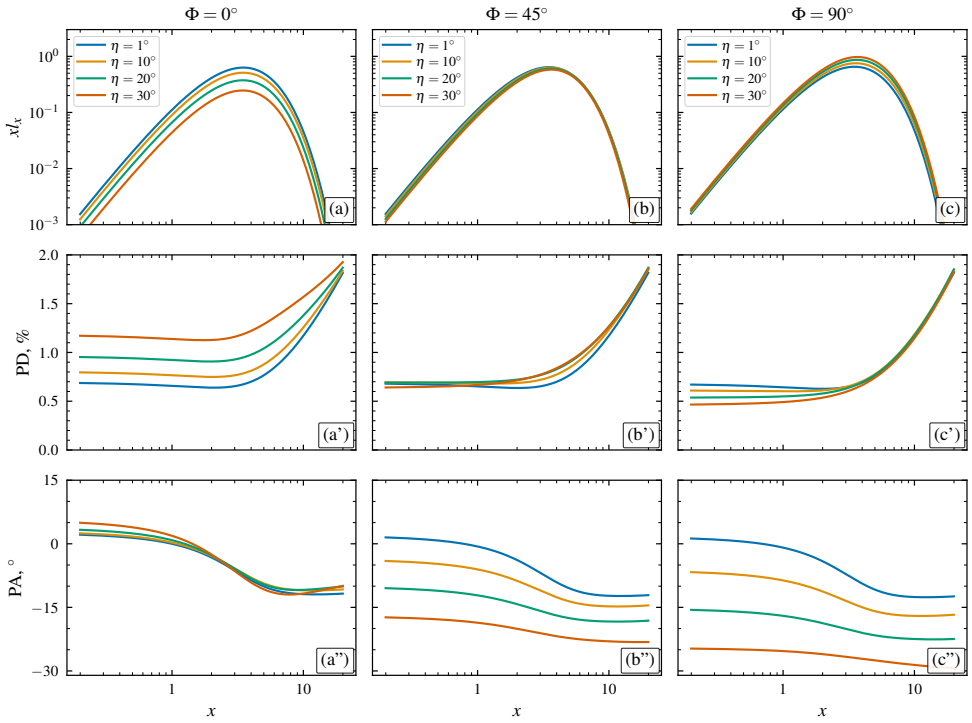


Fig. 3. Dimensionless luminosity xI_x, PD, and PA as functions of the dimensionless photon energy, x. Fiducial parameter values are listed in Table 1. Blue, orange, green, and red lines correspond to obliquity angles η of 1°, 10°, 20°, and 30°, respectively. Azimuthal angle Φ is 0° in panels (a)–(a"), 45° in panels (b)–(b"), and 90° in panels (c)–(c").

3.1. Tilt effects on the polarization signatures

In this section, we study the effect of the azimuthal angle Φ and the obliquity η on the energy dependence of luminosity, PD, and PA. We chose a rather wide SL with $\theta_{\rm min} = 60°$ and $\theta_{\rm max} = 120°$, so that varying η up to 30° would not break the continuity of the accretion flow. We fixed the inclination at $i = 75°$ and the SL equatorial velocity to $\beta_{\rm eq} = 0.35$; for these parameters, a relatively high PD is expected (B25). The combination pf parameters used for each case is listed in Table 1.

In Fig. 3, we consider three different values of the azimuthal angle, Φ, of 0°, 45°, and 90°. For each case, we show the dimensionless luminosity, PD, and PA for four different values of the misalignment angle η. In panels (a)–(a"), the observer is in the plane formed by the NS and disk axes (we denote this plane by τ). The dimensionless luminosity decreases with the obliquity angle η, while PD increases with η. In all cases, the emission is polarized perpendicular to the disk.

The increase in PD is caused by the partial coverage of Zone C by the accretion disk. As η increases, the contribution of Zone C to the total flux decreases, while the contributions of Zones A and B become more important. The reduced contribution of Zone C therefore leads to an increase in the net polarization. At higher energies, the contribution of Zone A becomes dominant. This explains both the increase in PD at higher energies and the slight change in PA with energy.

In panels (c)–(c") of Fig. 3, the plane τ is orthogonal to the xz-plane, in which the observer vector $\hat{\boldsymbol{k}}$ lies. In this geometry, changes in obliquity have a weaker effect on PD. The main effect of changing the obliquity appears at lower energies, where PD decreases with increasing obliquity. The PA, on the other hand, changes significantly with η, with PA $\approx -\eta$.

In this geometry, the accretion disk partially covers Zone B. The contribution of Zone B is most prominent at lower energies, where PD decreases with increasing obliquity. As η increases, a larger fraction of Zone B is covered, reducing the contribution of Zone B to the total emission. Since the emission from Zone B is more strongly polarized than that from Zone C, this leads to a decrease in PD. The emission then comes mainly from Zones A and C, and PA is determined by the orientation of Zone A with respect to the accretion disk plane. Since this orientation depends on η, this produces a correlation between the predicted PA and obliquity η.

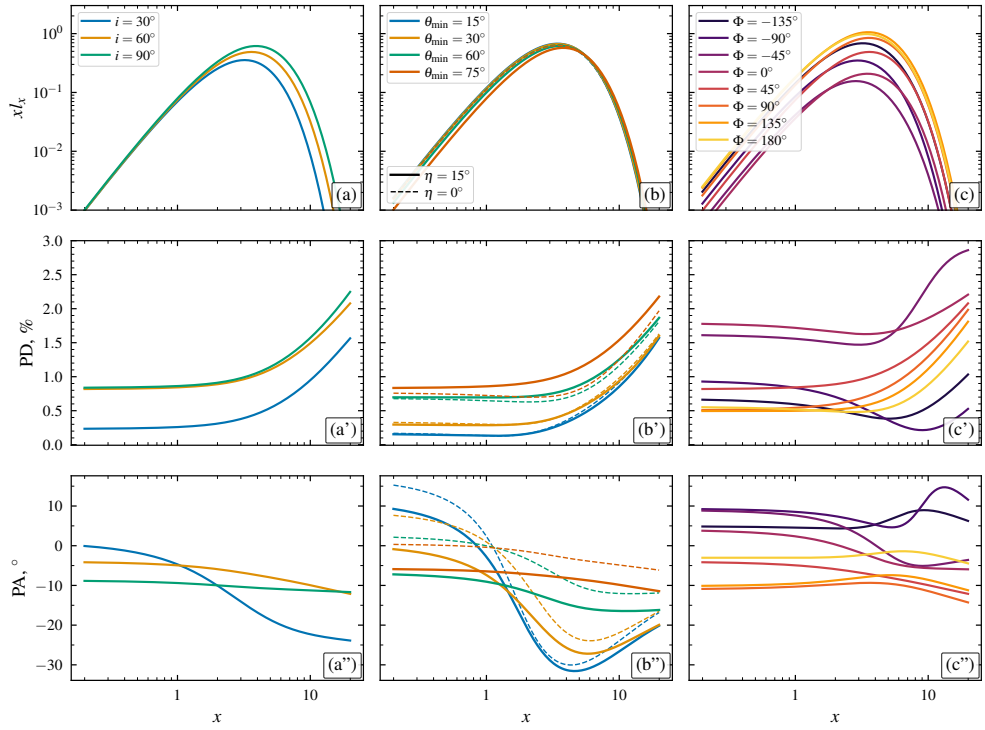


Fig. 4. Dimensionless luminosity xI_x, PD, and PA as functions of the dimensionless photon energy, x. Fiducial parameter values are listed in Table 1. Panels (a)–(a"): the orbital inclination is varied; blue, orange, and green lines correspond to 30°, 60°, and 90°, respectively. Panels (b)–(b"): the co-latitude of the SL edge $\theta_{\rm min}$ is varied; blue, orange, green, and red lines correspond to 15 °, 30°, 60°, and 75°, respectively. Solid lines correspond to $\eta = 15°$, while dashed lines correspond to the aligned case with $\eta = 0°$ from B25. Panels (c)–(c"): the azimuthal angle Φ is varied; the lines, colored according to the `inferno` palette, correspond to −135°, −90°, −45°, 0°, 45°, 90°, 135°, and 180°, respectively.

The case of $\Phi = 45°$ in panels (b)–(b") is less straightforward. It shows intermediate PD and a complex PA dependence on η, as expected for a combination of the behaviors seen in panels (a)–(a") and (c)–(c"). In this geometry, parts of both Zones B and C are covered by the accretion disk, so the mechanisms present in the two previous cases are present simultaneously. For PD, these two effects together result in little dependence of PD on η. For PA, the orientation of Zone A with respect to the accretion disk plane remains a dominant factor, as in panel (c"), although the PA-η relation is mildly affected by the different azimuthal angle Φ.

3.2. Parameter space study

Next, we considered the effects of changing the orbital inclination i, the co-latitude of the SL edge $\theta_{\rm min}$, and the azimuthal angle Φ for a fixed obliquity $\eta = 15°$. The full set of parameters for each panel is given in Table 1. The results are shown in Fig. 4.

Panels (a)–(a") illustrate the effect of changing the orbital inclination $i_{\rm orb}$. The results show the standard trend of PD increasing with orbital inclination and PA varying slightly around the direction orthogonal to the disk plane (B25). In the case of $i = 30°$, all four Zones contribute to the flux, while for the other two cases, Zone D does not. Panel (a) shows a shift in the peak energy, which is associated with the Doppler effect. For a fixed velocity $\beta_{\rm eq}$, the Doppler effect is stronger at higher inclinations, because the projection of the velocity onto the direction to the observer is larger at higher inclinations in the current configuration of the system.

In panels (b)–(b"), we showed the impact of the SL width by varying the edge co-latitude $\theta_{\rm min}$. For comparison, we also showed the corresponding results for an aligned star with dashed lines (B25). Since dimensionless luminosity is normalized to the surface area of the SL, panel (b) shows almost no effect of $\theta_{\rm min}$ on xI_x. Panel (b') shows that, similarly to the aligned case (B25), the narrower the SL, the higher the PD. In the case of $\theta_{\rm min} = 15°$, most of the NS surface is covered by the SL, and the geometry of the SL approaches a sphere, which contributes to depolarization (B25). This effect weakens with increasing $\theta_{\rm min}$.

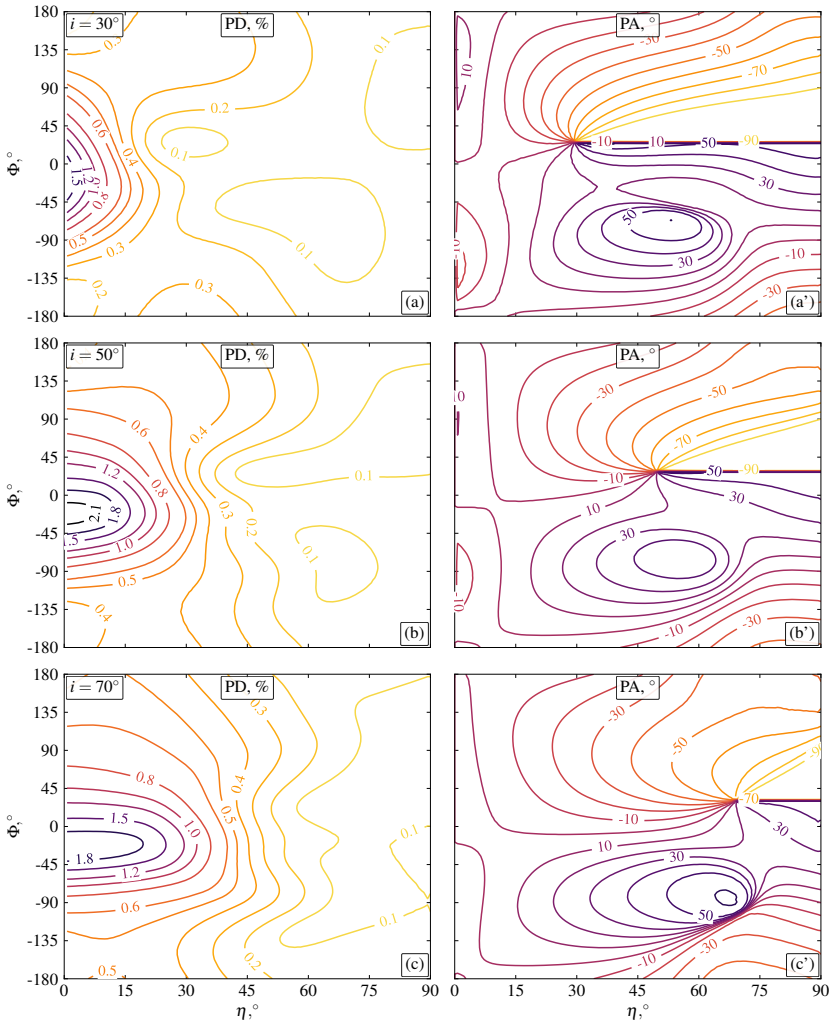


Fig. 5. Contour plots of PD and PA as functions of obliquity η and azimuthal angle Φ. Panels (a)–(a'): orbital inclination $i = 30°$; panels (b)–(b'): $i = 50°$; panels (c)–(c'): $i = 70°$. Remaining parameter values are listed in Table 1.

The misalignment in this case contributes to a minor increase in PD for $\theta_{\min} = 75°$ and $\theta_{\min} = 60°$, while the emission from a wider SL seems almost unaffected by the misalignment. Similarly, PA is mildly affected by the misalignment, with the difference being more noticeable for narrower SLs with $\theta_{\min} = 75°$ and $\theta_{\min} = 60°$. The reason behind this change with respect to the case of $\eta = 0°$ again lies in the partial covering of Zone C by the accretion disk and the slight asymmetry introduced by observing the system from $\Phi = 45°$. This effect is less present for a wider SL, where emission is depolarized.

In panels (c)–(c"), we show the effect of varying the azimuthal angle Φ. The dimensionless luminosity shown in panel (c) strongly depends on Φ. For $\Phi = 0°$ or $180°$, the problem is axially symmetric, similar to the case presented in Fig. 3, panels (a)–(a"). Zones A and B contribute equally to the flux. However, for $0° < \Phi < 180°$, Zone B is partially or completely covered by the accretion disk, and hence the peak energy increases. For

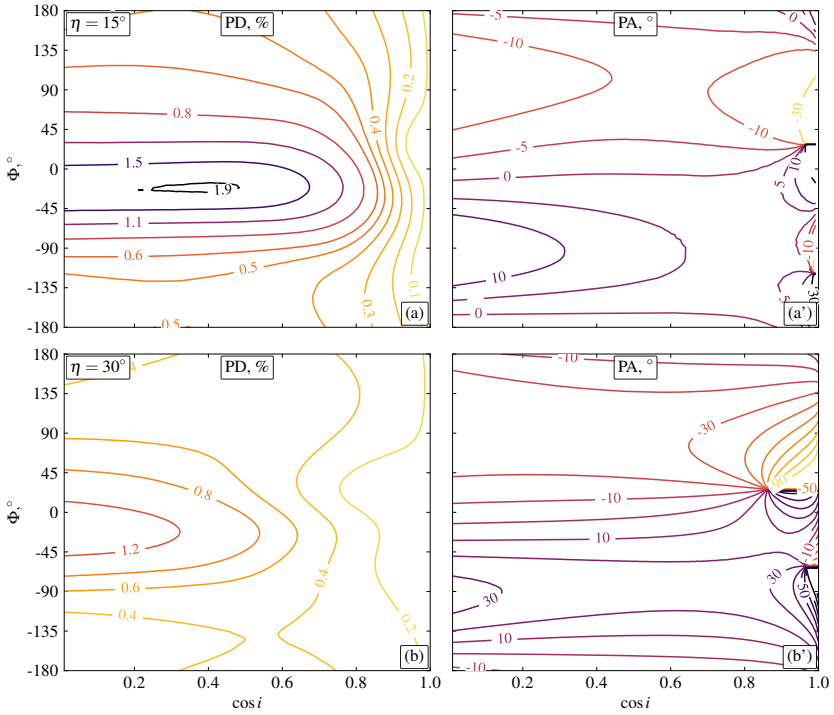


Fig. 6. Contour plots of PD and PA as functions of the azimuthal angle Φ and the cosine of the orbital inclination cos *i*. Panels (a)–(a'): obliquity $\eta = 15°$; panels (b)–(b'): $\eta = 30°$. Remaining parameter values are listed in Table 1.

$-180° < \Phi < 0°$, the situation is reversed: Zone A is partially or completely covered by the accretion disk, and the peak energy decreases. Since the luminosity is normalized to the full surface area of the SL, not to the visible part, the peak luminosity also changes significantly, increasing by an order of magnitude between the case of $\Phi = 0°$, where Zone C is covered by the accretion disk, and the case of $\Phi = 180°$, where a larger fraction of Zone C is visible, since the star is tilted in the direction opposite to the observer.

We note that for $\Phi = 0°$ and $\Phi = -45°$, the PD is higher than in other cases. The PA varies within a range of approximately 20° as Φ changes, first slowly decreasing as Φ increases from −45° to 135°, and then slowly increasing for the other hemisphere. This is caused by the fact that PA mostly depends on the minimal co-latitude that is covered by the SL, which changes slowly with the azimuthal angle in the misaligned case. For a larger obliquity angle η, a larger variation in PA is expected.

3.3. Monochromatic polarization as a function of orientation

After studying the energy dependence of spectropolarimetric properties, we fixed the photon energy and calculated PD and PA for all possible combinations of obliquity η and azimuthal angle Φ. We linked the co-latitude of the SL edge to the obliquity angle through the relation $\theta_{\rm min} = 90° - \eta$, so that there is never a gap between the SL and the accretion disk. In this configuration, the SL is wider for systems with larger misalignment. We kept the same equatorial flow velocity $\beta_{\rm eq} = 0.35$. To characterize the average PD and PA in the *IXPE* energy range, we chose to study monochromatic polarization at $E = 5$ keV. In the previous section, we used the dimensionless energy x, and since the energy is now expressed in keV, we also had to fix the effective temperature $T_{\rm eff}$ and the color correction $f_{\rm c}$ for the SL. Based on spectroscopic studies of WMNSs, we adopted $f_{\rm c}\, T_{\rm eff} = 2$ keV. As before, all the parameter values for each simulation are listed in Table 1.

In Fig. 5, the results are shown for three different orbital inclinations, *i*, of 30°, 50°, and 70°. The case of the lowest orbital inclination presented in panel (a) shows PD < 0.5%, except for the region of $\eta < 15°$. For small η, the width of the SL plays a crucial role, significantly increasing the polarization. Panels (b) and (c) show that, for moderate or high inclination, PD can remain higher than 1% even at larger values of η, which in this simulation correspond to a rather wide SL. We note that PD reaches its maximum for $-45° < \Phi < 0°$. Contrary to the results shown in panels (a'), (b'), and (c') of Fig. 3, PD is higher for smaller obliquity angles in this simulation. Here, η is connected to the SL width, and the effect of the SL width on PD dominates the

Table 2. Probability (in %) of detecting PD higher than the threshold for different obliquity values.

PD (%)	η (deg)					
	5	10	15	20	25	30
≥ 0.5	39	50	48	55	46	36
≥ 1.0	28	25	21	17	12	7.8
≥ 1.5	15	12	9.2	6.1	3.0	0.4
≥ 2.0	2.9	0.8	0.0	0.0	0.0	0.0

behavior, while in Fig. 3, the SL width was fixed. The PA is strongly influenced by the obliquity, as seen in panels (b") and (c") of Fig. 3. The behavior of the polarimetric properties shows a common topology for different inclinations; for instance, the PD maxima occur in similar regions in panels (b) and (c). PA depends strongly on both Φ and η at all considered inclinations.

Next, we investigated the probability of detecting the PD higher than the threshold for a fixed obliquity η. For this study, we assumed a flat distribution for both $\cos i$ and Φ. The results are shown in Fig. 6. We show the constant PD contours for two values of obliquity, η, of 15° and 30°. Contrary to panels (a') and (b') of Fig. 3, where the highest PD was expected for $\eta = 30°$, here we observe the decrease of PD with misalignment; this is due to the fact that SL is wider for $\eta = 30°$, since we set $\theta_{\min} = 90° - \eta$. The calculated probabilities of observing a PD higher than the threshold value are given in Table 2. We considered six obliquity values and four PD levels. We did not consider $\eta > 30°$, since PD drops rapidly at higher obliquity due to an increase in the SL width. Since the probability distribution of η is likely not flat, to understand the true probability of observing the system at a given level of PD, we need to convolve the reported probabilities with the probability distribution of η in the WMNS population. We can, however, conclude that only for a few values of η does the probability of observing a PD higher than 1% exceed 20%, and the 2% PD level is rarely reached, with a probability exceeding 1% only for $\eta = 5°$.

4. Discussion

The results presented in Sect. 3 show several important trends. Regarding the spectrum, the main result is that misalignment affects the spectral shape, an effect that should be taken into account when performing the spectral decomposition. For the PD, we note that breaking the axial symmetry increases the expected PD with respect to the aligned case presented in B25, with PD exceeding 2% for some parameter combinations (see Table 2 for examples). Regarding the PA, we conclude that misalignment in the system allows the polarization plane to take any orientation.

Before comparing the model predictions with the observational results, it is important to discuss the possibility of misalignment in a WMNS system. When an X-ray binary is formed following the collapse of a normal star into a compact object, the rotation axis of the compact object is not required to be aligned with the orbital axis (Wang et al. 2006). The accretion process reduces the obliquity, since angular momentum is transferred from the disk to the NS via the accretion flow. The timescale for the alignment process depends on the mass accretion rate, magnetic field strength, rotation rate of the NS, and other parameters.

Theoretical expectations for the alignment time in binaries are discussed in the literature for several subclasses of sources: for instance, de Kool & van Paradijs (1987) estimated the alignment time for millisecond pulsars at $\approx 10^6$ years, while Abolmasov et al. (2024) suggests a significantly shorter alignment time for strongly magnetized NSs. Martin et al. (2008) estimated an alignment time of 10^7 years for the black hole X-ray binary GRO J1655−40 is reported. However, no theoretical expectations have been derived for WMNSs. Although most of these objects are considered to be rather old (e.g. the age estimate of Cyg X-2 is 4×10^8 yr; King & Ritter 1999), some are known to be considerably younger, and possibly young enough to remain misaligned. For instance, the age of Sco X-1 is estimated to be 7×10^6 yr (Kar et al. 2025), while Cir X-1 is less than 5×10^3 yr old (Heinz et al. 2013). The alignment time can also be extended by additional factors related to binary evolution and by events occurring during it. For instance, if the accretion process has been episodic, or if the binary system is particularly wide, the accretion-driven alignment could take a significantly longer time (Laycock et al. 2025).

Cir X-1 as the first and most compelling candidate for a potentially misaligned WMNS. Apart from being the youngest known WMNS system, Cir X-1 is known to have precessing jets (Cowie et al. 2025) and a high eccentricity of 0.4–0.45 (Jonker et al. 2007; Johnston et al. 2016), with even higher values reported in the earlier work, e.g., 0.94 in Tauris et al. (1999). The presence of a kick during the supernova event in this system has been discussed as a possible explanation for both the jets and the eccentricity, and with an age of less than 10^4 yr, there may not have been sufficient time for the NS rotational axis to align with the orbital axis through accretion.

The *IXPE* observation of Cir X-1 in August 2023 revealed strong PA variability with spectral hardness and source state, as well as a PA that was misaligned with both the assumed disk plane and the jet axis. Obliquity in the system has been suggested as one of the possible explanations for the observed polarimetric behavior. Rankin et al. (2024) suggest that, based on the temporal evolution of PA, Cir X-1 exhibited different accretion-flow geometries during the observations, with the geometry during P3 including an SL. During that part of the observation, Cir X-1 had a PD of 1.4% and a PA= −12° neither orthogonal nor aligned with the jet position angle reported to be between −40° and −70°. If we assume the jet direction to be orthogonal to the accretion disk plane, the observed PA would correspond to 30° and 60° in our simulations. As shown in Fig. 5, such a PA is expected for an azimuthal angle Φ between $\approx -135°$ and $\approx -45°$ and an obliquity η larger than $\approx 30°$. More precise constraints on η are difficult to derive due to the uncertainty in the PA. We note that the exact numbers also depend on the inclination of the system and other parameters that are assumed rather than inferred, in the simulations. Accounting for both PD and PA does not tighten the constraints; Fig. 5 illustrates that PD does not reach 1.4% within the stated ranges of obliquity and azimuthal angles in our simulation, at least for the selected set of parameters. We can, however, conclude from Fig. 5 that higher inclinations are favored, since PD in the selected region rises with inclination. This could be interpreted as a hint of a relatively high inclination of the system. However, we note that the PD prediction is strongly affected by assumptions regarding the SL structure and composition; while we consider only scattering off electrons, introducing ions and accounting for absorption in the SL could significantly increase the expected PD (Ratheesh et al. 2024). Given these uncertainties, we do not derive any tighter constraints on the Cir X-1 geometry from the PD predictions.

Apart from Cir X-1, a few other systems have exhibited signs of misalignment based on *IXPE* observations. For instance, in GX 5−1, a variability of PA with energy by 60° was reported (Fabiani et al. 2024), which can be reproduced by our model. In

GX 13+1, misalignment could serve as an explanation for the PA variability with time (Bobrikova et al. 2024; Li et al. 2025). Although both of these systems are considered old, with an approximate age of 10^8 yr, little is known about the duration of their active accretion phase. We neither favor nor rule out misalignment as a possibility in these systems; rather, we provide a model to investigate the polarimetric properties of these objects under the assumption of misalignment. We look forward to studying the results of further spectropolarimetric observations of these systems.

5. Summary

We developed a model for the spectropolarimetric properties of the emission of a SL on a tilted WMNS, whose rotational axis is not aligned with that of the binary system. We investigated how luminosity, PD, and PA depend on energy and on the geometrical parameters of the system, such as the obliquity angle η, the azimuthal angle Φ, the inclination of the binary system i, and the co-latitude of the SL edge $\theta_{\rm min}$.

We conclude that the expected polarimetric properties of the SL emission depend strongly on the geometrical parameters of the system. First, we find that breaking the axial symmetry contributes to an increase in the PD of the SL emission. Additionally, we show that misalignment in the system could explain why the observed PA is neither aligned with nor orthogonal to the assumed disk plane or binary rotational axis. Consistent with the aligned case studied in B25, PD increases with energy and inclination and decreases with increasing SL width. We find that a higher PD is predicted for azimuthal angles in the range $\Phi = -45°$–$0°$. The effect of the obliquity angle strongly depends on the SL width, which is connected to the mass accretion rate (Inogamov & Sunyaev 1999). For luminous systems with a wider SL, PD is higher for larger values of η, as seen in Fig. 3; in less luminous systems, where the width of the layer is connected to the obliquity as shown in Sect. 3.3, PD is higher for lower obliquity.

In recent years, observations of several systems have shown indications of misalignment, and in this paper we predict their polarimetric properties under the assumption of misalignment. The formalism derived here can be used to interpret existing and upcoming spectropolarimetric observations of WMNSs. The misalignment scenario can be realized in cases in which transfer of angular momentum from the accretion disk has not significantly altered the orientation of the NS rotational axis. The most natural candidates for this scenario are young systems such as Cir X-1. Older systems like GX 13+1 and other WMNSs require episodic mass transfer or additional mechanisms to reduce the effect of the accretion process on the NS spin; in such cases, a non-negligible obliquity may persist even in older systems.

Acknowledgements. This research was supported by the grant 00240328 of the Finnish Cultural Foundation (AB), by the Research Council of Finland Centre of Excellence in Neutron-Star Physics (grant 374064) and grants 355672 and 372881 (AV). Nordita is supported in part by NordForsk.

References

Abolmasov, P., Biryukov, A., & Popov, S. B. 2024, Galaxies, 12, 7
Beloborodov, A. M. 2002, ApJ, 566, L85
Bobrikova, A., Poutanen, J., & Loktev, V. 2025, A&A, 696, A181
Bobrikova, A., Forsblom, S. V., Di Marco, A., et al. 2024, A&A, 688, A170
Chandrasekhar, S. 1960, Radiative transfer (New York: Dover)
Chandrasekhar, S., & Breen, F. H. 1947, ApJ, 105, 435
Connors, P. A., Piran, T., & Stark, R. F. 1980, ApJ, 235, 224
Coriat, M., Fender, R. P., Tasse, C., et al. 2019, MNRAS, 484, 1672
Cowie, F. J., Fender, R. P., Heywood, I., et al. 2025, MNRAS, 544, L37
de Kool, M., & van Paradijs, J. 1987, A&A, 173, 279
Di Marco, A. 2025, Astronomische Nachrichten, 346, e20240126
Dovčiak, M., Muleri, F., Goosmann, R. W., Karas, V., & Matt, G. 2008, MNRAS, 391, 32
Fabiani, S., Capitanio, F., Iaria, R., et al. 2024, A&A, 684, A137
Farinelli, R., Waghmare, A., Ducci, L., & Santangelo, A. 2024, A&A, 684, A62
Gilfanov, M., Revnivtsev, M., & Molkov, S. 2003, A&A, 410, 217
Gnarini, A., Ursini, F., Matt, G., et al. 2022, MNRAS, 514, 2561
—. 2025, A&A, 699, A230
Heinz, S., Sell, P., Fender, R. P., et al. 2013, ApJ, 779, 171
Homan, J., Steiner, J. F., Lin, D., et al. 2018, ApJ, 853, 157
Inogamov, N. A., & Sunyaev, R. A. 1999, Astronomy Letters, 25, 269
Johnston, H. M., Soria, R., & Gibson, J. 2016, MNRAS, 456, 347
Jonker, P. G., Nelemans, G., & Bassa, C. G. 2007, MNRAS, 374, 999
Kar, A., Ojha, P., & Bhattacharyya, S. 2025, ApJ, 980, 51
King, A. R., & Ritter, H. 1999, MNRAS, 309, 253
Lapidus, I. I., & Sunyaev, R. A. 1985, MNRAS, 217, 291
Laycock, S. G. T., Cappallo, R. C., Pradhan, P., Christodoulou, D. M., & Paul, B. 2025, ApJ, 978, 80
Li, H., Zhao, Q.-C., Feng, H., Tao, L., & Tsygankov, S. S. 2025, ApJ, 994, 41
Loktev, V., Veledina, A., & Poutanen, J. 2022, A&A, 660, A25
Luminet, J.-P. 1979, A&A, 75, 228
Martin, R. G., Tout, C. A., & Pringle, J. E. 2008, MNRAS, 387, 188
Matt, G. 1993, MNRAS, 260, 663
Nitindala, A. P., Veledina, A., & Poutanen, J. 2025, A&A, 694, A230
Poutanen, J. 2020a, A&A, 639, A33
—. 2020b, A&A, 641, A166
Poutanen, J., & Gierliński, M. 2003, MNRAS, 343, 1301
Poutanen, J., Nagendra, K. N., & Svensson, R. 1996, MNRAS, 283, 892
Rankin, J., La Monaca, F., Di Marco, A., et al. 2024, ApJ, 961, L8
Ratheesh, A., Dovčiak, M., Krawczynski, H., et al. 2024, ApJ, 964, 77
Rees, M. J. 1975, MNRAS, 171, 457
Revnivtsev, M. G., & Gilfanov, M. R. 2006, A&A, 453, 253
Shakura, N. I., & Sunyaev, R. A. 1973, A&A, 24, 337
—. 1988, Adv. Space Res., 8, 135
Sobolev, V. V. 1963, A treatise on radiative transfer (Princeton: Van Nostrand)
Suleimanov, V. F., Poutanen, J., & Werner, K. 2020, A&A, 639, A33
Sunyaev, R. A., & Titarchuk, L. G. 1985, A&A, 143, 374
Tauris, T. M., Fender, R. P., van den Heuvel, E. P. J., Johnston, H. M., & Wu, K. 1999, MNRAS, 310, 1165
Ursini, F., Gnarini, A., Capitanio, F., et al. 2024, Galaxies, 12, 43
Viironen, K., & Poutanen, J. 2004, A&A, 426, 985
Wang, C., Lai, D., & Han, J. L. 2006, ApJ, 639, 1007
Weisskopf, M. C., Soffitta, P., Baldini, L., et al. 2022, JATIS, 8, 026002

Appendix A: Polarized emission from an aligned spreading layer

To calculate the polarized emission from the SL, we first derived an equation for the polarized flux coming from a small surface element $\mathrm{d}F_E$, and then integrated that emission over the whole visible surface of the SL in the coordinate system associated with the NS rotation axis. Main equations have been derived in Poutanen (2020a) and Suleimanov et al. (2020). For the assumed spherical NS, the surface normal $\hat{\boldsymbol{n}}$ coincides with the radius-vector of the element $\hat{\boldsymbol{r}}$ and thus the angle ψ between $\hat{\boldsymbol{n}}$ and the direction to the observer $\hat{\boldsymbol{k}}$ is

$$\cos\psi \equiv \hat{\boldsymbol{k}}\cdot\hat{\boldsymbol{n}} = \cos i_*\cos\theta + \sin i_*\sin\theta\cos\phi, \tag{A.1}$$

where $\phi = 0$ when the element was closest to the observer. The emission angle $\alpha(\psi)$ (i.e., the angle to the surface normal in the external frame) was calculated using Beloborodov (2002) approximation

$$\cos\alpha(\psi) \equiv \hat{\boldsymbol{k}}_0\cdot\hat{\boldsymbol{n}} \approx 1-(1-u)(1-\cos\psi), \tag{A.2}$$

with the visibility condition for the surface element being $\cos\alpha > 0$. Here, $u = R_\mathrm{S}/R$ is the NS compactness, and $\hat{\boldsymbol{k}}_0$ is the unit vector of the photon momentum close to the surface,

$$\hat{\boldsymbol{k}}_0 = \frac{\sin\alpha\,\hat{\boldsymbol{k}} + \sin(\psi-\alpha)\,\hat{\boldsymbol{n}}}{\sin\psi}. \tag{A.3}$$

Similarly to B25, we defined the velocity of the material in the SL by the direction of the unit vector $\hat{\boldsymbol{v}} = (-\sin\phi, \cos\phi, 0)_*$ and the amplitude (in units of speed of light) as a function of latitude

$$\beta(\theta) = \beta_\mathrm{eq}\sin\theta = \frac{A\,v_\mathrm{kepl}}{c}\sin\theta = A\sqrt{\frac{u}{2\,(1-u)}}\sin\theta, \tag{A.4}$$

with $A < 1$ being a proportionality coefficient that scales equatorial velocity relative to the Keplerian velocity v_kepl in the Schwarzschild metric (Luminet 1979). The angle between the velocity vector and the photon direction is then (Poutanen & Gierliński 2003):

$$\cos\xi = \hat{\boldsymbol{v}}\cdot\hat{\boldsymbol{k}}_0 = \frac{\sin\alpha}{\sin\psi}\,\hat{\boldsymbol{v}}\cdot\hat{\boldsymbol{k}} = -\frac{\sin\alpha}{\sin\psi}\sin i_*\,\sin\phi\,. \tag{A.5}$$

We calculated the observed flux at energy E from the surface element with area $\mathrm{d}S = R^2\mathrm{d}\cos\theta\mathrm{d}\phi$ as follows:

$$\mathrm{d}F_E = I_E\mathrm{d}\Omega_\mathrm{obs} = \mathcal{D}\cos\alpha\frac{\mathrm{d}S}{D^2}, \tag{A.6}$$

where $\mathcal{D}$ is the lensing factor that is equal to one in the Beloborodov approximation.

To account accurately for the relativistic effects of the matter rotation, we moved to the frame co-rotating with the SL matter. We considered the SL element to be an electron-dominated semi-infinite slab (Chandrasekhar 1960; Sobolev 1963) so that we could compute the angular distribution and polarization of the escaping radiation. We assumed the local intensity $I'_{E'}(\alpha',\theta)$ to have a diluted blackbody shape, same as in Suleimanov et al. (2020) and B25, given by Eq. (7). The angle α' made by the photon momentum with the surface normal in the co-rotating frame is related to the emission angle α defined in Eq. (A.2) as (Poutanen & Gierliński 2003)

$$\cos\alpha' = \delta\cos\alpha, \tag{A.7}$$

where δ is the Doppler factor

$$\delta = \frac{1}{\gamma(1-\beta\cos\xi)} \tag{A.8}$$

and γ is the Lorentz factor

$$\gamma(\theta) = \frac{1}{\sqrt{1-\beta^2(\theta)}}. \tag{A.9}$$

The local intensity $I'_{E'}$ can depend on co-latitude θ but we consider here the effective temperature and the color correction factors to be constant throughout the SL. The observed intensity is related to the local one:

$$I_E = \left(\frac{E}{E'}\right)^3 I'_{E'}(\alpha',\theta) = \left(\delta\sqrt{1-u}\right)^3 I'_{E'}. \tag{A.10}$$

The total observed flux coming from the surface element was calculated as

$$\mathrm{d}F_E = \frac{R^2}{D^2}\cos\alpha\,\mathcal{D}\,\left(\delta\sqrt{1-u}\right)^3 I'_{E'}(\alpha',\theta)\,\mathrm{d}\cos\theta\,\mathrm{d}\phi, \tag{A.11}$$

where D is the distance to the source.

Polarimetric properties of the SL emission can be described by the Stokes vector:

$$\mathrm{d}\boldsymbol{F}(E) = \begin{pmatrix}\mathrm{d}F_I(E)\\ \mathrm{d}F_Q(E)\\ \mathrm{d}F_U(E)\end{pmatrix} = \mathrm{d}F_E\begin{pmatrix}1\\ P\cos 2\chi\\ P\sin 2\chi\end{pmatrix}, \tag{A.12}$$

where P is the PD of the escaping radiation, and χ is the PA. We calculated PD using the approximation from Viironen & Poutanen (2004) for a semi-infinite electron-scattering-dominated atmosphere (Chandrasekhar 1960):

$$P = P_\mathrm{es}(\alpha') = -\frac{1-\cos\alpha'}{1+3.582\cos\alpha'}\,0.1171, \tag{A.13}$$

and the PA with the formulae derived by Poutanen (2020b):

$$\tan\chi = \frac{\sin\theta\sin\phi + \beta\,A}{-\sin i_*\cos\theta + \cos i_*\sin\theta\cos\phi i_* - \beta\sin\phi\,C}, \tag{A.14}$$

where

$$\begin{aligned} A &= \frac{\sin\psi}{\sin\alpha}B + \frac{\cos\alpha-\cos\psi}{\sin\alpha\sin\psi}(\cos\phi - B\cos\psi),\\ B &= \sin i_*\sin\theta + \cos i_*\cos\theta\cos\phi,\\ C &= \frac{\sin\psi}{\sin\alpha}\cos\theta + \frac{\cos\alpha-\cos\psi}{\sin\alpha\sin\psi}(\cos i_* - \cos\theta\cos\psi). \end{aligned} \tag{A.15}$$

These equations account for the effects of rotation of polarization plane because of relativistic motion as well as for light bending in the Schwarzschild metric.